The activity of BAF complexes ensures forebrain development and brain patterning

Dissertation

Zur Erlangung des Grades

Doktor der Naturwissenschaften

Am Fachbereich Biologie

Der Johannes Gutenberg-Universität Mainz

Marie Kube

geb. am 04.10.1992 in Offenbach am Main

Mainz, 2024

Dekan: Prof. Dr. Eckhard Thines

1. Berichterstatter:

2. Berichterstatter:

Tag der mündlichen Prüfung: 27.02.2025

Table of Contents

Table of Abbreviations

aRGC	Apical radial glia cell
ASD	Autism Spectrum Disorder
ATAC	Assay for Transposase-Accessible Chromatin
ATP	Adenosine triphosphate
BAF	BRG1/BRM associated factor
BAFi	BAF inhibitor
bRGC	Basal radial glia cell
BSA	Bovine serum albumin
cBAF	Canonical BAF
cDNA	Complementary DNA
CF	Core Facility
CGE	Caudal ganglionic eminence
CHD	Chromodomain helicase DNA-binding
CRE	cis-regulatory element
CRISPR/Cas9	Clustered regulatory interspaced short palindromic repeats/CRISPR-associated protein 9
CSS	Coffin-Siris Syndrome
CT	Cycle threshold
CUT&Tag	Cleavage Under Target and Tagmentation
D/V	Dorsoventral/Dorsal-to-ventral
DAP	Differentially accessible peaks
DAPI	4′,6-diamidino-2-phenylindole
ddH2O	Double-distilled water
DEG	Differentially expressed gene
DMSO	Dimethyl sulfoxide
DNA	Deoxyribonucleic acid
DNMT	DNA methyltransferase
EB	Embryoid body
ECM	Extracellular matrix
esBAF	Embryonic stem cell BAF
ESC	Embryonic stem cell
ExN	Excitatory neuron
FC	Fold Change
FDR	False discovery rate
GE	Ganglionic eminence
GO	Gene Ontology

GRN	Gene regulatory network
H3K27ac	H3 acetylation at lysine 27
H3K27me3	H3 trimethylation at lysine 27
HAT	Histone acetyltransferase
HDAC	Histone deacetylase
hESC	Human embryonic stem cell
hiPSC	human induced pluripotent stem cells
IMB	Institute of molecular biology
InN	Inhibitory neuron
INO80	Inositol requiring 80
IPC	Intermediate Progenitor
iSVZ	Inner subventricular zone
ISWI	Imitation switch
KO	Knockout
LGE	Lateral ganglionic eminence
lncRNA	Long non-coding RNA
MGE	Medial ganglionic eminence
MSC	Mesenchymal cell
nBAF	Neuron-specific BAF
ncBAF/GBAF	Non-canonical BAF
NCBRS	Nicolaides-Baraitser Syndrome
NEC	Neural epithelial cell
NGS	Next Generation Sequencing
npBAF	Neural progenitor BAF
NPC	Neuroprogenitor cell
NSC	Neural stem cell
OPC	Oligodendrocyte precursor cell
oSVZ	Outer subventricular zone
PBAF	Polybromo-associated BAF
PBS	Phosphate-buffered saline
PCA	Principal component analysis
PCR	Polymerase chain reaction
pcw	post-conception week
PFA	Paraformaldehyde
qPCR	quantitative PCR
R/C	Rostrocaudal/Rostral-to-caudal
RG	Radial glia
RNA	Ribonucleic acid
rRNA	Ribosomal RNA
RT-qPCR	Reverse transcription quantitative PCR
seq	Sequencing
sgRNA/gRNA	Single-guideRNA
SVZ	Subventricular zone
TBS	Tris-bufferd saline
TF	Transcription factor
UMAP	Uniform manifold approximation and projection
WNN	Weighted Nearest Neighbor
WT	Wildtype

Table of Figures

Table of Tables

1 Summary

Proper brain formation during neurodevelopment relies on tightly regulated gene expression, orchestrated by factors such as the ATP-dependent BAF chromatin remodelling complexes. These complexes are essential for ensuring the timely and accurate activation of transcriptional programs. Mutations in BAF complex subunits are linked to neurodevelopmental disorders, including Coffin-Siris Syndrome, Nicolaides-Baraitser Syndrome, Autism Spectrum Disorder, and schizophrenia. Despite their significance, the molecular mechanisms by which BAF complex dysfunction disrupts neurodevelopment remain poorly understood.

To address this, human induced pluripotent stem cells (hiPSCs) were differentiated into brain organoids and subjected to temporary treatment with a BAF complex inhibitor targeting the ATPases SMARCA2 and SMARCA4 at different developmental stages. This approach enabled stage-specific and comprehensive analyses of organoid morphology, gene expression (RNA-seq), chromatin accessibility (ATAC-seq, CUT&Tag), protein localization (immunofluorescence), and single-cell dynamics (snRNA- and snATAC-seq) after inhibition of the BAF chromatin remodelling activity.

The results revealed distinct, stage-specific roles of BAF complexes in neurodevelopment, with the most severe effects observed in early neurodevelopmental stages (day 0–12). Early inhibition (day 0–6) resulted in severe disruption of forebrain identity, a shift towards caudal brain regions, disorganized outgrowths, and altered morphology. Inhibition from day 6–12 caused milder defects, including an increase in dorsal telencephalic subtypes, subtle caudalisation, and enlarged neural rosettes. Both phenotypes were linked to irreversible dysregulation of critical signalling pathways, including WNT, YAP, NOTCH, and BMP — key regulators of brain patterning, neural subtype specification, and axonogenesis. This dysregulation was evidenced by changes in gene expression and chromatin landscapes of signalling pathway genes, their targets, and other patterning and cell fate specification genes. Additionally, ARID1B-mutated hiPSC-derived brain organoids displayed altered chromatin accessibility in regions associated with neurodevelopment, providing insights into subunit-specific effects. Notably, the *ZIC1* and *ZIC4* gene loci were consistently dysregulated following BAF complex inhibition and in the ARID1B-mutated model system, suggesting that these ZIC genes are commonly deregulated upon different BAF complex perturbations.

In conclusion, this study highlights the critical, stage-specific functions of BAF complexes in neurodevelopment. By modulating chromatin accessibility and signalling pathways, BAF complexes regulate brain patterning and neural subtype specification. These findings enhance the understanding of how BAF complex dysfunction contributes to neurodevelopmental disorders and provide a foundation for future therapeutic strategies.

2 Zusammenfassung

Die Entwicklung des Gehirns erfordert eine präzise Kontrolle der Genexpression, die unter anderem durch die ATP-abhängigen BAF Chromatin-Remodellierungs-Komplexe vermittelt wird. Diese Komplexe sind entscheidend für die Aktivierung transkriptioneller Programme und spielen eine zentrale Rolle in zahlreichen Entwicklungsprozessen. Insbesondere die neuronale Entwicklung ist anfällig für Mutationen in BAF-Komplex-Untereinheiten, die mit Erkrankungen wie dem Coffin-Siris-Syndrom, dem Nicolaides-Baraitser-Syndrom, Autismus-Spektrum-Störungen und Schizophrenie assoziiert sind.

Zur Untersuchung der kontextabhängigen Funktionen dieser Komplexe während der Entwicklung des menschlichen Gehirns wurden humane induzierte pluripotente Stammzellen zu Gehirnorganoiden differenziert und in verschiedenen Entwicklungsstadien mit einem Inhibitor behandelt, der die SMARCA2- und SMARCA4-ATPasen der BAF Komplexe blockiert. Diese Methode ermöglichte stadienspezifische, sowie umfassende Analysen morphologischer Veränderungen, transkriptioneller Veränderungen (RNA-Seq), Chromatinmodifikationen (ATAC-seq, CUT&Tag-seq), Proteinlokalisierungen mittels Immunfluoreszenzfärbung und Einzelzelldynamiken (snRNA- und snATAC-seq) nach Störung der BAF Chromatinremodellierungsaktivität.

Die Ergebnisse zeigten, dass die BAF-Komplexe stadienspezifische Funktionen erfüllen, wobei die schwerwiegendsten Effekte in frühen Entwicklungsphasen (Tag 0–12) auftraten. Eine Hemmung in den Tagen 0–6 führte zu einer starken Beeinträchtigung der Vorderhirnidentität, einer Verschiebung hin zu kaudalen Gehirnregionen sowie veränderten morphologischen Eigenschaften. Eine spätere Hemmung (Tag 6–12) verursachte eine Zunahme dorsaler telencephaler Zelltypen und eine milde Kaudalisierung. Beide Phänotypen waren durch eine irreversible Dysregulation zentraler Signalwege wie WNT, YAP, NOTCH und BMP geprägt, die essentiell für die Gehirnregionalisierung sind. Zusätzlich wiesen *ARID1B*-mutierte Organoide eine veränderte Chromatinzugänglichkeit auf, insbesondere an den *ZIC1*- und *ZIC4*-Genloci. Dies deutet darauf hin, dass diese Regionen bei verschiedenen Störungen der BAF-Komplexe dereguliert werden.

Zusammenfassend belegen die Ergebnisse, dass BAF-Komplexe stadienspezifische Funktionen während der neuronalen Entwicklung ausüben. Diese beruhen auf der Regulation der Chromatinzugänglichkeit in Genregionen, die für die Regionalisierung und Zellspezifikation wichtig sind, sowie der Koordination zentraler Signalwege, die diese Prozesse steuern. Die gewonnenen Erkenntnisse bieten neue Einblicke in die Mechanismen neuroentwicklungsbedingter Störungen und eröffnen Perspektiven für potenzielle therapeutische Ansätze.

3 Introduction

3.1 Human brain development

The human brain is an astonishing complex organ, yet it origins from a microscopic tube formed following gastrulation. Human brain development is a prolonged process that begins with neurulation at the end of the third post-conception week (pcw) and continues for 20 to 25 years postnatally to reach full maturation[1]. The formation of this intricate structure involves the generation of approximately 170 billion cells, comprising a diverse array of neuronal and non-neuronal subtypes, along with the formation of trillions of synaptic connections[2,3].

Given this vast anatomical and functional complexity, the precise regulation of cellular proliferation, differentiation, and maturation in a highly coordinated manner is essential. Consequently, brain development follows a tightly orchestrated sequence of neurodevelopmental stages, which partially overlap in time and include the production of specific neuronal and glial subtypes, ultimately forming functional circuits. These stages span neurulation, neurogenesis, neuronal migration, differentiation and neurite outgrowth, followed later by gliogenesis, synaptogenesis, myelination, and synaptic pruning - each critical for the proper formation and integration of the brain's architecture and function[4–6] (**Figure 3.1-1**).

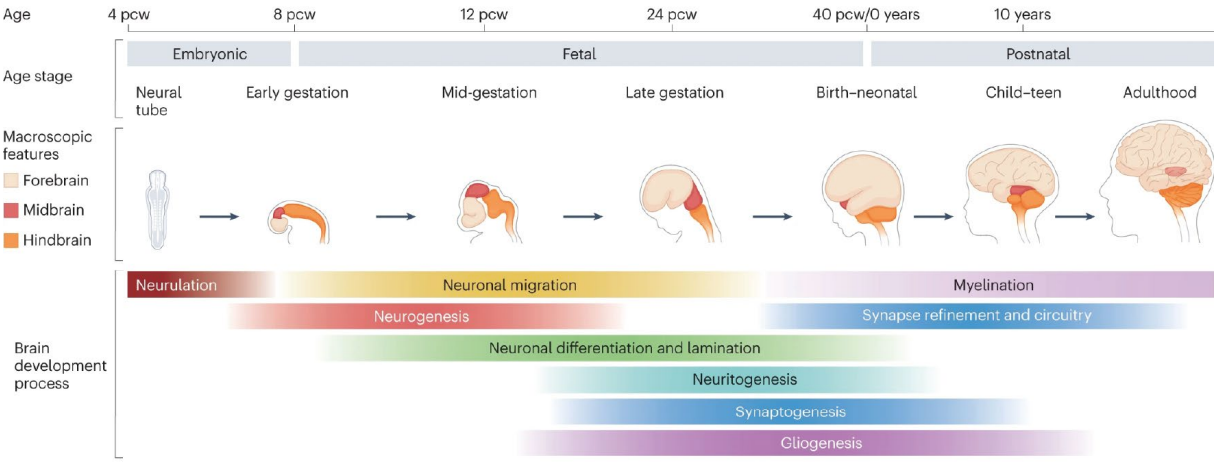

Figure 3.1-1: ***Timeline of human brain development.*** *Human neurodevelopment proceeds through partially overlapping processes, each contributing to the structural and cellular transformations that shape the brain from its origin, the neural tube. pcw = post-conception week Figure from reference*[7].

Hence, examining the transformations of the neural tube and the driving molecular mechanisms throughout embryonic and fetal brain development provides valuable insights into the brain's organization and the integration of its distinct compartments. Since this project focus on embryonic and partially fetal human brain development, the following sections will provide an overview of neurodevelopmental processes occurring between pcw 4 and 13.

3.1.1 Embryonic brain regionalization

Human embryonic tissue specification begins with gastrulation from pcw 2-3, a process leading to the conversion of embryonic tissue into the three primary germ layers ectoderm, endoderm and mesoderm (**Figure 3.1-2 A**). Morphogenesis of these layers is strictly orchestrated and results in cellular diversification to generate hundreds of specialized cells within the human body. At pcw 3, the ectoderm undergoes further specification by a process called neurulation, marking the onset of neurodevelopment and involves the invagination and closure of the neural plate into the neural tube[1,8]. The formation of the neural tube creates a cavity, which later becomes the ventricular system, lined by a monolayer of rapidly proliferating neuroepithelial stem cells.

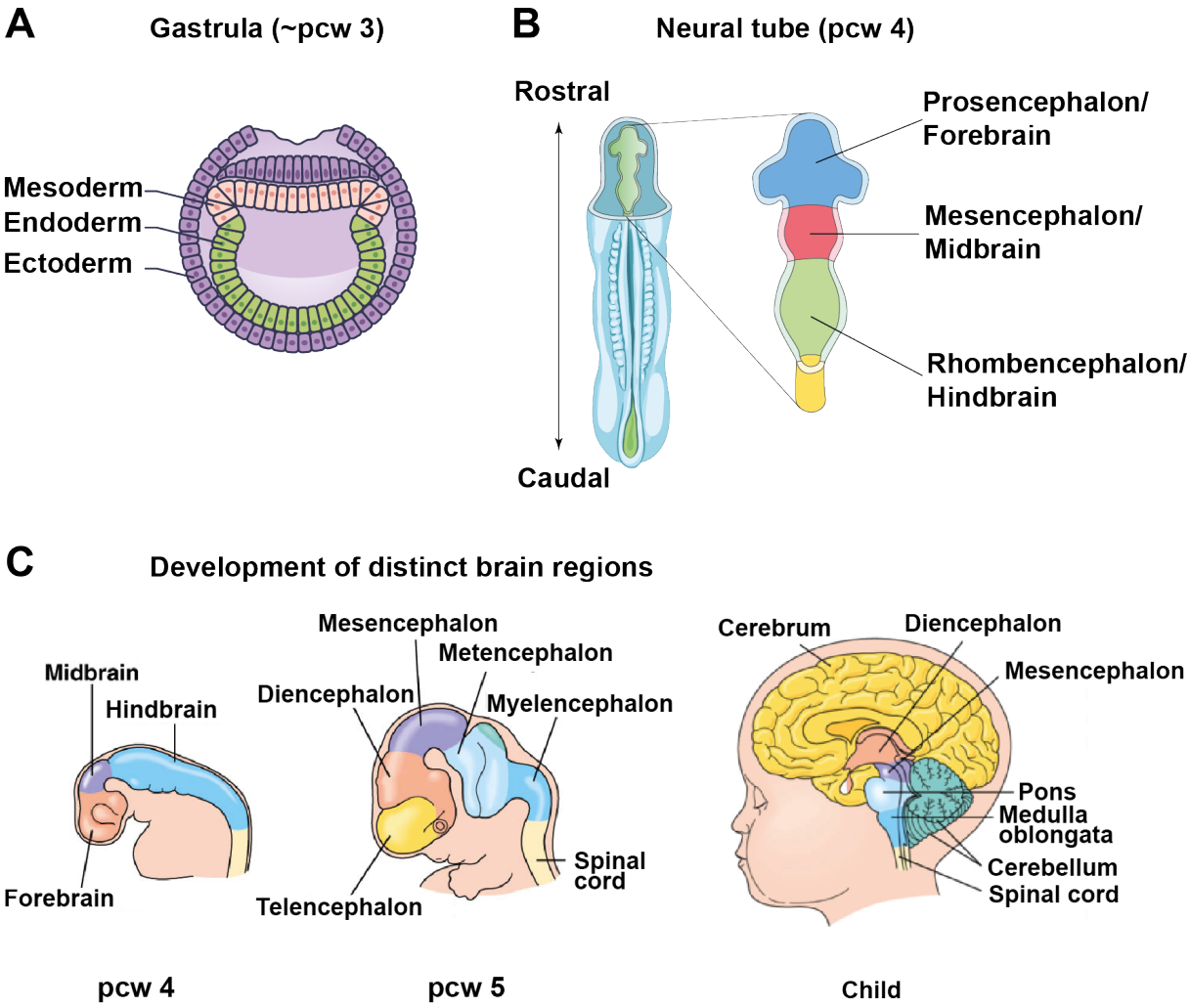

Figure 3.1-2: Embryonic brain regionalization.*A) During gastrulation (~ pcw 3), the three germ layers endoderm, ectoderm and mesoderm form. B) At pcw 4 the primary brain vesicles become apparent. C) The primary brain vesicles develop over time into distinct brain regions. pcw = post-conception week. Figure C) edited from reference[9].*

Just before the tube's closure is complete, the rostral portion expands, and by pcw 4, the primary brain vesicles — prosencephalon (forebrain precursor), mesencephalon (midbrain precursor), and rhombencephalon (hindbrain precursor) — become apparent[1] (**Figure 3.1-2**

B). By pcw 7, secondary vesicles form, with the prosencephalon dividing into the telencephalon and diencephalon, while the rhombencephalon differentiates into the metencephalon and myelencephalon[1]. From these structures mature brain regions differentiate during fetal and postnatal brain development. Among others, the telencephalon gives rise to the cerebral cortex, white matter and basal nuclei, while the diencephalon generates thalamus, hypothalamus and epithalamus. Structures arising from the mesencephalon during development mainly include rostral parts of the brain stem, consisting of cerebral peduncles, tegmentum and tectum, while the metencephalon gives rise to the pons and the cerebellum. Lastly, the myelencephalon differentiates into the medulla oblongata[10] (**Figure 3.1-2 C**).

To understand how all of these transformations of the neural tube are regulated and finally achieved over time, the molecular processes of brain patterning need to be elucidated.

3.1.2 Molecular mechanisms in early brain patterning

Neural patterning processes reflect the overall shape transformations of the developing embryonic brain and later on ensure proper regionalization of the adult brain. These patterning processes are driven by internal and external cues regulated by morphogens and can be segregated into two signalling centres that facilitate the cell fate specification along the rostrocaudal and along the dorsoventral axis.

3.1.2.1 Rostral-to-caudal patterning

Rostrocaudal (R/C) patterning is considered to be the initial step in regionalization, occurring before neurulation but during gastrulation (pcw 2-3)[11–13]. Here, the gene expression of orthodenticle homeobox 2 (*OTX2*) and gastrulation brain homeobox 2 (*GBX2*) mark the rostral and caudal neural tube, respectively. Nascent neural tissue adopts rostral identity by default, while the following division into rostral and caudal identity is achieved by morphogens that inhibit rostral and promote caudal specific gene expression. These include retinoic acid (RA)[14,15], fibroblast growth factor (FGF)[16–18] and WNT signalling[13] (**Figure 3.1-3**). Although patterning is studied for over 50 years, specific mechanisms driving the patterning processes in mammalian context are not yet completely understood.

However, FGFs most probably exert their caudalising function through two distinct mechanisms. One mechanism involves their regulation of homeobox (HOX) and caudal transcription factor (CDX) genes[19,20], while the second one is thought to be the expression of *FGF4*/*FGF8* in posterior mesoderm from where they can act as endogenous caudalising factors[21–23]. In addition, FGF8 was shown to be expressed at the isthmic organizer[24–26], a domain that forms the rostral end of the hindbrain and inhibits the expression of the rostral marker OTX2 in the caudal regions[27] (**Figure 3.1-3**).

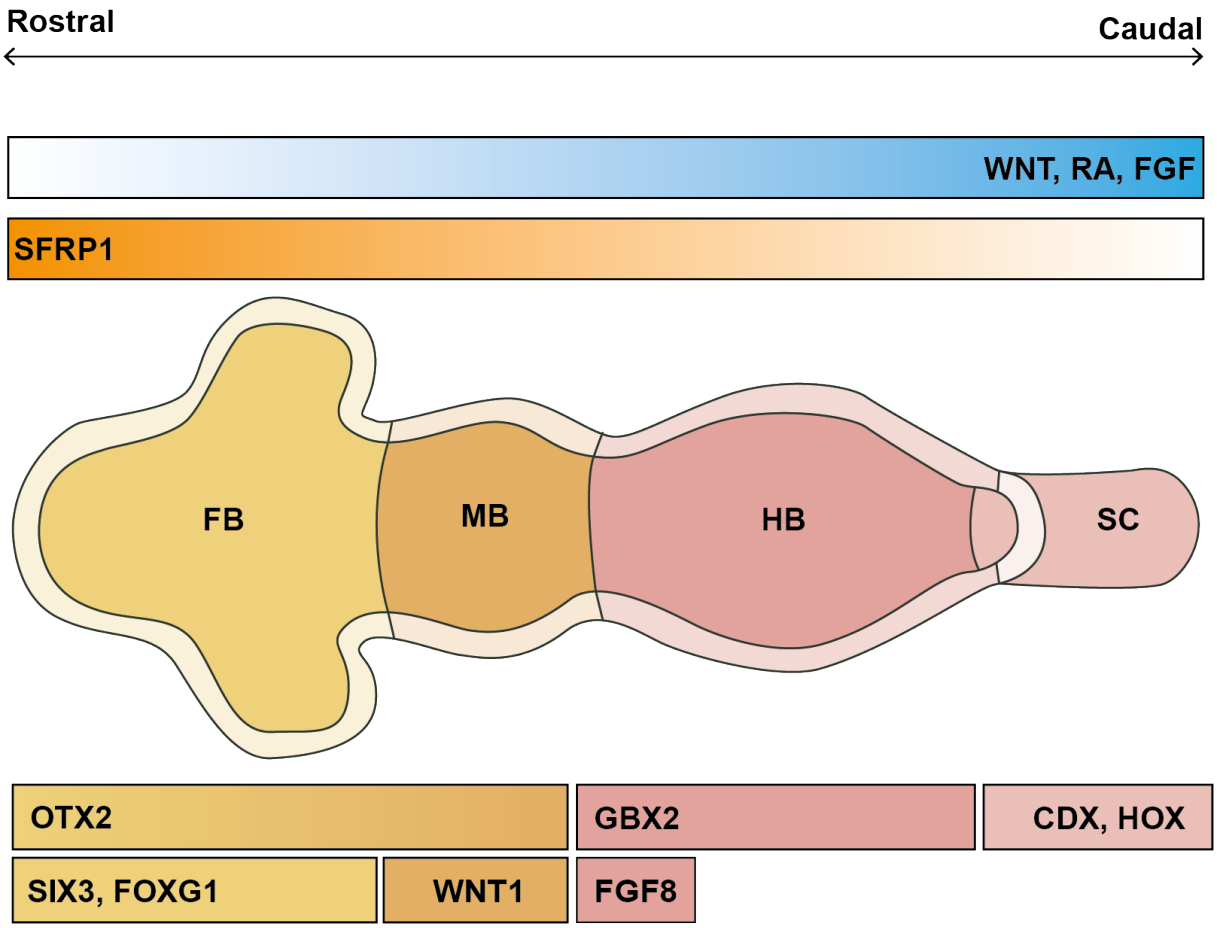

Figure 3.1-3: Rostrocaudal neural tube patterning (pcw 4). *The schematic shows the key morphogens in rostrocaudal patterning as well as a subset of their target genes. WNT, RA, and FGF signalling act as morphogens with a gradient from high caudal to low rostral levels, promoting the expression of caudal-specific genes such as GBX2, CDX, and HOX genes. In the rostral neural tube, WNT-antagonizing factors like SFRP1 inhibit WNT activity, supporting the expression of rostral markers like OTX2, FOXG1, and SIX3. FB = forebrain, MB = midbrain, HB = hindbrain, SC = spinal cord. The upper bars indicate the morphogen gradients along the rostrocaudal axis, while the lower bars show regions where specific marker genes are expressed.*

RA exerts similar functions during caudalisation as FGF, including the regulation of CDX and HOX genes (**Figure 3.1-3**). Here, it was shown that in chick embryos RA preferentially regulates the expression of more anterior HOX genes (e.g. *Hoxb1*, *Hoxb3-5*), while FGF exerts its function on more posterior HOX genes (e.g. *Hoxb6-9*)[19]. Additionally, RA and FGF are antagonizing factors[28]. For instance, during caudal axial elongation, FGF signalling maintains the stem zone (in human, the caudal neural tube would be the corresponding area), while RA signalling promotes the exit of cells from this zone, thereby facilitating neural and somitic differentiation. This is reflected in the mutually exclusive expression patterns of Raldh2, the enzyme responsible for RA synthesis and now known as ALDHLA2, and Fgf8, with Fgf8 localized to the stem zone and Raldh2 expressed rostrally in the presomitic and somitic mesoderm[29].

WNT signalling plays a dual role in brain patterning, functioning both as a caudalising and dorsalising morphogen. In the context of the neural tube R/C axis, WNT signalling inhibits the expression of rostral marker genes like *OTX2*[18,30] while promoting the expression of caudal-

specific markers such as *GBX2*[31]. Notably, in prosencephalon specification, WNT activation induces the expression of iroquois homeobox 3 (*IRX3*) in the diencephalon, which subsequently inhibits SIX homeobox 3 (*SIX3*). In contrast, *SIX3*, a key marker for the telencephalon, activates sonic hedgehog (SHH) signalling. This activation then drives the expression of forkhead box G1 (*FOXG1*), a gene essential for forebrain development and expressed in all forebrain cells[32–34].

Amongst others, WNT signalling activity is finely regulated by modulators such as dickkopf related proteins (DKKs), cerberus (CER) and secreted frizzled-related proteins (SFRPs), which ensure accurate regionalization. Notably, *SFRP1* is expressed in a gradient along the rostral-to-caudal axis of the neural tube to antagonize WNT activity[35,36] (**Figure 3.1-3**).

Lastly, the expression of distinct WNT ligands along the R/C axis underscores their specific roles in regional patterning throughout neurodevelopment. For instance, WNT8A regulates neuroectodermal-specific marker gene expression during gastrulation[37], while other WNT ligands, such as WNT1, WNT2B, WNT3, WNT3A and WNT4 show partially overlapping expression extending from caudal diencephalon to the spinal cord[38–42]. Notably, in first-trimester human embryos, especially WNT1 and WNT2B were found to be primarily expressed in diencephalon and midbrain[42] (**Figure 3.1-4 C**). This distribution of distinct WNT ligands suggests that one of their key functions is to maintain regional boundaries, thereby facilitating proper cell specification across different brain regions. This is illustrated by WNT1, which is expressed in the caudal diencephalon and supports sustained FGF8 expression in the isthmus[43].

In summary, the morphogens WNT, RA and FGF, along with their modulators, ensure rostral-to-caudal neural tube patterning. They facilitate the expression of caudal-specific marker genes while inhibiting those linked to the rostral region and modulating rostral morphogen activity. The interplay among these factors is vital for establishing boundaries and refining distinct brain regions.

3.1.2.2 Dorsal-to-ventral patterning

Dorsal-to-ventral (D/V) patterning of the neural tube begins during neurulation and is regulated by specific transcription factors (TFs) such as GLI family zinc finger 3 (GLI3)[44–47], FOXG1[48–50] and paired box 6 (PAX6)[51,52]. These are regulated by morphogen gradients, primarily WNT and bone-morphogenetic protein (BMP) on the dorsal side and sonic hedgehog (SHH) as well as FGF on the ventral side (**Figure 3.1-4**). Although the majority of studies in this context have focused on the spinal cord, and many of the underlying processes are similar in more rostral regions of the neural tube, this section will primarily elucidate the dorsal-ventral patterning of the neural tube region that develops into the forebrain.

SHH is initially expressed in the notochord, a ventral structure located beneath the neural tube. This induces SHH expression in ventral neural tube cells, known as floor plate cells, which subsequently act as a secondary source of SHH to activate ventral-specific marker genes, such as NK2 homeobox 1 (*NKX2.1*)[52–54]. The resulting signalling cascade modulates the activity of GLI transcription factors, which function as either activators or repressors of SHH target genes dependent on its presence or absence. In vertebrates, three distinct GLI proteins are involved in SHH signalling: GLI1, which functions exclusively as an activator, and GLI2 and GLI3, which can act as both activators and repressors. In the presence of SHH, full-length GLI proteins activate SHH target genes. In its absence, GLI2 is completely degraded, while GLI3 is cleaved at its C-terminus, converting into a repressor that inhibits SHH pathway targets[55,56]. A key role of SHH in the ventral neural tube is preventing this conversion of GLI3 into its repressive form, which explains the dorsal-to-ventral gradient of GLI3 expression. Hence, the early subdivision that establishes the future dorsal and ventral telencephalon is influenced, at least in part, by the dorsalising effects of GLI3 expression and the ventralising effects of SHH activity. GLI1, in contrast, forms a ventral-to-dorsal gradient, establishing an inverse relationship with GLI3[57,58]. GLI2, meanwhile, is uniformly expressed along the neural tube, suggesting it may not be entirely SHH-dependent[55,58] (**Figure 3.1-4**).

Notably, FOXG1, a downstream effector of SHH, plays a crucial role in ventral specification. This transcription factor serves multiple functions in forebrain development and is expressed throughout the telencephalon, with a gradient from high levels ventrally to lower levels dorsally[59]. FOXG1 directly inhibits WNT signalling, which prevents the establishment of dorsal identities[60]. Although, this indicates that SHH and FOXG1 act independently in specifying ventral fates, both promote the expression of FGF8[60,61] (**Figure 3.1-4**).

Although FGFs are not the main regulators of D/V patterning, FGF8 and FGF15 are maintained by SHH and play key roles in ventral specification[44,45,62]. Additionally, FGF3, FGF8, and FGF17 are expressed in the anterior neural ridge and later in the ventral telencephalon[42,63–65], while FGF receptors have been shown to be essential for ventral precursor cell generation[66,67]. Although FGF and SHH collaborate in promoting ventral cell fates, FGFs also possess ventralising properties that function independently of SHH, suggesting a complementary yet distinct role in ventral specification[67]. Notably, FGF8 has been shown to specify ventral telencephalic fate by acting synergistically with FOXG1 as both factors enhance each other's expression during ventral neural tube specification[61,67–69] (**Figure 3.1-4**).

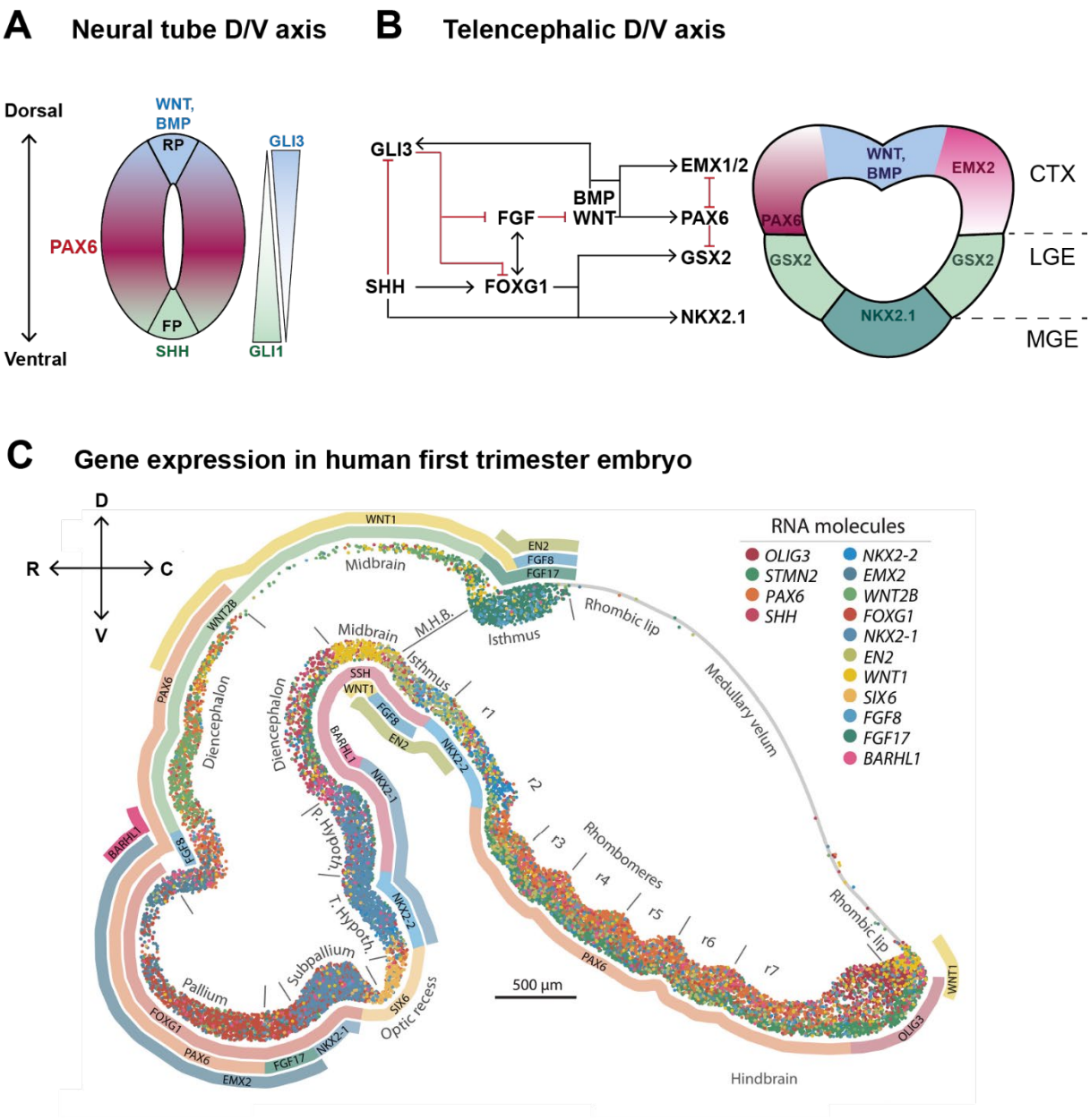

Figure 3.1-4: Dorsoventral patterning of the neural tube (~pcw 4-14). *A) Early dorsoventral neural tube patterning is primarily established by the dorsalising effects of GLI3 (blue gradient), maintained by BMP and WNT, and the ventralising effects of SHH activity and its respective target GLI1 (green gradient), while the dorsalising TF PAX6 (red gradient) sharpens the border between dorsal and ventral telencephalon. RP = roof plate, FP = floor plate. B) The gene regulatory network induced by the interplay of SHH and FGF in the ventral telencephalon as well as BMP and WNT in the dorsal telencephalon facilitates the region identity marker gene expression. Among these genes PAX6 (dark red gradient) is specific for the rostral-lateral cortex, EMX2 (light red gradient) is specific for the caudal-medial cortex, while LGE and MGE are marked by the expression of GSX2 and NKX2.1, respectively. CTX = cortex, LGE = lateral ganglionic eminence, MGE = medial ganglionic eminence. C) The schematic illustrates the gene expression in a sagittal section of a human first trimester embryo. M.H.B = midbrain-hindbrain boundary, D = dorsal, V = ventral. R = rostral, C = caudal. Figure C from reference[42].*

BMPs play a complementary role in fate specification. These proteins are expressed in the ectoderm before neurulation and later localize to the dorsal neural tube, the roof plate. In contrast, their antagonists — noggin, chordin, and follistatin — are expressed in the ventral neural tube to inhibit this signalling[70–72]. The BMP pathway sustains *GLI3* expression, reinforcing dorsal identity and opposing SHH signalling, while also antagonizing FOXG1 and

FGF8 activity[70,73]. Key BMP target genes involved in neural tube patterning include *PAX6*, msh homeobox 1 (*MSX1*), and developing brain homeobox 2 (*DBX2*), with the latter two primarily expressed in the spinal cord[74] (**Figure 3.1-4**).

WNT signalling works in conjunction with BMP to sustain dorsal fates by directly targeting dorsal-specific marker genes that inhibit SHH signalling and specify dorsal cell types. These genes include *GLI3*, *PAX6*, neurogenin 2 (*NEUROG2*), and in cooperation with BMP, empty spiracles homeobox 2 (*EMX2*)[75–77]. Additionally, GLI3 is required to maintain the dorsal marker genes expression of *EMX1* and *EMX2*, further reinforcing its role as a marker of the dorsal telencephalon[46] (**Figure 3.1-4**).

As development progresses and the telencephalon differentiates, WNT signalling becomes increasingly crucial for establishing dorsal fate. The invagination of the roof plate gives rise to the cortical hem, a key patterning centre rich in BMPs (e.g., BMP2, BMP4, BMP6, BMP7)[78] and WNTs (e.g., WNT2B, WNT3A, WNT5A), facilitating dorsal specification and boundary development, similar to neural tube patterning mechanisms[79]. For instance, WNT3A and a receptor involved in WNT signalling, the low-density lipoprotein receptor-related protein 6 (LRP6), are essential for maintaining dorsal neural precursors[80,81]. Additionally, WNT signalling along with BMP type 1 receptors, BMPR1A and BMPR1B support the formation of specialized brain regions, including the most dorsally positioned choroid plexus and the hippocampus, a part of the cerebral cortex derived from the dorsal telencephalon[73,82–84]. Noteworthy, the factors NEUROG1, NEUROG2, GLI3 and the LIM homeobox transcription factor 2 (LHX2) significantly influence cortical regions, with LHX2 serving as a critical selector of neocortical identity[85–87].

Simultaneously, the ganglionic eminences (GEs) develop as transient structures in the ventral brain during embryonic development, consisting of three main subdivisions: the medial (MGE), lateral (LGE), and caudal (CGE) ganglionic eminences. Their proper development relies on SHH signalling and is characterized by distinct marker gene expression: MGE expresses *NKX2.1* and *LHX6*, LGE expresses GS homeobox 2 (*GSX2*) and *DLX1*/*2*, while CGE exhibits molecular features shared with both MGE and LGE[88] (**Figure 3.1-4**).

In summary, the opposing actions of GLI3 dorsally and SHH ventrally establish the early division of the D/V axis. FGF and FOXG1 contribute to ventralisation, both in synergy with and independently of SHH. On the dorsal side, WNT and BMP signalling maintain dorsal markers like GLI3 while inhibiting ventralising signals. As development advances, the dorsal telencephalon forms the cerebral cortex, while the ventral region gives rise to the ganglionic eminences, each producing specific neural cell subtypes during neurogenesis (pcw 7-27)[4,6].

Neural subtype generation can, in fact, be considered a late patterning event, as it is partially dependent on regional identity. The upcoming section will explore this process in detail through the example of cortical lamination.

3.1.3 Cellular subtype specification in the cerebral cortex

The ectodermal layer that forms the neural tube generates a diverse array of cell types essential for vertebrate embryonic development. Among these are cranial neural crest cells, a multipotent progenitor population that originates at the neural plate border during early gastrulation. Neural crest cells arise from the dorsal edges of the neural folds during neural tube closure, with their formation indirectly stimulated by interactions between the neural plate and the epidermal ectoderm. These interactions induce the neural folds, which subsequently give rise to neural crest cells and other dorsal neural tube derivatives. The specification processes of neural crest cells are primarily governed by signalling modules, including BMP, NOTCH, WNT, and FGF pathways[89]. These signals activate transcription factors such as PAX genes, ZIC family members, snail family transcriptional repressor 2 (*SNAI2*), and *FOXD3*, with *SNAI2* and *FOXD3* being uniquely expressed in neural crest cells, marking them within the dorsal neural tube. Additional transcription factors, including SOX10 and SOX9, further guide neural crest differentiation and migratory capacity[90–92]. Following specification, neural crest cells undergo epithelial-to-mesenchymal transition (EMT), enabling their migration along distinct pathways to diverse embryonic regions. Upon reaching their destinations, these cells differentiate into an extensive array of derivatives, including skeletal elements like bone and cartilage, melanocytes, neurons, glial cells, and connective tissue. Cranial neural crest cells, in particular, contribute to much of the craniofacial skeleton, peripheral nervous system components, and other specialized structures. Disruptions in their development are associated with congenital anomalies, including craniofacial malformations[93].

Simultaneously, during cranial neural crest development, neural epithelial cells (NECs) within the neural tube proliferate rapidly through symmetric divisions to establish a progenitor pool that supports ongoing neurogenesis (pcw 4–7)[4]. These progenitors are already primed to differentiate into specific cell types based on their localization. Once the regions of the neuroepithelium are defined, cells undergo morphological and molecular transitions, giving rise to specialized neural cell types in a process known as neurogenesis (pcw 7-27)[4]. To illustrate how these cells emerge from a pluripotent pool, cortical lamination serves as a model for differentiation. While numerous regulators contribute to the intricate processes of neurogenesis and cortical development, this section will focus on the most prominent mechanisms and key regulators, such as regional gene gradients (e.g., *EMX2*, *PAX6*, *FOXG1*, *NKX2.1*) and signalling pathways like NOTCH and WNT. These selected factors provide

critical insights into the regulation of progenitor proliferation, differentiation, and the establishment of neural cell identity.

Initially, NECs within the neural tube are arranged apico-basally, with their apical side facing the ventricular zone (the innermost layer of the neural tube) and the basal side oriented toward the pial surface (outer layer). Apical NECs are tightly connected by adherens and tight junctions, which play critical roles in cell maturation, adhesion, and the regulation of ion and molecule distribution[94]. Basally, these cells are anchored to the extracellular matrix (ECM) via integrins, which activate intracellular signalling pathways and maintain contact with the ECM. During the proliferative phase, NECs are influenced by the localized expression of transcription factors PAX6 and EMX2, which are distributed in opposing gradients: EMX2 predominantly in the caudal-medial regions and PAX6 in the more rostral-lateral regions of the proliferative zone that partitions the dorsal from the ventral telencephalon (**Figure 3.1-4 B, Figure 3.1-5 A**).

Just prior neurogenesis, apical NECs lose their tight junctions and begin to express specifying genes such as *PAX6*, SRY-box transcription factor 2 (*SOX2*), nestin (*NES*) and vimentin (*VIM*), which leads to their transformation into apical radial glia cells (aRGCs)[95]. These extend basal processes toward the pial surface, forming a scaffold for future neuronal migration. Like NECs, aRGCs are multipotent and initially undergo symmetric cell division to expand the progenitor pool. However, as development progresses, they gradually shift to asymmetric cell division, generating one aRGC and a daughter cell with increased commitment. The committed daughter cell can either migrate to the pial surface, where it differentiates into a neuron and forms the preplate, or migrate to the subventricular zone (SVZ) and become an intermediate progenitor cell (IPC). IPCs primarily divide symmetrically into neurons and thereby contribute to the cortical layer formation.

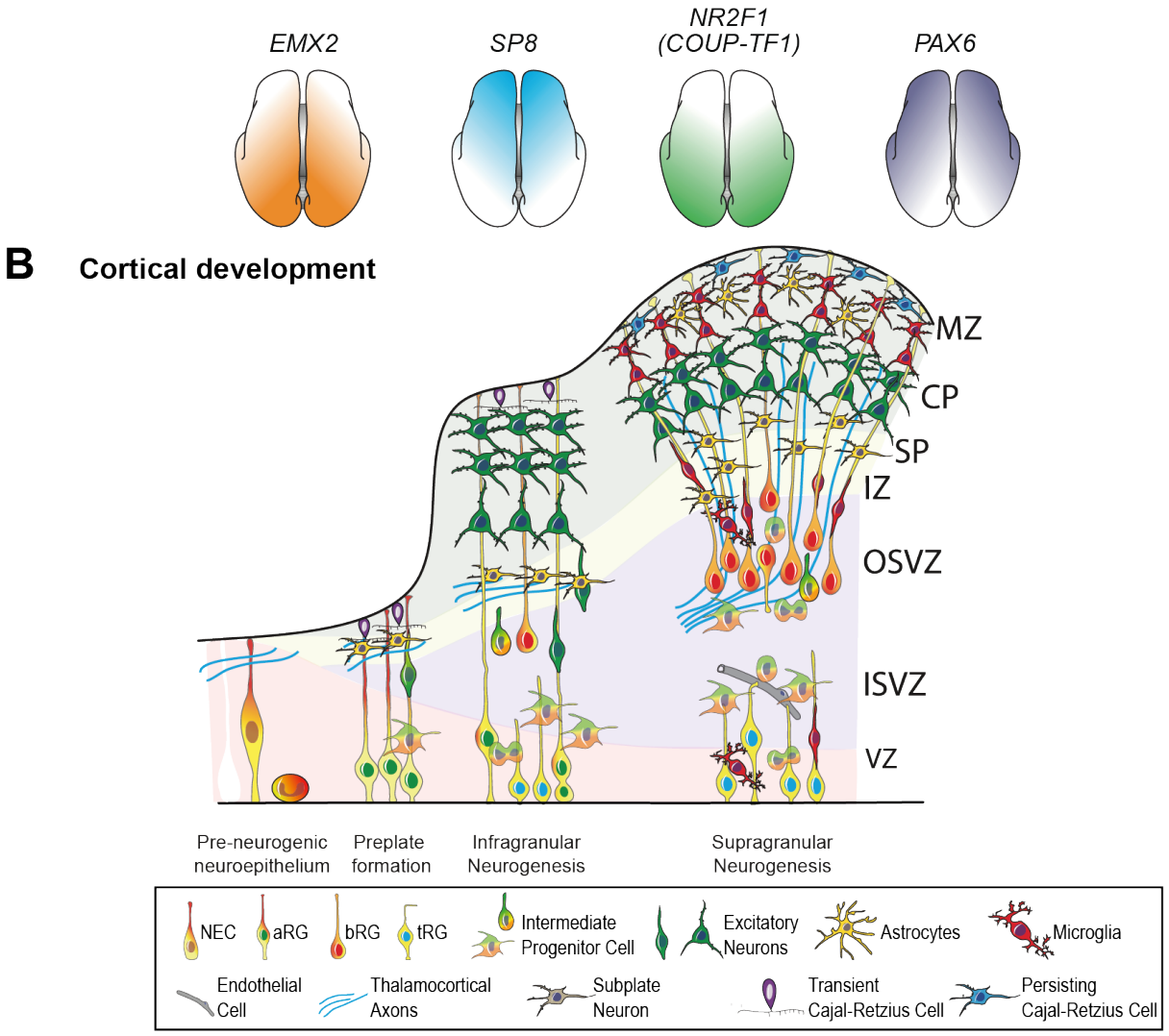

Figure 3.1-5: Scheme of key processes during cortical neurogenesis. *A) Area-specifc cell fates are established by morphogen and TF gradients across the developing neuroepithelium. B) Schematic representation of cellular differentiation and cortical layer formation during neurogenesis. The x-axis denotes different developmental stages. NEC = neuroepithelial cell, aRG = apical radial glia, bRG = basal radial glia, tRG = truncated basal radial glia (a molecular distinct radial glia cell that emerges around pcw 14-14.5[96]), VZ = ventricular zone, ISVZ = inner subventricular zone, OSVZ = outer subventricular zone, IZ = intermediate zone, SP = subplate, CP = cortical plate, MZ = marginal zone. C) Timeline of key processes in neurogenesis and cortical layer formation. Pcw = post-conception week. Figure adapted from reference[97].*

The switch from symmetric to asymmetric cell division is pivotal for balancing progenitor pool expansion and the production of neural subtypes during neurogenesis. This transition is

governed by intrinsic transcription factors and extrinsic signalling pathways, including NOTCH signalling, which inhibits differentiation and promotes self-renewal to favour symmetric cell division[98,99]. Lateral inhibition of NOTCH signalling ensures the balance between progenitor maintenance and neuronal differentiation by activating Hes family BHLH transcription tactor 1 (*HES1*) in neighbouring cells to maintain their progenitor state, while cells with reduced NOTCH activity express proneural genes (e.g., *NEUROG2*, Achaete-Scute family BHLH transcription factor 1 (*ASCL1*)) to initiate differentiation[100–102]. This mechanism facilitates the orderly generation of neurons while preserving the progenitor pool. In particular, NOTCH1 supports radial glia identity during mammalian embryogenesis[103]. Interestingly, the effects of NOTCH signalling evolve over developmental time; along with FGF signalling, it promotes glial cell fate commitment at later stages of development[103–105]. Similarly, WNT signalling initially drives the expansion of RGCs but later shifts to support neurogenesis by promoting the terminal differentiation of IPCs[106,107]. Furthermore, FOXG1 regulates the cell cycle, ensuring controlled neural stem and progenitor cell proliferation while suppressing premature neuronal differentiation[61,108].

This underscores that the cell fate decision and following specification processes are very much influenced by the cells localization along the different gradients of signalling pathway activity and transcription factor expression as well as the developmental time in which the cells are affected by the respective factors.

Around pcw 10, some aRGCs migrate into the SVZ, losing their connection to the ventricular zone but retaining contact with the pial surface. These cells, known as basal radial glia cells (bRGCs), are multipotent progenitors that primarily generate highly proliferative intermediate progenitor cells (IPCs) and neurons through asymmetric cell division (**Figure 3.1-5**). While bRGCs express transcription factors similar to those of apical radial glia cells (aRGCs) during neurogenesis, they also express cell-type-specific genes. One such gene is leukemia inhibitory factor (LIF), which has recently been shown to regulate the proliferation and differentiation of bRGCs. Notably, increased LIF expression is associated with the differentiation of inhibitory interneurons[109].

Due to their increased proliferative capacity, bRGs are considered key players in human cortical expansion and further subdivide the SVZ in inner (iSVZ) and outer zones (oSVZ). While the iSVZ is mostly populated by aRGs and IPCs, the oSVZ primarily consists of bRGs[110]. IPCs and neurons generated by the RGs migrate towards the pial surface using the RG processes as scaffold to the developing cortical plate that builds up in an inside-out fashion. Here, early-born neurons settle in deeper layers (layer V-VI; pcw ~ 7-13) and later-born neurons migrate in upper layers (layer II-IV; pcw 13-27)[111,112]. Layer I stands out as the first cortical structure to

form, driven by a transient population of pioneer neurons known as Cajal-Retzius cells, which emerge around pcw 5[113]. These cells play a crucial role in early cortical development but largely undergo programmed cell death between pcw 23–28, with only a small number surviving thereafter[114,115]. This leaves layer I as a relatively neuron-sparse region mainly consisting of axons and dendritic connections post-natally. However during development, Cajal-Retzius cells are essential for cortical lamination as they secrete the glycoprotein reelin that controls the migration of the cortical glutamatergic projection neurons[116,117]. Noteworthy, glutamatergic neurons (mainly excitatory) are generated by the progenitors residing in the dorsal telencephalon and migrate radially into the cortical plate, while GABAergic interneurons (mainly inhibitory) are produced in the ganglionic eminences of the ventral telencephalon from which they migrate tangentially into the cortical plate[118–120]. Interestingly, FOXG1 also plays a key role in regulating multiple laminar fate decisions. It suppresses the production of T-box brain transcription factor 1 (TBR1)-expressing layer I/VI neurons in progenitor cells, promoting instead the production of FEZ family zinc finger 2 (FEZF2)/ BCL11 transcription factor B (BCL11B)-expressing layer V neurons. In early post-mitotic neurons, FOXG1 inhibits COUP transcription factor I (COUP-TFI), facilitating a switch from RAR related orphan receptor B (RORB)-expressing layer IV neurons to SATB homeobox 2 (SATB2)/ POU Class 3 homeobox 2 (POU3F2)-expressing neurons specific for layers II/III[121–124] (**Figure 3.1-5**). In the ventral telencephalon, NKX2.1 plays a pivotal role in generating GABAergic interneurons. It achieves this by promoting a permissive chromatin state at regulatory regions of genes critical for forebrain and GABAergic cell development, enabling the recruitment of additional transcription factors essential for lineage specification. Specifically, the combinatorial binding of LHX6 and NKX2.1 activates the gene expression program required for the development and migration of interneurons[125].

Following neurogenesis, the RGCs undergo a cell fate switch that results in the production of glial cells such as astrocytes and oligodendrocytes, with the first astrocytes developing already around pcw 15[126,127] (**Figure 3.1-5**). This process, known as gliogenesis, will not be explored in further detail here but relies on similar fate commitment factors as those involved in neurogenesis.

Taken together, NECs differentiate into RGs, which self-renew by symmetric cell division to expand the progenitor pool and give rise to more committed cell types such as IPCs and neurons via asymmetric division. As cells commit to specific fates, they lose self-renewal capacity and begin expressing genes that define their respective subtypes. These processes are governed by two key factors: (1) the spatial localization within the brain, driven by regional gene gradients such as *EMX2* and *PAX6* in the dorsal telencephalon and *NKX2.1* in the ventral telencephalon, alongside signalling pathways like NOTCH and WNT; (2) the developmental

timing, as the regulatory environment evolves, influencing cell fate decisions at different stages. Together, these mechanisms ensure the precise formation of specialized neurons and the establishment of cortical layers.

Even small perturbations in signalling activity, target gene expression, or regional accessibility can lead to significant disruptions in brain patterning, affecting brain region identity and the specification of their respective cell types. This underscores the critical importance of regulatory mechanisms in preventing neurodevelopmental pathologies, a topic that will be explored in the following sections.

3.2 Regulation of gene expression

The regulation of gene expression is a critical process that orchestrates the spatial, temporal, and quantitative control of gene activity across cellular systems. It is essential for maintaining cellular homeostasis and function, facilitating responses to external stimuli, and driving developmental and differentiation processes. These regulatory mechanisms operate through a multistep process governed by both internal and external signals.
For instance, TFs play a central role by binding to specific DNA regions, known as cis-regulatory elements (CREs) — promoters, enhancers, insulators, and silencers — that control gene transcription. In addition, signal transduction pathways modulate gene expression by activating TFs in response to external cues, thereby integrating environmental signals with transcriptional regulation[128].

Beyond TFs, CREs, and signalling pathways, non-coding RNAs such as miRNAs and lncRNAs further regulate gene expression, either through interactions with the transcription machinery or by acting at the post-transcriptional level. These RNAs are particularly important during neurodevelopment, where they influence cell fate decisions[129,130].

Furthermore, epigenetic factors modulate chromatin structure and accessibility through distinct mechanisms. Histone modifiers, such as histone acetyltransferases (HATs) and histone deacetylases (HDACs), alter histone properties by adding or removing chemical groups. DNA methyltransferases (DNMTs) modify DNA directly by adding methyl groups, repressing chromatin accessibility and gene expression. Lastly, chromatin remodelling complexes, of which four major families are recognized in eukaryotes, further shape the chromatin landscape by altering nucleosome positioning[128]. These families include imitation switch (ISWI), Inositol requiring 80 (INO80), chromodomain helicase DNA-binding (CHD), and BRG1/BRM associated factor (BAF) complexes, with BAF complexes being the most prominent in regulating chromatin accessibility[131–133]. Additionally, BAF complexes play critical roles in various developmental processes[134–141]. The following sections will explore the role of BAF complexes in neurodevelopment and their implications in disease.

3.2.1 BAF complexes

The polymorphic, ATP-dependent BRG1/BRM-associated factor (BAF) complexes dynamically regulate DNA accessibility by sliding or ejecting nucleosomes, a process critical for controlling gene expression, differentiation, and other essential cellular functions like DNA replication and repair. Each BAF complex is composed of up to 15 subunits encoded by over 29 genes, which assemble in a tissue-specific and context-dependent manner, enabling BAF complexes to adapt to specific cellular requirements.

Structurally, BAF complexes adopt a characteristic C-shaped configuration, with three primary modules working together to achieve nucleosome remodelling. The ATPase module, which includes the SWI/SNF related, matrix associated, actin dependent regulator of chromatin (SMARC), subfamily A, member 2 and 4 (SMARCA2/SMARCA4) subunit, catalyses ATP hydrolysis to generate mechanical force. This force creates transient distortions at the DNA-histone interface, leading to small DNA loops being pushed along the histone surface, ultimately sliding the nucleosome along the DNA strand[142]. Closely associated with this ATPase module is the ARP module consisting of the actin-related proteins actin beta (ACTB), actin like 6A/B (ACTL6A/ACTL6B), and B-cell lymphoma/leukemia protein 7 A/B/C (BCL7A/BCL7B/BCL7C). It regulates the ATPase activity and DNA translocation, facilitating the conformational changes necessary for effective nucleosome remodelling[143]. Finally, the core module, containing proteins such as AT-rich interactive domain-containing protein (ARID) 1A/B (ARID1A/ARID1B), ARID2, and SMARC subfamily C 1/2 (SMARCC1/SMARCC2), stabilizes the complex and incorporates a variety of binding domains that allow BAF complexes to precisely target specific genomic regions. This module's bromodomains, akin to those in the BAF complex ATPases, recognize acetylated lysine residues; chromodomains bind to tri-methylated lysines; and PHD fingers detect H3K4 methylation states. Additional DNA-binding motifs, such as zinc fingers and AT-hooks, further enhance the complex's specificity for particular DNA sequences. Through their protein and histone interaction domains, BAF complexes recognize binding sites based on DNA sequences or targeting molecules (e.g., transcription factors or lncRNAs) while also responding to local chromatin states influenced by histone modifications. This intricate targeting mechanism allows BAF complexes to finely regulate chromatin accessibility, particularly at promoter and enhancer regions, in response to changes in cellular signalling and developmental cues[143–145] (**Figure 3.2-1**).

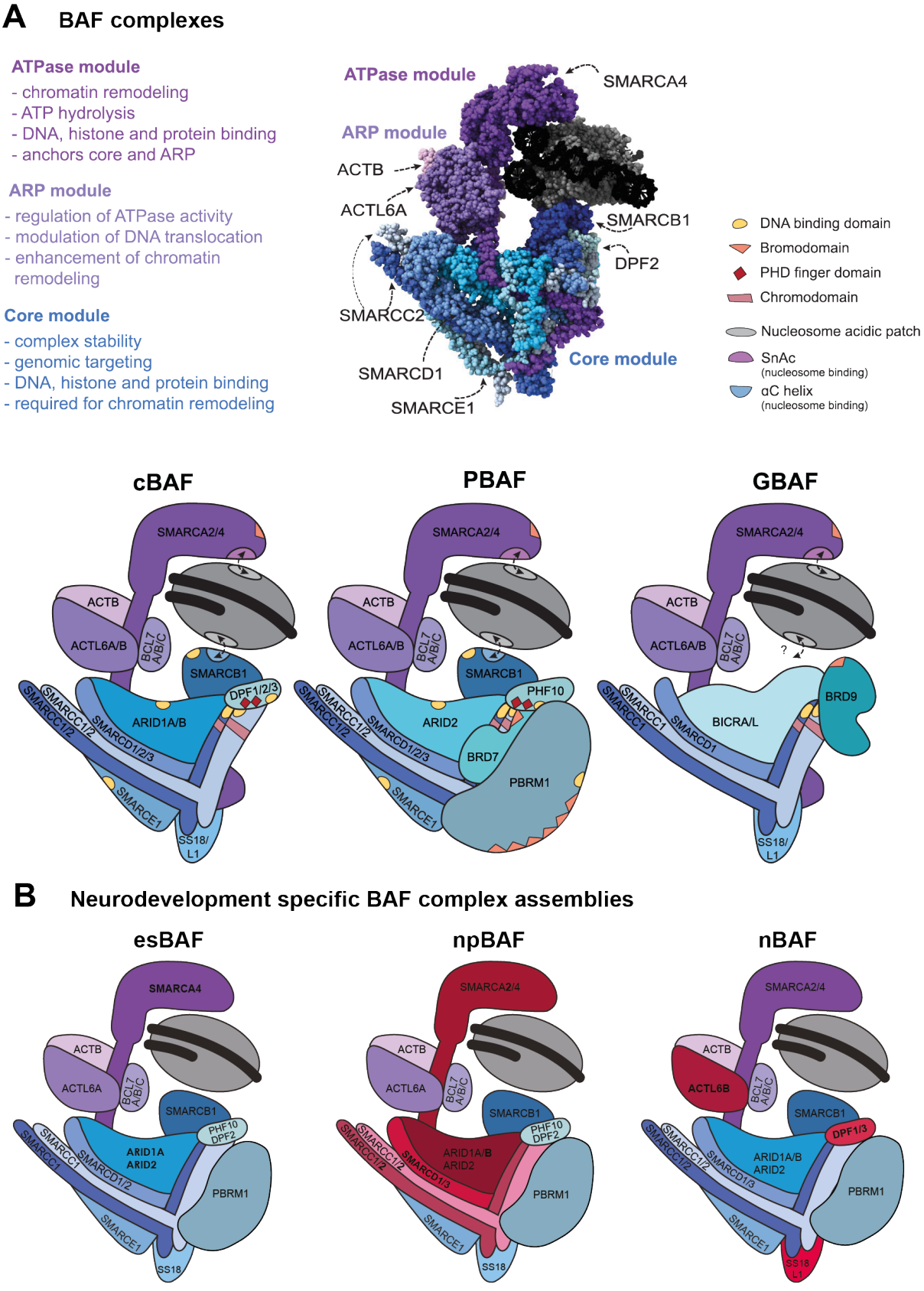

Figure 3.2-1: BAF complexes. *A) The upper panel displays the cryo-EM structure of the cBAF complex bound to a nucleosome, with key features of the three distinct modules described. The text and subunits associated with the ATPase and ARP modules are highlighted in purple, while those corresponding to the core module are shown in blue. The lower panel illustrates the subunits present in the three main BAF complex classes, including their DNA and histone-binding domains. B) A schematic illustrating BAF complex subunit switches during neurodevelopment, with the switching subunits marked in bold text and highlighted in red colour. Figure adapted from reference*[145].

Based on specific incorporated subunits, three main classes of BAF complexes can be distinguished: canonical BAF (cBAF), polybromo-associated BAF (PBAF) and non-canonical BAF (ncBAF/GBAF)[140,145]. These exist in various compositions in each cell, due to the fact that particular complex positions can be occupied by paralogous subunits[146]. Noteworthy, the core subunits ARID1A, ARID1B and ARID2 not only represent mutually exclusive subunits, but also allow distinction between the three main BAF complex classes by their incorporation. Here, cBAF contains either ARID1A or ARID1B, PBAF is associated with ARID2 incorporation and ncBAF does not contain an ARID subunit at all. Moreover, the subunit composition of BAF complexes undergo changes during development, a process needed to provide the required chromatin landscape for differentiation and cell type-specific function (**Figure 3.2-1**).

Neurodevelopment provides a clear example of this dynamic assembly process: during neurogenesis, as stem cells commit to the neural lineage, they transition into neural progenitor cells and ultimately exit the mitotic stage to differentiate into neurons. Throughout this progression, BAF complex assembly shifts correspondingly from the embryonic stem cell BAF (esBAF) to the neural progenitor BAF (npBAF), and finally to the neuron-specific BAF (nBAF)[140,146–149]. This progression suggests a critical role for BAF complexes in neurodevelopment. The presence of specific BAF subtypes at distinct developmental stages suggests that tailored subunit compositions may direct the complexes to genomic sites essential for each phase of neurogenesis, ensuring that the necessary chromatin remodelling occurs precisely as neural cells mature. The following section will explore the role of BAF complexes in neurodevelopment and disease, based on current understanding and recent findings.

3.2.2 BAF complexes in neurodevelopment and disease

BAF complexes play a pivotal role across the various stages of neurodevelopment, orchestrating essential processes like neural specification, cell proliferation, and differentiation. Their tissue- and stage-specific subunit compositions allow these complexes to dynamically respond to developmental cues and cellular environments. By exploring their function in embryonic stem cells and examining their impact on specific neurodevelopmental disorders, we can begin to uncover the critical mechanisms through which BAF complexes influence brain development and understand the implications when these processes are disrupted.

In embryonic stem cells (ESCs), BAF complexes have a unique composition that supports their essential role early in development. SMARCA4, the ATPase of esBAF complexes, is one of the earliest expressed genes post-fertilization, and its depletion leads to reduced H3K4me2 in mouse zygotes, underscoring its foundational role in chromatin regulation at this stage[135]. Not only does SMARCA4, together with SMARCC1, regulate the pluripotency factors octamer binding transcription factor 4 (OCT4), SOX2, and nanog homeobox (NANOG) to support self-

renewal, but it also promotes cellular proliferation[135,150,151]. Complete loss of SMARCA4, SMARCC1, or SMARC subfamily B1 (SMARCB1) leads to embryonic lethality[152–154], contrasting with SMARCA2 loss, which is linked to increased body size in mice[155]. In neurodevelopment, SMARCA4 is crucial for neural tube closure[152,156], while its loss in nestin-positive cells compromises the neural progenitor pool, resulting in cortical and midbrain thinning, disrupted cerebellar development, and perinatal lethality[157,158]. These shared subunits, such as SMARCA4 and SMARCC1, are found in all neural BAF conformations (esBAF, npBAF, and nBAF), highlighting their essential roles across neurodevelopmental stages. Along with SMARCC2, these subunits contribute to neural specification, neuronal maturation, and the differentiation of glial cells, including astrocytes, oligodendrocytes, and Schwann cells[156,158–166]. Subunits shared between esBAF and npBAF, such as ACTL6A, PHD finger protein 10 (PHF10), and SS18 subunit of BAF chromatin remodelling complex (SS18), are also critical for neural stem cell (NSC) proliferation[147,167,168]. As neural progenitor cells differentiate into neurons, BAF complexes undergo essential subunit transitions, forming the neuron-specific nBAF complexes. This transition must be tightly regulated, as premature or delayed incorporation of nBAF-specific subunits can result in severe phenotypic disruptions, such as dendritic abnormalities linked to ACTL6B or SS18L1 deficiency[169,170]. Conversely, artificially inducing nBAF assembly in fibroblasts can drive neuronal conversion, illustrating the BAF complexes' pivotal role in neurodevelopmental processes[171]. These findings underscore the critical role of BAF complexes in neurodevelopmental processes, emphasizing how subunit composition and transition timing direct complex targeting and ensure the expression of genes appropriate to each neurodevelopmental stage. This critical role of BAF complexes is mirrored in clinical contexts, where disruptions in their function are increasingly recognized as underlying factors in various neurodevelopmental disorders.

Frequent mutations in BAF subunit genes are implicated in neurodevelopmental disorders, including Coffin-Siris Syndrome (CSS), Nicolaides-Baraitser Syndrome (NCBRS), Autism Spectrum Disorder (ASD), and schizophrenia. These mutations primarily affect core BAF subunits, such as ARID1A, ARID1B, and ARID2, along with ATPase subunits SMARCA2 and SMARCA4. Interestingly, *ARID1A*, *ARID1B*, and *ARID2* mutations are often loss-of-function, whereas *SMARCA2* and *SMARCA4* typically present dominant negative missense mutations. Among others, heterozygous mutations in *ARID1A*, *ARID1B* and *SMARCA4* are strongly associated with CSS[172], while *ARID2* mutations are linked to CSS-like phenotypes[173,174] and *SMARCA2* mutations with NCBRS[175]. In human ESCs, NCBRS-associated *SMARCA2* mutations impair neural progenitor differentiation, largely through enhancer reorganization, resulting in lost SRY-box transcription factor 3 (*SOX3*) neural enhancers and the rise of astrocyte-specific enhancers[176]. Similarly, *ARID1B* mutations disrupt neural progenitor transitions to oligodendrocyte and interneuron precursor cells, affecting the excitatory and

inhibitory neuronal balance[177,178]. Recent studies have also shown that SMARCA4 restricts dorsal cell fates early in neurodevelopment[179].

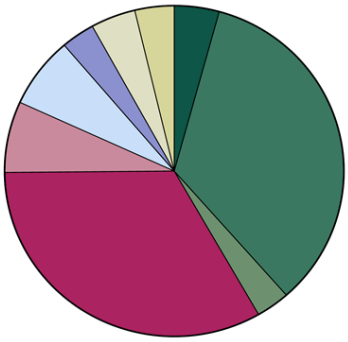

ARID1A	4.3%
ARID1B	**34.2%**
ARID2	3.2%
SMARCA2	**33.2%**
SMARCA4	7.0%
SMARCB1	7.0%
SMARCE1	3.2%
DPF2	4.3%
SOX11	3.7%

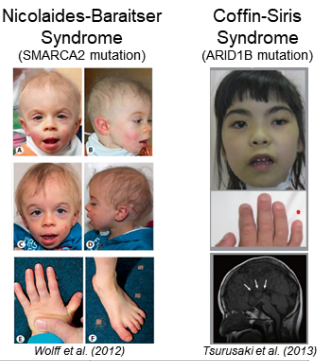

Subunit	BAF complex subclasses	Mutation		Phenotype	Source
ARID1A	cBAF	Nonsense, frameshift indel, missense variant cluster	Loss-of-function mutations	CSS	*Tsurusaki et al. 2012, Lee and Ki 2021*
ARID1B	cBAF	Translocation, frameshift indel, nonsense, missense, microdeletion		ID, **CSS**, ASD, NCBRS, Schizophrenia, Hirschsprung's disease	*Halgren et al. 2012, Santen et al.2012, Smith et al. 2016, Takenouchi et al. 2016, Lu et al. 2021*
ARID2	PBAF	Frameshift indel		CSS/CSS-like	*Bramswig et al.2017, van Paemel et al. 2017*
SMARCA2	cBAF, PBAF, ncBAF	Partial deletion, missense, intronic alteration, duplication	Dominant-negative missense mutations	CSS, **NCBRS**, Schizophrenia	*Koga et al. 2009, Wolff et al. 2012, Tang et al. 2017, Karaer 2020*
SMARCA4	cBAF, PBAF, ncBAF	Partial deletion, missense		**CSS**, ASD	*Tsurusaki et al. 2012, Errichiello et al. 2017, Qian et al. 2021*

Figure 3.2-2: Overview of the mutational prevalence in BAF complex subunits associated with neurodevelopmental disorders. *The core subunits (ARID1A, ARID1B, and ARID2), ATPase subunits (SMARCA2 and SMARCA4), and auxiliary subunits (SMARCB1, SMARCE1, DPF2), along with SOX11, are highlighted. While SMARCA2 and SMARCA4 mutations are predominantly dominant-negative missense mutations (table, red section), ARID subunit mutations are primarily loss-of-function (LOF) mutations (table, green section). In the upper right corner, representative cases are shown: an NCBRS patient with a SMARCA2 mutation and a CSS patient with an ARID1B mutation. Abbreviations: ID = Intellectual Disability, CSS = Coffin-Siris Syndrome, NCBRS = Nicolaides-Baraitser Syndrome, ASD = Autism Spectrum Disorder*[180–193].

Despite recent progress in understanding the role of BAF complexes in human neurodevelopment, much remains unknown. Unresolved areas include the molecular mechanisms behind observed phenotypes, specific cell types affected at different neurodevelopmental stages, chromatin alterations, and pathway disruptions.

Until recently, much of what we know about BAF complex function in neurodevelopment stemmed from animal models, as there were few suitable systems for investigating human neurodevelopment. However, with the advent of cerebral organoids about a decade ago, scientists now have a cellular system to study early human brain development in a controlled, human-specific context.

3.3 Cerebral organoids: Modelling human neurodevelopment and disease

Disorders affecting the nervous system are a major cause of disability, contributing to approximately 11.1 million deaths per year worldwide[194], yet neurodevelopmental processes and their underlying molecular mechanisms remain poorly understood. This limited

understanding is partly due to past reliance on animal models and post-mortem human brain tissue for research into human brain development and neurological diseases. Studies of post-mortem tissue provide detailed insight into specific disorders within a unique genomic context, but they face constraints related to limited sample availability, variability in neurodevelopmental stage, and lack of access to early developmental processes. As a result, early neurodevelopmental dynamics remain largely unexplored.

Animal models have been instrumental in addressing this gap by helping to elucidate the genomic, epigenomic, and pathological pathways involved in certain neurological disorders[195–198]. However, while these models offer *in vivo* applications across various developmental stages and behavioural outcomes, their developmental processes and brain structures differ significantly from those of humans. In comparison to animal models such as Xenopus, Drosophila, and mice, key differences in humans include brain size, the timing of neurodevelopmental processes, cellular composition, and the presence of a six-layered gyrencephalic cortex[199,200]. These distinctions have posed challenges in translating findings from animal models to clinical treatments, with interspecies differences in pharmacodynamics, metabolism, and genetic backgrounds limiting therapeutic progress[201–203]. Ethical considerations around animal research have also driven interest in physiologically relevant human brain models.

Hence, a two-dimensional (2D) culture model has been commonly used, where hiPSCs are differentiated into various neural cell types[204–208]. This method, especially when patient-derived cells are used, allows for the study of personalized genomic backgrounds and holds promise for individualized medical treatments[209,210]. However, 2D cell cultures lack the complex, *in vivo* cellular interactions essential for understanding cell growth and function within the human brain's microenvironment[211].

To address these limitations, hiPSC-derived brain organoids have emerged as a ground-breaking 3D model that mimics early human embryonic brain formation. These organoids form neural rosette structures, radial arrays of columnar cells with a central lumen, expressing markers similar to neuroepithelial cells of the neural tube. Their cytoarchitecture closely resembles that of the early human brain, comprising progenitors, neurons, and astrocytes that emerge in a sequential order consistent with in vivo development[212–216] (**Figure 3.3-1**). During the initial weeks of culture, brain organoids consist predominantly of symmetrically dividing progenitor cells, with the first neurons emerging around the neural rosette structures after approximately 20 days. Extended cultivation allows organoids to reach postnatal-like features, with some characteristics appearing after around a year of growth[217]. Importantly, the increased production of neurons in humans is attributed to the significant expansion of basal radial glial cells (bRGs), of which rodents have only a limited number. This disparity

underscores why rodents are not the ideal model for studying human cortical development. In contrast, one of the advantages of brain organoids is their ability to effectively recapitulate the development of bRGs[212]. Altogether, this system effectively models the cellular diversity and interactions of early brain development within a human genetic context, providing valuable insights into cell growth, maturation, and function. Additionally, different brain organoid models can be used based on research objectives. For example, unguided protocols allow for self-directed development, creating structures from various brain regions without added morphogens[212]. Guided protocols, in contrast, use specific factors to produce region-specific organoids, including those resembling the cerebrum[218], striatum[219], hippocampus[220], midbrain[221], thalamus[222], hypothalamus[223], choroid plexus[224], or cerebellum[225]. New approaches using mixed cultures or structurally connected organoids (assembloids) also enable better modelling of intercellular connections[226].

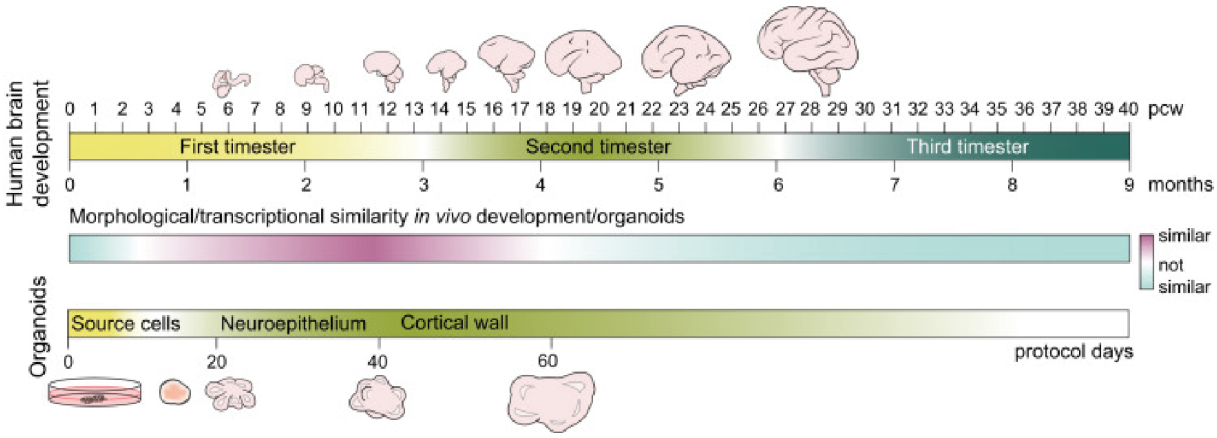

Figure 3.3-1: Comparison between human brain and organoid development. *The morphological and transcriptional similarities between brain organoids and the human brain are shown in pink in the middle bar. The developmental timeframe covered by the brain organoid model spans approximately post-conception weeks (pcw) 4–17, while stages beyond this period are less accurately recapitulated. Pcw = post-conception week. Figure from reference[227].*

Organoids derived from patient-specific or genetically engineered iPSCs have enabled the modelling of numerous neurological and neurodevelopmental disorders, including, among others, microcephaly[212], Seckle syndrome[228], ASD[178,229], Rett-syndrome[230], genetic lissencephaly[231,232], and fragile X syndrome[233]. Furthermore, cerebral organoids now facilitate studies on glioblastoma[234,235] and neurodegenerative diseases like Alzheimer's, with enhancements such as including vascular systems or microglia to mimic disease-relevant interactions in the brain[236–238].

While brain organoid models offer powerful insights into human neurodevelopment and disease, they come with limitations that must be carefully considered. One significant challenge is their rapid growth in culture, which eventually outpaces passive oxygen diffusion and nutrient supply. This leads to the formation of necrotic cores, potentially inducing cellular stress that may influence cell type specification, a concern particularly relevant for long-term

cultures[239]. Although recent advances, such as vascularized organoids, have improved nutrient delivery to the inner regions of organoids[237,240–242], further refinement is still required. Another limitation is the inherent variability of the progenitor cell pool, which can impact the robustness and reproducibility of results. Despite new protocols aimed at standardizing this variability[215], studies should be carefully designed to capture consistent trends rather than organoid-specific differences. Additionally, brain organoids largely represent early developmental stages and often lack non-neuronal cell types, such as oligodendrocytes, which differentiate from RGCs at later stages of brain development and play essential roles like guiding interneuron migration[243]. However, specific culture conditions can induce the generation of oligodendrocytes in brain organoids[244–246]. Moreover, organoids do not yet replicate the intricate, six-layered organization of the human cortex, though some recent techniques have improved layer separation[247]. While organoids can represent distinct brain regions or can be combined into assembloids, they do not fully capture the complex arrangement and neural circuitry of the human brain. As noted, brain organoids primarily recapitulate early developmental processes, whereas later stages, such as gliogenesis, myelination, and synaptogenesis, are less effectively modelled. Furthermore, behavioural outcomes cannot be assessed in an *in vitro* system.

In summary, while brain organoids are powerful tools for studying neurodevelopmental processes and diseases, particularly those occurring in early developmental stages, selecting the appropriate organoid protocol requires careful evaluation and planning to align with specific research objectives.

3.4 Aims of the thesis

First insights into how perturbations in BAF complexes contribute to neurodevelopmental diseases can be gained by examining their roles in physiological neurodevelopmental processes. Most studies in this area have primarily focused on specific subunits and have utilized mouse models. To date, little is understood about how the malfunction or loss of BAF complexes disrupts developmental processes, affects specific cell types, or drives underlying molecular changes in humans. To address this knowledge gap, the objectives of this study include:

1) Elucidating how BAF complexes are involved in human neurodevelopmental processes by characterizing morphological alterations upon BAF complexes perturbation.

   To study the effect of BAF complex perturbation, hiPSC-derived cerebral organoids were used in combination with distinct treatment intervals of an allosteric inhibitor targeting the ATPases (SMARCA2/SMARCA4) of BAF complexes. Distinct treatment intervals were selected across organoid development to capture key developmental stages. Both treated and DMSO control organoids were monitored over time using brightfield microscopy and analysed for neural-specific protein expression through immunofluorescence staining. This approach allowed to characterize cerebral organoids at a cellular level under both physiological and BAF-perturbed conditions.

2) Investigating the molecular mechanisms by which BAF complexes exert their functions and how their perturbation affects the chromatin landscape and the regulation of gene expression in a context-dependent manner.

   This aim was achieved by applying sequencing techniques to treated and untreated cerebral organoid samples at various developmental stages (days 0, 6, 12, 17, and 35). Bulk RNA sequencing (RNA-seq) was conducted across the entire organoid timeline to identify key candidates for further investigation. For these selected samples, bulk ATAC-seq and CUT&Tag-seq were employed at early stages to capture the chromatin landscape immediately following BAF inhibitor treatment. Additionally, at the end of the differentiation protocol, single-nuclei RNA and ATAC sequencing (Multiome) enabled the correlation of gene expression with chromatin accessibility data across different cell types. This approach allowed for the construction of a gene regulatory network under both BAF-perturbed and unperturbed conditions, along with insights into cell type distribution changes within the distinct samples.

3) Identifying the clinically relevant consequences of BAF complex perturbation during early neurodevelopment.

   To gain initial insights, cerebral organoids treated early in development with a BAF inhibitor or derived from hiPSCs heterozygous mutated for ARID1B were analysed, with long-term culture maintained (up to day 120) and monitored by microscopy. Gene expression changes in treated compared to control samples were assessed through RT-qPCR (real-time quantitative polymerase chain reaction) to explore potential resilience mechanisms. Chromatin accessibility changes between treated, mutated, and control samples were analysed using ATAC-seq. GO term and motif enrichment analyses further provided insights into the clinical relevance of these models and the role of BAF complexes in contributing to the observed phenotypes.

4 Material and Methods

4.1 Materials

4.1.1 Antibodies

Table 4.1-1: List of antibodies used for immunofluorescence staining, western blotting and CUT&Tag.

Antibodies						
Name	**Target**	**Clone**	**Host**	**Cat. #**	**Lot #**	**Supplier**
Anti-ARID1B antibody [2D2]	ARID1B	2D2	Mouse	ab57461	GR3345290-3	Abcam
Anti-alpha Tubulin antibody [DM1A] - Loading Control	α-tubulin/TUBA1A	DM1A	Mouse	ab7291	GR3341361-10	Abcam
Goat anti-Mouse IgG (H+L) Secondary Antibody, HRP	Gamma immunoglobins heavy and light chains	Polyclonal	Goat	62-6520	WA319701	Thermo Fisher Scientific
Goat anti-Rabbit IgG (H+L) Secondary Antibody, HRP	Purified Rabbit IgG, whole molecule	Polyclonal	Goat	31466	GR3197113-5	Thermo Fisher Scientific
Brg1 (D1Q7F) Rabbit mAb	SMARCA4/BRG1	D1Q7F	Rabbit	49360	3	Cell Signaling Technology
Anti-Histone H3 (acetyl K27) antibody - ChIP Grade	H3K27ac	Poly-clonal	Rabbit	ab4729	1086546-1	Abcam
Tri-Methyl-Histone H3 (Lys27) (C36B11)	H3K27me3	C36B11	Rabbit	9733	19	Cell Signaling Technology
Guinea Pig anti-Rabbit IgG	Purified Rabbit IgG, whole molecule	Poly-clonal	Guinea pig	ABIN101961	NE-200-032405	Antikoerper online
Anti-RBFOX3 antibody produced in rabbit	RBFOX3	Poly-clonal	Rabbit	HPA030790	000009384	Sigma-Aldrich
Anti-NeuroD1 antibody [3H8] - BSA and Azide free	NEUROD1	3H8	Mouse	ab60704	GR183942-1	Abcam

Antibodies						
Name	**Target**	**Clone**	**Host**	**Cat. #**	**Lot #**	**Supplier**
Anti-PAX3 antibody produced in rabbit	PAX3	Poly-clonal	Rabbit	HPA063659	000002309	Sigma-Aldrich
Anti-FOXG1 antibody [EPR18987]	FOXG1	EPR18987	Rabbit	ab196868	EPR18987	Abcam
DLX1 (E4T1L) Rabbit mAb	DLX1	E4T1L	Rabbit	96585	E4T1L	Cell Signaling Technology
Anti-EMX1 antibody produced in rabbit	EMX1	Poly-clonal	Rabbit	HPA006421	35051	Sigma-Aldrich
Purified anti-Tubulin β 3 (TUBB3) Antibody	TUJ1	TUJ1	Mouse	MMS-435P-100	B401364	BioLegend
Alexa Fluor® 594 anti-MAP2 Antibody	MAP2	SMI52	Mouse	801802	B358846	BioLegend
Goat anti-Mouse IgG (H+L) Highly Cross-Adsorbed Secondary Antibody, Alexa Fluor™ Plus 488	Gamma immunoglobins heavy and light chains	Poly-clonal	Goat	A32723	WJ329963	Thermo Fisher Sceintific

4.1.2 Buffers and solutions

Table 4.1-2: Recipe or source of buffers and solutions used in this study (self-made or produced in-house).

Self-made	
Name	**Recipe**
0.2 M Sodiumorthovanadate	-1.839 g Sodiumorthovanadate dissolved in 25 ml ddH_2O -Adjust pH to 10 (solution will turn orange) -Boil until solution turns back transparent -Adjust to pH 10 and adjust the volume to 50 ml with ddH_2O
20 % SDS	-Dissolve 200 g SDS in 800 ml H_2O -Heat to 68 °C to solute the crystals -Adjust pH to 7.2 -Adjust volume to 1 l with H_2O
20 X TBS	-48 g Tris base -176 g NaCl -Dissolve in 900 ml ddH_2O -Adjust pH to 7.6 -Add ddH_2O to a final volume of 1 l

Self-made	
Name	**Recipe**
4 X Laemmli buffer	-17.6 ml 0.5 M TRIS pH 6.8 -17.6 ml glycerol -8.8 ml 20 % SDS -100 mg bromophenol blue
RIPA Buffer	-10 ml 1 M TRIS pH8 -2 ml NP-40 -1g Sodiumdeoxycholate -2ml 10 % SDS -6 ml 5 M NaCl -2 ml 0.5 M EDTA -2 ml Glycerol -0.5 ml 1 M $MgCl_2$ -2ml 0.2 M Sodiumorthovandate -H_2O up to 200 ml
TBS-T	-1 X TBS -0.1 % Tween-20
IMB Media Lab and Protein Production	
Name	**Supplier and Recipe**
First Strand Buffer, 5 X	IMB CF Protein Production -250 mM Tris-Cl (pH 8.0 at room temperature) -375 mM KCl -15 mM $MgCl_2$
LB agar plates with ampicillin (LB-Amp Plates)	IMB Media Lab, L-20_P -1.5 % (w/v) Agar -100 µg/ml Ampicillin -Ultrapure water
LB Media, Luria broth	IMB Media Lab, L-10_M -0.17 M NaCl -1 % (w/v) Peptone (from meat) -0.5 % (w/v) Yeast extract -Ultrapure water -adjusted to pH 7.0 ± 0.2
PBS, 5 X Phosphate Buffered Saline pH 7.5	IMB Media Lab, P-003RT -685 mM NaCl -13.5 mM KCl -50 mM Na_2HPO_4 -8 mM KH_2PO_4 -Ultrapure water -adjusted to pH 7.4 ± 0.1
SDS running buffer, 10 X	IMB Media Lab, S-10_L -1 % (v/v) SDS -0.25 M Tris -1.9 M Glycine -Ultrapure water
Transfer buffer, 10 X	IMB Media Lab, T-10_L -1.9 M Glycine -0.25 M Tris -Ultrapure water (-15 % MeOH before use)

Table 4.1-3: List of Buffers, solutions and cell culture media as well as supplements used in this study.

Buffers, solutions, media and supplements		
Name	**Supplier**	**Cat #**
2 % Digitonin solution (CHR 103)	Merck Chemicals GmbH	CHR103
20 X Nuclei Buffer (Part of Chromium Next GEM Single Cell Multiome ATAC + Gene Expression Reagent Bundle, 4 rxns)	10X Genomics	1000285

Buffers, solutions, media and supplements		
Name	**Supplier**	**Cat #**
Anti-Adherence Rinsing Solution	Stem Cell Technologies	7010
B27 supplement, 50 X	Thermo Fisher Scientific	17504044
B27 supplement minus vitamin A, 50 X	Thermo Fisher Scientific	12587010
Cell Recovery Solution	Corning	354253
CloneR, Cloning Supplement 10 X	Stem Cell Technologies	5889
Cryopreservation medium, CryoStor CS10	BioLife Solutions, Inc.	210502
DMEM/F-12 Media	Gibco	11320033
dNTP, Deoxynucleotide (dNTP) Solution Set	New England BioLabs GmbH	N0446S
DPBS, Dulbecco's Balanced Salt Solution, no calcium, no magnesium	Gibco	14190144
FSC 22 Blue Frozen Section Media	Leica	3801481
Gel loading dye purple 6x	New England BioLabs GmbH	B7024S
GlutaMAX™ Supplement	Gibco	35050061
MACS® BSA Stock solution	Miltenyi Biotec	130-091-376
Matrigel® Growth Factor Reduced (GFR) Basement Membrane Mix	Corning	354230
Matrigel® hESC-Qualified Matrix	Corning	354277
MEM Non-Essential Amino Acids (NEAA) Solution	Gibco	11140050
N2 Supplement	Gibco	17502048
Neurobasal™ Media	Gibco	21103049
Oligo(DT) 18 Primer	Thermo Fisher	SO132
PageRuler™ Plus Prestained Protein Ladder	Thermo Fisher Scientific	26620
Penicillin-Streptomycin (5000 U/ml)	Gibco	15070063
Pierce ECL Western Blotting Substrate	Fisher Scientific GmbH	10455145
Ponceaus S Solution	Sigma-Aldrich	P7170-1L
ProLong gold Antifade reagent	Fisher Sientific GmbH	P36934
Protector RNase Inhibitor (40 U/µl)	Sigma-Aldrich	3335402001
Puromycin solution	InvivoGen	ant-pr-1
rCutsmart™ Buffer / 10 X CutSmart® Buffer	New England BioLabs GmbH	B6004S
ReLeSR passaging solution	Stem Cell Technologies	5872
Rnase Inhibitor, Murine	New England BioLabs GmbH	M0314S
Stem cell medium, StemMACS™ iPS-Brew XF, human	Miltenyi Biotec	130-104-368
SureCast™ 40 % Acrylamide solution	Thermo Fisher Scientific	HC2040
SureCast™ 40 % Ammonium Persulfate (APS)	Thermo Fisher Scientific	HC2005
SureCast™ Resolving Buffer	Thermo Fisher Scientific	HC2215
SureCast™ Stacking Buffer	Thermo Fisher Scientific	HC2112
SureCast™ TEMED	Fisher Scientific GmbH	HC2006
SYBR Green I Nucleic Acid Gel Stain	Fisher Scientific GmbH	10710004
SYBR™ Safe DNA gel stain	Thermo Fisher Scientific	S33102

4.1.3 Cell lines

Table 4.1-4: List of cell lines used in this study.

Cell line	Sex	Source
HMGU1 (ISFi001-A (RRID:CVCL YT30))	male	Institute for stem cell Research, Helmholtz Center München

Cell line	Sex	Source
HMGU1 ARID1B$^{+/-}$	male	Self-generated CRISPR/Cas9-induced c.2406del; predicted effect: frameshift (p.G804Afs15X)
BIHi242	female	Max Delbrück Center Berlin, Ralf Kühn
BIHi001-A	male	Max Delbrück Center Berlin, Ralf Kühn

4.1.4 Chemicals and consumables

Table 4.1-5: List of consumables used in this study.

Consumable	Supplier	Cat #
10 cm culture dish, Falcon® 100 mm TC-treated Cell Culture Dish	Corning	353003
384-well plates, MicroAmp™ Optical 384-Well Reaction Plate with Barcode	Applied Biosystems	4309849
6-well, 12-well, 24-well tissue culture plates	Sarstedt, Corning (24-well)	83.3920, 83.3921, 353047 (24-well)
70 µm strainer, Greiner Bio-One CELLSTAR™ EASYstrainer™	Greiner Bio-One	542070
96-well plates, Library preparation qualified	Bio-Rad	HSP9601
Blotting Sponges	Thermo Fisher Scientific	EI9052
Cryomolds, 10 mm x 10 mm x 5 mm / 15 mm x 15 mm x 5 mm	Sakura Finetek	4565, 4566
Cryo-vials	Sarstedt	72.379
DNA LoBind tubes, 1.5 ml	Eppendorf	301108051
FACS tube, Falcon® Round-Bottom Tubes with Cell Strainer Cap, 5 ml	Corning	352235
Filter paper, 3mm CHR Blotting Paper Sheets	GE Healthcare	3030-917
Filter tips, P1000, P200, P20, P10/20 pipette filter tips	StarLab	S1122-1730-C, S1120-8710-C, S1123,1710-C, S1120-3710-C
Insulin syringes, U-100 insulin 29G needle	BD Biosciences	324824
PAP-Pen, 2 mm tip width	Sigma-Aldrich	Z672548
Parafilm M	Amcor	PM-996
PCR tubes (0.2 ml), Cer.0.2 ml 8 Strip StarPCR® Tubes/Caps	STARLAB GmbH	A1402-3700
PVDF membrane, 0.45 µm	Thermo Fisher Scientific	88518
Tips, P1000, P200, P10/20 pipette tips	StarLab	S1111-6701-C, S1113-1700-C, S1110-3700-C,
Tubes, 1.5 ml, 2.0 ml	Sarstedt	72.706.400, 72.695.500
Tubes, 15 ml, 50 ml	Sarstedt	62.554.502, 62.547.254
Ultra-low attachement plate, Nunclon™ Sphera™ 96-Well, Nunclon Sphera-Treated, U-Shaped-Bottom Microplate	Thermo Fisher Scientific	174925
X-tra adhesive microscope slides	Leica	3800206AE

Table 4.1-6: List of chemicals used in this study.

Chemicals	Supplier	Cat #
2-Mercaptoethanol	Sigma-Aldrich	63689-100ML-F
Acetone	Carl Roth	5025.2
Agarose	Sigma-Aldrich	A9539-500G
Ampicillin (100 mg/ml)	IMB Media Lab	A-10_A
AMPure XP Beads	CF Genomics, Beckman Coulter	A63881
Bromophenol Blue	Sigma Aldrich	B0126

Chemicals	Supplier	Cat #
BSA, Albumin Fraktion V	Carl Roth	8076.4
Calcium chloride dihydrate, $CaCl_2 \cdot 2H_2O$	Sigma-Aldrich	C3306-100G
complete™, EDTA-free Protease Inhibior	Sigma-Aldrich	4693132001
Concanavalin A beads BioMag®Plus	Polysciences Europe GmbH	86057-3
DAPI, 4,6-Diamidino-2-phenylindol	Thermo Fisher Scientific	1530306
DMF (N,N-Dimethylformamide)	Sigma-Aldrich	319937
DMSO, Dimethyl sulfoxide	Sigma-Aldrich	41639-100ML
Ethanol 96 % vergällt	Carl Roth	T171.4
Ethanol, Absolute, Molecular Biology Grade	Fisher Scientific	16606002
Glycerol	Sigma-Aldrich	G5516-500ML
Heparin Sodium	Sigma-Aldrich	H3149-50KU
HEPES	Sigma-Aldrich	H3375
Insulin solution, human recombinant	Sigma-Aldrich	I9278-5ML
Isopropanol, >=99.5%	Sigma-Aldrich	109827
Kaliumchloride, KCl	Carl Roth	6781.4
Kaliumhydroxide, KOH	Carl Roth	P747.2
L-Aascrobic acid, free acid gamma-irradiat	Sigma-Aldrich	A4403-100MG
Magnesium chloride hexahydrate, $Cl_2Mg \cdot 6H_2O$	Fisher Scientific	BP214-500
Manganese(II)chloride, MnCl2	Sigma-Aldrich	63535-50G-F
Methanol, >=99.8%	Sigma-Aldrich	179337
NP-40, Nonidet P40 substitute	Sigma-Aldrich	11754599001
Nuclease-Free Water	Thermo Fisher Scientific	4387936
Paraformaldehyde 16 % Solution EM Grade	Electron Microscopy Sciences	15710
Phosphatase inhibitor, PhosSTOP	Sigma-Aldrich	4906837001
PIC, Protease Inhibitor Cocktail	Sigma-Aldrich	P8340
Skim milk powder	Sigma-Aldrich	70166-500g
Sodium bicarbonate, $NaHCO_3$	Sigma-Aldrich	S5761-500G
Sodium chloride, NaCl	Sigma-Aldrich	S3014-500G
Sodium orthovanadate, Na_3VO_4	Sigma-Aldrich	S6508-50G
Spermidine	Sigma-Aldrich	S0266-5G
Sucrose, >= 99.5% (GC)	Sigma-Aldrich	S7903-1KG
Tris Base Crystals	Fisher Scientific	BP152-1
Triton X-100	Sigma-Aldrich	T8787-250ML
Tween-20	Sigma-Aldrich	P9416

4.1.5 Enzymes

Table 4.1-7: List of enzymes or enzyme-containing mixtures used in this study.

Enzyme	Supplier	Cat #	Purpose
Tn5	IMB Protein Production Core Facility	PPCF Staff (Room 00.433)	Tagmentation (ATAC)
pA-Tn5	IMB Protein Production Core Facility	PPCF Staff (Room 00.433)	Tagmentation (CUT&Tag)
Superscript II reverse transcriptase	IMB Protein Production Core Facility	PPCF Enzyme Freezer (Room 00.433)	cDNA preparation

Enzyme	Supplier	Cat #	Purpose
Power SYBR Green PCR Mix	Applied Biosystems	4367659	cDNA amplification (RT-qPCR)
NEBNext Ultra II Q5 Master Mix	NEB	M0544S	DNA amplification (PCR)
DNase I & DNase Buffer	NEB	M0303S	DNA digest
Quick CIP	NEB	M0525S	Dephosphorylation of DNA ends
Accutase	Sigma-Aldrich	A6964	Dissociation / single cell suspension
BbsI-HF	NEB	R3539S	Digest of plasmid (Cloning)
2 X HiFi Hot Start Ready Mix	Roche	KK2601	PCR mix (Amplicon sequencing)
0.05 % Trypsin-EDTA	Gibco	25300054	Dissociation of brain organoids
Proteinase K	Sigma-Aldrich	P2308-100MG	Protein digest for nuclei acid isolation

4.1.6 Compounds

Table 4.1-8: List of compounds used in this study.

Compound	Supplier	Cat #
BRM014	Hycultec	HY-119374
ACBI1	opnMe, Böhringer Ingelheim	ACBI1
Y-27632	StemCell, Biogems, Apollo Scientific, TargetMol	72304, 1293823, BISN0135, T1725

4.1.7 Kits

Table 4.1-9: List of kits used in this study.

Kit	Supplier	Cat #	Pupose
MiniElute PCR Purification Kit	Qiagen	28006	DNA extraction and purification
Agilent High Sensitivity DNA Kit	Agilent Technologies	5067-4626	DNA electrophoresis with the Bioanalyzer system
ZymoPURE II Plasmid Midiprep Kit	Zymo Research	D4201	Plasmid DNA isolation (from 50-100 mL bacterial culture)
QIAPrep Spin Miniprep Kit	Qiagen	27106	Plasmid DNA isolation (from 5 mL bacterial culture)
Monarch DNA Gel Extraction Kit	NEB	T1020L	DNA purification from agarose gels
E.Z.N.A. HP Total RNA Isolation Kit	Omega Bio-Tek	R6812-02	Isolation of RNA (cerebral organoids from day 35 and older)
E.Z.N.A. MicoElute Total RNA Kit	Omega Bio-Tek	R6831-02	Isolation of RNA (hiPSCs, embryoid bodies and cerebral organoids from day 6-17)
Qubit dsDNA HS Assay Kit	Invitrogen	Q32854	DNA quantification
Pierce BCA Protein Assay Kit	Thermo Fisher Scientifc	10741395	Protein quantification
Quick Ligation Kit	NEB	M2200L	Ligation of cohesive end or blunt end DNA fragments
jetOptimus	Polyplus, Satorius	101000051	Transfection of hiPSCs
Monarch® Genomic DNA Purification Kit	NEB	T3010S	Genomic DNA isolation
Qubit dsDNA HS Assay Kit	Thermo Fisher Scientific	Q32854	DNA concentration measurement
Clarity Western ECL Substrate	Bio-Rad	1705061	Western Blot band detection
Quick Ligation Kit	NEB	M2200S	Ligation of cohesive or blunt DNA ends (Cloning)
QuantSeq 3' mRNA-Seq Library Prep Kit FWD	Lexogen	LEX-194.96	Library preparation bulk RNA-seq

Kit	Supplier	Cat #	Pupose
NextSeq 500/550 High Output single-read (SR) Kit v2.5 (75 Cycles)	Illumina	20024906	bulk RNA-sequencing
Chromium Next GEM Single Cell Multiome ATAC + Gene Expression Reagent Bundle	10X Genomics	1000285	Multiome
Chromium Next GEM Chip J Single Cell Kit, 16 rxns	10X Genomics	1000230	Multiome
Dual Index Kit TT Set A 96 rxns	10X Genomics	1000215	Multiome
NextSeq 1000/2000 P2 Reagents (100 Cycles)	Illumina	20046811	Multiome Sequencing
NextSeq 2000 P3 Reagents (100 Cycles)	Illumina	20040559	Bulk ATAC-sequencing

4.1.8 Laboratory equipment/devices

Table 4.1-10: List of laboratory equipment used in this study.

Equipment	Supplier
2100 Bioanalyzer	Agilent
Cell counter, Celldrop FLCellCounter	DeNOVIX
Cell Sorter, BD FACSAria III SORP	BD Biosciences
Centrifuge table top (mini, Sprout Plus)	Biozym
Centrifuge, 5425 (tissue culture)	Eppendorf
Centrifuge, 5427R G (cooling)	Eppendorf
Centrifuge, 5430R (cooling)	Eppendorf
Centrifuge, 5804G (tissue culture)	Eppendorf
Centrifuge, table top Fresco 21 (cooling)	Thermo Fisher Scientific
Centrifuge, table top IIPico21 (bacterial culture)	Thermo Fisher Scientific
ChemiDoc MP V3 Touch Imaging System	Bio-Rad
CO2-incuabtor, HERAcell240i (hiPSC culture)	Thermo Fisher Scientific
CO2-incubator, Steri-Cult	Thermo Fisher Scientific
Cryosection device, Cryostat Leica CS3050S	Leica
Electrophoresis System, XCell SureLock Mini-Cell Electrophoresis System	Thermo Fisher Scientific
Fine scale, Sartorius SecuraSemi	Sartorius AG
Freezer (-150 °C)	Sanyo
Freezer (-20 °C)	Liebherr
Freezer (-80 °C)	Sanyo
Freezing container, Mr. Frosty	Thermo Fisher Scientific
Fridge (4 °C)	Liebherr
Glass plates SureCast	Thermo Fisher Scientific
Incubator, bacterial culture agar plates, KB53	Binder
Incubator, liquid bacterial culture, Multitron Standard	Infors HT
Laminar flow hood, BSC-SG403 EN	Dometic
Magnetic rack, 1.5 / 2 ml tubes, DynaMag2	Thermo Fisher Scientific
Magnetic rack, 96-well plate, IMAG-96P	Corning
Magnetic rack, PCR tubes	3D-printed by E-Lab IMB
Microscope, (widefield) Thunder	Leica
Microscope, BC43 Spinning Disk Confocal Microscope	Oxford Instruments
Microscope, DM IL LED	Leica
Microscope, EVOS M5000c Imaging System	Thermo Fisher Scientific
Microscope, Stereo microscope M205FA	Leica
Microscope, Thunder widefield Microscope	Leica

Equipment	Supplier
Microwave, MS28F303TAS	Samsung
Multifuge, X3 (bacterial culture)	Thermo Fisher Scientific
Multifuge, X3R (cooling; swinging-bucket rotor)	Thermo Fisher Scientific
NextSeq 500	Illumina
NextSeq2000	Illumina
Nutator (room temperature), Polymax 1040	Heidolph Instruments
Nutator, GyroMiniNutatingMixer (cold room)	Labnet
Orbital-Shaker, Celltron InforsHT	Infors AG
Orbital-Shaker, DOS-10L	neoLab
PIPETBOY acu 2	INTEGRA Biosciences
Plate reader, Infinite M200 Pro	Tecan
PowerPacBasic	Bio-Rad
PowerPacHC	Bio-Rad
Qubit 2.0 Fluorometer	Life Technologies
Real-time PCR system, QuantStudio™ 5	Applied Biosystems
Rocking platform, Duomax1030	Heidolph Instruments
Roller mixer, RM5-30V (cold room)	Zipperer GmbH
Scale, ED822-0CE	Sartorius AG
Spectrophoto-/Fluorometer DS-11FX	DeNOVIX
Spinning Wheel (Rotator)	Sunlab
Thermal cycler, Biometra TAdvanced	Analytik Jena
Thermomixer, C	Eppendorf
Thermomixer, Comfort	Eppendorf
Tilt/roller mixer, RS-TR05	Phoenix Instruments
Tweezers, 5-Inox-H (sharp)	DUMONT
ViiA™ 7 Real-Time PCR System	Applied Biosystems
Vortexer, IKAMS3	IKA
Vortexer, LSE	Corning
Vortexer, VortexGenie2	Scientific Industries, Inc.
Waterbath, 1002	GFL
Waterbath, TW20	Julabo

4.1.9 Oligonucleotide sequences

Table 4.1-11: List of oligonucleotides used in this study.

Target	Oligo #	Sequence (5' to 3')	Purpose
Tn5ME-A	274	TCGTCGGCAGCGTCAGATGTGTATAAGAGACAG	Tn5 adapter
Tn5ME-B	275	GTCTCGTGGGCTCGGAGATGTGTATAAGAGACAG	Tn5 adapter
Tn5ME	276	CTGTCTCTTATACACATCT	Tn5 adapter
ARID1B	341R	GACGTGTGCTCTTCCGATCTGCTTCCTACAGGAGAGCCAAC	Amplicon-seq
ARID1B	342F	CTACACGACGCTCTTCCGATCTGGCAGCCCAATGGATCCAA	Amplicon-seq
ARID1B	349R	GACGTGTGCTCTTCCGATCTGGTACTGCATTCCGGCCATG	Amplicon-seq
ARID1A	344F	CTACACGACGCTCTTCCGATCTCACCAAGTTGTATGAGCTGGGTG	Amplicon-seq
ARID1A	351R	GACGTGTGCTCTTCCGATCTAGTCAATCCACCAATCTCCTTCAC	Amplicon-seq
ARID2	347F	CTACACGACGCTCTTCCGATCTAGATTTTCTTAGATTGTTCACGTTCAGAC	Amplicon-seq

Target	Oligo #	Sequence (5' to 3')	Purpose
ARID2	352R	GACGTGTGCTCTTCCGATCTGGAAAAGTCACTACTACTC ACCGC	Amplicon-seq
NANOG	11F	AACCTCAGCTACAAACAGGTGA	RT-qPCR
NANOG	11R	TCTGCGTCACACCATTGCTA	RT-qPCR
ATP5F1B	168F	CAGCAGATTTTGGCAGGTGAA	RT-qPCR
ATP5F1B	168R	ACCCCTCACGATGAATGCTC	RT-qPCR
FOXG1	169F	TGGCCCATGTCGCCCTTCCT	RT-qPCR
FOXG1	169R	GCCGACGTGGTGCCGTTGTA	RT-qPCR
SATB2	189F	CACTGCAAAGCCAAGCACC	RT-qPCR
SATB2	189R	CTCCATGCTGCTCCGACTC	RT-qPCR
TBR2	194F	CACCGCCACCAAACTGAGA	RT-qPCR
TBR2	194R	ACAGGTCACCCATTTGCCC	RT-qPCR
MAP2	196F	GGGAGGATGAAGAGGGTGCC	RT-qPCR
MAP2	196R	GAACTATCCTTGCAGACACCTCC	RT-qPCR
SOX2	262F	CGGCAGCTACAGCATGATG	RT-qPCR
SOX2	262R	TACTCTCCTCTTTTGCACCC	RT-qPCR
CTIP2	263F	TCCAGAGCAATCTCATCGTG	RT-qPCR
CTIP2	263R	GCATGTGCGTCTTCATGTG	RT-qPCR
TUJ1	265F	TGATGAACATGGCATCGAC	RT-qPCR
TUJ1	265R	TATTTGCCACCTGTGGCTTC	RT-qPCR
NeuN	266F	GAGGAGTGGCCCGTTCTG	RT-qPCR
NeuN	266R	AGGCGGAGGAGGGTACTG	RT-qPCR
GAPDH	34F	GTGAAGGTCGGAGTCAACGG	RT-qPCR
GAPDH	34R	AGTTGAGGTCAATGAAGGGGT C	RT-qPCR
DCX	40F	GAAGCAAGTCTCCAGCTGACTC	RT-qPCR
DCX	40R	GGCAGGTACAGGTCCTTGTG	RT-qPCR
vGLUT1	41F	TTTCTACGTCTACGGCAGCTT	RT-qPCR
vGLUT1	41R	CTCGATGTACTTGCGCTCCT	RT-qPCR
GABBR1	45F	CACACTCCACAACCCTACCC	RT-qPCR
GABBR1	45R	AGGTCGTCCAGAGTCGAAGT	RT-qPCR
S100B	47F	GAAGGGAGGGAGACAAGCAC	RT-qPCR
S100B	47R	CCTCCTGCTCTTTGATTTCCTCT	RT-qPCR
OLIG2	48F	AAATCGCATCCAGATTTTCGGG	RT-qPCR
OLIG2	48R	CCGGCAGAAAAAGGTCATCG	RT-qPCR
TBR1	55F	TGTGATTTTGGCGGATCCCA	RT-qPCR
TBR1	55R	AGACCCGATTTCCTTGCACA	RT-qPCR
EMX1	573F	CTTCTTCGGCCACCGCTT	RT-qPCR
EMX1	573R	AGTGGTTCTTCTCGAAGGCG	RT-qPCR
GBX2	575F	CAGGCTTCGCTCGTCGG	RT-qPCR
GBX2	575R	GCTGTAGTCCACATCGCTCT	RT-qPCR
OTX2	576F	TTGCTAGAGCAGCCCTCACT	RT-qPCR
OTX2	576R	GGGTTTGGAGCAGTGGAACTTA	RT-qPCR
NKX2-1	578F	ACCAGGACACCATGAGGAAC	RT-qPCR
NKX2-1	578R	CGCCGACAGGTACTTCTGTT	RT-qPCR
PAX6	57F	GGTCTTCAAGCAACAACAGCA	RT-qPCR
PAX6	57R	CCCTAGTTAAAGTCTTCCCCCTTT	RT-qPCR
LMX1A	588F	CATCGAGCAGAGTGTCTACAGC	RT-qPCR
LMX1A	588R	TGTCGTCGCTATCCAGGTCATG	RT-qPCR
DLX5	599F	CAGCCAAAGCTTATGCCGAC	RT-qPCR

Target	Oligo #	Sequence (5' to 3')	Purpose
DLX5	599R	CGGTCACTTCTTTCTCTGGCT	RT-qPCR
FEZF2	601F	TGAAGGAAAACTCGGCCCTG	RT-qPCR
FEZF2	601R	GTGAGCGTTAAACACCTTGCC	RT-qPCR
gRNA1 ARID1B	3a	CACCGCTGCCCATGCCATACAACTG	CRISPR/Cas9 gRNA
gRNA1 ARID1B	3b	AAACCAGTTGTATGGCATGGGCAGC	CRISPR/Cas9 gRNA
gRNA3 ARID1B	5a	ACCGCTCAGCAGTCAGTGCATCCGT	CRISPR/Cas9 gRNA
gRNA3 ARID1B	5b	TAAAACGGATGCACTGACTGCTGAG	CRISPR/Cas9 gRNA
gRNA4 ARID1A	91a	CACCGATGTGGGTGGACCGTTATC	CRISPR/Cas9 gRNA
gRNA4 ARID1A	91b	AAACGATAACGGTCCACCCACATC	CRISPR/Cas9 gRNA
gRNA1 ARID2	6a	CACCGAGGTTTCTGAGAAGAATCAG	CRISPR/Cas9 gRNA
gRNA1 ARID2	6b	AAACCTGATTCTTCTCAGAAACCTC	CRISPR/Cas9 gRNA
noMX	61	AATGATACGGCGACCACCGAGATCTACACTCGTCGGCAGCGTCAGATGTG	Library ATAC/CUT&Tag
Index i7 Ad2.1	62	CAAGCAGAAGACGGCATACGAGATTCGCCTTAGTCTCGTGGGCTCGGAGATGT	Library ATAC/CUT&Tag
Index i7 Ad2.2	206	CAAGCAGAAGACGGCATACGAGATCTAGTACGGTCTCGTGGGCTCGGAGATGT	Library ATAC/CUT&Tag
Index i7 Ad2.3	207	CAAGCAGAAGACGGCATACGAGATTTCTGCCTGTCTCGTGGGCTCGGAGATGT	Library ATAC/CUT&Tag
Index i7 Ad2.4	208	CAAGCAGAAGACGGCATACGAGATGCTCAGGAGTCTCGTGGGCTCGGAGATGT	Library ATAC/CUT&Tag
Index i7 Ad2.6	210	CAAGCAGAAGACGGCATACGAGATCATGCCTAGTCTCGTGGGCTCGGAGATGT	Library ATAC/CUT&Tag
Index i7 Ad2.7	211	CAAGCAGAAGACGGCATACGAGATGTAGAGAGGTCTCGTGGGCTCGGAGATGT	Library ATAC/CUT&Tag
Index i7 Ad2.9	213	CAAGCAGAAGACGGCATACGAGATAGCGTAGCGTCTCGTGGGCTCGGAGATGT	Library ATAC/CUT&Tag
Index i7 Ad2.10	214	CAAGCAGAAGACGGCATACGAGATCAGCCTCGGTCTCGTGGGCTCGGAGATGT	Library ATAC/CUT&Tag
Index i7 Ad2.11	215	CAAGCAGAAGACGGCATACGAGATTGCCTCTTGTCTCGTGGGCTCGGAGATGT	Library ATAC/CUT&Tag
Index i7 Ad2.12	216	CAAGCAGAAGACGGCATACGAGATTCCTCTACGTCTCGTGGGCTCGGAGATGT	Library ATAC/CUT&Tag
Index i7 Ad2.13	217	CAAGCAGAAGACGGCATACGAGATATCACGACGTCTCGTGGGCTCGGAGATGT	Library ATAC/CUT&Tag
Index i7 Ad2.14	218	CAAGCAGAAGACGGCATACGAGATACAGTGGTGTCTCGTGGGCTCGGAGATGT	Library ATAC/CUT&Tag
Index i7 Ad2.15	219	CAAGCAGAAGACGGCATACGAGATCAGATCCAGTCTCGTGGGCTCGGAGATGT	Library ATAC/CUT&Tag
Index i7 Ad2.16	220	CAAGCAGAAGACGGCATACGAGATACAAACGGGTCTCGTGGGCTCGGAGATGT	Library ATAC/CUT&Tag
Index i7 Ad2.17	221	CAAGCAGAAGACGGCATACGAGATACCCAGCAGTCTCGTGGGCTCGGAGATGT	Library ATAC/CUT&Tag
Index i7 Ad2.18	222	CAAGCAGAAGACGGCATACGAGATAACCCCTCGTCTCGTGGGCTCGGAGATGT	Library ATAC/CUT&Tag
Index i7 Ad2.19	223	CAAGCAGAAGACGGCATACGAGATCCCAACCTGTCTCGTGGGCTCGGAGATGT	Library ATAC/CUT&Tag
Index i7 Ad2.20	224	CAAGCAGAAGACGGCATACGAGATCACCACACGTCTCGTGGGCTCGGAGATGT	Library ATAC/CUT&Tag
Index i7 Ad2.21	225	CAAGCAGAAGACGGCATACGAGATGAAACCCAGTCTCGTGGGCTCGGAGATGT	Library ATAC/CUT&Tag
Index i7 Ad2.22	226	CAAGCAGAAGACGGCATACGAGATTGTGACCAGTCTCGTGGGCTCGGAGATGT	Library ATAC/CUT&Tag
Index i7 Ad2.23	227	CAAGCAGAAGACGGCATACGAGATAGGGTCAAGTCTCGTGGGCTCGGAGATGT	Library ATAC/CUT&Tag
Index i7 Ad2.37	305	CAAGCAGAAGACGGCATACGAGATAATTCTTGGTCTCGTGGGCTCGGAGATGT	Library ATAC/CUT&Tag

Target	Oligo #	Sequence (5' to 3')	Purpose
Index i7 Ad2.38	306	CAAGCAGAAGACGGCATACGAGATGGCATTTCGTCTCG TGGGCTCGGAGATGT	Library ATAC/CUT&Tag
Index i5 501	487	AATGATACGGCGACCACCGAGATCTACACTAGATCGCT CGTCGGCAGCGTCAGATGTGTA	Library ATAC/CUT&Tag
Index i5 502	488	AATGATACGGCGACCACCGAGATCTACACCTCTCTATTC GTCGGCAGCGTCAGATGTGTA	Library ATAC/CUT&Tag
Index i5 503	489	AATGATACGGCGACCACCGAGATCTACACTATCCTCTTC GTCGGCAGCGTCAGATGTGTA	Library ATAC/CUT&Tag
Index i5 504	490	AATGATACGGCGACCACCGAGATCTACACAGAGTAGAT CGTCGGCAGCGTCAGATGTGTA	Library ATAC/CUT&Tag
Index i5 505	491	AATGATACGGCGACCACCGAGATCTACACGTAAGGAGT CGTCGGCAGCGTCAGATGTGTA	Library ATAC/CUT&Tag
Index i5 506	492	AATGATACGGCGACCACCGAGATCTACACACTGCATATC GTCGGCAGCGTCAGATGTGTA	Library ATAC/CUT&Tag
Index i7 D701	D701	GATCGGAAGAGCACACGTCTGAACTCCAGTCACATTACT CGATCTCGTATGCCGTCTTCTGCTTG	Library Amplicon-seq
Index i7 D702	D702	GATCGGAAGAGCACACGTCTGAACTCCAGTCACTCCGG AGAATCTCGTATGCCGTCTTCTGCTTG	Library Amplicon-seq
Index i7 D703	D703	GATCGGAAGAGCACACGTCTGAACTCCAGTCACCGCTC ATTATCTCGTATGCCGTCTTCTGCTTG	Library Amplicon-seq
Index i7 D704	D704	GATCGGAAGAGCACACGTCTGAACTCCAGTCACGAGAT TCCATCTCGTATGCCGTCTTCTGCTTG	Library Amplicon-seq
Index i7 D705	D705	GATCGGAAGAGCACACGTCTGAACTCCAGTCACATTCA GAAATCTCGTATGCCGTCTTCTGCTTG	Library Amplicon-seq
Index i7 D706	D706	GATCGGAAGAGCACACGTCTGAACTCCAGTCACGAATT CGTATCTCGTATGCCGTCTTCTGCTTG	Library Amplicon-seq
Index i7 D707	D707	GATCGGAAGAGCACACGTCTGAACTCCAGTCACCTGAA GCTATCTCGTATGCCGTCTTCTGCTTG	Library Amplicon-seq
Index i7 D708	D708	GATCGGAAGAGCACACGTCTGAACTCCAGTCACTAATG CGCATCTCGTATGCCGTCTTCTGCTTG	Library Amplicon-seq
Index i7 D709	D709	GATCGGAAGAGCACACGTCTGAACTCCAGTCACCGGCT ATGATCTCGTATGCCGTCTTCTGCTTG	Library Amplicon-seq
Index i7 D710	D710	GATCGGAAGAGCACACGTCTGAACTCCAGTCACTCCGC GAAATCTCGTATGCCGTCTTCTGCTTG	Library Amplicon-seq
Index i7 D711	D711	GATCGGAAGAGCACACGTCTGAACTCCAGTCACTCTCG CGCATCTCGTATGCCGTCTTCTGCTTG	Library Amplicon-seq
Index i7 D712	D712	GATCGGAAGAGCACACGTCTGAACTCCAGTCACAGCGA TAGATCTCGTATGCCGTCTTCTGCTTG	Library Amplicon-seq
Index i5 D501	D501	AATGATACGGCGACCACCGAGATCTACACAGGCTATAA CACTCTTTCCCTACACGACGCTCTTCCGATCT	Library Amplicon-seq
Index i5 D502	D502	AATGATACGGCGACCACCGAGATCTACACGCCTCTATAC ACTCTTTCCCTACACGACGCTCTTCCGATCT	Library Amplicon-seq
Index i5 D503	D503	AATGATACGGCGACCACCGAGATCTACACAGGATAGGA CACTCTTTCCCTACACGACGCTCTTCCGATCT	Library Amplicon-seq
Index i5 D504	D504	AATGATACGGCGACCACCGAGATCTACACTCAGAGCCA CACTCTTTCCCTACACGACGCTCTTCCGATCT	Library Amplicon-seq
Index i5 D505	D505	AATGATACGGCGACCACCGAGATCTACACCTTCGCCTA CACTCTTTCCCTACACGACGCTCTTCCGATCT	Library Amplicon-seq
Index i5 D506	D506	AATGATACGGCGACCACCGAGATCTACACTAAGATTAAC ACTCTTTCCCTACACGACGCTCTTCCGATCT	Library Amplicon-seq
Index i5 D507	D507	AATGATACGGCGACCACCGAGATCTACACACGTCCTGA CACTCTTTCCCTACACGACGCTCTTCCGATCT	Library Amplicon-seq
Index i5 D508	D508	AATGATACGGCGACCACCGAGATCTACACGTCAGTACA CACTCTTTCCCTACACGACGCTCTTCCGATCT	Library Amplicon-seq

4.1.10 Plasmids and bacteria

Table 4.1-12: List of plasmids and bacteria strain used in this study.

Plasmid/Bacteria	Supplier	Cat #
pX459, pSpCas9(BB)-2A-Puro (PX459) V2.0	Addgene	62988
pDG459, pSpCas9(BB)-2A-Puro (PX459) V2.0	Addgene	100901
NEB® 5-alpha Competent E. coli, DH5α	NEB	C2987H

4.1.11 Software

Table 4.1-13: List of software used in this study.

Software	Version
10X Genomics Cell Ranger ARC	2.0
BD FACSDiva	v9.7
bowtie2	2.4.5
ChIPseeker	1.34.1
chromVAR	1.20.2
ClusterProfiler	4.10.0
Cutadapt	3.4, 4.0
deepTools	3.5.1
DEseq2	1.42.0
Design & Analysis Software	2.6.0
DiffBind	3.8.3
FastQC	0.11.9
FastQScreen	0.15.2
Fiji ImageJ	2.14.0, 1.54m
ggraph	2.1.0
Image Lab	6.0.1
Graph Pad Prism	10
Loupe Browser	8
Macs2	2.1.2
Omero	5.8.3
Pando	1.0.3
QuantStudio Real-Time PCR Software	1.3
R	4.2.2, 4.3.2
SCTransform	2
Seurat	4.3.0
Signac	1.9.0
Snapgene	6.2.2
Snapseed	0.1.0
Souporcell	2.0
STAR	2.7
Subread	2.0
Tecan i-control	2.0.10.0

4.2 Methods

4.2.1 Tissue culture

4.2.1.1 Thawing and freezing of hiPSCs

Tissue culture plates were coated with hESC-qualified Matrigel (Corning) to facilitate cell attachment under feeder-free conditions. Matrigel was thawed gradually on ice and diluted in ice-cold DMEM/F12 medium according to the batch-specific dilution factor. The diluted Matrigel solution was evenly distributed to cover the bottom of the plates, which were then incubated at 37 °C for 20 minutes (HERAcell 240i, Thermo Fisher Scientific) or alternatively at 4 °C

overnight (fridge, Liebherr). Once coated, plates were sealed with parafilm and stored at 4 °C for up to three weeks.

The cells were thawed rapidly in a 37 °C water bath (Julabo) for approximately 3 minutes. To resuspend the thawed cells gently, 1 ml of stem cell medium (Miltenyi Biotec) supplemented with 10 µM Y-27632 (e.g., Biogems) was added dropwise. The cell suspension was then transferred to a 15 ml tube and centrifuged at 300 × g for 5 minutes (centrifuge 5425, Eppendorf). After carefully aspirating the supernatant, the cell pellet was resuspended in 1 ml of the same medium. The suspension was subsequently plated into 1–2 wells of a Matrigel-coated 6-well plate (Sarstedt), with the final medium volume adjusted to 2 ml per well.

For cryopreservation, the culture medium was removed, and the cells were washed with DPBS (Gibco) while still in the plate. After aspirating the DPBS, the cells were detached by incubating the plate with ReLeSR (Stem Cell Technologies) passaging solution for 3 minutes at room temperature. Once the passaging solution was removed, the cells were gently detached and resuspended in cryopreservation medium (CellBanker2 or CryoStor CS10). A volume of 500 µl of the cell suspension was then aliquoted into cryovials (Sarstedt). The vials were gradually cooled to -80 °C (Sanyo) at a controlled rate of 1 °C per minute using a Mr. Frosty freezing container (Thermo Fisher Scientific) filled with isopropanol (Sigma-Aldrich). For long-term storage, the cryovials were subsequently transferred to a -150 °C freezer (Sanyo).

4.2.1.2 Human induced pluripotent stem cell (hiPSC) culture

The hiPSCs were cultured in stem cell medium (StemMACS iPS-Brew XP medium, Miltenyi Biotec) at 37 °C, 5% CO_2, and 5% O_2 under humidified atmosphere (HERAcell 240i, Thermo Fisher Scientific), with daily medium changes and a double feed provided over the weekend. Cell quality was monitored daily using the EVOS M5000c microscope (Thermo Fisher Scientific), assessing confluence, the presence of differentiated cells, and stem-like morphological characteristics.

Once the cell colonies reached approximately 70–80% confluence, they were passaged into fresh Matrigel-coated wells of a 6-well plate. To achieve this, the culture medium was first aspirated, and the cells were incubated in ReLeSR passaging solution for 2–3 minutes at room temperature. Following incubation, the passaging solution was aspirated, and the cells were detached from the well bottom by gently spraying 1 ml of fresh stem cell medium onto the colonies. The detached cells were then resuspended and split into clumps, which were seeded into new Matrigel-coated wells at a 1:10 ratio to maintain consistent culture quality and growth conditions.

4.2.1.3 Brain organoid culture

Table 4.2-1: Recipe of Neural Induction Medium (NIM).

Neural Induction Medium (NIM)		
Component	**Quantity**	**Final concentration**
DMEM/F12	48.45 ml	96.9 %
N2 Supplement, 100 X	0.5 ml	1 X
GlutaMAX, 100 X	0.5 ml	1 X
MEM-NEAA, 100 X	0.5 ml	1 X
Heparin solution, 1 mg/ml	50 µl	1 µg/ml

Table 4.2-2: Recipe of Differentiation (Diff.) Medium –VitA.

Diff. Medium -VitA		
Component	**Quantity**	**Final concentration**
DMEM/F12	118.72 ml	47.5 %
Neurobasal Medium	118.72 ml	47.5 %
B27 minus vitamin A supplement, 100 X	5 ml	2 X
GlutaMAX, 100 X	2.5 ml	1 X
Pen/Strep, 5000 U/ml	2.5 ml	47.6 U/ml
N2 Supplement, 100 X	1.25 ml	0.5 X
MEM-NEAA, 100 X	1.25 ml	0.5 X
Human insulin, 11.1 mg/ml	62.5 µl	0.025 % / 2.78 µg/ml

Table 4.2-3: Recipe of Differentiation (Diff.) Medium +VitA.

Diff. Medium +VitA		
Component	**Quantity**	**Final Concentration**
DMEM/F12	116,7 ml	46.7 %
Neurobasal Medium	116,7 ml	46.7 %
B27 supplement (with vitamin A), 100 X	5.0 ml	2 X
GlutaMAX, 100 X	2.5 ml	1 X
Pen/Strep, 5000 U/ml	2.5 ml	1 X
N2 Supplement, 100 X	2.5 ml	1 X
L-Ascorbic acid, 40 mM	2.5 ml	400 µM
MEM-NEAA, 100 X	1.25 ml	0.5 X
Human insulin, 11.1 mg/ml	62.5 µl	0.025 % / 2.78 µg/ml
Sodium bicarbonate	250 mg	1 mg/ml

Brain organoids were generated following a previously published protocol[212,248]. Briefly, hiPSCs were maintained in culture until they reached 70–80% confluence. To generate a single-cell suspension, the culture medium was removed, and the cells were washed with DPBS (Gibco) before incubating with 500 µl of Accutase (Sigma-Aldrich) for 3 minutes at 37 °C (HERAcell 240i, Thermo Fisher Scientific). Cells were then detached by gently resuspending them in 1 ml of stem cell medium supplemented with 10 µM Y-27632 (e.g., Biogems). The cell suspension was transferred to a 15 ml tube containing 4.5 ml of the same medium and centrifuged at 300 x g for 5 minutes (5425, Eppendorf). After removing the supernatant, the cells were resuspended in 1 ml of fresh stem cell medium containing 10 µM Y-27632, and their concentration was determined.

Next, 4,500 cells per well in 150 µl were seeded into ultra-low attachment, U-shaped bottom 96-well plates (Thermo Fisher Scientific). The seeding day was designated as day 0 of the differentiation procedure. The plates were incubated under stem cell culture conditions to allow the formation of embryoid bodies. On day 3, the medium was replaced with fresh stem cell medium, and on day 6, it was switched to Neural Induction Medium (NIM, **Table 4.2-1**). From this point onward, the medium was refreshed every other day until day 12.

At day 12, the embryoid bodies were embedded in GFR Matrigel (Corning) and transferred into 10 cm tissue culture plates (Corning) containing 10 ml of differentiation medium without vitamin A (Diff. Medium –VitA, **Table 4.2-2**). The plates were incubated at 37 °C, 5% CO_2 in a humidified atmosphere (Steri-Cult, Thermo Fisher Scientific), with medium changes every other day until day 17. On day 17, the medium was replaced with differentiation medium containing vitamin A (Diff. Medium +VitA, **Table 4.2-3**), and the plates were placed on an orbital shaker (Infors AG) at 55 rpm to enhance medium flow through the growing organoids, ensuring adequate nutrient supply. The medium was refreshed every other day until the end of the differentiation protocol, which extended to either day 35 or day 120, depending on the experimental requirements.

BAF complex inhibition experiments were performed by supplementing the medium with either the PROTAC ACBI1 (opnMe, Böhringer Ingelheim) or the allosteric SMARCA2/SMARCA4 inhibitor BRM014 (Hycultec) at a final concentration of 1 µM. Treatments were administered during the specified timeframes (e.g., day 0–6 for BAFi d0-6 samples) and were refreshed with each media change. Control samples were treated in parallel by supplementing the medium with 0.001% DMSO (Sigma-Aldrich) to account for solvent effects.

4.2.2 Knock-out (KO) cell line generation

Cells with mutations in either of the ARID subunits were generated using the CRISPR/Cas9 system[249,250]. This involved transfecting hiPSCs with plasmids carrying Cas9 and specific single-guide RNAs (sgRNAs) targeting the respective ARID subunit genes. Following puromycin-based selection, individual clones were isolated and expanded. Validation of successful gene editing was performed using sequencing to confirm the targeted mutation and western blot analysis to verify protein expression levels. The detailed methodology for these procedures is described in the following sections.

4.2.2.1 Cloning

The initial step involved designing sgRNAs using the VBC Score guide RNA web interface (https://vbc-score.org/). To anneal the oligos for guide RNA generation, 2 µl of each oligo (100 µM) was mixed with 10 µl of 10 X CutSmart Buffer (NEB) and 86 µl of nuclease-free water

(Thermo Fisher Scientific). This mixture was incubated at 95 °C (Thermomixer C, Eppendorf) for 5 minutes and allowed to cool gradually to room temperature over approximately 3 hours.

Concurrently, 5 µg of the plasmids pX459 and pDG459 were digested in separate 50 µl reactions with the restriction enzyme BbsI-HF (NEB) in the presence of CutSmart Buffer. The digestion reactions were incubated at 37 °C (Thermomixer C, Eppendorf) for 4 hours and subsequently purified using the QIAPrep® Spin Miniprep Kit (Qiagen). The concentrations of the digested plasmids were measured using a spectrophoto-/fluorometer (DeNOVIX DS-11FX).

Ligation was performed using the Quick Ligation Kit (NEB). Briefly, 50 ng of each digested vector was combined with 2 µl of the sgRNA, 5 µl of 2 X Quick Ligase Buffer (NEB), 0.5 µl of Quick Ligase (NEB), and nuclease-free H_2O to a final reaction volume of 10 µl. The reaction was incubated at room temperature for 15 minutes and subsequently transformed into *E. coli* DH5α cells (NEB). To perform the transformation, 5 µl of the ligated vector was added to 50 µl of DH5α cells, followed by incubation on ice for 30 minutes, a 30-second heat shock at 42 °C (waterbath, GFL), and cooling on ice for 2 minutes. Then, 250 µl of LB media (luria broth, IMB Media Lab) was added to the cells, which were incubated at 37 °C (Thermomixer C, Eppendorf) with shaking at 350 rpm for 1 hour.

Afterward, 200 µl of the bacterial culture was plated on ampicillin-supplemented LB agar plates (IMB Media Lab) and incubated overnight at 37 °C (incubator, Binder). The following day, individual colonies were picked with a P200 pipette tip and inoculated in LB medium containing 10 µg/mL ampicillin. Cultures were incubated overnight at 37 °C with shaking at 350 rpm (incubator, Infors HT). Glycerol stocks were prepared by mixing 50 µl of bacterial culture with 2 ml of LB medium supplemented with 50 % glycerol (Sigma-Aldrich). DNA was extracted using the QIAPrep® Spin Miniprep Kit (Qiagen) and sequenced by StarSEQ to verify the constructs.

Positive clones were amplified further from the glycerol stocks, and the DNA was extracted using the ZymoPURE II Plasmid Midiprep Kit (Zymo Research). The purified plasmids were stored at -20 °C for subsequent use.

4.2.2.2 Transfection

As hiPSCs grow in colonies rather than single cells, they were dissociated into single cells 1–2 days prior to transfection with Cas9 and sgRNA-containing plasmids to increase their surface area and transfection efficiency. During this period, the cells were maintained in stem cell medium supplemented with 1 X CloneR (Stem Cell Technologies). On the day of transfection, the medium was refreshed with fresh stem cell medium containing CloneR, and transfection

was performed using 5 µg of the respective plasmid and the jetOptimus Kit (Polyplus, Satorius), following the manufacturer's protocol.

The following day, the medium was replaced with stem cell medium containing 100 µg/mL puromycin (InvivoGen) and 10 µM Y-27632 (e.g., Biogems) to select for successfully transfected cells. The selection process lasted for 48 hours, with daily medium changes. Once selection was complete, the cells were expanded and sparsely seeded as single cells into 10 cm dishes (Corning) to generate single-cell-derived colonies.

After colony formation, individual clones were picked under the EVOS M5000c microscope, transferred into separate wells of a 24-well plate (Corning), and further expanded for subsequent cryopreservation. To validate the clones, cryopreserved cells were gradually thawed and expanded for DNA and protein extraction to confirm successful editing and characterize the clones.

4.2.2.3 Amplicon-sequencing

To identify the mutations present in each clone, genomic DNA was extracted using the Monarch® Genomic DNA Purification Kit (NEB). Primers were designed to flank the genomic regions targeted by the sgRNAs, and these regions were amplified via PCR using the 2 X KAPA HiFi Hot Start Ready Mix (Roche). Typically, 100 ng of genomic DNA was used per reaction. If DNA concentration was insufficient, the maximum available amount was utilized, and the PCR cycle number was increased from 20 to 22. The PCR reaction setup and the PCR program (TAdvanced, Biometra) used are detailed in **Table 4.2-4**, **Table 4.2-5**, **Table 4.2-6**, **Table 4.2-7**, **Table 4.2-8** and **Table 4.2-9**.

Table 4.2-4: PCR reaction to amplify ARID1A gRNA4 amplicons. *Max. = maximum amount of DNA available.*

Component	1 X	Final concentration
Nuclease-free water	Up to 25 µl	-
10 µM fwd primer (#344F)	0.75 µl	0.3 µM
10 µM rev primer (#351R)	0.75 µl	0.3 µM
2 X HiFi Hot Start Ready Mix	12.5 µl	1 X
DNA	Max./100 ng	Max./100 ng

Table 4.2-5: PCR reaction to amplify ARID1B gRNA1 amplicons. *Max. = maximum amount of DNA available.*

Component	1 X	Final concentration
Nuclease-free water	Up to 25 µl	-
10 µM fwd primer (#342F)	0.75 µl	0.3 µM
10 µM rev primer (#349R)	0.75 µl	0.3 µM
2 X HiFi Hot Start Ready Mix	12.5 µl	1 X
DNA	Max./100 ng	Max./100 ng

Table 4.2-6: PCR reaction to amplify ARID1B gRNA3 amplicons. *Max. = maximum amount of DNA available.*

Component	1 X	Final concentration
Nuclease-free water	Up to 25 µl	-
10 µM fwd primer (#340F)	0.75 µl	0.3 µM
10 µM rev primer (#341R)	0.75 µl	0.3 µM
2 X HiFi Hot Start Ready Mix	12.5 µl	1 X
DNA	Max./100 ng	Max./100 ng

Table 4.2-7: PCR reaction to amplify ARID1B amplicons flanking gRNA1 and gRNA3. *Max. = maximum amount of DNA available.*

Component	1 X	Final concentration
Nuclease-free water	Up to 25 µl	-
10 µM fwd primer (#342F)	0.75 µl	0.3 µM
10 µM rev primer (#341R)	0.75 µl	0.3 µM
2 X HiFi Hot Start Ready Mix	12.5 µl	1 X
DNA	Max./100 ng	Max./100 ng

Table 4.2-8: PCR reaction to amplify ARID2 gRNA1 amplicons. *Max. = maximum amount of DNA available.*

Component	1 X	Final concentration
Nuclease-free water	Up to 25 µl	-
10 µM fwd primer (#347F)	1.25 µl	0.5 µM
10 µM rev primer (#352R)	1.25 µl	0.5 µM
2 X HiFi Hot Start Ready Mix	12.5 µl	1 X
DNA	Max./100 ng	Max./100 ng
$MgCl_2$ (10 mM) –optional-	2.5 µl	1 mM

Table 4.2-9: PCR program to amplify amplicons.*The melting temperature (Tm) for ARID1A and ARID2 amplicons was set to 65.5°C. For ARID1B, the Tm was set to 68°C for amplifying amplicons flanking gRNA1 and gRNA3, as well as for gRNA3 alone, and 70°C for the gRNA1.*

Temperature [°C]	Time [sec]	Cycles
95	180	1x
98	20	20/22x
65.5/68/70	15	
72	15	
72	60	1x

Following amplification, the DNA was purified using AMPure XP Beads (Core Facility (CF) Genomics, Beckman Coulter) in a 1:1 volumetric ratio of beads to DNA. Briefly, 25 µl of AMPure XP beads were mixed with 25 µl of PCR product and incubated for 10 minutes at room temperature. Samples were placed on a magnetic rack (Corning) to clear the supernatant, which was discarded. The beads were washed twice with 200 µl of 80 % ethanol (Fisher Scientific). After removing residual ethanol, the beads were air-dried for 10 minutes at room temperature. DNA was eluted by resuspending the beads in 13 µl of nuclease-free water and incubating for 2 minutes at room temperature. The supernatant was transferred to a fresh tube using a magnetic rack.

To uniquely index each sample (**Table 4.1-11**), a second PCR was performed using the 2 X KAPA HiFi Hot Start Ready Mix (**Table 4.2-10**), followed by another round of DNA purification

using the same AMPure XP bead protocol. DNA concentration was quantified using the Qubit dsDNA HS Assay Kit (Thermo Fisher Scientific), and quality was checked for selected samples using a Bioanalyzer (Agilent, High Sensitivity DNA Kit).

Table 4.2-10: PCR reaction for unique indexing of each sample

Component	1 X	Final concentration
Nuclease-free water	Up to 25 µl	-
10 µM Index i7	0.75 µl	0.3 µM
10 µM Index i5	0.75 µl	0.3 µM
2 X HiFi Hot Start Ready Mix	12.5 µl	1 X
PCR Product	11 µl	-

Table 4.2-11: PCR program for unique indexing of each sample

Temperature [°C]	Time [sec]	Cycles
95	180	1 X
98	20	10 X
65	15	
72	15	
72	60	1 X

The samples were pooled into a 4 nM amplicon library, which was submitted to the IMB CF Genomics for sequencing. Genomic DNA from hiPSCs (2 %) was included alongside the amplicon pool (98 %) for sequencing. The library was sequenced on a NextSeq 500 High Output flow cell, using paired-end reads with R1 (85 cycles), R2 (65 cycles), and dual-index reads (2 × 8 cycles).

Following sequencing, the IMB CF Bioinformatics team analysed the data to identify variants within the amplicons for each clone. This analysis involved mapping sequencing reads to the reference genome, identifying insertions, deletions, and substitutions in the target regions, and determining the zygosity of observed mutations. The results provided a detailed characterization of mutations in each clone, facilitating the validation of successful gene editing.

Reads were aligned to the ENCODE reference genome GRCh38.p13 (release 35) using BWA-MEM (v.0.7.15)[251]. Variant calling was performed using the Genome Analysis Toolkit (GATK v.4.2.6.1)[252] according to the GATK Best Practices workflow for germline short variant discovery (https://gatk.broadinstitute.org/hc/en-us/articles/360035535932-Germline-short-variant-discovery-SNPs-Indels). Variants were identified using GATK HaplotypeCaller and GenotypeGVCFs against the reference genome. Subsequently, variants were filtered with GATK VariantFiltration based on the following criteria: for SNPs, Quality by Depth (QD) less than 2, Strand Odds Ratio (SOR) greater than 3, Fisher Strand (FS) greater than 60, Root Mean Square Mapping Quality (MQ) less than 40.0, MQ Rank Sum less than -12.5, and Read

Position Rank Sum less than -8; for INDELs, QD less than 2, SOR greater than 10, FS greater than 200, and Read Position Rank Sum less than -20.

Filtered variants were subsequently annotated using SnpEff (v.5.0e)[253] to provide additional insights into their potential functional impacts. This comprehensive analysis enabled accurate mutation profiling and supported downstream evaluations of editing efficiency and specificity.

Additionally, DNA libraries containing untreated genomic DNA were analysed for chromosomal abnormalities and structural variants that might have arisen during cell culture handling. Copy number and beta allele frequency profiles were computed, and copy number alterations were identified using Control-FREEC (v.11.6)[254]. This analysis provided critical insights into the genomic integrity of the samples, ensuring the reliability of downstream results.

4.2.3 Protein detection

Protein detection was performed using either western blotting or immunofluorescence staining. The methodologies employed for these techniques are detailed in the following sections.

4.2.3.1 Western Blot

Cells or brain organoids were collected, and proteins were extracted using the following protocol. Depending on the sample size, samples were resuspended in 20–50 µl of RIPA buffer in DNA LoBind tubes (Eppendorf). To enhance membrane disruption, the samples were passed five times through a U-100 Insulin 29G needle (BD Biosciences). The tubes were then incubated on a spinning wheel at 4 °C for 1 hour.

After incubation, the samples were centrifuged at 13,000 x g for 10 minutes at 4 °C to separate the protein-containing supernatant from cellular debris. The supernatant was carefully transferred to a fresh DNA LoBind tube, and protein concentration was quantified on a plate reader (Infinite M200 Pro, Tecan) using the BCA Assay (Thermo Fisher Scientific) following the manufacturer's instructions. Finally, the protein extracts were either stored at −80 °C (Sanyo) for future use or directly processed for Western blot analysis. To ensure optimal protein separation, 4 X Laemmli buffer[255] was added to the samples, which were then denatured at 95 °C (Thermomixer C, Eppendorf) for 5 minutes. After denaturation, the samples were centrifuged (5427R G, Eppendorf) at 13,000 x g for 10 minutes to remove aggregates, ensuring a clear supernatant. The prepared samples, along with a protein ladder (PageRuler Plus, Thermo Fisher Scientific), were loaded onto an SDS gel comprising a 4 % stacking gel and a 7 % resolving gel (SureCast, Thermo Fisher Scientific;

Table 4.2-12 and **Table 4.2-13**). The gel was placed in a chamber filled with 1x SDS Running Buffer (Media Lab). Electrophoresis (XCell II SureLock Mini-Cell Electrophoresis System, Thermo Fisher Scientific) was initially performed at a constant 80 V until the samples migrated

through the stacking gel, after which the voltage was increased to 140 V and maintained constant until the samples fully traversed the resolving gel.

Table 4.2-12: 4% stacking gel recipe.

Component	1 X	Final concentration
SureCast Acrylamide (40%)	0.3 ml	4 %
SureCast Resolving Buffer	0.75 ml	-
Distilled water	1.92 ml	-
SureCast APS (10%)	30 µl	0.1 %
SureCast TEMED	3 µl	0.001 % (v/v)

Table 4.2-13: 7% resolving gel recipe.

Component	1 X	Final concentration
SureCast Acrylamide (40%)	1.4 ml	7 %
SureCast Stacking Buffer	2.0 ml	-
Distilled water	4.5 ml	-
SureCast APS (10%)	80 µl	0.1 %
SureCast TEMED	8 µl	0.001 % (v/v)

After electrophoresis, the separated proteins were transferred onto a PVDF membrane (Thermo Fisher Scientific) using a wet-transfer method. Sponges (Thermo Fisher Scientific) and filter paper (GE Healthcare) were soaked in 1 X Transfer Buffer (Media Lab) containing 15 % methanol (Sigma-Aldrich) to assemble the blotting sandwich (**Figure 4.2-1**). The transfer was performed at a constant 200 mA for approximately 1.5 hours.

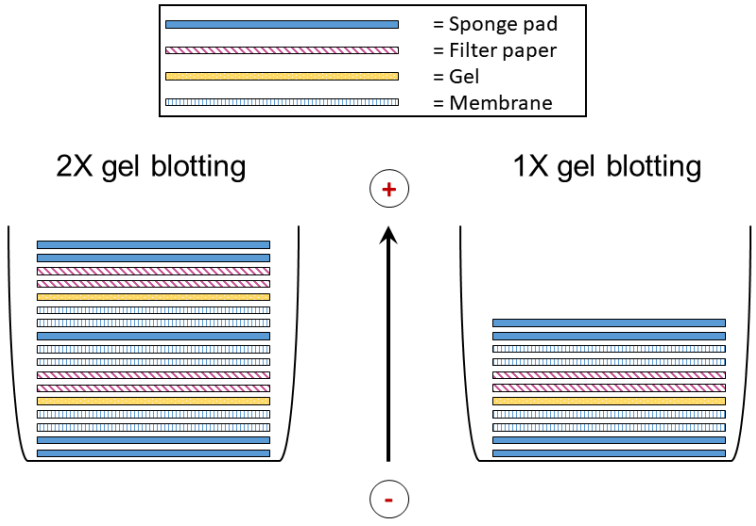

Figure 4.2-1: Schematic of blotting sandwich assembly.

Following the transfer, the PVDF membrane was rinsed briefly with double-distilled water (ddH_2O) and then incubated in blocking buffer (5 % milk in TBS-T) for 1 hour on an orbital shaker (90 rpm, neoLab). After blocking, the membrane was cut as necessary and incubated overnight at 4 °C on a roller mixer (RM5-30V, Zipperer GmbH) with primary antibodies targeting the loading control (α-tubulin, **Table 4.1-1**) and the protein of interest (ARID1B, **Table 4.1-1**) diluted in blocking buffer. The next day, the membranes were washed four times with TBS-T

for 10 minutes each, followed by a 1-hour incubation on a roller mixer (RS-TR05, Phoenix instruments) at room temperature with a secondary antibody (**Table 4.1-1**). After incubation, the membranes were washed four more times in TBS-T for 10 minutes each.

Finally, detection was carried out using the Clarity Western ECL Substrate (Bio-Rad) according to the manufacturer's instructions. The signal was visualized using the ChemiDoc imaging system (Bio-Rad).

Quantification of the protein bands was performed using the Image Lab 6.0.1 software (Bio-Rad). The intensity of the target protein bands was normalized to the respective loading control for each sample. Ratios of the normalized target protein band intensities to the corresponding control were calculated to facilitate comparative analysis.

4.2.3.2 Immunofluorescence staining

For spatial resolution of target protein expression, brain organoids were harvested, washed in DPBS (Gibco), and fixed in 4 % PFA (Electron Microscopy Sciences) at 4 °C on a nutator (Labnet). The fixation time was adjusted based on organoid size (1 hour per mm of diameter). Post-fixation, the organoids were washed three times in DPBS and sequentially incubated in 15 % sucrose (Sigma-Aldrich) and then 30 % sucrose. Each incubation continued until the organoids settled at the bottom of the tube, ensuring tissue stabilization and preventing ice crystal formation during freezing.

The organoids were then transferred to a cryomold (Sakura Finetek) and embedded in FSC 22 Blue Frozen Section Media (Leica). The mold was placed on dry ice to rapidly freeze the tissue. For long-term storage, the embedded samples were stored at -80 °C (freezer, Sanyo). To prepare for sectioning, samples were equilibrated to -20 °C (freezer, Liebherr) by transferring them from -80 °C one day before use.

Cryosectioning was performed at 12 µm thickness using a Cryostat Leica CS3050S set at chamber temperature (CT) -22 °C and object temperature (OT) -20 °C. The sections were mounted on adhesive microscope slides (X-tra adhesive microscope slides, Leica), dried at room temperature for 1 hour, and stored at 4 °C until further use.

Before staining, the cryosections were dried for 10 minutes at room temperature and washed in 1 X PBS (IMB Media Lab) for 10 minutes. Secondary fixation was performed by incubating the slides in acetone (Carl Roth) on ice for 10 minutes, followed by another 10-minute wash in 1 X PBS. The slides were then dried with a tissue, and the sections were encircled using a PAP Pen (Sigma-Aldrich) to create hydrophobic barriers.

For permeabilization, sections were incubated in 0.3 % Triton-X100 (Sigma-Aldrich) in 1 X PBS for 5 minutes and subsequently washed three times in 1 X PBS for 5 minutes each. Blocking

was carried out using 5 % BSA (Carl Roth) in 1 X PBS for 1 hour at room temperature. Primary antibody incubation was performed overnight at 4 °C in a humidified chamber, with the antibodies diluted in blocking solution.

The following day, sections were washed three times in 1 X PBS-T (0.05 % Tween-20, Sigma-Aldrich) for 5 minutes each. They were then incubated with a fluorescently labelled secondary antibody and DAPI (Thermo Fisher Scientific), both diluted in blocking solution, for 1 hour at room temperature in the dark within a humidified chamber. After incubation, slides were washed twice in PBS-T for 5 minutes each, followed by a final wash in PBS for 5 minutes. Sections were dried and mounted using ProLong Gold Antifade Mounting Medium (Thermo Fisher Scientific). Mounted slides were stored at 4 °C to dry and for later use.

Imaging was performed using the THUNDER widefield microscope (Leica) with a 40x objective or the BC43 Spinning Disk Confocal Microscope (Oxford Instruments). Image quantification was conducted in ImageJ using a macro that generated a nuclear mask by selecting DAPI-stained nuclei. The signal for the target protein was measured within the nuclear mask, and the ratio of the target protein-positive area to the total nuclear area was calculated to determine the percentage of cells positive for the protein of interest within the organoids. Specifically, the macro runs in Fiji (Image J v1.54m) via the OMERO batch process plugin[256]. The macro includes steps for image duplication, background subtraction, nuclear segmentation using Otsu's thresholding, FOXG1 signal selection based on nuclear masks, and area fraction analysis. The detailed macro script is as follows:

```
ImageName = getTitle();
run("Set Measurements...", "area area_fraction redirect=None decimal=3");
roiManager("Set Color", "yellow");
run("Duplicate...", "title=[nuclei area] duplicate channels=1");
selectWindow(ImageName);
run("Duplicate...", "title=[FOXG1] duplicate channels=2");
//transformation of 16bit image to 8 bit image
selectWindow("nuclei area");
run("8-bit");
 //background substraction channel 1 (nuclei)
run("Subtract Background...", "rolling=200 sliding");
run("Median...", "radius=2");
setOption("ScaleConversions", true);
//segmentation of nuclei by automatic thresholding with the algorithm “Otsu dark”
setAutoThreshold("Otsu dark");
run("Convert to Mask");
rename(ImageName + "_nuclei mask");
//analysis of nuclei area (µm2) and area fraction related to the whole image
run("Analyze Particles...", "size=1-Infinity display clear summarize add");
//selectImage(ImageName + "_nuclei mask");
run("Divide...", "value=255");
setMinAndMax(0, 1);
roiManager("Show All without labels");
roiManager("Show None");
```

```
//selects the FOXG1 signal in the second channel based on the nuclear mask
imageCalculator("Multiply create", "FOXG1", ImageName + "_nuclei mask");
selectImage("Result of FOXG1");
//run("Brightness/Contrast...");
rename(ImageName + "_FOXG1 selected");
run("Median...", "radius=3");
setMinAndMax(0, 500);
//segmentation of FOXG1 by automatic thresholding with the algorithm “Default dark”
setAutoThreshold("Default dark");
setOption("BlackBackground", true);
run("Convert to Mask");
//analysis of FOXG1 area (µm2) and area fraction related to the whole image
run("Analyze Particles...", "size=1-Infinity circularity=0.1-1.00 display clear summarize add");
selectImage(ImageName);
roiManager("Show All without labels");
```

4.2.4 Gene expression and chromatin landscape analysis

To examine changes in gene expression and chromatin accessibility in brain organoids treated with BRM014, various molecular biological techniques were applied. The specific methods employed will be described in detail in the following sections.

4.2.4.1 RNA extraction

Samples were collected in 1.5 ml tubes (Sarstedt), and the supernatant was removed prior to RNA extraction. RNA isolation was performed using either the E.Z.N.A. Total RNA Kit I (Omega-Biotek) or the E.Z.N.A. MicroElute Total RNA Kit (Omega Bio-Tek), depending on the sample size. RNA from smaller samples, such as hiPSCs and embryoid bodies at days 6 and 12, was extracted using the MicroElute Kit. For larger samples, including organoids from day 17 onwards, the Total RNA Kit I was used.

To begin RNA purification, the samples were lysed in the respective kit's lysis buffer and dissociated using a U-100 Insulin 29G needle (BD Biosciences) on ice. RNA was eluted in either 20 µl (MicroElute Kit) or 50 µl (Total RNA Kit I) of nuclease-free water, as instructed by the manufacturer. RNA was quantified using a spectrophoto-/fluorometer (DeNovix) to assess its concentration and quality. Depending on experimental requirements, the RNA was either immediately processed for downstream applications or stored at -80 °C (Sanyo) for long-term preservation.

4.2.4.2 cDNA synthesis

After RNA extraction, cDNA synthesis was initiated with a DNA digestion step to remove any contaminating genomic DNA. Equal amounts of RNA (in ng) were used for all samples processed together, with the volume adjusted to 8 µl using nuclease-free water. To each sample, 1 µl DNase I (NEB) and 1 µl 10x DNase Buffer (NEB) were added, followed by

incubation at 37 °C for 10 minutes. The reaction was heat-inactivated at 75 °C (Thermomixer C, Eppendorf) for 10 minutes using a thermomixer (Thermomixer C, Eppendorf).

Subsequently, 1 µl oligo(dT)$_{18}$ (Thermo Fisher Scientific) and 1 µl dNTP mix (NEB) were added to each sample, which was then incubated at 65 °C for 5 minutes to prime the RNA. Reverse transcription was performed by adding 4 µl First Strand Buffer (IMB CF Protein Production), 2 µl 0.1 M DTT (IMB CF Protein Production), 1 µl RNAse Inhibitor (NEB), and 1 µl Reverse Transcriptase (IMB CF Protein Production) to each sample. The reaction mixture was incubated at 42 °C for 1 hour, followed by heat inactivation at 70 °C for 10 minutes. The resulting cDNA was diluted in 80 µl nuclease-free water, stored at -20 °C (freezer, Liebherr), or directly used for RT-qPCR.

4.2.4.3 RT-qPCR

For RT-qPCR, reaction mixtures were prepared by combining 1 µl of each 25 µM primer forward/reverse pair, 1 µl cDNA, 5 µl Power SYBR™ Green PCR Master Mix (applied biosystems), and 3 µl nuclease-free water in the wells of a 384-well plate (applied biosystems), with each target and sample analysed in technical triplicates. To ensure accurate normalization, two control genes, such as *GAPDH* and *ATP5F1B*, were included on each plate for calculating delta Ct values.

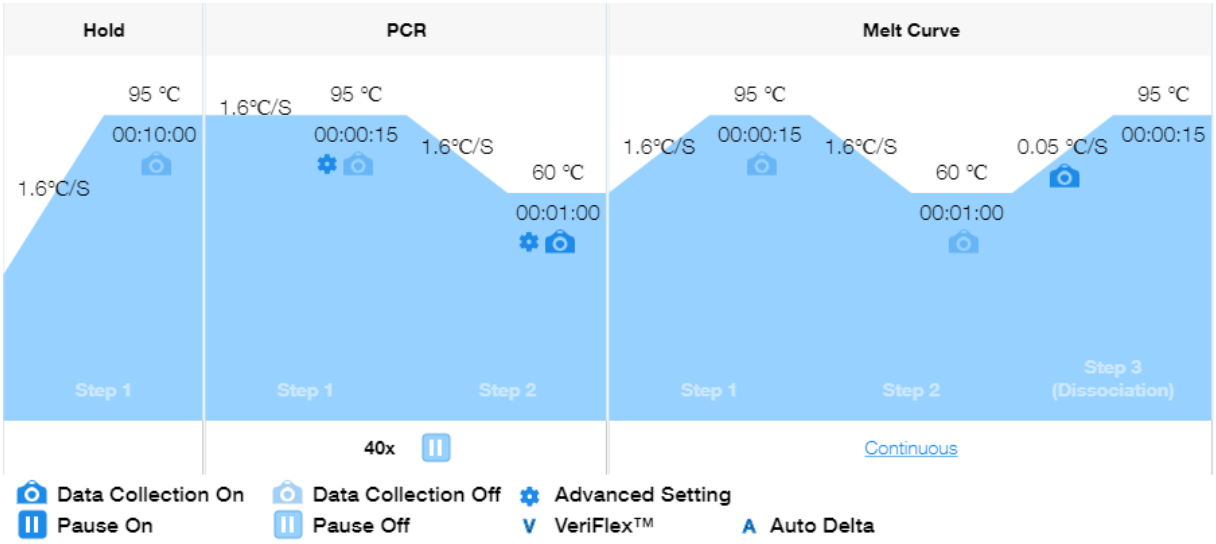

Figure 4.2-2: RT-qPCR setup for gene expression analysis.

The reactions were performed using the QuantStudio 5 and ViiA7 systems (applied biosystems), and data were analysed with Design & Analysis Software v2.6.0 and QuantStudio Real-Time PCR Software v1.3. A detailed overview of the RT-qPCR cycling conditions is provided in the **Figure 4.2-2**. The results were normalized to the control genes *GAPDH* or *ATP5F1B*, and the log2 fold change (log2FC) was calculated to compare the sample of interest with its respective control.

4.2.4.4 Bulk RNA-sequencing

Bulk RNA-seq was performed on hiPSCs and cerebral organoids at various stages of differentiation (days 0, 6, 12, 17, and 35). Samples were collected at the respective time points, and RNA was extracted as described in the RNA extraction section (4.2.4.1 RNA extraction). A total of four biological replicates were generated, each consisting of 3-6 embryoid bodies or organoids to minimize experimental bias, as organoids show considerable variation. The samples were then sent to IMB CF Genomics for further processing.

For samples 1-72 (replicate 1-3), NGS library preparation was performed using Lexogen's QuantSeq 3' mRNA-Seq Library Prep Kit FWD, following the standard protocol (015UG009V0260). Libraries were prepared with 41 ng of RNA and amplified in 17 PCR cycles. The libraries were profiled using the High Sensitivity DNA Kit on a 2100 Bioanalyzer (Agilent Technologies) and quantified using the Qubit dsDNA HS Assay Kit on a Qubit 2.0 Fluorometer (Life Technologies). All 72 libraries were pooled in equimolar ratios and sequenced on a NextSeq 500 High Output Flowcell, single-read (SR) for 1x84 cycles, plus 7 cycles for the index read.

For samples 73-98 (replicate 4), NGS library preparation was similarly performed using Lexogen's QuantSeq 3' mRNA-Seq Library Prep Kit FWD (015UG009V0260), with a starting amount of 22 ng RNA and amplification in 18 PCR cycles. Libraries were profiled and quantified as described above. All 26 libraries were pooled with 48 samples from another project in equimolar ratios and sequenced on a NextSeq 500 High Output Flowcell, single-read (SR) for 1x84 cycles, plus 7 cycles for the index read.

The results were processed by the IMB CF Bioinformatics.

Reads were trimmed to remove Illumina adapter sequences using Cutadapt (v.3.4)[257]. Subsequently, they were aligned to the ENCODE reference genome GRCh38.p13 (release 35) using STAR (v.2.7)[258] with default parameters, except for modifications to --outFilterMismatchNoverLmax 0.04 and --outFilterMismatchNmax 999. Only uniquely mapped reads were retained for downstream analyses. Coverage signal tracks (bigWigs) for primary alignments were generated with DeepTools (v.3.5.1)[259].

Read summarization at the gene level, focusing on exon-aligned reads, was performed using Subread FeatureCounts (v.2.0)[260] with default settings. Pairwise differential expression analyses between experimental groups were conducted in R (v.4.3.2) using the DESeq2 package (v.1.42.0)[261]. Genes were considered differentially expressed only if they met the criteria of an adjusted false discovery rate (FDR) < 0.01 and a log2 fold change significantly different from zero.

Sets of upregulated and downregulated genes were further analyzed for overrepresented Gene Ontology (GO) terms using the ClusterProfiler package (v.4.10.0)[262] in R. GO term enrichment analysis was conducted with a significance threshold of adjusted p-value < 0.01 to ensure robust findings.

4.2.4.5 Multiome (single nuclei RNA- and ATAC-sequencing)

Table 4.2-14: Recipe of the Multiome 1 X Lysis Buffer.

1 X Lysis Buffer		
Component	**Quantity**	**Final concentration**
TRIS-HCl, pH 7.4, 1 M	20 µl	10 mM
NaCl, 5 M	4 µl	10 mM
$MgCl_2$, 1 M	6 µl	3 mM
Tween-20, 10 %	20 µl	0.1 %
NP-40, 10 %	20 µl	0.1 %
Digitonin, 2 %	10 µl	0.01 %
BSA, 10 %	200 µl	1 %
DTT, 0.1 M	20 µl	1 mM
RNase Inhibitor, 40 U/µl	50 µl	1 U/µl
Nuclease-free water	1650 µl	-

Table 4.2-15: Recipe of the Multiome Lysis Dilution Buffer.

Lysis Dilution Buffer		
Component	**Quantity**	**Final concentration**
TRIS-HCl, pH 7.4, 1 M	40 µl	10 mM
NaCl, 5 M	8 µl	10 mM
$MgCl_2$, 1 M	12 µl	3 mM
BSA, 10 %	400 µl	1 %
DTT, 0.1 M	40 µl	1 mM
RNase Inhibitor, 40 U/µl	100 µl	1 U/µl
Nuclease-free water	3400 µl	-

Table 4.2-16: Recipe of the Multiome 0.3 X Lysis Buffer.

0.3 X Lysis Buffer		
Component	**Quantity**	**Final concentration**
Lysis Buffer, 1 X	1350 µl	0.3 X
Lysis Dilution Buffer	3150 µl	-

Table 4.2-17: Recipe of the Multiome Wash Buffer.

Wash Buffer		
Component	**Quantity**	**Final concentration**
TRIS-HCl, pH 7.4, 1 M	240 µl	10 mM
NaCl, 5 M	48 µl	10 mM
$MgCl_2$, 1 M	72 µl	3 mM
Tween-20, 10 %	240 µl	0.1 %
BSA, 10 %	2400 µl	1 %
DTT, 0.1 M	240 µl	1 mM
RNase Inhibitor, 40 U/µl	600 µl	1 U/µl
Nuclease-free water	20160 µl	-

Sample preparation

Brain organoids were generated simultaneously but independently from three hiPSC lines (HMGU1, BIHi242, and BIHi001-A) under three distinct conditions: DMSO, BAFi d0-6, and BAFi d6-12. At day 35, five organoids per sample were collected and roughly dissociated using sharp tweezers (DUMONT) in a 15 ml tube (Sarstedt). To remove dead cells prior to enzymatic dissociation, 2 ml of DPBS (Gibco) was added to the tissue. The tube was inverted three times, and once the tissue sections settled at the bottom, the supernatant was carefully removed without disturbing the loose pellet. This washing process was repeated until the supernatant appeared clear. For enzymatic dissociation, tissue fragments were transferred to a 2 ml LoBind tube (Eppendorf), and 500 µl of a 9:1 Accutase (Sigma-Aldrich) to 0.05 % trypsin (Thermo Fisher Scientific) mixture was added. The tubes were briefly vortexed (IKAMS3, IKA) and incubated on a thermomixer at 37 °C (Comfort, Eppendorf) with shaking at 350 rpm. Every five minutes, the samples were removed from the thermomixer, vortexed, and checked under a microscope (EVOS M5000c) until no large tissue sections were visible. This process was completed within approximately 20 minutes. To stop the enzymatic dissociation, 500 µl of ice-cold DPBS was added to the suspension, and any remaining cloudy material floating on the surface was carefully removed. The samples were centrifuged at 600 x g for 5 minutes at 4 °C in a swing-bucket rotor centrifuge (X3R, Thermo Fisher Scientific). After removing the supernatant, the pellet was resuspended in 500 µl of ice-cold DPBS, and the cell suspension was passed through a 70 µm strainer (Greiner Bio-One) to eliminate larger debris. The samples were centrifuged again under the same conditions. Nuclei extraction was initiated by carefully removing the supernatant and adding 300 µl of 0.3 X lysis buffer (**Table 4.2-16**) to the pellet. The pellet was resuspended by gentle pipetting and incubated on ice, with the lysis progress monitored under a microscope (EVOS M5000c) to ensure nuclei quality. Once the lysis process was completed, which typically took about 5 minutes, it was halted by adding 750 µl of chilled Wash Buffer (**Table 4.2-17**). The suspension was centrifuged at 600 x g for 5 minutes at 4 °C, and the supernatant was removed. This washing step was repeated two more times to ensure thorough cleaning. Following the final wash, the nuclei were resuspended in DPBS containing 2 % BSA, 1 U/µl Protector RNase inhibitor and 1 µg/ml DAPI and passed through a 35 µm strainer (tube with strainer, Corning). The samples were then submitted to the IMB CF Cytometry, where cell debris was removed via sorting with a 70 µm nozzle (BD Biosciences, BD FACSAria III SORP). After sorting, the nuclei were counted using a cell counter (DeNOVIX), and their integrity was verified again under the microscope (DM IL LED, Leica). Nuclei from different hiPSC lines belonging to the same experimental condition were pooled in equimolar ratios. The pooled nuclei were counted, centrifuged at 600 x g for 10 minutes at 4 °C, and the resulting pellet was resuspended in 1 X Nuclei Buffer (10X Genomics,

Nuclei Buffer) to reach a final concentration of 4,000 nuclei per µl. A minimum of 5 µl from each condition was then handed over to the IMB CF Genomics for further processing.

Sample processing prior sequencing

Next generation sequencing (NGS) library prep was performed with 10X Genomics' Chromium Next GEM Single Cell Multiome ATAC + Gene Expression Reagent Bundle, following Chromium Next GEM Single Cell Multiome ATAC + Gene Expression User Guide (May 2021) (Document # CG000338 RevD). 10,000 single nuclei were targeted per sample. Gene expression libraries were amplified in 14 PCR cycles whereas ATAC libraries were prepared in 7 PCR cycles.

Libraries were profiled in a High Sensitivity DNA chip on a 2100 Bioanalyzer (Agilent technologies) and quantified using the Qubit HS dsDNA Assay Kit, in a Qubit 2.0 Fluorometer (Life technologies).

Sequencing

For gene expression analysis, all samples were pooled in equimolar ratios and sequenced on a single NextSeq 2000 P2 (100 cycles) flow cell using paired-end sequencing with the following read structure: Read 1 with 28 cycles, Read 2 with 90 cycles, and two 10-cycle reads for the dual index. Gene expression samples 4, 5, and 6 underwent re-sequencing on a second NextSeq 2000 P2 (100 cycles) flow cell under identical sequencing conditions.

For ATAC-seq, the samples were similarly pooled in equimolar ratios and sequenced on a single NextSeq 2000 P2 (100 cycles) flow cell using paired-end sequencing. The read structure consisted of two 53-cycle reads for Read 1 and Read 2, 8 cycles for Index 1, and 24 cycles for Index 2. ATAC-seq samples 4, 5, and 6 were also re-sequenced on a second NextSeq 2000 P2 (100 cycles) flow cell under the same conditions.

Bioinformatics data processing

To ensure high-quality data for downstream analyses, the raw sequence quality and rRNA content of ATAC and RNA-Seq FASTQ files were assessed using FastQC (v.0.11.9)[263] and FastQScreen (v.0.15.2)[264]. These tools provided detailed quality metrics, enabling the identification of potential sequencing issues. Both datasets were then analysed jointly using 10X Genomics Cell Ranger ARC software (v.2.0)[265], which aligns reads to the reference genome GRCh38 (ensembl98, refdata-cellranger-arc-GRCh38-2020-A-2.0.0). This process generated count matrices for both RNA and ATAC datasets, which were subsequently used for integration and downstream analysis. Organoid nuclei derived from three different hiPSC lines were pooled within each group library as biological replicates. To recover replicate identities, which were lost during pooling, RNA-Seq BAM files were analyzed using the

souporcell tool (v.2.0)[266]. Souporcell utilizes natural genetic variation to deconvolute pooled samples. Doublets, defined as cells originating from two distinct replicates, were excluded. Replicate identities across groups were aligned using the "shared_samples.py" script provided by souporcell. External genetic data allowed mapping of deconvoluted replicates back to their original sample identities. These replicate identities were cross-referenced with ATAC-Seq data using shared cell barcodes. Notably, Replicate 3 was removed from the dataset due to its divergent phenotype and gene expression profile.

Further downstream analysis was performed in R (v.4.2.2) using the Seurat (v.4.3.0)[267] and Signac (v.1.9.0)[268] R toolkits. RNA and ATAC count matrices, along with peak sets called by Cell Ranger, were combined into a Seurat object for unified analysis. Quality control filtering was applied at the single-cell level to exclude cells that did not meet specific criteria. Cells with library sizes between 1,000 and 50,000 counts for both ATAC and RNA data were retained. Additionally, cells were required to have a fraction of reads in peaks greater than 0.3, a fraction of reads in blacklisted regions less than 0.05, a nucleosome signal below 2, a transcription start site (TSS) enrichment score above 1, and a mitochondrial count fraction below 20 %.

RNA-Seq data was normalized and transformed using the SCTransform (v.2) function from the sctransform R package[269]. DNA accessibility data was processed using latent semantic indexing (LSI) as implemented in Signac.

To enable comparative analyses across experimental conditions and replicates, datasets were integrated using Seurat's integration pipeline (v4.3.0) correcting for batch effects[270]. This approach identifies anchor cells with similar expression across datasets through canonical correlation analysis and mutual nearest neighbour analysis. The integration aligns datasets in a shared low-dimensional space, effectively correcting for batch effects while preserving biological signals.

A Weighted Nearest Neighbor (WNN) graph was constructed to represent both gene expression (SCT) and DNA accessibility (LSI) modalities. This graph was used for clustering cells with the Louvain algorithm as implemented in Seurat. Cluster annotations were performed using the Snapseed Python tool (v.0.1.0), which assigns cell types based on a hierarchical marker list provided by the Human Neural Organoid Atlas (HNOCA)[271]. Snapseed generates cell type annotations across five levels of specificity. To ensure meaningful annotation, a manual curation step was added to integrate information from annotation levels 1–3 where applicable (**Table 7.1-3**).

Differentially expressed genes (DEGs) and differentially accessible peaks (DAPs) between experimental groups were identified using Seurat's FindMarkers function. DEGs were detected using a Wilcoxon Rank Sum test, while DAPs were identified using a logistic regression model

combined with a likelihood ratio test. Only features with an adjusted p-value less than 0.05 were considered significant.

Differentially accessible peak sets were subjected to motif enrichment analysis using the JASPAR2020 motif database. A hypergeometric test identified significantly enriched motifs with adjusted p-values below 0.05. To visualize motif activities per cell, motif activity scores were computed with chromVAR (v.1.20.2)[272].

Gene regulatory networks were inferred using the Pando R package (v.1.0.3)[216], which models gene expression based on TF expression and the accessibility of their putative binding sites. Target genes for network inference were defined either as variable features across the dataset or as DEGs identified from pseudo-bulk differential expression analyses. TF modules consisting of TFs and their target genes were extracted using default parameters in Pando. Sub-graphs of the TF networks were visualized using the ggraph R package (v.2.1.0)[273]. This pipeline ensured robust and integrative analysis of multi-modal single-cell data, enabling detailed insights into gene expression, chromatin accessibility, and regulatory networks.

4.2.4.6 Tn5 adaptor complex assembly

For both ATAC and CUT&Tag-seq experiments, Tn5 enzymes (Tn5 / pA-Tn5) produced by the IMB CF Protein Production were utilized. These enzymes, not preloaded with adaptors, required an assembly process prior to use. The adaptors were assembled as follows:

Each oligo was first reconstituted with nuclease-free water (Thermo Fisher Scientific) to a final concentration of 100 µM. Two separate oligo mixes were then prepared in equimolar proportions. Mix 1 consisted of 10 µl of Tn5MErev and 10 µl of Tn5ME-A, while Mix 2 contained 10 µl of Tn5MErev and 10 µl of Tn5ME-B. These mixes were subjected to incubation in a thermocycler at 95 °C (TAdvanced, Biometra), followed by a gradual cooling to room temperature at a rate of -0.5 °C per 15 seconds over 40 minutes.

Subsequently, 19 µl of Mix 1 was combined with 19 µl of Mix 2 and 162 µl of the respective Tn5 enzyme. This mixture was gently resuspended and incubated at room temperature for one hour. The resulting Tn5 adaptor complexes were aliquoted in 20 µl volumes and stored at -20 °C (Liebherr) for future use. Efficiency tests were performed on each Tn5 batch prior to application in experiments to ensure functionality.

4.2.4.7 ATAC-sequencing

Table 4.2-18: Recipe of Nuclei Extraction Buffer.

Nuclei Extraction Buffer		
Component	**Quantity**	**Final concentration**
HEPES-KOH, pH 7.5, 1 M	100 µl	20 mM
KCl, 1 M	50 µl	10 mM
Triton X-100, 10 %	50 µl	0.1 %
Glycerol, 50 %	200 µl	20 %
Spermidine, 2 M	12.5 µl	0.5 mM
PIC, 25 X	200 µl	1 X
Nuclease-free water	4387.5 µl	-

Table 4.2-19: Recipe of the 2 X Transposition Buffer.

2X Transposition Buffer		
Component	**Quantity**	**Final concentration**
TRIS/HCl, pH 7.6, 1 M	200 µl	20 mM
$MgCl_2$, 0.5 M	200 µl	10 mM
DMF, N,N-Dimethylformamide	2 ml	20 %
Nuclease-free water	7.6 ml	-

To investigate changes in chromatin accessibility upon BAF complex inhibition, bulk ATAC-seq was performed on samples collected immediately after treatment and in long-term organoids. These included samples treated during early organoid development (DMSO, BAFi d0-6, and BAFi d6-12, collected at days 6, 12, and 120) as well as heterozygous ARID1B KO organoids at day 120.

For early time points (days 6 and 12), 96 DMSO- and BAFi d6-12-treated embryoid bodies and 144 BAFi d0-6 embryoid bodies were collected per condition and time point per replicate. The embryoid bodies were transferred to 1.5 ml LoBind tubes (Eppendorf), and the supernatant was removed. They were resuspended in 250 µl of Accutase (Sigma-Aldrich) and incubated at 37°C on a thermomixer (Comfort, Eppendorf) with shaking (450 rpm) for 3–10 minutes, with close monitoring to ensure complete dissociation without cellular damage. Once dissociation was achieved, the reaction was stopped by adding 1 ml DPBS (Gibco) containing 5 % BSA (Miltenyi Biotec). The cells were then spun down at 300 x g for 5 minutes (5425, Eppendorf), the supernatant was removed, and the samples were passed through a 35 µm strainer (tube with strainer, Corning) to obtain a single-cell suspension. Finally, cells were counted (Celldrop FLCellCounter, DeNOVIX), and 50,000 cells per condition were allocated into separate LoBind tubes for the transposase reaction.

For long-term organoids (day 120), the preparation followed the Multiome experiment protocol, with adjustments for nuclei extraction. Two organoids per condition were processed. After enzymatic dissociation (using Accutase-trypsin treatment and subsequent washes), the supernatant was removed, and the cells were washed again in 1 ml DPBS before being spun

down at 600 x g (centrifuge 5430R, Eppendorf) for 3 minutes at room temperature. The pellet was resuspended in 500 µl of nuclei extraction buffer (**Table 4.2-18**) and incubated on ice for 10 minutes. Nuclei were then isolated by centrifugation at 1300 x g for 4 minutes at 4 °C (Multifuge X3R, Thermo Fisher Scientific). The supernatant was discarded, and the nuclei were washed with 1 ml DPBS, followed by a second centrifugation step at 1300 x g for 4 minutes at 4 °C (Multifuge X3R, Thermo Fisher Scientific). After the final wash, the nuclei were resuspended in Wash Buffer (**Table 4.2-25**), checked for quality under a microscope (EVOS M5000c), and counted (Celldrop FLCellCounter, DeNOVIX). A total of 50,000 nuclei per condition were transferred into fresh 1.5 ml LoBind tubes (Eppendorf) for the transposase reaction. From this point onward, all samples, regardless of time point, followed the same processing steps. Samples were spun down at 600 x g for 10 minutes at 4 °C (table top centrifuge Fresco 21, Thermo Fisher Scientific), and the supernatant was carefully removed to avoid disturbing the pellet. Nuclei were resuspended in 50 µl of Transposition Solution (**Table 4.2-20**) and incubated at 37 °C for 30 minutes with shaking at 450 rpm (Thermomixer Comfort, Eppendorf). DNA was subsequently extracted using the Qiagen MiniElute PCR Purification Kit, following the manufacturer's protocol, and eluted in 12 µl of the kit's elution buffer.

Table 4.2-20: Recipe of the Transposition Solution.

Transposition Solution		
Component	**Quantity**	**Final concentration**
2 X Transposition Buffer	25 µl	1 X
Tn5 (pre-loaded)	2.0 µl	-
Digitonin, 2 %	1.25 µl	0.05 %
Nuclease-free water	21.75 µl	-

Next, a qPCR was carried out to determine the proper cycle number for each sample. Here, the reaction was set up as can be seen in **Table 4.2-21** each reaction was pipetted into a well of a 384-well plate (applied biosystems) and run in the QuantStudio 5 thermocycler (Applied Biosystems) according to the setup found in **Table 4.2-22**.

Table 4.2-21: qPCR reaction for cycle number determination.

Component	1 X	Final concentration
Nuclease-free water	2.9 µl	-
25 µM Index primer 1 noMx #61	0.5 µl	1.25 µM
25 µM Index primer 2 barcode #62	0.5 µl	1.25 µM
100x SYBR Green	0.1 µl	1 X
Q5 HF 2X MM	5.0 µl	1 X
Tagmented Sample	1.0 µl	-

Table 4.2-22: qPCR cycling program.

Temperature [°C]	Time [sec]	Cycles
72	300	1x
98	30	1x
98	10	25x
63	30	
72	30	1x

The quantification cycle (Cq) value of each sample was used to determine the appropriate number of PCR cycles for library preparation. By tailoring the cycle number to the specific Cq value, overamplification during library preparation was effectively avoided. Subsequently, PCR was performed to uniquely barcode each sample, using the respective rounded-off Cq value as the cycle number for each. Details of the PCR reaction and setup are provided in **Table 4.2-23** and **Table 4.2-24**.

Table 4.2-23: PCR reaction for library preparation.

Component	1 X	Final concentration
Nuclease-free water	10.0 µl	-
25 µM Index primer 1 barcode i7	2.5 µl	1.25 µM
25 µM Index primer 2 barcode i5	2.5 µl	1.25 µM
Q5 HF 2 X MM	25.0 µl	1 X
Tagmented Sample	10.0 µl	-

Table 4.2-24: PCR cycling program.

Temperature [°C]	Time [sec]	Cycles
72	300	1x
98	30	1x
98	10	Cq for each sample
63	30	
72	30	1x
4	hold	hold

DNA purification was carried out in 96-well plates (Bio-Rad) using AMPure XP beads (IMB CF Genomics, Beckman Coulter) based on solid-phase reversible immobilization (SPRI) technology. The process included two purification steps: the first using a bead-to-sample ratio of 1:1.4 and the second with ratios of 1:0.5 and 1:1.4.

Initially, 70 µl of beads were added to 50 µl of each sample, mixed thoroughly, and incubated at room temperature for 10 minutes. The mixture was then transferred to the 96-well plate and placed on a magnetic rack (Corning). Once the suspension cleared (approximately 10 minutes), the supernatant was carefully removed, and the beads were washed twice with 150 µl of freshly prepared 80% ethanol (Fisher Scientific GmbH). After drying for approximately 5 minutes, the beads were resuspended in 50 µl of elution buffer (Qiagen MiniElute PCR Purification Kit) and removed from the magnet. Following a 10-minute incubation at room

temperature, the plate was returned to the magnet, and the cleared supernatant was transferred to new wells.

For the second purification step, 25 µl of AMPure XP beads was added to the transferred supernatant, mixed, and incubated at room temperature for 10 minutes. The plate was then placed back on the magnet, and the cleared supernatant was transferred into fresh wells. Subsequently, 45 µl of AMPure XP beads was added, mixed, and incubated for another 10 minutes at room temperature. After placing the plate on the magnet and removing the supernatant, the beads were washed twice with 150 µl of freshly prepared 80% ethanol and allowed to dry. The beads were resuspended in 15 µl of elution buffer (Qiagen MiniElute PCR Purification Kit) and incubated at room temperature for 10 minutes. Finally, the plate was placed back on the magnet, and the cleared supernatant was transferred to fresh 0.5-ml PCR tubes.

DNA concentration was measured using the Qubit dsDNA HS Assay Kit (Thermo Fisher Scientific) with a DeNovix spectrophotometer/fluorometer, and quality control was performed by running the samples on Bioanalyzer chips (2100 Bioanalyzer, Agilent) to assess the presence of a typical nucleosomal pattern. The samples were pooled to create a 4 nM library, which was submitted to the IMB CF Genomics. Sequencing was performed on a NextSeq 2000 P3 (100 cycles) Flowcell, using paired-end sequencing for 2×61 cycles, with dual indexing (2×8 cycles).

The raw sequencing data were subsequently processed by the IMB CF Bioinformatics.

Sequencing reads were trimmed to remove Illumina adapter sequences using cutadapt (v4.0)[257] and aligned to the GRCh38.p13 (release 35) reference genome using bowtie2 (v2.4.5)[274] with the "--very-sensitive" preset. Multimapping and duplicate reads were removed before generating coverage tracks and heatmaps using deepTools (v3.5.1)[259]. Peak calling was performed using macs2 (v2.1.2)[275] with IgG samples serving as controls. Peaks were filtered against the ENCODE unified GRCh38 blacklist (https://www.encodeproject.org/annotations/ENCSR636HFF) and annotated with proximal gene features using the ChIPseeker R-package (v1.34.1)[276]. Differential binding analysis was conducted using the DiffBind R-package (v3.8.3)[277]. Consensus peak sets were created for samples treated with the same antibody, retaining peaks present in at least two replicates. Peaks were re-centered around consensus summits with a size of 400 bp (200 bp on either side). Library size normalization was performed using 15 kb background bins. Differentially bound sites between sample groups were identified using the DESeq2 method within DiffBind, with an FDR threshold of <0.05 applied to determine significance.

4.2.4.8 CUT&Tag-sequencing

Table 4.2-25: Recipe of the Wash Buffer.

Wash Buffer		
Component	**Quantity**	**Final concentration**
HEPES-KOH, pH 7.5, 1 M	40 µl	20 mM
NaCl, 5 M	60 µl	150 mM
Spermidine, 2 M	2.5 µl	0.5 mM
PIC, 25 X	80 µl	1 X
Nuclease-free water	1819.5 µl	-

Table 4.2-26: Recipe of the CUT&Tag Binding Buffer.

Binding Buffer		
Component	**Quantity**	**Final concentration**
HEPES-KOH, pH 7.5, 1 M	200 µl	20 mM
KCl, 1 M	100 µl	10 mM
$CaCl_2$, 1 M	10 µl	1 mM
$MnCl_2$, 1 M	10 µl	1 mM
Nuclease-free water	9670 µl	-

Table 4.2-27: Recipe of the CUT&Tag Dig-Wash Buffer.

Dig-Wash Buffer		
Component	**Quantity**	**Final concentration**
Digitonin, 2%	50 µl	0.05 %
Wash Buffer	2 ml	-

Table 4.2-28: Recipe of the CUT&Tag Antibody Buffer (AB).

Antibody Buffer (AB)		
Component	**Quantity**	**Final concentration**
EDTA, 0.5 M	8 µl	2 mM
BSA, 10 % (Miltenyi Biotec)	20 µl	0.1 %
Dig-Wash Buffer	2 ml	-

Table 4.2-29: Recipe of the CUT&Tag Dig-300 Buffer.

Dig-300 Buffer		
Component	**Quantity**	**Final concentration**
HEPES-KOH, pH 7.5, 1 M	40 µl	20 mM
NaCl, 5 M	120 µl	300 mM
Spermidine, 2 M	0.5 µl	0.5 mM
Digitonin, 2 %	10 µl	0.01 %
PIC, 25 X	80 µl	1 X
Nuclease-free water	1765.5 µl	-

Table 4.2-30: Recipe of CUT&Tag Tagmentation Buffer.

Tagmentation Buffer		
Component	**Quantity**	**Final concentration**
Dig-300 Buffer	5 ml	-
$MgCl_2$, 1 M	50 µl	10 mM

Table 4.2-31: Recipe of CUT&Tag Stop Solution.

Stop Solution		
Component	**Quantity**	**Final concentration**
EDTA, 0.5 M	5 µl	320 M
SDS, 10 %	1.5 µl	2 %
Proteinase K	1.25 µl	-

To comprehensively analyse chromatin landscape changes, bulk CUT&Tag sequencing was performed to profile the histone marks H3K27ac, H3K27me3, and the BAF complex subunits ARID1A and SMARCA4. This analysis was conducted on samples treated with BAF inhibitors (BRM014) during d0-6 and d6-12, collected immediately after treatment at days 6 and 12. Due to technical limitations, only one replicate of the BAFi d6-12 samples was processed. As a single replicate precludes statistical analyses, these samples were excluded from further interpretation. The protocol followed the previously published methods from the Henikoff group[278,279].

Briefly, samples treated with DMSO, BAFi d0-6, and BAFi d6-12 were collected on days 6 and 12 and processed according to the ATAC-sequencing protocol up to the cell counting step. A total of 50,000 cells per target and condition were transferred into fresh tubes, centrifuged at 300 × g (5427R G, Eppendorf), and resuspended in 1 ml DPBS. Cells were then bound to Concanavalin A-coated beads (BioMag Plus, Polysciences Europe GmbH), prepared by activating 10 µl beads per sample in 500 µl Binding Buffer Table **4.2-26**). Beads were washed once by magnetic separation with 500 µl of Binding Buffer and then resuspended in 50 µl of the same buffer per sample.

After binding, bead-bound cells were resuspended in 25 µl of Antibody Buffer (AB, **Table 4.2-28**) and transferred to 0.2 ml PCR tubes (STARLAB GmbH). Primary antibodies diluted 1:50 in AB were added, and the samples were gently resuspended, yielding a final dilution of 1:100. Samples were incubated overnight at 4 °C on a nutator (Labnet). Subsequent rinsing and washing steps were performed to minimize shear forces on bead-bound cells. During rinses, liquid was pipetted gently along the tube wall near the beads without full resuspension. For washes, tube orientation was reversed on the magnetic rack, ensuring smooth bead travel to the opposite wall.

Following overnight incubation with the antibodies, beads were separated on a magnet (3D printed by IMB E-Lab), and the primary antibody solution was aspirated. Samples were rinsed with 50 µl Dig-Wash Buffer (**Table 4.2-27**) before incubating with a secondary antibody (diluted 1:100 in Dig-Wash Buffer) for 60 minutes at room temperature on a nutator (Polymax 1040, heidolph instruments). After incubation, beads were washed with Dig-Wash Buffer and incubated with pA-Tn5 adaptor complex in Dig-300 Buffer (final dilution 1:100, **Table 4.2-29**). Bead-bound cells were gently resuspended in 100 µl of the complex and incubated at room

temperature for 1 hour on a nutator (Polymax 1040, heidolph instruments). Subsequently, samples were rinsed and washed with Dig-300 buffer before proceeding to tagmentation.

Tagmentation was initiated by resuspending the beads in 150 µl Tagmentation Buffer (**Table 4.2-30**) and incubating at 37 °C for 1 hour on a thermomixer (Comfort, Eppendorf) with gentle shaking. Tagmentation was stopped by adding 7.75 µl of Stop Solution (**Table 4.2-31**) per sample, followed by gentle resuspension and incubation at 55 °C for 1 hour (Thermomixer Comfort, Eppendorf). DNA fragments were extracted using the MiniElute Kit (Qiagen) and eluted in 11 µl of the elution buffer provided in the kit. A 10 µl aliquot from each sample was used for library preparation.

PCR amplification conditions and the composition of the PCR reaction mixture are detailed in **Table 4.2-33** and **Table 4.2-32**, respectively. Amplified libraries were purified using AMPure XP beads (IMB CF Genomics, Beckman Coulter), following the protocol described in the ATAC-sequencing section. Library quality was evaluated using a High-Sensitivity DNA Bioanalyzer Chip (Agilent Technologies), while DNA concentrations were quantified with the Qubit dsDNA HS Assay Kit (Invitrogen), following the manufacturer's protocols. Samples were pooled to create a 4 nM library pool, which was subsequently handed over to the IMB CF Genomics for sequencing. Libraries were sequenced using a NextSeq 2000 P3 (100 cycles) flow cell in paired-end mode (2 × 61 cycles) with dual indexing (2 × 8 cycles).

Table 4.2-32: PCR reaction for library preparation.

Component	1 X	Final concentration
Nuclease-free H_2O	10.0 µl	-
25 µM Index primer 1 barcode i7	2.5 µl	1.25 µM
25 µM Index primer 2 barcode i5	2.5 µl	1.25 µM
Q5 HF 2X MM	25.0 µl	1 X
Tagmented Sample	10.0 µl	-

Table 4.2-33: PCR cycling program.

Temperature [°C]	Time [sec]	Cycles
72	300	1x
98	30	1x
98	10	14x
63	30	
72	60	1x
8	hold	hold

Sequencing reads were trimmed to remove Illumina adapter sequences using cutadapt (v4.0)[257] and aligned to the GRCh38.p13 (release 35) reference genome using bowtie2 (v2.4.5)[274] with the "--very-sensitive" preset. Multimapping and duplicate reads were removed before generating coverage tracks and heatmaps using deepTools (v3.5.1)[259]. Peak calling was performed using macs2 (v2.1.2)[275] with IgG samples serving as controls. Peaks were filtered against the ENCODE unified GRCh38 blacklist

(https://www.encodeproject.org/annotations/ENCSR636HFF) and annotated with proximal gene features using the ChIPseeker R-package (v1.34.1)[276]. Differential binding analysis was conducted using the DiffBind R-package (v3.8.3)[277]. Consensus peak sets were created for samples treated with the same antibody, retaining peaks present in at least two replicates. Peaks were re-centered around consensus summits with a size of 400 bp (200 bp on either side). Library size normalization was performed using 15 kb background bins. Differentially bound sites between sample groups were identified using the DESeq2 method within DiffBind, with an FDR threshold of <0.05 applied to determine significance.

5 Results

5.1 BAF complexes inhibition during brain organoid development affects morphology

To investigate the role of BAF complexes across distinct neurodevelopmental stages and to elucidate dysregulated molecular processes resulting from BAF complex perturbation, we differentiated human induced pluripotent stem cells (hiPSCs) into cerebral organoids to model early human brain development[212,248]. To gain insights into BAF complex function over the course of neurodevelopment, we treated cells and organoids with the allosteric SMARCA2/SMARCA4 inhibitor (BRM014[280]) at defined developmental intervals. This treatment induces rapid, efficient changes in chromatin accessibility and serves as a proxy for the molecular disruptions observed following genetic depletion of both BAF complex ATPases[281,282] (**Figure 5.1-1 A**).

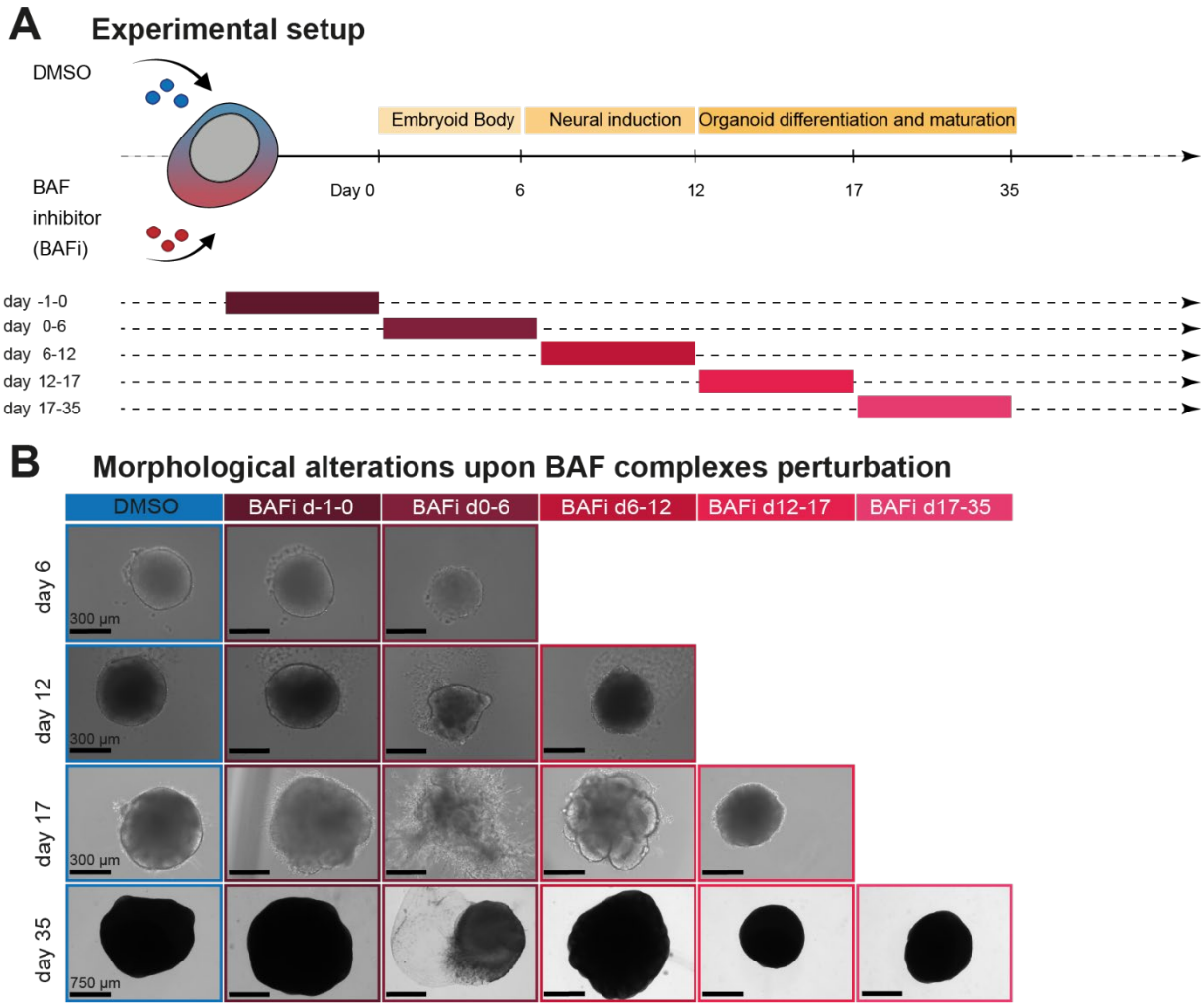

Figure 5.1-1: Perturbing BAF complexes along initial phases of brain development lead to morphological alterations. *A) The experimental approach is schematically depicted. Cells and organoids were treated at distinct developmental phases along the brain organoid differentiation timeline. BAFi treatment = 1 µM BRM014, DMSO control = 0.001%. B) Brightfield images (EVOS M5000c) were taken on day 6, 12, 17 and 35 along the differentiation timeline.*

To initially assess alterations following BAF complex perturbation in morphology and evaluate effects on neural fate commitment, samples were monitored over time using brightfield microscopy and with immunofluorescence staining performed at the differentiation endpoint on day 35. In control conditions (DMSO), hiPSCs seeded into a 96-well plate form embryoid bodies (EBs) by day 6, which are directed toward neural fate commitment and characterized by the formation of an epithelial layer (neuroectoderm). By day 12, EBs are provided with an extracellular matrix to facilitate self-organization into 3D brain organoids, which display distinct borders and characteristic neural rosettes (**Figure 5.1-1 B**). Inhibition of BAF complexes at different neurodevelopmental phases led to pronounced morphological alterations. For instance, samples treated with BRM014 immediately post-seeding (BAFi day 0-6) developed elongated, highly divergent outgrowths. Moreover, by day 17, these samples exhibited a complete loss of their typically more circular and smooth-bordered structure and displayed few, if any, neural rosettes commonly observed in brain organoids (**Figure 5.1-1 B**, **Figure 5.1-2**).

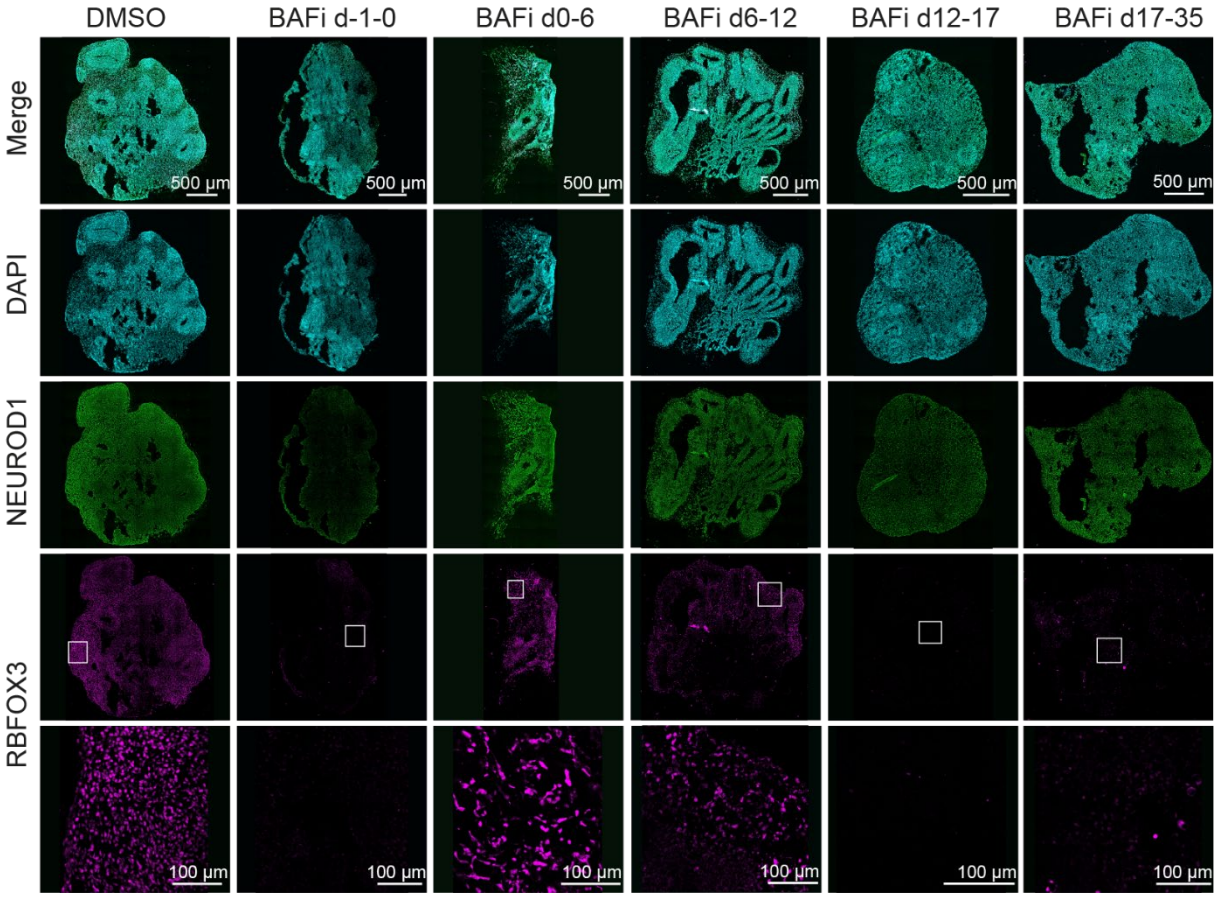

Figure 5.1-2: BAF complex inhibition alters brain organoid morphology without affecting early neural fate commitment. *Representative immunofluorescence images show 35-day-old organoids stained for the neural progenitor cell (NPC) marker NEUROD1 (green) and the mature neuron marker RBFOX3 (magenta). White rectangles in the upper RBFOX3 image mark the region of interest, shown below at higher magnification. Images are from 12 µm sections, acquired with a 40x objective on a Leica Thunder microscope.*

In contrast, organoids treated prior to seeding (BAFi d-1-0) displayed morphological development similar to DMSO-treated samples. Organoids exposed to BAF complex inhibition during the neural induction phase (BAFi d6-12) exhibited an increased number and size of

neural rosettes, which were particularly pronounced around day 17. Samples treated during later stages, specifically BAFi d12-17 and BAFi d17-35, were smaller and more circular compared to the DMSO controls, with a notable absence of neural rosette structures following BAF perturbation (**Figure 5.1-1 B**, **Figure 5.1-2**). Neural fate commitment appeared independent of BAF complex perturbation, as organoids derived from both DMSO and BRM014-treated conditions consistently expressed the neural progenitor marker neurogenic differentiation 1 (NEUROD1, **Figure 5.1-2**) and neural markers class III beta-tubulin (TUJ1) and microtubule associated protein 2 (MAP2), the latter being expressed in early neurons (**Figure 7.2-1**, **Figure 7.2-2**). However, the maturation of committed neural cells was influenced by BAF complex inhibition. The mature neuron marker RNA binding fox-1 homolog 3 (RBFOX3), typically expressed in neuronal nuclei, was prominently detected in DMSO, BAFi d0-6, and BAFi d6-12 samples, while little to no signal was observed in organoids derived from BAFi d-1-0, BAFi d12-17, and BAFi d17-35 conditions (**Figure 5.1-2**). However, this observation does not fully align with *RBFOX3* gene expression data, which indicated downregulation only in the BAFi d17-35 condition at day 35 (**Figure 5.2-2 B**). Collectively, these findings indicate that proper BAF complex function is crucial across all initial phases of brain development, likely regulating distinct processes. BAF inhibition not only leads to morphological changes in brain organoid development but also impacts the maturation potential of committed neural cells.

After confirming that BAF inhibitor treatment does not prevent early neural fate commitment and observing morphological alterations alongside disturbances in neural maturation, it became essential to rule out significant off-target effects of the inhibitor. To address this, the PROTAC ACBI1, which targets and degrades the BAF complex ATPases SMARCA2/SMARCA4, was included in the brain organoid differentiation and treatment protocol. Although DMSO is commonly used as a solvent in molecular assays, it can influence cellular metabolism, gene expression, and the chromatin landscape[283–287]. Since both the inhibitor and the PROTAC are dissolved in DMSO, a DMSO control was essential to account for any solvent-related effects on neurodevelopmental progression. To assess the potential impact of the low-dose DMSO, an untreated control was also included alongside the DMSO control (**Figure 5.1-3**). Throughout the differentiation protocol, samples treated with BRM014 or ACBI1 at different timeframes (day 0-6, 6-12, 12-17, and 17-36) and both controls (DMSO and untreated) were collected at days 12, 17, and 35. Over time, morphological alterations were monitored and gene expression changes relative to hiPSCs (day 0) were evaluated by RT-qPCR, focusing on a subset of neural marker genes (**Figure 5.1-3**). Specifically, markers were chosen to capture potential treatment-related changes across neural development stages: NSC markers (*NANOG*, *SOX2*), NPC markers (*PAX6*, *TUJ1*), general neuronal markers (*FOXG1*, *MAP2*), cortical layer and neuronal subtype markers (eomesodermin

(*EOMES)*, *TBR1*, *BCL11B*, *SATB2*, solute carrier (SLC) family 17 member 7 (*SLC17A7)*, and gamma-aminobutyric acid type B receptor subunit 1 (*GABBR1)*), as well as a glial marker (oligodendrocyte transcription factor 2 (*OLIG2)*).

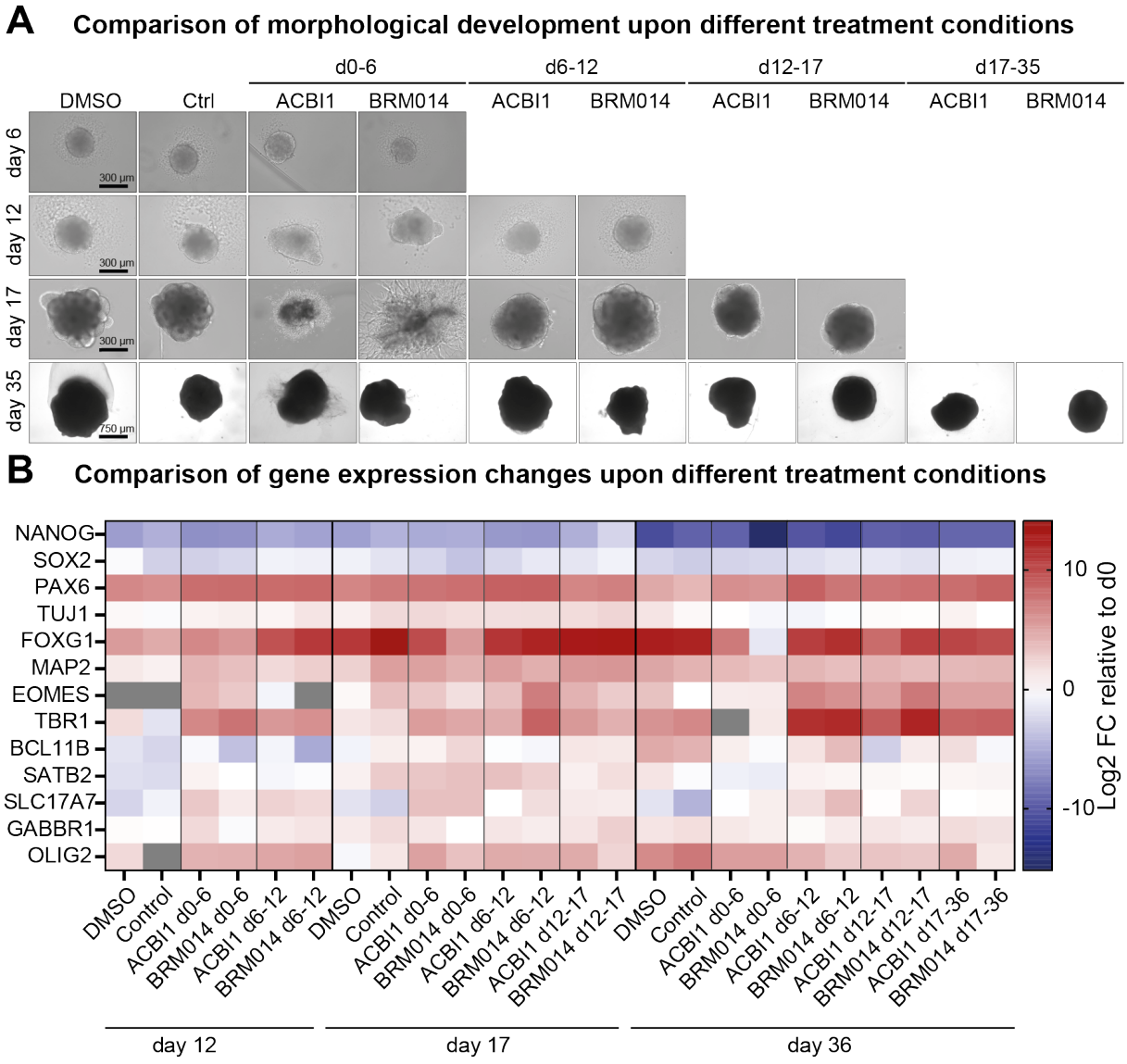

Figure 5.1-3: Gene expression changes remain similar between untreated and DMSO control organoids, while BAF inhibition by PROTAC and BRM014 leads to consistent expression alterations. *A) Brightfield images (EVOS M5000) were taken on day 6, 12, 17 and 35 along the differentiation timeline. B) Cerebral organoids were generated, with samples collected at days 12, 17, and 36 (n=1). RT-qPCR analysis shows the logarithmic 2-fold change (log2 FC) relative to day 0 hiPSCs for a subset of neural marker genes, displayed in a heatmap. Both the inhibitor (BRM014) and the PROTAC were applied at 1 µM, with DMSO-treated samples containing 0.001% DMSO. Grey fields in the heatmap indicate undetectable gene expression, Sample names indicate the treatment condition and timeframe (d = day). Control = untreated.*

Changes in morphology were influenced by the developmental stage and treatment timeframe rather than by the specific treatment agent. That is, morphological outcomes were comparable regardless of whether BAF ATPases were inhibited with BRM014 or degraded with ACBI1, as well as between DMSO and untreated controls. For example, both ACBI1 and BRM014 treatments from day 0-6 resulted in organoids with highly divergent outgrowths by day 17, though the effect was less pronounced in the ACBI1 condition. This similarity in morphological

alterations persisted across other treatment timeframes and sample days (**Figure 5.1-3 A**). Overall, gene expression trends were similar between the two controls, as well as between the inhibitor (BRM014) and the PROTAC (ACBI1) treatments, with only minor exceptions. For instance, *OLIG2* expression was undetectable in the untreated control at day 12 but was already lowly expressed in the DMSO control. Additionally, *FOXG1* expression was more affected by BRM014 treatment (BAFi d0-6) than by ACBI1 treatment (ACBI1 d0-6) across all sample days (**Figure 5.1-3 B**). Specifically, at day 36, ACBI1 treatment resulted in an increase in *FOXG1* expression compared to day 0, whereas BRM014 treatment led to a decrease. Compared to the DMSO control at day 36, *FOXG1* levels were reduced under both ACBI1 and BRM014 treatments. These differences, however, were limited to individual genes rather than the entire gene set associated with each neurodevelopmental stage, and the overall morphology was consistent across treatments. Therefore, these minor variations were considered negligible. To account for sample variance within each condition, three to four EBs or organoids were analysed per sample, however, only a single biological replicate was tested in this setup. This limitation may explain the subtle differences observed between the DMSO and untreated controls as well as between PROTAC- and inhibitor-treated samples.

Collectively, these findings support the use of BRM014 and DMSO in further experiments to study BAF complex functions across neurodevelopmental stages, as ACBI1 and BRM014 exhibited comparable effects on morphology and gene expression, while DMSO and untreated controls showed similar outcomes. The results described in the following sections were obtained from experiments conducted according to the approach illustrated in **Figure 5.1-1**, with BRM014 as the BAF complex inhibitor and DMSO as the control.

5.2 BAF complexes are involved in neurodevelopmental gene programs

Observing that BAF complex inhibition led to developmental stage-dependent changes in brain organoid morphology prompted an investigation into the underlying gene expression changes. RNA sequencing (RNA-seq) was performed at various time points along the brain organoid differentiation timeline. Specifically, hiPSCs were differentiated into brain organoids and treated with BRM014 at stages day -1-0, 0-6, 6-12, 12-17, and 17-35, along with a DMSO control. For this setup, four replicates were generated and monitored over time by microscopy. Samples were collected at the end of each treatment period (days 0, 6, 12, 17, and 35) and isolated RNA was subsequently subjected to sequencing.

Principal component analysis (PCA) of DMSO-treated samples showed a gradual gene expression shift mostly along PC1, indicating progressive differentiation (**Figure 5.2-1**). BRM014-treated samples generally followed this trend, though BAF inhibition at early stages

induced premature expression patterns, converging closer to DMSO by day 35, possibly reflecting compensatory mechanisms. Consistent with more severe phenotypic outcomes, samples treated during d0-6 and d6-12 displayed the highest number of differentially expressed genes (DEGs) (**Figure 5.2-1 A, B**). These RNA-seq findings confirmed that gene expression changes occurred both over the differentiation timeline and across treatment conditions. Notably, the greatest DEG increases appeared immediately after BRM014 treatment, with d0-6 samples showing the highest DEG count and only gradual recovery, suggesting heightened sensitivity to BAF complex loss during early neurodevelopment.

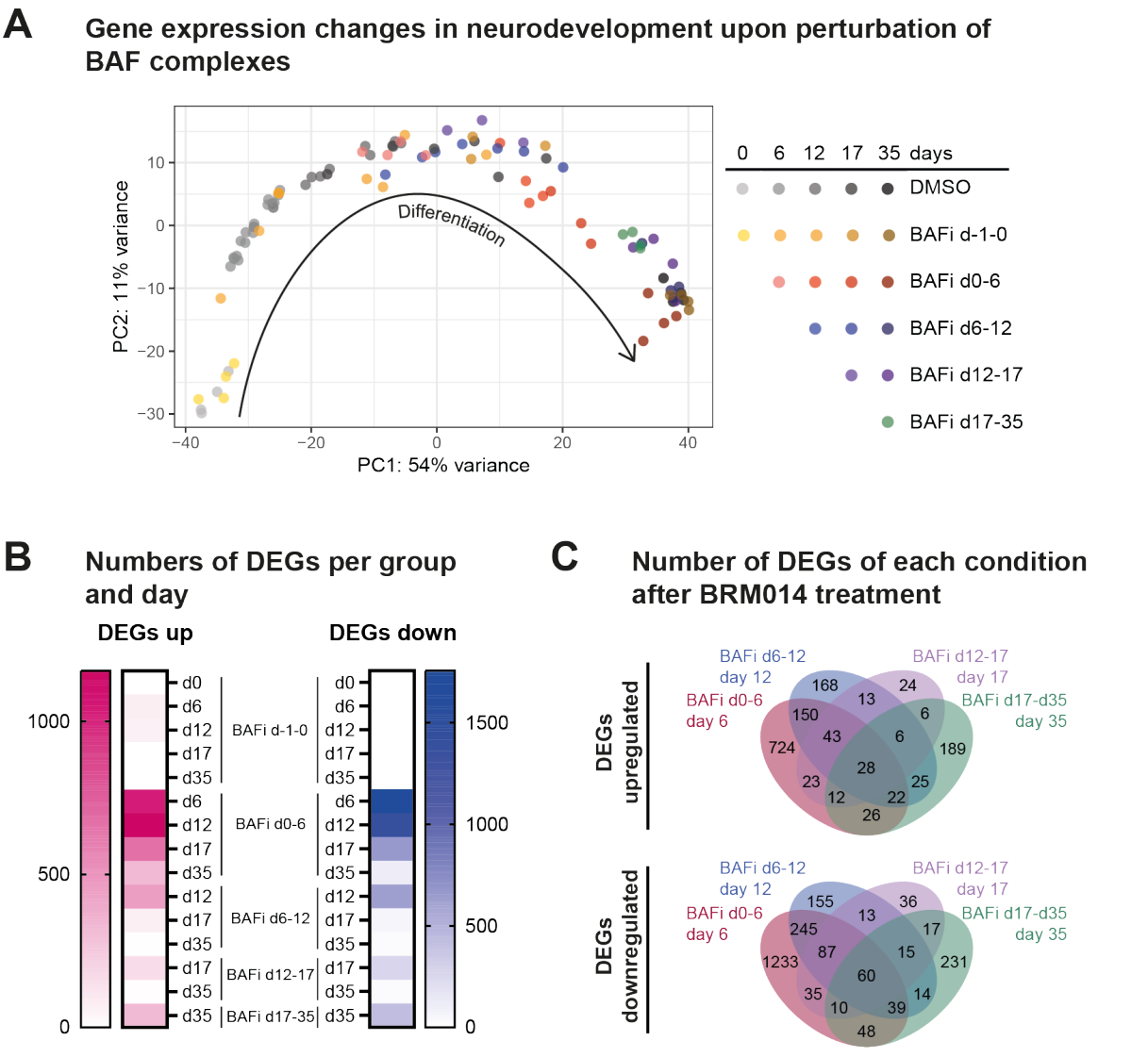

Figure 5.2-1: The inhibition of BAF complexes during neurodevelopment leads to phase-dependent gene expression changes. *A) Principal component analysis (PCA) plot of the 500 genes with the highest variance across all samples from the bulk RNA-sequencing dataset. B) Heatmap depicting the number of DEGs across all samples C) Venn diagram showing the intersections of differentially expressed genes (DEGs) in BAFi samples treated from d0-6 (red), d6-12 (blue), d12-17 (violet), and d17-35 (green), directly following the BRM014 treatment timeframe. d= day.*

In contrast, d-1-0 samples aligned closely with DMSO controls, while d6-12 and d12-17 samples showed initial DEG increases followed by more rapid recovery (**Figure 5.2-1 B**). Interestingly, several DEGs were shared across samples and timepoints, indicating the

presence of BAF-specific targets that are independent of developmental stage (**Figure 5.2-1 C**). Interestingly, shared DEGs included genes involved in key neurodevelopmental signalling pathways, such as WNT (e.g., lymphoid enhancer binding factor 1 (*LEF1*), which was upregulated) and NOTCH (e.g., *NOTCH1*, which was downregulated), indicating potential dysregulation of these pathways upon BAF inhibition (**Table 7.1-1**).

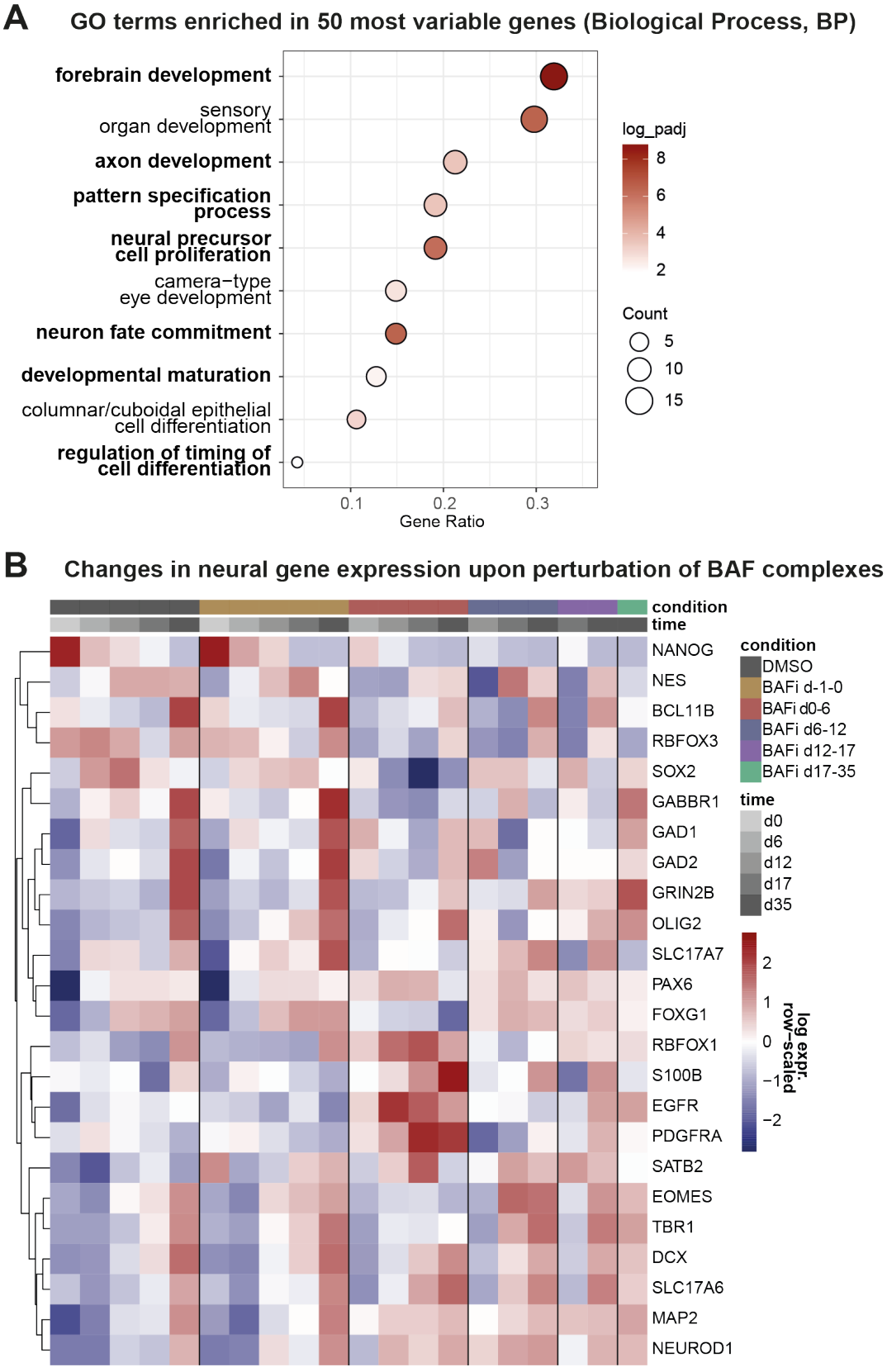

Figure 5.2-2: Neurodevelopmental processes and genes are particularly affected by BAF complex inhibition. *A) Dot plot depicting a Gene Ontology (GO) term analysis[288] of the 50 most variable genes across all samples. The x-axis represents the gene ratio, calculated as the number of genes associated with a given GO term divided by the total number of genes included in the analysis. Gene count = the absolute number of genes from the input dataset associated with a specific GO term, log_padj = logarithmically transformed adjusted p-value (FDR-adjusted p-value with FDR < 0.01). B) Clustered heatmap of a neural marker gene set showing the logarithmically transformed and row-scaled gene expression values for all samples of the bulk RNA-seq data set. d = day.*

The GO term analysis of the 50 most variable genes across all samples and time points supported this observation, revealing that, regardless of treatment condition or sample day, most genes with the highest variance were linked to nervous system development and regulatory mechanisms, including cell fate determination, cellular maturation processes and patterning (**Figure 5.2-2 A**). Notably, genes with the highest variance across all samples and time points also included genes differentially expressed across the differentiation timecourse of the DMSO control group. Consequently, GO terms related to neurodevelopment may partially reflect differentiation processes occurring in the DMSO control samples as they matured into brain organoids over time. In contrast, BAFi d-1-0 samples exhibited minimal to no differentially expressed genes over time, which may result in less prominent representation in these analyses. Nevertheless, the findings provided an initial indication of candidate genes and processes affected by the treatment.

Further specification of gene expression changes across all samples was obtained by examining a subset of genes typically involved in neural fate and cell type commitment (**Figure 5.2-2 B**). BAFi d-1-0 samples showed a similar gene expression pattern overtime as the DMSO control supporting the observation that it had the lowest number of DEGs. In contrast, BAFi d0-6 samples displayed an early decrease in the stem cell marker NANOG from day 6 onwards, alongside early expression of NPC markers (*PAX6*, doublecortin (*DCX*)), immature neuron markers at day 12 (*MAP2*, *NEUROD1*), as well as mature neuron and early glial markers at days 12, 17, and 35 (*MAP2*, *SLC17A6*, *SATB2*, *OLIG2*, epidermal growth factor receptor (*EGFR*), platelet derived growth factor receptor alpha (*PDGFRA*), S100 calcium-binding protein B (*S100B*)). Interestingly, *RBFOX1* showed increased expression from day 6 onwards in BAFi d0-6 samples. While it does not mark a specific neural subtype, it is predominantly expressed in neurons and plays crucial roles in neurodevelopment, particularly in synaptic function and plasticity[289–291]. Altered expression or mutations in this gene have been linked to neurodevelopmental disorders such as ASD[289,290,292,293]. These observations suggest that BAF complex function may regulate genes essential for neurodevelopment, including those associated with such diseases. While similar genes were affected in BAFi d6-12, d12-17, and d17-35 samples, the extent of gene perturbation decreased progressively with later BAF inhibition during organoid development. These findings reinforce previous observations that BAF inhibition at early stages (BAFi d0-6 and BAFi d6-12) induces premature expression patterns, whereas neurodevelopmental processes at later stages (BAFi d12-17 and BAFi d17-35) show greater resilience to BAF complex disruption. Notably, BAFi d-1-0 was an exception, exhibiting minimal morphological or molecular changes, likely due to the shorter treatment duration. Extended BAF complex inhibition in hiPSCs was not feasible as it led to rapid cell death, consistent with the essential role of BAF complexes in maintaining self-renewal and pluripotency in stem cells[150,151,294].

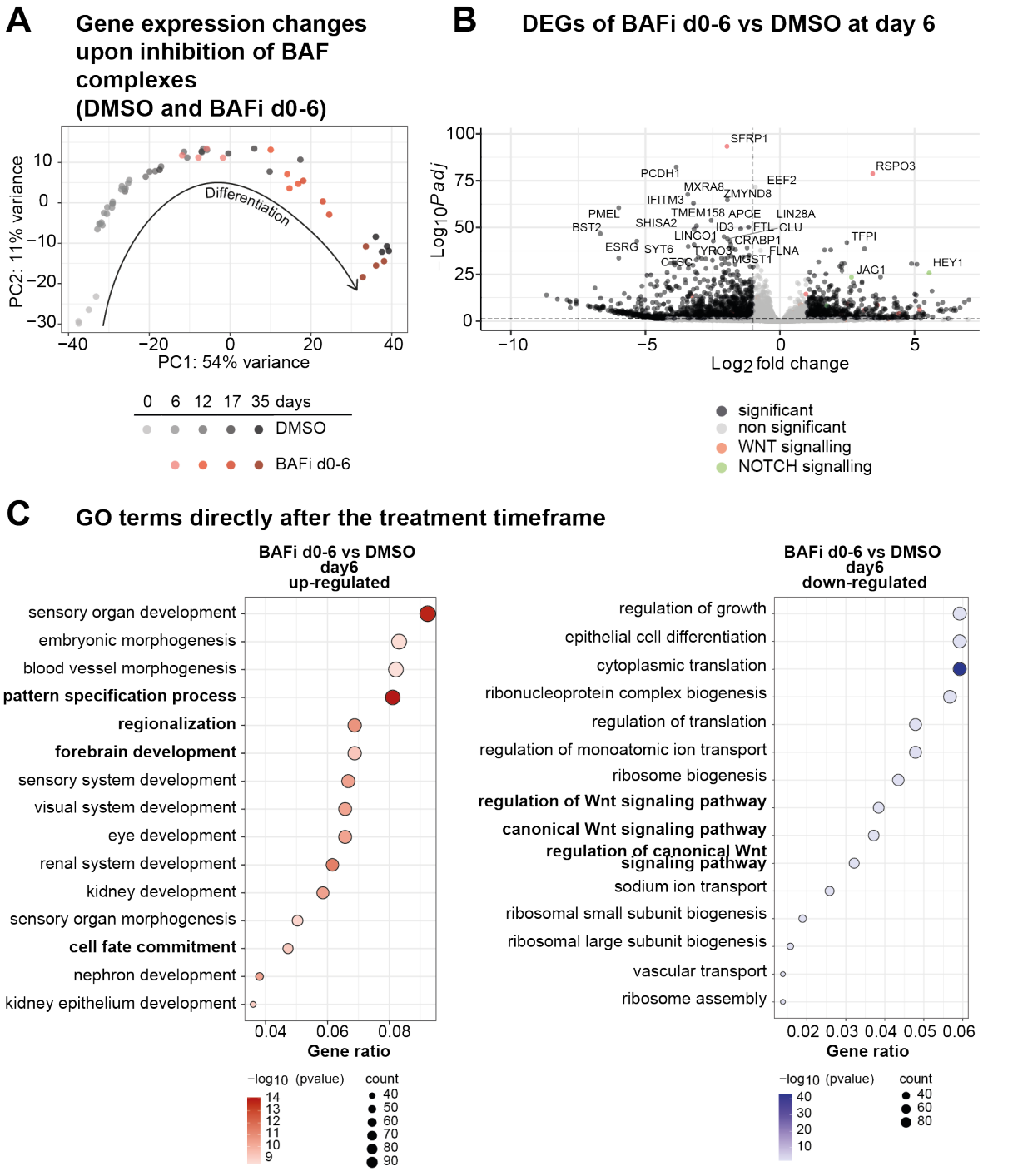

Figure 5.2-3: DEGs between BAFi d0-6 and DMSO samples indicate the involvement of BAF complexes in WNT and NOTCH signalling, as well as brain patterning and cell fate commitment processes. *A) PCA plot of the 500 genes with the highest variance across all samples from the bulk RNA-sequencing dataset, showing only the data points for DMSO and BAFi d0-6 samples. B) Volcano plot showing DEGs between BAFi d0-6 and DMSO at day 6, with log2 fold change on the x-axis and significance (–log10 padj) on the y-axis. Genes involved in WNT signalling are highlighted in red, while genes involved in NOTCH signalling are highlighted in green. C) GO term analysis[288] using the DEGs from BAFi d0-6 versus DMSO at day 6 The x-axis represents the gene ratio, calculated as the number of genes associated with a given GO term divided by the total number of genes included in the analysis. Gene count = the absolute number of genes from the input dataset associated with a specific GO term, –log10 padj = logarithmically transformed negative adjusted p-value, where p-values are adjusted using the false discovery rate (FDR) method (FDR < 0.01); d = day.*

Taken together, the data obtained suggest that proper BAF complex function is critical during early neurodevelopmental processes.

After validating BAF complexes essential role in neurodevelopmental processes and especially in neural cell type specification in early phases of neurodevelopment, we decided to focus on the treatment conditions showing the most pronounced phenotype (BAFi d0-6 and BAFi d6-12) for further analyses.

The PCA plot in **Figure 5.2-3 A**, showing only DMSO and BAFi d0-6 over time, supports the observation that the BAFi d0-6 samples exhibit precocious gene programs, as the samples from day 6 cluster with the DMSO samples from day 12. In terms of gene expression, this sample appears to be consistently one developmental step ahead until day 17, after which it converges again with the DMSO control at day 35.

The volcano plot, displaying DEGs of BAFi d0-6 relative to the DMSO control, reveals several affected genes involved in the NOTCH (green) and WNT (red) signalling pathways. Notably, many NOTCH-associated genes are upregulated, including the NOTCH target *HEY1* (hes related family BHLH transcription factor with YRPW motif 1) and *JAG1* (jagged canonical notch ligand 1), both known to support neural progenitor maintenance and inhibit early neuronal differentiation[295,296]. This observation of upregulated NOTCH signaling genes contrasts with the precocious expression of neural differentiation and maturation marker genes in BAFi d0-6 samples. It suggests that an alternative gene regulatory network may compensate for or counteract this effect, ultimately driving the upregulation of maturation marker gene expression. Among the most prominent DEGs, *SFRP1* is significantly downregulated. Typically expressed in rostral neural tube regions during neurulation, *SFRP1* acts as a potent WNT inhibitor[35,36]. In contrast, *RSPO3* (R-spondin 3) is upregulated and known to enhance WNT signalling activity[297] (**Figure 5.2-3 B**). Given that NOTCH signalling contributes to neural cell fate commitment and WNT signalling to brain patterning, it is consistent that the GO terms for DEGs between DMSO and BAFi d0-6 reflect these roles. Specifically, upregulated terms include 'pattern specification,' 'regionalization,' and 'cell fate commitment,' while 'regulation of WNT signalling' appears among the terms enriched in the downregulated genes (**Figure 5.2-3 C**). Thus, BAF complex inhibition results in deregulation of genes associated to these pathways, resulting in altered neurodevelopmental processes.

When comparing the morphology of BAFi d0-6 organoids to DMSO-treated controls, notable differences in cellular outgrowth were observed in the BAFi d0-6 samples. The morphology of these cells resembled that of neural crest cells, as seen in murine neural crest cells derived from a neural tube model system (**Figure 5.2-4 A**)[298]. This prompted an investigation into the expression of genes associated with neural crest cell development. Several neural crest-related genes, including *MSX1*, *MSX2* (Msh homeobox 2), *PAX3* (Paired box gene 3), and

TFAP2A (Transcription factor AP-2 alpha)[298–301], were markedly upregulated immediately following treatment. In contrast, *SOX10* was strongly downregulated at both day 6 and day 12 but exhibited increased expression from day 17 onward in BAFi d0-6 samples compared to the DMSO controls (**Figure 5.2-4 B**).

While these genes are not exclusively markers of neural crest cells and also play broader roles in development, their upregulation, coupled with the observed cellular morphology, suggests that BAF complex inhibition during days 0–6 of brain organoid development may promote the emergence of cells with neural crest-like characteristics. However, it is important to note that this conclusion cannot be definitively validated in the context of bulk RNA-seq data alone.

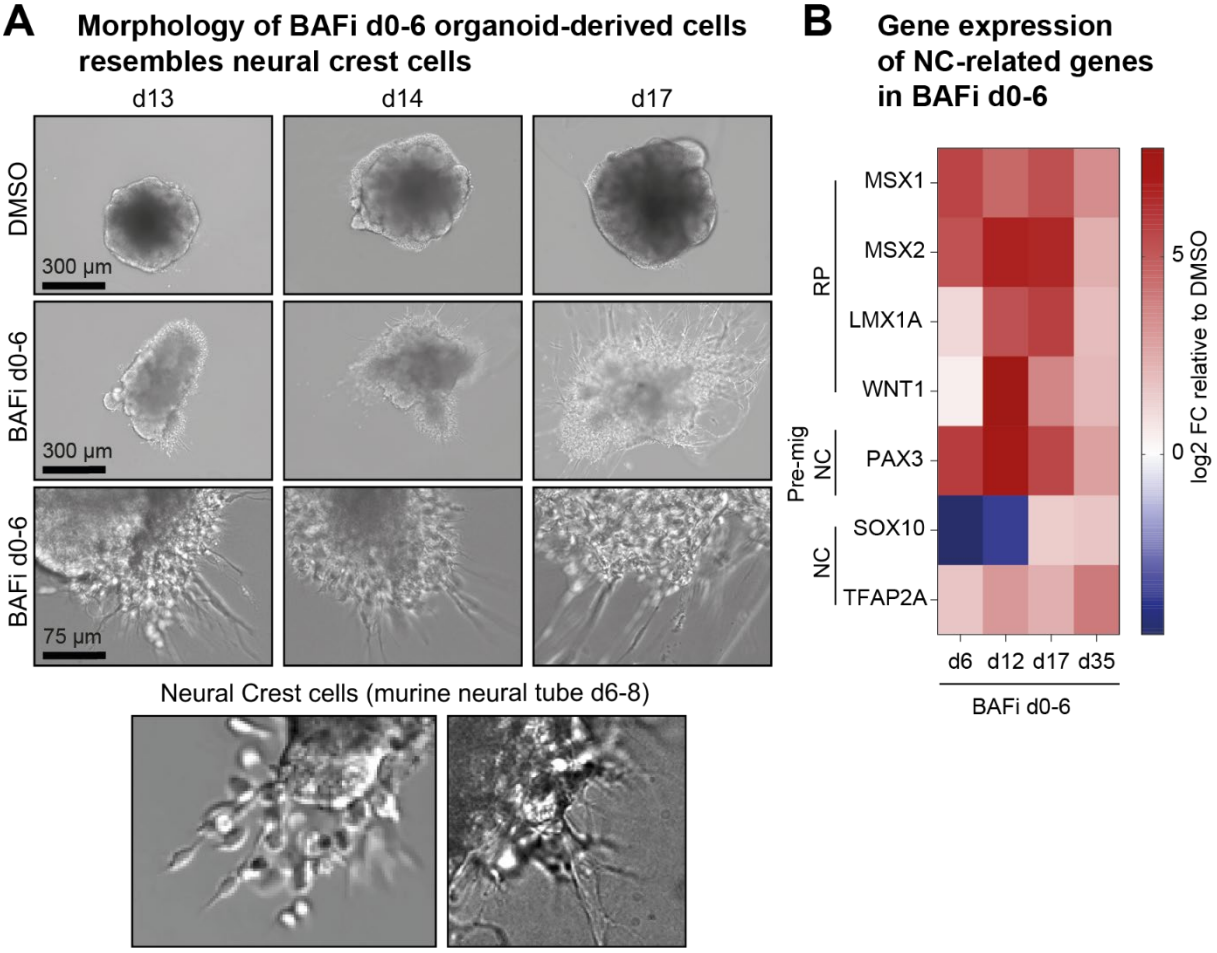

Figure 5.2-4: Morphological and gene expression changes indicate neural crest cell development in BAFi-d0-6 organoids. *A) Representative images of DMSO and BAFi d0-6 organoids at days 13, 14, and 17, alongside reference images of murine neural crest cells (NC) from the neural tube[298], highlighting similarities in cellular morphology. Murine neural crest cell images are adapted from the referenced source for comparison. B) Log_2 fold-change expression of neural crest-related genes in BAFi d0-6 organoids relative to DMSO controls at days 6, 12, 17, and 35 (n=4, bulk RNA-seq). This data reflects temporal gene expression shifts associated with neural crest development. RP = roof plate, Pre-mig NC = pre-migratory neural crest cells, NC = neural crest cells. d = day.*

Inhibiting BAF complexes one developmental stage later, from days 6-12 in brain organoid development, affects neurodevelopmental processes in ways partially distinct from the changes observed with earlier inhibition (BAFi d0-6). In the PCA plot, BAFi d6-12 samples cluster closely with their respective DMSO counterparts across developmental timepoints.

They diverge only slightly immediately post-treatment (day 12), showing a minor shift toward DMSO day 17 samples (**Figure 5.2-5 A**).

In the volcano plot, several DEGs associated with NOTCH and WNT signalling are evident in BAFi d6-12 samples compared to DMSO, though to a lesser degree than in BAFi d0-6 samples. Among these, the downregulation of *SFRP1* suggests increased WNT signalling activity, similarly to BAFi d0-6. Upregulated DEGs in BAFi d6-12 include genes involved in neuronal differentiation and axonal development, such as *VCAN* (versican) and *ONECUT3* (one cut homeobox 3), which are known to promote neuronal differentiation and neurite outgrowth[302,303].

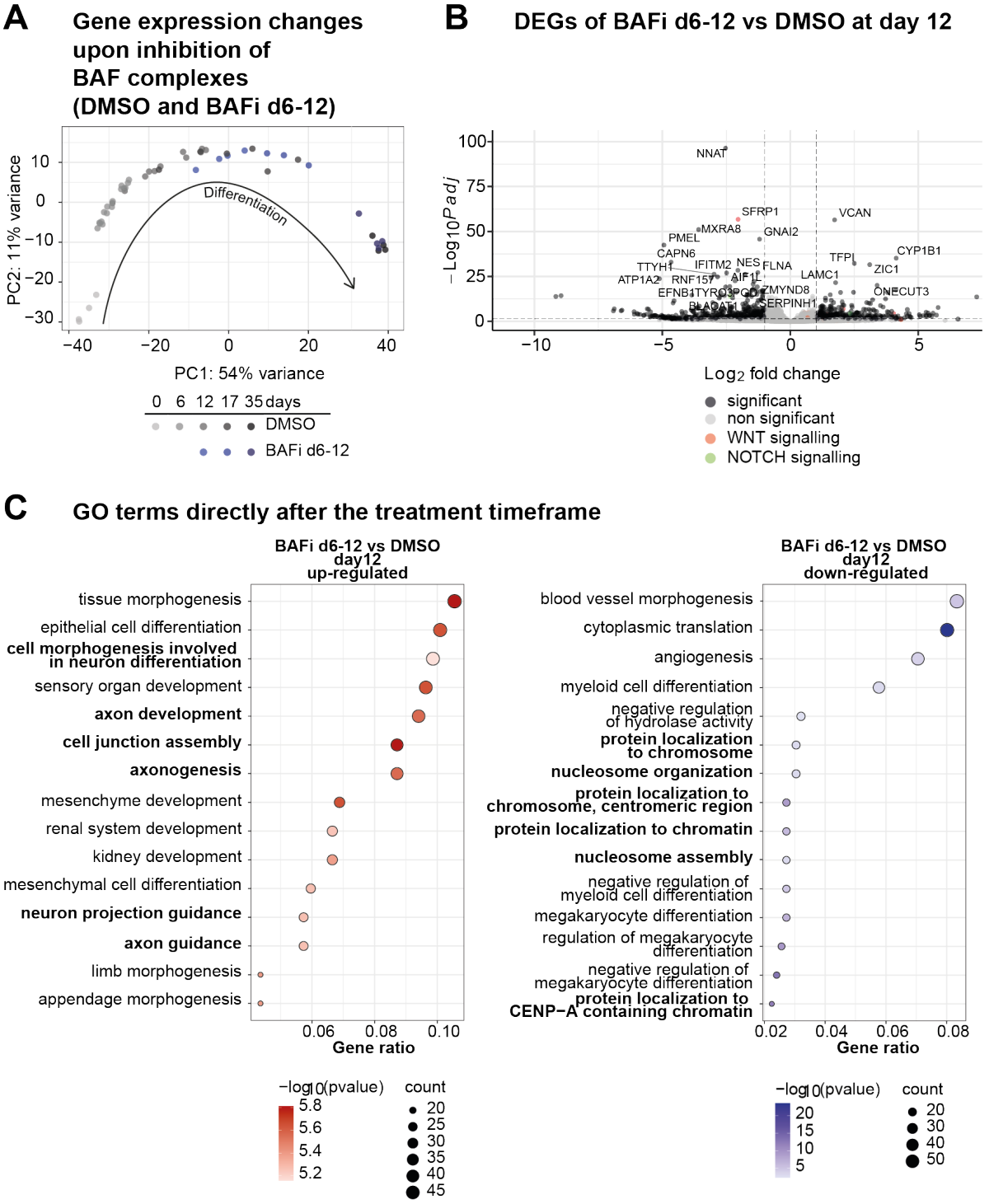

Figure 5.2-5: DEGs between BAFi d6-12 and DMSO samples indicate the involvement of BAF complexes in WNT signalling, as well as axon development and protein localization to chromatin. *A) PCA plot of the 500 genes with the highest variance across all samples from the bulk RNA-sequencing dataset, showing only the data points for DMSO and BAFi d6-12 samples. B) Volcano plot showing DEGs between BAFi d6-12 and DMSO at day 12, with log2 fold change on the x-axis and significance (–log10 padj) on the y-axis. Genes involved in WNT signalling are highlighted in red, while genes involved in NOTCH signalling are highlighted in green. C) GO term analysis[288] using the DEGs from BAFi d6-12 versus DMSO at day 12. –log10 padj = logarithmically transformed negative adjusted p-value, where p-values are adjusted using the false discovery rate (FDR) method (FDR < 0.01); d = day.*

While differentiation-related genes are upregulated in BAFi d6-12 samples, stem cell-associated genes, such as *NES* (nestin), a well-known marker of neural stem and progenitor

cells[304], are downregulated (**Figure 5.2-5 B**). This trend is evident in the GO terms, with "axon development" and "axon guidance" standing out as prominent upregulated terms. In contrast, GO terms of the downregulated genes primarily emphasize disruptions in "protein localization to chromatin". This finding aligns with the role of BAF complexes as chromatin remodelers, facilitating chromatin accessibility and recruiting specific proteins to target regions. Consequently, BAF complex loss likely disrupts chromatin accessibility and protein recruitment at these critical chromatin sites (**Figure 5.2-5 C**).

Collectively, the RNA-seq analysis shows that the loss of BAF complex activity most significantly impacts early developmental stages, such as neurulation and the onset of neurogenesis. This is reflected in the brain organoid model, with treatments during days 0-6 and 6-12 showing the most substantial gene expression changes. These differences were associated with dysregulation in key neurodevelopmental signalling pathways, such as NOTCH and WNT, which are critical for cell fate commitment, differentiation, maturation, and patterning, as reflected by the corresponding GO terms. While similarities exist between the two treatment timeframes, it is important to note that BAF inhibition from days 0-6 affected developmental processes in a distinct manner compared to treatment during days 6-12.

Given that RNA-seq provided initial insights into the affected neurodevelopmental stages, further analysis at the single-cell level is needed to explore the cellular subtypes involved and their specific responses to BAF inhibition

5.3 Cell fate decisions require proper BAF complexes function

To investigate cell type-specific changes upon BAF complexes loss during developmental stages d0-6 and d6-12, a droplet-based microfluidic single-nuclei sequencing system was employed. Brain organoids were generated using three hiPSC lines (HMGU1, BIHi001-A, BIHi242) under three conditions: DMSO (control), BAFi d0-6, and BAFi d6-12. At day 35, organoid tissues were dissociated, nuclei were extracted, and subjected to fluorescence-activated cell sorting (FACS). Nuclei from the same treatment condition were pooled in equal proportions and analysed using a combined single-nuclei RNA-sequencing (snRNA-seq) and single-nuclei assay for transposase-accessible chromatin with sequencing (snATAC-seq) pipeline (10x Genomics; Multiome).

The sequencing data were demultiplexed using single-nucleotide variants specific to each hiPSC line. Following, RNA-seq data were integrated with ATAC-seq data using a Signac-based processing pipeline from Stuart Lab[270,305], effectively correcting for batch effects.

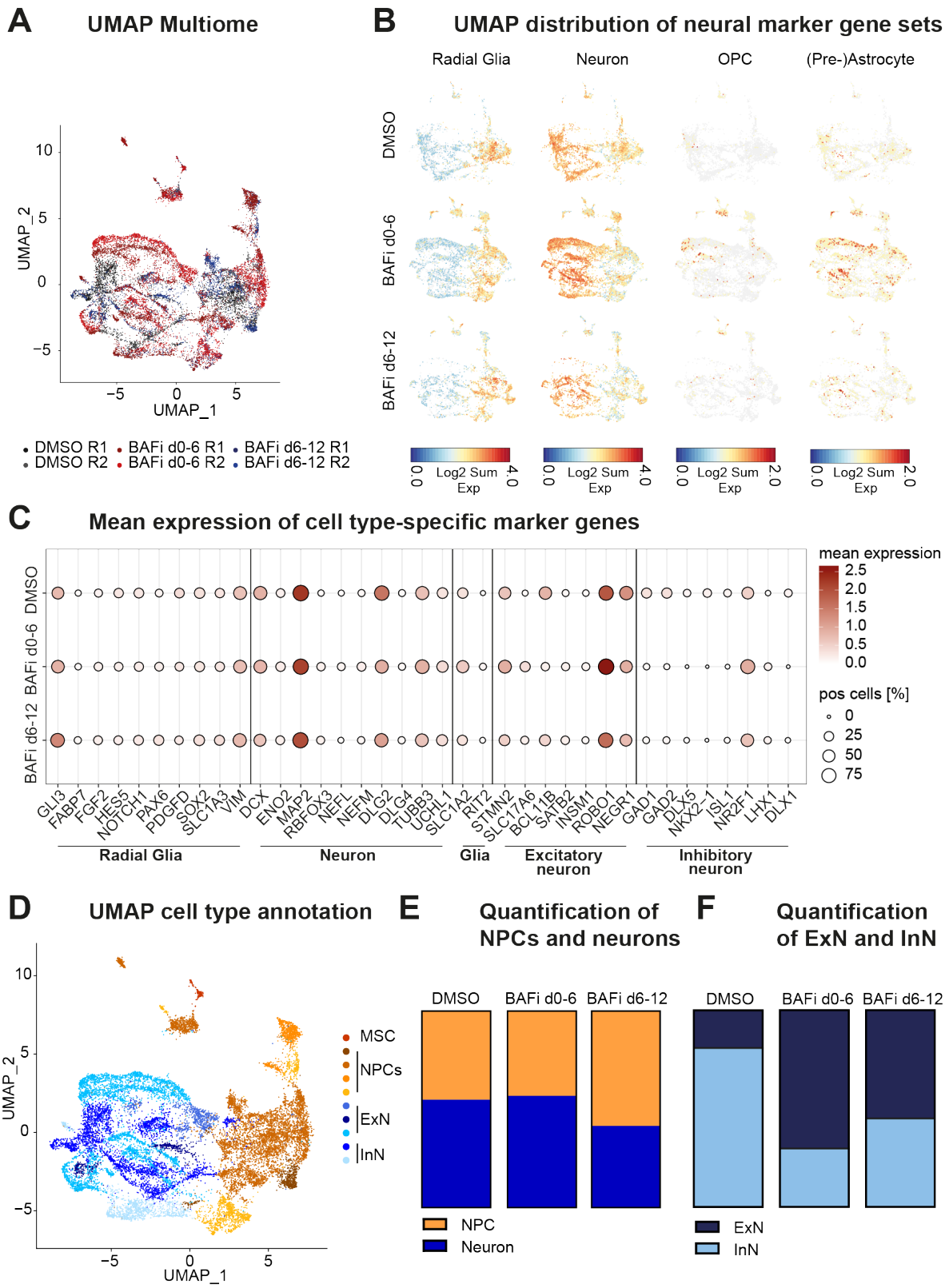

Figure 5.3-1: BAF complex function is essential for cell fate decisions during neurodevelopment. *A) Uniform Manifold Approximation and Projection (UMAP) of batch-corrected single-nuclei RNA-/ATAC-sequencing data from DMSO (grey), BAFi d0-6 (red), and BAFi d6-12 (blue) organoids, derived from two hiPSC lines (BIHi242 = R1 and HMGU1 = R2). B) Split UMAPs of DMSO, BAFi d0-6, and BAFi d6-12 groups, showing the log2 sum expression of neural marker gene lists (10x Loupe Browser; see **Table 7.1-2**). C) Dot plot displaying the mean expression levels of cell type-specific marker genes and the percentage of positive cells per condition. D) UMAP annotated for cell type[42,271] (see Methods and **Table 7.1-3** for further details). E) Bar chart showing the percentage distribution of NPCs and neurons in each condition. F) Bar chart showing the percentage distribution of inhibitory and excitatory neurons in each group. OPC = oligodendrocyte precursor cell, MSC = mesenchymal cell, NPC = neuroprogenitor cell, ExN = excitatory neuron, InN = Inhibitory neuron.*

The data set visualized via uniform manifold approximation and projection (UMAP), enabling correlation of gene expression changes with chromatin accessibility alterations at the single-nucleus level (**Figure 5.3-1**). This integrated dataset is referred to as the Multiome dataset throughout this analysis.

Notably, during organoid generation, one replicate (BIHi001-A) misdifferentiated, as reflected in its sequencing results. Consequently, it was excluded from further analyses.

While the two replicates of each condition clustered closely together, the clusters representing the three groups (DMSO, BAFi d0-6, and BAFi d6-12) were distinctly distributed within the UMAP (**Figure 5.3-1 A**). To gain initial insights into cell type distributions across the groups, the expression of neural marker genes (**Table 7.1-2**) was analysed in the UMAP (**Figure 5.3-1 B).** This cell type distribution was quantified by plotting the mean expression levels and the percentage of marker-positive cells for each group. For clarity, only a subset of marker genes that were highly expressed or showed differences among groups was included in the graph (**Figure 5.3-1 C**). Radial glia marker genes, such as *GLI3* and *VIM*, were most highly expressed in nuclei located on the right side of the UMAP, while general neuronal markers like *MAP2* and *TUBB3* (also known as *TUJ1*) showed progressively higher expression towards the left side. This spatial pattern was consistent across all groups, with a similar percentage of radial glia and neuronal marker-positive cells observed in DMSO, BAFi d0-6, and BAFi d6-12 (**Figure 5.3-1 C**). Interestingly, a small population of oligodendrocyte precursor cells (OPCs), identified by specific marker gene expression, was predominantly associated with BAFi d0-6 nuclei. Pre-astrocytic markers (e.g., *SLC1A2*) exhibited a scattered expression pattern across the UMAP, with a slightly increased percentage of positive cells in BAFi d0-6 samples (**Figure 5.3-1 B & C**). This indicates the presence of nuclei in an intermediate fate commitment state rather than a clearly defined pre-astrocytic population. In summary, the samples predominantly comprised immature neural states, such as radial glia, alongside maturing neurons, with subtle group-specific variations in less prevalent cell populations. To examine cell type-specific effects, the dataset was annotated using Snapseed (see methods section for more detailed description; **Table 7.1-3**)[42,271].

This approach allowed the assignment of each nucleus to a cell type based on the combined expression of multiple marker genes (**Figure 5.3-1 D**). Since day 35 brain organoids primarily model early neurodevelopment and its associated cell types, mature neuronal subtypes are not expected. To simplify annotation, cells expressing genes characteristic of more differentiated neuronal subtypes were categorized as neurons (**Figure 5.3-1 D-F**, blue colours). However, these cells are likely in an intermediate differentiation state, primed for their respective neuronal lineages. The annotation revealed a generally consistent distribution of NPCs and neurons between DMSO controls and BAFi d0-6 samples, reflecting a similar

balance between immature and more mature cell types. The BAFi d6-12 group displayed a slight shift, with a higher proportion of NPCs compared to neurons, indicating a tendency toward a less differentiated cell population under this condition (**Figure 5.3-1 E**). A more pronounced difference was observed in the ratio of excitatory to inhibitory neurons across the groups. The majority of inhibitory neurons were associated with the DMSO-treated samples, whereas BAFi d0-6 organoids exhibited a predominance of excitatory neurons. Notably, BAFi d6-12 organoids displayed a more balanced distribution of inhibitory and excitatory neurons (**Figure 5.3-1 D & F**). During forebrain development, most inhibitory neurons originate from ventral brain regions, such as the medial, lateral, and caudal ganglionic eminences[120,306]. In contrast, the dorsal forebrain predominantly gives rise to excitatory neurons[307,308]. These findings suggest that BAF complexes play a crucial role in regulating cell fate commitment, potentially by regulating brain region identity.

5.4 Early brain patterning is dependent on BAF complexes

Building on the hypothesis that BAF complexes ensure proper brain regionalization, the cell type annotation was expanded to include brain region identity marker genes (**Figure 5.4-1 A**). This approach facilitated a more detailed analysis of how BAF complex perturbation influences regional identity during neurodevelopment. Given that day 35 brain organoids primarily model early neurodevelopment and its associated cell types, regional identity was predominantly analysed in NPCs, while neuronal nuclei were broadly categorized as telencephalic or non-telencephalic, with the latter encompassing caudal brain regions beyond the telencephalon.
Additionally, mesenchymal stem cells (MSCs) were unexpectedly identified across all three groups, with the lowest proportion in DMSO-treated samples (0.3%), followed by BAFi d0-6 (1.2%), and the highest proportion in BAFi d6-12 samples (1.7%) (**Figure 5.4-1 A**). In the central nervous system, MSCs share characteristics with pericytes, which regulate blood-brain barrier function, a vascular structure originating from mesenchyme surrounding the neural tube[309]. Vascular development follows a rostrocaudal pattern, with the rhombencephalon being the first region to undergo vascularization due to elevated levels of growth factors such as WNT, BMP, and FGF[310,311]. During brain organoid development, a subset of cells can undergo misdifferentiation, failing to fully commit to a neural lineage. Another possibility is that the annotated mesenchymal cells originate from a potential neural crest population, which may be present in BAFi d0-6 samples at day 17. Neural crest cells are known for their exceptional differentiation potential, including the capacity to give rise to mesenchymal cells. Moreover, they share certain marker genes, such as *MSX2*[312] (**Figure 5.2-4 B**), with mesenchymal lineages, supporting this hypothesis. As this population represented only a very small fraction across all groups, it was not analysed in further detail.

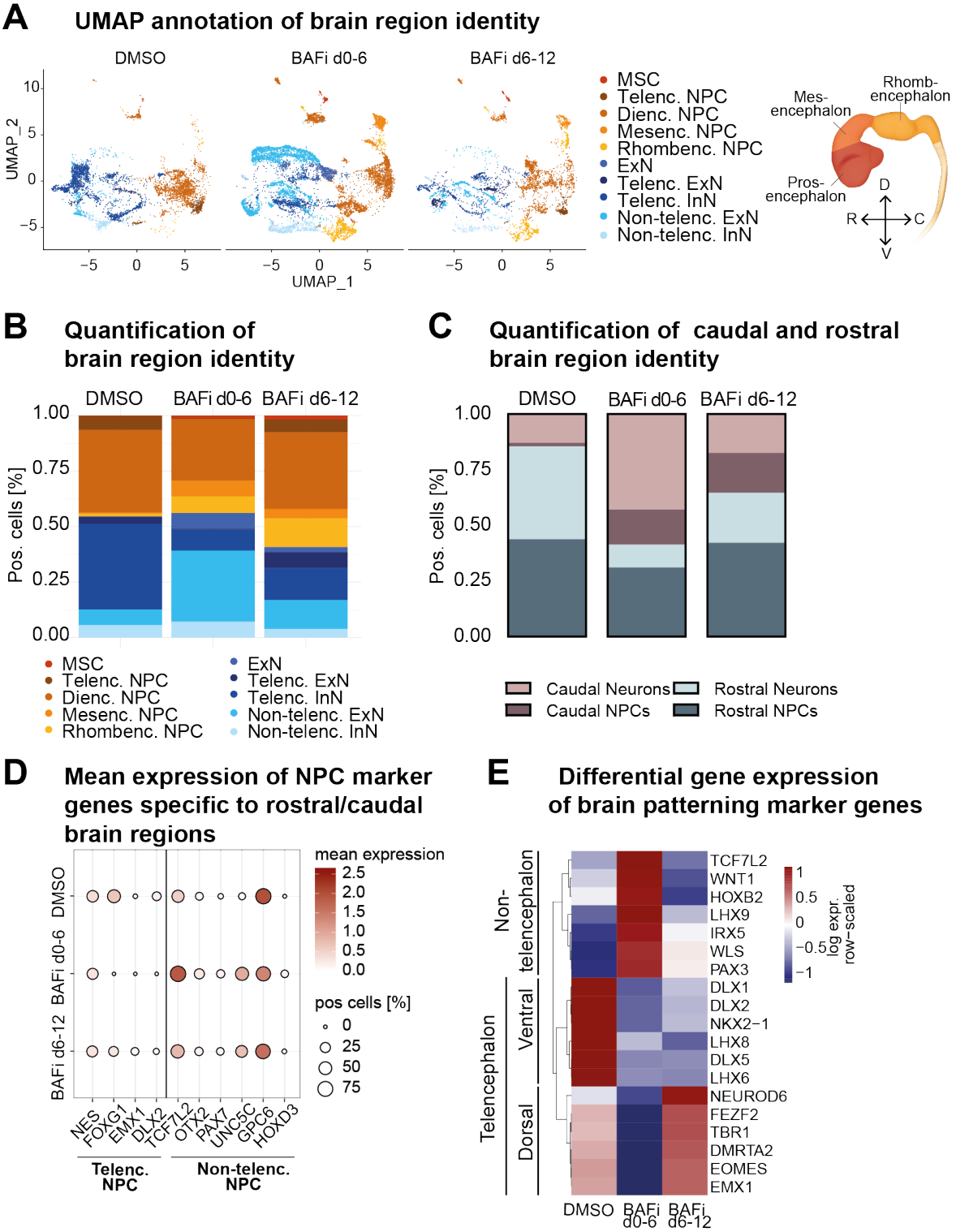

Figure 5.4-1: Brain patterning processes depend on BAF complex function. *A) UMAP annotated for neural cell types with brain region identity, alongside a schematic of a 4 pcw brain for orientation (see Methods and* ***Table 7.1-3*** *for details) B) Quantification of cell type distribution: Bar chart showing the percentage distribution of annotated cell types per condition. C) Quantification of caudal and rostral NPCs and neurons: Bar chart illustrating the percentage of cell types with rostral and caudal brain identities per condition. D) Dot plot displaying the mean expression levels (color-coded) of cell type-specific marker genes, with circle size indicating the percentage of positive cells per group (Mutliome data set, day 35). E) Heatmap of row-scaled logarithmic expression levels (RPKM) of patterning marker genes from the bulk RNA-seq data set in DMSO, BAFi d0-6, and BAFi d6-12 samples. D = dorsal, V = ventral, R = rostral, C = caudal, MSC = mesenchymal stem cell, Telenc. = telencephalon, Dienc. = diencephalon, Mesenc. = mesencephalon, Rhombenc. = rhombencephalon, NPC = neuroprogenitor cell, ExN = excitatory neuron, InN = inhibitory neuron, Pos cells = positive cells, d = day, log expr. row-scaled = logarithmic transformed and row-scaled RPKM (Reads per kilobase of transcript per million mapped reads) values.*

However, the increased proportion of misdifferentiated cells in BAF complex-inhibited samples underscores the dysregulation of critical signalling pathways involved in brain development and patterning.

Quantification of regional cell types revealed an increased proportion of mesencephalic and rhombencephalic NPCs in BAF inhibitor-treated samples compared to DMSO controls, with the largest proportions observed in BAFi d0-6 samples.

This was reflected by a higher percentage and mean expression of cells positive for non-telencephalic NPCs marker genes such as *TCF7L2* (transcription factor 7-like 2), a key player of the WNT signalling pathway, or *UNC5C* (unc-5 netrin receptor C), mainly expressed in rhombencephalic NPCs (**Figure 5.4-1 D**)[42,271].

Conversely, little to no cells positive for telencephalic NPC marker genes such as *FOXG1*, *EMX1* or *DLX2* were detected in BAFi d0-6 samples (**Figure 5.4-1 D**).

This caudalisation of brain region identity in BAFi d0-6 samples extended to neurons, which exhibited the highest proportion of non-telencephalic identities (~43 %) among the three groups (**Figure 5.4-1 B, C**).

In contrast, the cell type distribution in BAFi d6-12 samples more closely resembled that of the DMSO control, with the primary difference being a higher proportion of NPCs, particularly rhombencephalic NPCs. Notably, BAFi d6-12 samples also contained a slightly higher overall proportion of NPCs compared to DMSO and BAFi d0-6. BAFi d6-12 samples had a higher proportion of non-telencephalic excitatory neurons compared to DMSO controls, where excitatory neurons were generally scarce. They also showed an increased proportion of telencephalic excitatory neurons relative to both DMSO and BAFi d0-6 samples (**Figure 5.4-1 B, C**).

In summary, the annotation of cell types based on brain region identity revealed that BAFi-treated samples displayed a higher proportion of caudal cell types and an overall lower proportion of inhibitory neurons. These observations suggest distinct regional identities, with DMSO samples predominantly reflecting ventral telencephalic identity, BAFi d0-6 samples showing a more non-telencephalic or caudal identity, and BAFi d6-12 samples aligning more closely with a dorsal telencephalic identity.

Analysis of dorsal and ventral telencephalon marker genes in the bulk RNA-seq dataset further validated these findings, demonstrating a stronger dorsal telencephalic identity in BAFi d6-12 organoids compared to both DMSO and BAFi d0-6 organoids. Conversely, DMSO organoids had the highest expression of ventral telencephalon marker genes, while BAFi d0-6 organoids showed the strongest expression of non-telencephalic marker genes (**Figure 5.4-1 D**).

These observations suggest the activation of distinct gene regulatory programs specific to each group. Given that these unique gene regulatory networks are likely the primary drivers of the observed patterning phenotypes, a more detailed analysis of each group was conducted.

5.4.1 BAF complexes ensure forebrain identity

To investigate how BAF complex inhibition from day 0 to day 6 (BAFi d0-6) leads to an increased proportion of caudal cell types by day 35 of brain organoid development, the expression of telencephalic and non-telencephalic marker genes was analysed over the developmental timeline (**Figure 5.4-2 A**).

A key transcription factor driving forebrain development, FOXG1, showed high expression in DMSO-treated samples at day 35 alongside other forebrain marker genes (**Figure 5.4-2 A**, **B**). In contrast, BAFi d0-6 samples exhibited decreasing expression of forebrain marker genes over time, accompanied by increasing expression of genes associated with more caudal, non-telencephalic brain regions (**Figure 5.4-2 A, B**). This trend was evident as early as day 6, immediately following treatment, and peaked at day 35, when regional brain identity appeared to be established. Chromatin accessibility data further supported this observation, revealing an inaccessible *FOXG1* locus in BAFi d0-6 samples at day 35 (**Figure 5.4-2 C**). Consistently, protein-level analysis showed little to no FOXG1-positive cells in these samples at the same time point (**Figure 5.4-3 A, B**). In contrast, BAFi d0–6 samples exhibited numerous PAX3-positive cells, a feature absent in DMSO control-derived organoids. In the controls, only a faint cytoplasmic signal, likely attributable to staining artefacts, was detected, with no nuclear localization observed (**Figure 5.4-3 C**). This finding further supports the non-telencephalic identity of BAFi d0-6 samples.

Interestingly, *FOXG1*, along with other forebrain markers such as *RORB* and *ARX* (aristaless-related homeobox)[313,314], was slightly upregulated immediately following BAF inhibition at day 6 compared to DMSO controls. However, this transient upregulation was insufficient to establish or maintain forebrain identity, as these markers were progressively downregulated over the time course. This observation suggests that these genes may not be direct targets of BAF complexes, instead, their later repression may be mediated by factors activated upon BAF inhibition. In contrast, *FOXH1* (forkhead box H1), an early forebrain marker[315], was downregulated immediately after treatment at day 6 and remained lower expressed until day 17. Conversely, *WLS* (WNT ligand secretion mediator), an early caudal marker during brain development[315], displayed the opposite expression trend, which was further supported by increased accessibility of the *WLS* locus in BAFi d0-6 samples at day 35 (**Figure 5.4-2 D**). Additionally, other WNT signalling-related genes, including *PAX3* (paired box gene 3)[316,317], *IRX3*, *WNT1*, *TCF7L2*, and *GBX2*, were upregulated in BAFi d0-6 samples at specific time points during differentiation. This suggests that dysregulated WNT signalling upon BAF inhibition may be a driving factor behind the observed caudalised phenotype. After confirming the caudal brain identity of BAFi d0-6 samples at the RNA, protein, and chromatin levels, attention was turned to the gene regulatory networks (GRNs) driving this phenotype at day 35.

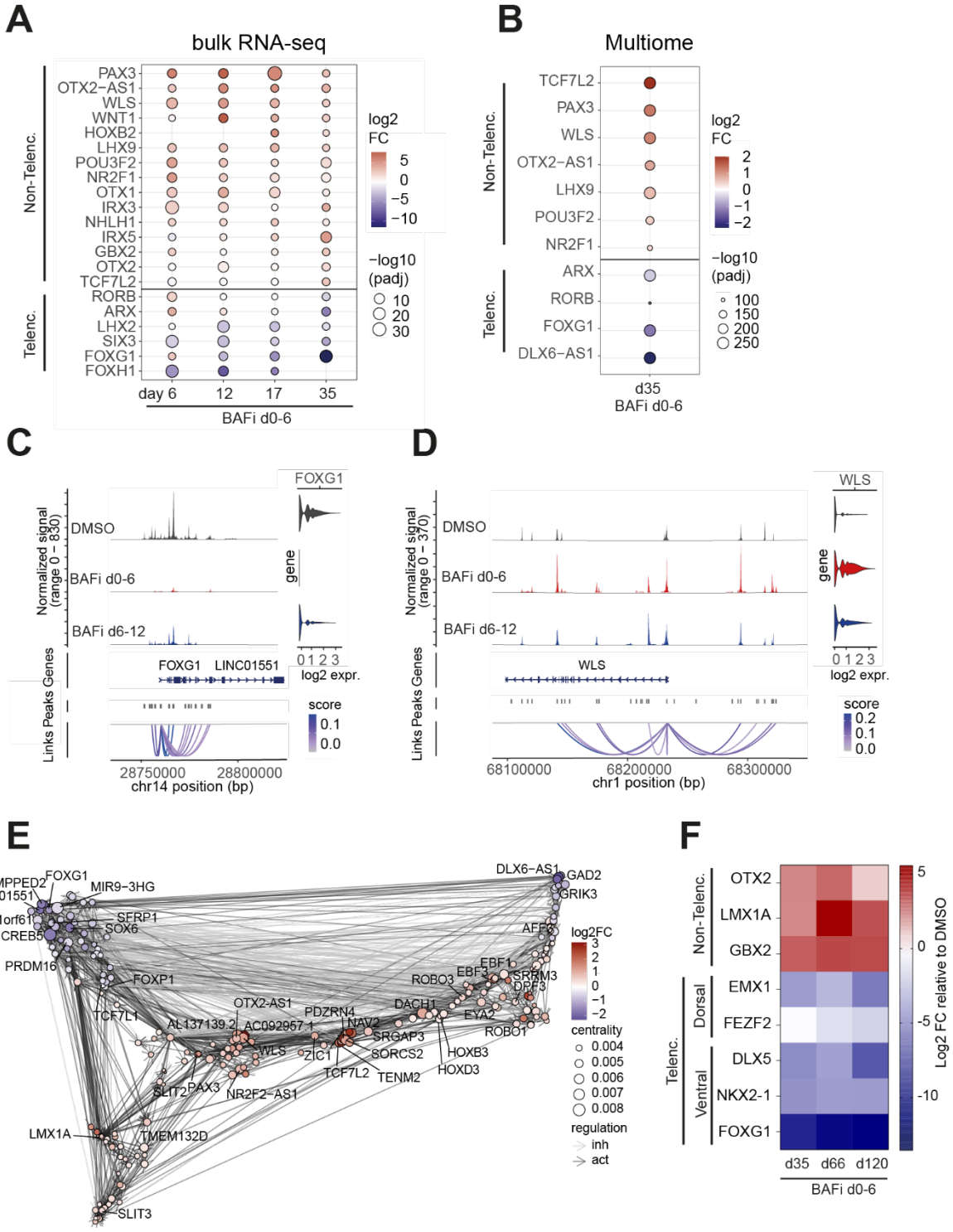

Figure 5.4-2: BAF complexes ensure forebrain cell identity during neurulation. *A) Dot plot showing the log2 fold change (FC) (color-coded) and significance (–log10 p-adj, represented by circle size) of telencephalic and non-telencephalic brain patterning marker genes in DMSO and BAFi d0-6 samples over time (bulk RNA-seq). B) Dot plot displaying log2 FC (color) and significance (–log10 p-adj, circle size) at day 35 from the Multiome dataset. C) ATAC-seq track showing the chromatin accessibility (left) and violin plot of log2 expression (right) of the forebrain-specific gene FOXG1 in DMSO, BAFi d0-6, and BAFi d6-12 samples at day 35 (Multiome dataset). D) ATAC-seq track and showing the chromatin accessibility (left) and violin plot of log2 expression (right) of the caudalising gene WLS in DMSO, BAFi d0-6, and BAFi d6-12 samples at day 35 (Multiome dataset). E) Gene regulatory network (GRN) plot created with Pando[216], illustrating DEGs between DMSO and BAFi d0-6. Log2 FC is indicated by color, network centrality by circle size, and predicted gene interactions by arrow color (black = activating, grey = inhibiting). F) Heatmap showing RT-qPCR-derived log2 FC of patterning genes in BAFi d0-6 relative to DMSO on days 35, 66, and 120 (n=2). The values were normalized to the housekeeping gene ATP5F1B. d = day, FC = fold-change, p-adj. = adjusted p-value, where p-values being adjusted using the false discovery rate (FDR) method (FDR < 0.01).*

To achieve this, the Pando framework[216], a tool that integrates multi-omic data and predicts transcription factor binding sites, was employed to generate a GRN based on the DEGs between DMSO and BAFi d0-6 samples (**Figure 5.4-2 E**).

Notably, TFs associated with forebrain development, such as *CREB5*, the antisense RNA *DLX6-AS1*, and the long non-coding RNA *LINC01551*[42,216], as well as factors involved in inhibitory neuron development like *GAD2* (glutamate decarboxylase 2)[318] *SOX6* (SRY-box transcription factor 6)[319], exhibited low expression in BAFi d0-6 samples but high centrality within the DMSO network (**Figure 5.4-2 E**). These TFs likely represent the key regulators of ventral forebrain-specific GRNs in DMSO organoids. Conversely, genes associated with non-telencephalic fate commitment and caudalisation, including *TCF7L2*, *WLS*, *LMX1A* (LIM Homeobox Transcription Factor 1 Alpha), *PAX3* as well as the antisense RNA *OTX2-AS1*[42,216,320], were upregulated in BAFi d0-6 samples and showed high centrality within their network, suggesting they are primary drivers of the GRNs in the BAFi d0-6 organoids (**Figure 5.4-2 E**). Additionally, genes associated with axon guidance, including *SLIT2* (slit guidance ligand 2), *SLIT3*, and *ROBO1* (roundabout guidance receptor 1), were also upregulated in BAFi d0-6 samples. Although these genes exhibited lower centrality within the GRN, their increased expression suggests that axon guidance signalling may also be dysregulated alongside the caudalised phenotype.

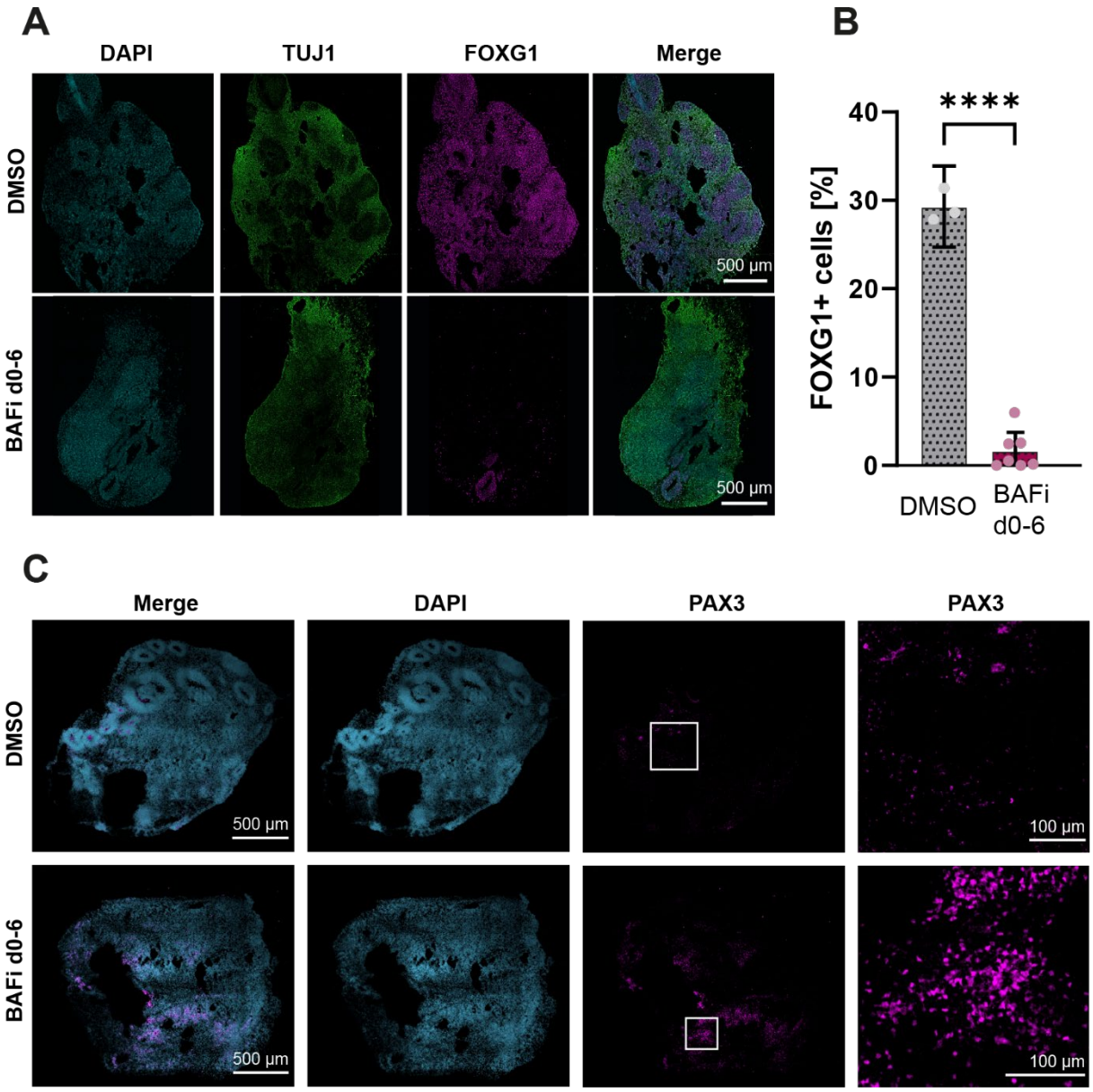

Figure 5.4-3: BAF complex inhibition during early neurulation promotes caudal cell fate commitment. *A) Representative immunofluorescence images of DMSO and BAFi d0-6 samples, stained for the DNA marker DAPI (cyan), the neural fate commitment marker TUJ1 (green), and the forebrain-specific marker FOXG1 (magenta). Images are from 12 µm sections, acquired using a 40x objective on a Leica Thunder microscope. B) Bar chart showing the percentage of FOXG1-positive cells in DMSO (grey, n = 3) and BAFi d0-6 samples (n = 7). Quantification details are provided in the Methods section. Unpaired t-test, **** = p < 0.0001. C) Representative immunofluorescence images of DMSO and BAFi d0-6 samples, stained for the DNA marker DAPI (cyan) and the non-telencephalic identity marker PAX3 (magenta). White rectangles in the left PAX3 image indicate regions of interest, shown on the right at higher magnification. Images were acquired from 12 µm sections using a 20x objective on a BC43 spinning disk confocal microscope (Oxford Instruments).*

This caudalised phenotype could not be reversed by withdrawing the BAF inhibitor, as evidenced by the continued downregulation of *FOXG1*, *EMX1*, *FEZF2*, *DLX5* and *NKX2-1* and the persistent upregulation of caudal region-associated genes, such as *GBX2*, *OTX2*, and *LMX1A*[31,321], even at days 66 and 120 (**Figure 5.4-2 F**).

In summary, BAF inhibition during early developmental stages (BAFi d0-6), corresponding to early neurulation, suppresses forebrain-specific marker genes while promoting the expression of caudal brain region identity markers. This phenotype remains irreversible over time, even

after the removal of the inhibitor. The upregulation of multiple WNT signalling-related genes and their integration into the GRN at day 35 strongly implicates dysregulated WNT signalling, a known caudalising factor, as a potential key driver of this phenotype.

5.4.2 BAF complexes ensure forebrain patterning

To investigate how BAF perturbation during late neurulation and the onset of neurogenesis (d6-12) results in an increased dorsal cell population during brain organoid development, the expression of dorsal and ventral telencephalon marker genes was analysed over the developmental timeline. In BAFi d6-12 samples, dorsal telencephalon marker genes showed a gradual increase in expression over time, while ventral marker gene expression decreased (**Figure 5.4-4 A**, **B**). Interestingly, dorsal pattern specification was not evident immediately after treatment (day 12) but became apparent from day 17 onwards. Directly after treatment, ventral telencephalon marker genes, particularly members of the distal-less homeobox (DLX) family (*DLX1*, *DLX2*, *DLX5*, *DLX6*)[322,323] and *DLX6-AS1*[324], were highly upregulated.

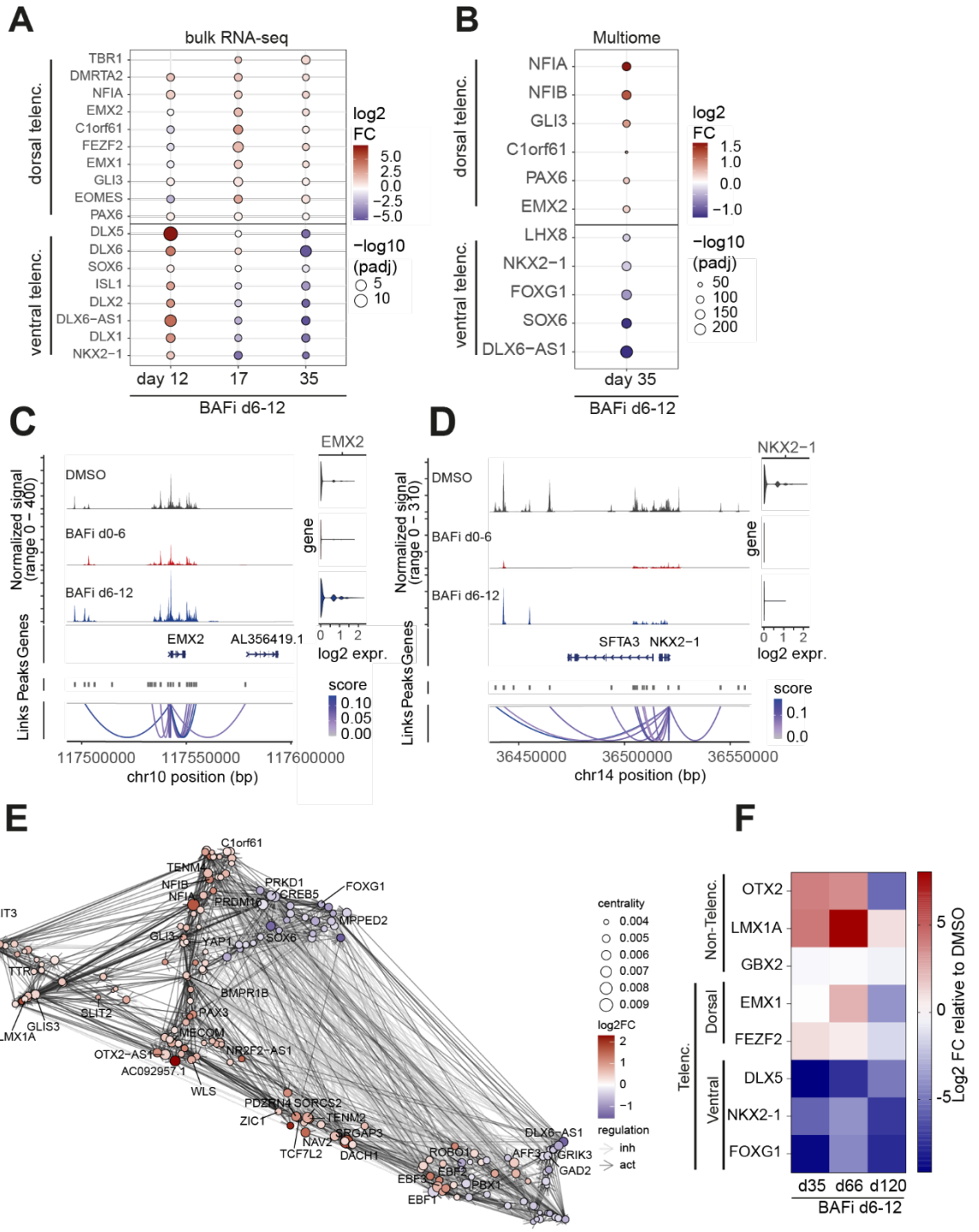

Figure 5.4-4: BAF complexes ensure forebrain patterning processes. *A) Dot plot showing the log2 FC (color-coded) and significance (–log10 p-adj, represented by circle size) of dorsal and ventral telencephalon marker genes in DMSO and BAFi d6-12 samples over time (bulk RNA-seq). B) Dot plot displaying log2 FC (color) and significance (–log10 p-adj, circle size) at day 35 from the Multiome dataset. C) ATAC-seq track showing the chromatin accessibility (left) and violin plot of log2 expression (right) of the dorsal telencephalon-specific gene EMX2 in DMSO, BAFi d0-6, and BAFi d6-12 samples at day 35 (Multiome dataset). D) ATAC-seq track showing the chromatin accessibility (left) and violin plot of log2 expression (right) of the ventral telencephalon-specific gene NKX2-1 in DMSO, BAFi d0-6, and BAFi d6-12 samples at day 35 (Multiome dataset). E) Gene regulatory network (GRN) plot created with Pando[216], illustrating DEGs between DMSO and BAFi d6-12. Log2 FC is indicated by color, network centrality by circle size, and predicted gene interactions by arrow color (black = activating, grey = inhibiting). F) Heatmap showing RT-qPCR-derived log2 FC of patterning genes in BAFi d0-6 relative to DMSO on days 35, 66, and 120 (n=2). The values were normalized with the housekeeping gene ATP5F1B. d = day, FC = fold change, p-adj. = adjusted p-value, where p-values being adjusted using the false discovery rate (FDR) method (FDR < 0.01).*

In contrast, dorsal-specific markers such as *GLI3*, *DMRTA2* (DMRT Like Family A2)[325], *NFIA* (Nuclear factor I A)[326], and *EOMES*[177] exhibited only slight upregulation or were downregulated at day 12, with their expression increasing significantly from day 17 onwards. This discrepancy suggests that BAF complexes play a critical role in regulating upstream gene programs that influence dorsoventral pattern specification, rather than directly targeting these marker genes. At day 35, the dorsal telencephalon identity of BAFi d6-12 organoids was validated at the protein level (**Figure 5.4-5**).

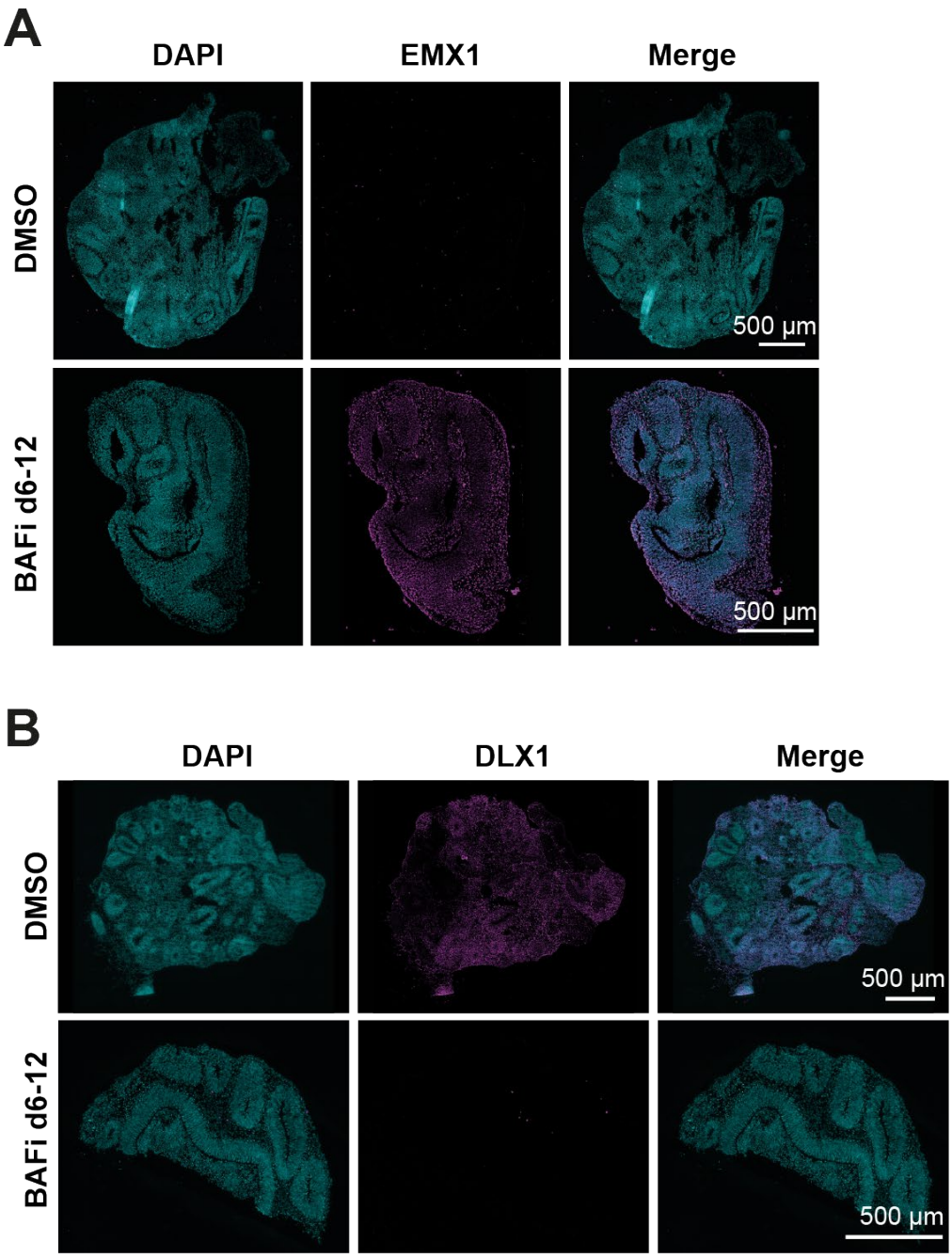

Figure 5.4-5: BAF complex inhibition from day 6-12 promotes dorsal cell fate commitment. *A) Representative immunofluorescence images of DMSO and BAFi d6-12 samples, stained for the DNA marker DAPI (cyan) and the dorsal telencephalon marker EMX1 (magenta). B) Representative immunofluorescence images of DMSO and BAFi d6-12 samples, stained for the DNA marker DAPI (cyan) and the ventral telencephalon marker DLX1 (magenta). Images (A,B) are from 12 µm sections, acquired using a 40x objective on a Leica Thunder microscope.*

While *DLX1* (ventral marker) expression was restricted to DMSO-treated organoids, *EMX1* (dorsal marker) was detected exclusively in BAFi d6-12 samples at day 35 (**Figure 5.4-5**). Chromatin accessibility data further supported these findings, showing enrichment of open chromatin regions associated with dorsal markers such as *EMX2* in BAFi d6-12 samples, while regions linked to ventral markers like *NKX2.1* were more accessible in DMSO controls (**Figure 5.4-4 C, D**).

After confirming a more dorsal telencephalon identity in BAFi d6-12 organoids at day 35, the GRNs driving dorsoventral identities in these organoids were further examined using Pando[216], focussing on DEGs between BAFi d6-12 and DMSO samples. The GRN analysis identified *NFIA* and *DACH1*, a transcription factor involved in forebrain development, as potential key regulators of the dorsalising program in BAFi d6-12 organoids. Conversely, ventral forebrain development in DMSO organoids is likely established by factors such as *FOXG1*, *DLX6-AS1*, and *SOX6* (**Figure 5.4-4 E**). Notably, the GRN of BAFi d6-12 samples not only highlighted dorsal- or ventral-specific marker genes but also included genes involved in WNT signalling (e.g., *WLS*, *TCF7L2*) and axon guidance (e.g., *SLIT2*, *SLIT3*, *ROBO1*), mirroring observations from BAFi d0-6 samples. Additionally, *YAP1* (yes1 associated transcriptional regulator), a key factor in YAP signalling, was found to be upregulated in BAFi d6-12 samples. While these genes did not exhibit the highest centrality within the GRN, they may still contribute to the phenotype observed in BAFi d6-12 samples, also beyond the dorsalisation. For example, *SLIT2*, predominantly expressed in the choroid plexus[327], the most dorsal structure in the forebrain during development and marked by *TTR*[328], was upregulated in BAFi d6-12 samples. The increased expression of *TTR* in BAFi d6-12 samples further supports the association with dorsal brain regions. This suggests that distinct brain regions are induced in BAFi d6-12 samples with the expression of genes associated with region-specific functions rather than general regional specification (**Figure 5.4-4 E**).

This dorsalised phenotype in BAFi d6-12 samples persisted over time, as increased expression of dorsal marker genes (*EMX1* and *FEZF2*) was observed at day 66. Similarly, markers associated with caudal regions (*OTX2*, *GBX2*, and *LMX1A*) remained elevated. However, by day 120, the expression of dorsal and caudal markers showed a slight decrease, indicating either partial recovery in BAFi d-12 or enhanced differentiation of cells into dorsal and caudal brain region identities in DMSO samples. Importantly, ventral telencephalon marker genes (*FOXG1*, *DLX5* and *NKX2.1*) remained downregulated at day 120 (**Figure 5.4-4 F**). These data sugggest that while DMSO controls may progressively increase dorsal populations over time, BAFi d6-12 samples show a reduced capacity to generate ventral populations to the same extent as the controls (**Figure 7.2-3**).

Collectively, BAF complex inhibition from days 6 to 12 increases the proportion of dorsal telencephalic cell types by activating dorsalising gene programs over time. This activation appears to be indirect, as it becomes evident only after the treatment period, rather than immediately, suggesting BAF complexes to regulate gene programs upstream of the dorsoventral patterning. Along with the dorsalised phenotype, dysregulation of genes involved in WNT, YAP, and axon guidance signalling was observed, potentially contributing to the overall phenotype. However, while WNT signalling was found to be affected already at day 12 directly after the treatment (**Figure 5.2-5**) and is known to promote dorsalisation[76,77,329], it remains unclear whether YAP and axon guidance signalling pathways are activated as a consequence of the dorsalised phenotype, drive dorsalisation due to BAF inhibitor-induced disruption, or represent changes independent of dorsalisation. While the dorsalised phenotype shows partial recovery over time, with a slight decrease in dorsal marker gene expression by day 120 (**Figure 7.2-3**), the expression of ventral marker genes remains low compared to controls. This indicates that BAF inhibition from days 6 to 12 impairs the ability to generate or expand ventral cell populations, unlike DMSO-treated organoids, which can generate both dorsal and ventral populations (**Figure 7.2-3**).

5.5 Direct effects of BAF inhibition on the chromatin landscape

Gene program analysis of day 35 organoids confirmed the caudalised and dorsalised phenotypes following BAF complex inhibition during the early and late neurulation phases. However, the immediate chromatin changes induced post-treatment remain elusive. Since BAF complexes are ATP-dependent chromatin remodelers, the changes in chromatin accessibility upon BAF inhibition are likely the main driver of the observed gene expression alterations. To identify affected genomic sites and their impact on dysregulated gene programs, bulk ATAC-seq was performed on DMSO, BAFi d0-6, and BAFi d6-12 samples at days 6 and 12. Additionally, CUT&Tag analysis was performed to investigate the binding of BAF subunits, such as SMARCA4, alongside markers of active enhancers (H3K27ac) and silent regions (H3K27me3). However, due to technical limitations, CUT&Tag data were only available for BAFi d0-6 samples, and analysis of BAFi d6-12 samples could not be conducted. These analyses link BAF-specific chromatin changes to specific regions, shedding light on the chromatin landscape alterations driving the observed gene regulatory shifts and patterning phenotypes.

Gene expression analysis at day 6 following BAF complex inhibition (BAFi d0-6) revealed increased expression of caudal marker genes, such as *WLS* and *IRX3*, accompanied by reduced expression of forebrain markers, including *SIX3*, *FOXH1*, and *SFRP1*. Interestingly, the forebrain marker *FOXG1* exhibited a transient upregulation immediately after treatment before being downregulated from day 12 onwards. These findings indicate a disruption in the

regional identity gene programs regulated by BAF complexes during early neurodevelopment (**Figure 5.5-1 A**).

To explore how the inhibition of BAF complexes mediates the observed changes via chromatin accessibility alterations, ATAC-seq was conducted on BAFi d0-6 samples at days 6 and 12. Differential accessibility was observed across multiple genomic regions, with the most significant changes occurring immediately after the treatment on day 6, where a total of 58564 differential accessible regions were identified (**Figure 5.5-1 B**). By day 12, this number decreased to 9002 (**Figure 5.5-1 C**), suggesting a gradual recovery of the chromatin landscape after the inhibitor was removed. Since BAF complexes are known to primarily enhance chromatin accessibility, the majority of differential regions in BAFi d0-6 samples showed decreased accessibility at both day 6 and day 12. However, not all changes in chromatin accessibility directly corresponded to the observed gene expression alterations.. For example, although *WLS* expression was upregulated at day 6, chromatin accessibility at a distal intergenic region associated with *WLS* was reduced. Conversely, two intronic regions of *WLS* exhibited increased accessibility, suggesting a potential compensatory role. Intronic regions can act as enhancers[330], and their increased accessibility may drive the observed upregulation of WLS despite the reduced accessibility of the distal locus. Notably, by day 12, the region with the most significant accessibility change in *WLS* became more open, aligning with its elevated expression.

The impact of BAF complex inhibition extended to additional WNT pathway-related genes. For example, the negative WNT regulator *NKD1* (NKD inhibitor of WNT signalling pathway 1)[331,332] and *SENP2* (SUMO-specific peptidase 2), a factor known to destabilize β-catenin[333,334], exhibited reduced chromatin accessibility. This suggests that BAF complexes typically target these regions to modulate WNT signalling under physiological conditions. Concurrently, regions associated with YAP signalling, such as *TEAD1*, demonstrated increased accessibility in BAFi d0-6 samples, potentially contributing to the caudalised phenotype observed at later stages[315], such as day 35. These chromatin alterations collectively point to dysregulated WNT and YAP signalling as key drivers of the altered developmental trajectories in BAFi-treated brain organoids.

Further supporting the caudalised and dorsalised fate, ZIC family genes, including *ZIC4*, showed consistently increased accessibility at both day 6 and day 12[335–338]. Similarly, the key dorsal factor *GLI3*[46] displayed higher accessibility at day 6, while *BMP4*[339] regions became more accessible at day 12 (**Figure 5.5-1 B, C**). The altered accessibility of WNT-related genomic regions in BAFi d0-6 samples is consistent with the GO analysis, which identified terms such as "cell-cell signalling by WNT" and "regulation of WNT signalling pathway" as among the most enriched GO terms linked to the regions with increased accessibility (**Figure**

5.5-1 D). Surprisingly, "forebrain development" also emerged among the top upregulated GO terms at day 6, suggesting that not all forebrain-associated genes were disrupted immediately following treatment. However, by day 35, forebrain identity was significantly diminished, potentially driven by the cumulative effects of dysregulated WNT and YAP signalling pathways.

Interestingly, several GO terms were associated with both upregulated and downregulated regions, including "axonogenesis" and "axon guidance" (**Figure 5.5-1 C**, **D**). This aligns with bulk RNA-seq data showing dysregulation of several axon guidance genes upon BAF complexes inhibition. However, no clear trend toward overall upregulation or downregulation of these pathways was observed. This ambiguity may stem from differential accessibility at distinct sites annotated to the same gene, with some regions becoming more accessible and others less so. Additionally, it is possible that different axon guidance-related genes exhibit opposing patterns of chromatin accessibility. Despite this complexity, the observed changes suggest substantial dysregulation of axon guidance pathways.

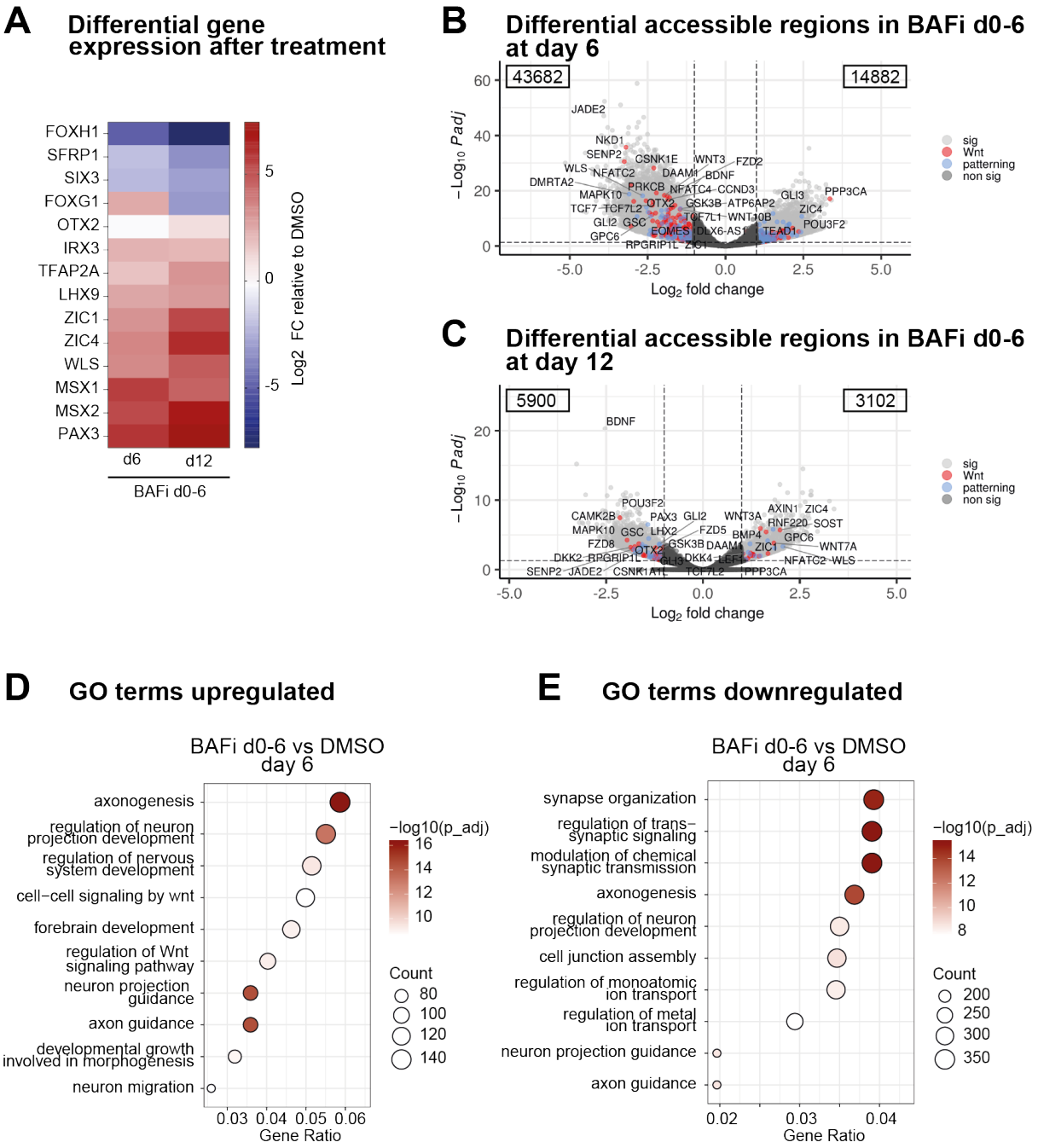

Figure 5.5-1: Early gene expression and chromatin accessibility alterations in BAFi d0-6 samples. *A) Heatmap showing the log2 fold expression change of patterning and cell type-specific marker genes relative to DMSO controls in BAFi d0-6 samples at day 6 (immediately post-treatment) and day 12 (n = 4, bulk RNA-seq). B, C) Volcano plots of differentially accessible regions (bulk ATAC-seq, n = 8) in BAFi d0-6 samples at day 6 (B) and day 12 (C). The x-axis represents log2 fold change (FC) of BAFi d0-6 versus DMSO, and the y-axis shows statistical significance (–log10 adjusted p-value). The numbers in the upper corners of the volcano plots indicate the count of regions with decreased accessibility (left) and increased accessibility (right). Regions associated with patterning-related genes are highlighted in blue, and those linked to WNT signalling are marked in red. Significantly altered regions are shown in light grey, while non-significant regions are marked in dark grey. Selected regions are labelled. D, E) GO term analysis[288] of upregulated (D) and downregulated (E) accessible regions in BAFi d0-6 samples (FDR < 0.01, bulk ATAC-seq, n = 8). The x-axis represents the gene ratio, calculated as the number of genes associated with a given GO term divided by the total number of genes included in the analysis. Gene count = the absolute number of genes from the input dataset associated with a specific GO term, d = day; –log10 padj = logarithmically transformed adjusted p-value; sig = significant; non sig = non-significant.*

In summary, these findings show that BAF complex inhibition during early neurodevelopment disrupts chromatin accessibility in a manner that promotes caudalisation, potentially driven by

alterations in WNT and YAP signalling pathways. The interplay between chromatin dynamics and transcriptional changes underscores the pivotal role of BAF complexes in regulating spatiotemporal gene expression programs critical for forebrain specification.

To gain deeper insight into the interplay between enhancer and repressed chromatin regions and to explore direct BAF complex binding, bulk CUT&Tag-seq[278,279] was performed for H3K27ac (active chromatin regions), H3K27me3 (repressed chromatin regions), and SMARCA4 (BAF complexes) (**Figure 5.5-2**). The results aligned with the ATAC-seq findings, offering a more nuanced view of regulatory region dynamics. At the *FOXH1* locus, reduced H3K27ac and increased H3K27me3 corroborated decreased gene expression observed in RNA-seq (**Figure 5.5-1 A**, **Figure 5.5-2 A**, **B**), suggesting an early caudalisation event. Similarly, *ZIC1 and ZIC4* loci displayed elevated H3K27ac, consistent with their increased accessibility and transcription (**Figure 5.5-1 A**, **B Figure 5.5-2 A**). Regions associated with *YAP1* and *TEAD1* also showed enhanced H3K27ac (**Figure 5.5-2 A**), further implicating YAP signalling in the caudalised phenotype.

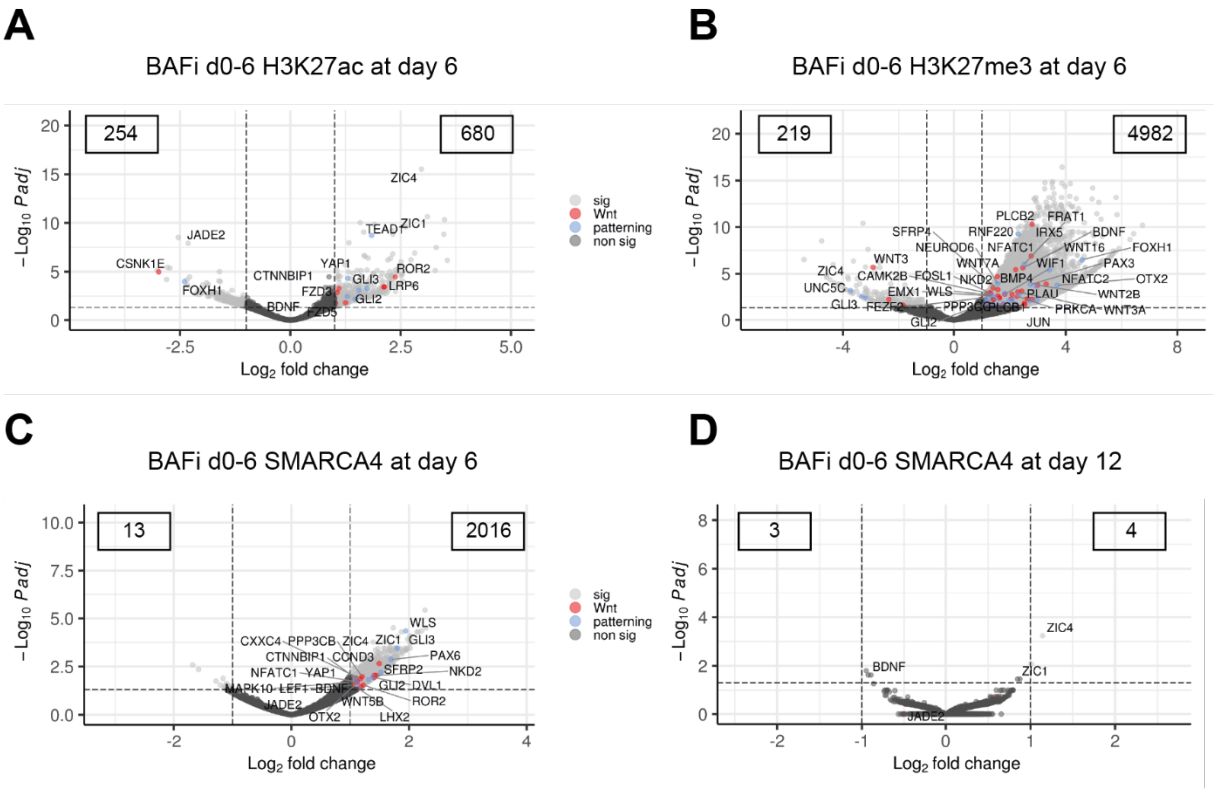

Figure 5.5-2: Early epigenetic alterations in BAFi d0-6 organoids. *A-D) Volcano plots showing differential binding sites for H3K27ac (A), H3K27me3 (B), and SMARCA4 (C) in BAFi d0-6 samples at day 6, and for SMARCA4 at day 12 (D). The x-axis represents the log2 fold change, while the y-axis indicates statistical significance (–log10 adjusted p-value; FDR < 0.01, bulk CUT&Tag-seq, n = 2–3). Regions associated with patterning-related genes are highlighted in blue, and those linked to WNT signalling are shown in red. The numbers in the upper corners of the volcano plots indicate the count of regions with decreased binding (left) and increased binding (right).sig = significant; non sig = non-significant; d = day, –log10 padj, = logarithmically transformed adjusted p-value.*

Interestingly, while inhibitors of the WNT signalling pathway, such as *WIF1*[340,341], *NKD2*[331], and *SFRP4*[342], exhibited increased H3K27me3, *WLS* showed both elevated H3K27me3 and

increased expression, presenting a notable discrepancy (**Figure 5.5-1 A**, **Figure 5.5-2 B**). SMARCA4 enrichment at loci including *WLS*, *ZIC1*, *ZIC4*, *NKD2*, *SENP2*, and *YAP1* in BAFi d0-6 samples suggests that pertubed BAF complexes target these regions (**Figure 5.5-2 C**). This inhibition rendered these complexes incapable of effective nucleosome remodelling. Instead, transcriptional upregulation at loci such as *ZIC1*, *ZIC4*, *WLS*, and *YAP1* may be driven by downstream factors potentially recruited by SMARCA4. A similar pattern was observed for the dorsalising factor GLI3, which displayed increased accessibility and elevated H3K27ac in BAFi d0-6 samples at day 6, coupled with enriched SMARCA4 binding at the same region.

By day 12, SMARCA4 binding largely returned to physiological patterns, with the notable exception of sustained enrichment at ZIC loci (**Figure 5.5-2 D**). However, despite the withdrawal of the inhibitor, differential chromatin accessibility and gene expression persisted. This suggests that a distinct gene regulatory program was initiated during the inhibition period, which continued to drive transcriptional changes even after BAF complexes resumed normal function.

Taken together, these findings demonstrate that BAF complex inhibition disrupts chromatin landscapes at key regulatory regions, leading to transcriptional dysregulation of patterning genes and signalling pathways such as WNT and YAP, which likely drive the caudalised phenotype. This dysregulation is evident at several loci, including the ZIC genes, where increased chromatin accessibility and elevated H3K27ac correlate with transcriptional upregulation, reinforcing their role in this phenotypic shift. Interestingly, SMARCA4 enrichment was observed at multiple loci, including ZIC, in BAFi d0-6 samples, despite the inhibition of its ATPase activity, which prevents effective chromatin remodelling. This raises questions about the functional implications of SMARCA4 binding under these conditions, suggesting it may mark these regions without directly driving transcriptional regulation or contribute indirectly by recruiting downstream factors that enhance transcription at these sites. Potential explanations for this apparent discrepancy will be addressed in the discussion. Overall, these results underscore the pivotal role of BAF complexes in orchestrating spatiotemporal gene expression programs that are critical for forebrain specification and broader neurodevelopmental processes.

In BAFi d6-12 samples, dynamic changes in patterning gene expression were observed over time. Initially, dorsal identity factors such as *GLI3*, *BMP7*, and *BHLHE22* were slightly upregulated, while ventral patterning genes, including *DLX1* and *DLX5*, were also elevated. However, by day 17, this trend reversed, with ventral-associated genes showing decreased expression and dorsal markers becoming more prominent (**Figure 5.5-3 A**). These shifts coincided with evidence of heightened WNT signalling activity. For instance, the WNT signalling inhibitor *SFRP1* was downregulated, while active WNT signalling components, such

as *RSPO3*[297], *IRX3*[32], and *MSX2*[343,344], were upregulated (**Figure 5.5-3 A**). Since WNT signalling exerts both caudalising and dorsalising effects, these alterations suggest a complex dysregulation of patterning processes, favouring a shift towards caudal and dorsal cell fates. This interpretation is further supported by the increased expression of dorsal markers and glutamatergic neuron-associated genes (e.g., *BHLHE22*)[345].

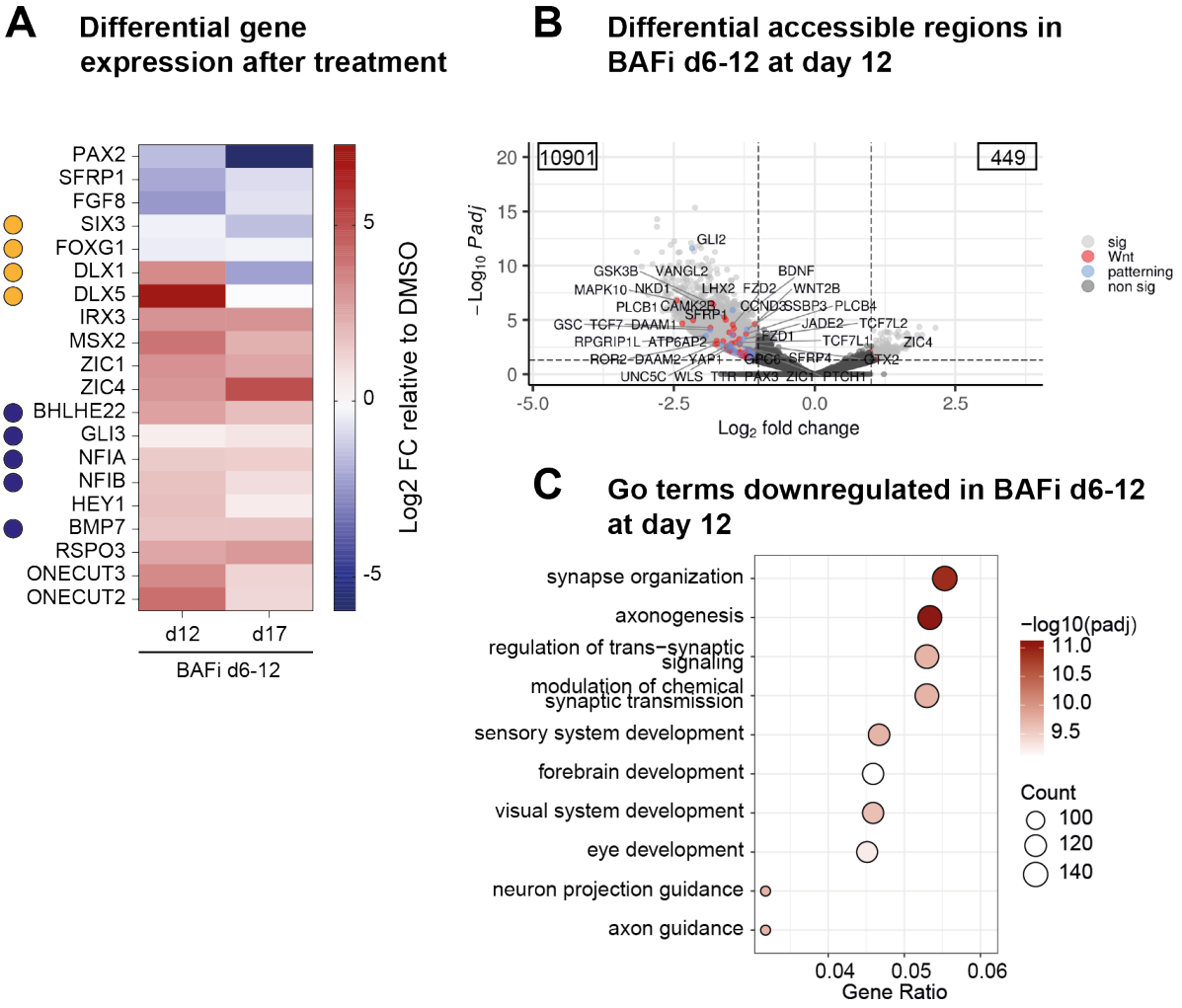

Figure 5.5-3: Early gene expression and chromatin accessibility alterations in BAFi d6-12 samples. *A) Heatmap showing the log2 fold change (FC) expression of patterning and cell type-specific marker genes in BAFi d6-12 samples at day 12 (immediately post-treatment) and day 17 relative to DMSO controls (n = 4, bulk RNA-seq). Yellow circle = Genes associated with ventral telencephalon patterning, blue circle = genes associated with dorsal telencephalon patterning. B) Volcano plot of differentially accessible regions (bulk ATAC-seq, n = 8) in BAFi d6-12 samples at day 12. The x-axis represents log2 fold change, and the y-axis shows statistical significance (–log10 adjusted p-value). Regions associated with patterning-related genes are highlighted in blue, and those linked to WNT signalling are marked in red. Significantly altered regions are shown in light grey, while non-significant regions are marked in dark grey. Genes associated with selected regions are labelled. The numbers in the upper corners of the volcano plots indicate the count of regions with decreased accessibility (left) and increased accessibility (right). C) GO term analysis[288] of downregulated accessible regions in BAFi d6-12 samples (FDR < 0.01, bulk ATAC-seq, n = 8). The x-axis represents the gene ratio, calculated as the number of genes associated with a given GO term divided by the total number of genes included in the analysis. Gene count = the absolute number of genes from the input dataset associated with a specific GO term, d = day, –log10 padj = logarithmically transformed adjusted p-value, sig = significant, non sig = non-significant.*

The chromatin accessibility data at day 12 provide additional insights into these transcriptional changes. Regions associated with key WNT signalling inhibitors, such as *NKD1*[332], *GSK3B*[346], *SFRP1*, and *SFRP4*[342], displayed reduced accessibility, suggesting heightened WNT

signalling activity in BAFi d6-12 samples (**Figure 5.5-3 B**). This observation provides a potential explanation for the transcriptional upregulation of WNT target genes, including *IRX3*[347] and *MSX2*[343,344] (**Figure 5.5-3 A**). Intriguingly, *LHX2*, a pivotal determinant of dorsal telencephalic identity[86], also showed reduced accessibility at this stage. This suggests that dorsal fate commitment in BAFi d6-12 samples was not fully established immediately following treatment, as reflected by the concurrent expression of ventral markers. The increased WNT activity observed early on may have initiated a dorsal gene program, which became more fully established at later stages, such as day 35.

Interestingly, regions associated with non-telencephalic genes, including *WLS*, *YAP1*[315], and *UNC5C*[42,348], were also less accessible at day 12 (**Figure 5.5-3 B**). This finding appears inconsistent with the partial caudalised phenotype of BAFi d6-12 samples but may reflect intermediate stages of patterning that become resolved over time. While the caudalisation in these samples was less pronounced than in BAFi d0-6 samples, a similar pattern of increased accessibility at ZIC loci, particularly *ZIC4*, was observed (**Figure 5.5-3 B**). These findings indicate that ZIC loci generally exhibit higher accessibility and expression under BAF complex perturbation, such as when ATPase activity is inhibited. Although ZIC genes are not direct determinants of caudal fates during early development, their later association with caudal cell types supports the observed caudalisation at day 35.

The impact of BAF complex inhibition extended beyond WNT signalling to include other pathways critical for neurodevelopment. Dysregulation of BMP and NOTCH signalling was evident, with increased expression of the NOTCH effector *HEY1* highlighting the broader disruption of signalling networks (**Figure 5.5-3 A**). GO analysis further revealed that regions with reduced accessibility were enriched for terms related to “forebrain development,” “axonogenesis,” and “axon guidance,” mirroring findings in BAFi d0-6 samples (**Figure 5.5-1 D**, **E**, **Figure 5.5-3 C**). Notably, as most regions with differential accessibility exhibited reduced accessibility, the GO analysis primarily focused on downregulated genomic regions.

These results highlight the profound and lasting effects of BAF complex inhibition during days 6 to 12 of brain organoid development. The disruption of chromatin accessibility and transcriptional regulation at key loci affected signalling pathways, patterning genes, and cell fate determinants. Specifically, reduced accessibility at WNT inhibitors such as *SFRP1* and *SFRP4* likely contributed to the dorsalised and caudalised phenotypes observed at day 35. Additionally, increased accessibility at ZIC loci underscores the involvement of these regions in driving caudal cell fates. Importantly, the observed dysregulation extended beyond WNT signalling to include BMP and NOTCH pathways, as well as processes like forebrain development, axonogenesis, and axon guidance. These findings emphasize that disruption of

BAF complexes during late neurulation initiates a distinct gene regulatory program, leading to long-lasting effects on cell fate and brain region identity.

Altogether, chromatin landscape analysis of BAFi d0-6 and BAFi d6-12 samples using bulk ATAC-seq and CUT&Tag provided insights into the direct effects of BAF complex inhibition. These analyses revealed chromatin dysregulation that influenced transcriptional outcomes, aligning with changes observed at the transcriptional level. Genomic regions associated with WNT and YAP signalling were particularly differentially accessible, likely contributing to the initiation of the caudalising and dorsalising gene programs induced by BAF inhibition. Additionally, conserved differential accessibility at loci such as the ZIC genomic regions across different samples and time points suggests these sites commonly respond to malfunctioning BAF complexes during brain development.

5.6 BAF complexes perturbation in a long-term neurodevelopmental context

As a final step, long-term effects of BAF complex inhibition were analysed to assess its impact on brain organoid development over extended culture periods. Brain organoids were cultured until day 120 and examined for gene expression (via RT-qPCR), morphology, and chromatin accessibility changes. These analyses included BAFi d0-6 and BAFi d6-12 samples, as well as a heterozygous *ARID1B* knockout (KO) hiPSC line. This approach aimed to compare the effects of early and complete BAF inhibition during long-term culture and to evaluate the consequences of mutating a single subunit. Given that heterozygous *ARID1B* mutations are highly prevalent in neurodevelopmental disorders[182,183,186,191,349], this investigation offers clinically relevant insights. However, *ARID1B* mutations can occur at various sites within the gene, primarily through loss-of-function mutations that reduce expression levels. Since the data were derived from a single clone, the general applicability of these results requires further investigation.

5.6.1 Gene programs affected by early BAF complexes inhibition during neurodevelopment cannot be rescued over time

On the morphological level, BAFi d0-6 organoids exhibited a striking reduction in size compared to DMSO controls, while the BAFi d6-12 samples showed an increase in size (**Figure 5.6-1 A**). Regarding gene expression, specific neural subtype markers and patterning genes were examined. Both BAF inhibitor-treated groups displayed a decrease in the progenitor marker *DCX*[350], as well as the mature neuronal marker *SATB2*[351]. However, a slight increase in *SATB2* expression at day 35 and *RBFOX3*[352] at day 66 indicated a modest shift towards earlier maturation in BAFi conditions, although this effect was less pronounced than

at earlier timepoints. This suggests a partial recovery of maturation in these samples over time, though differences compared to DMSO controls persisted (**Figure 5.6-1 B**).

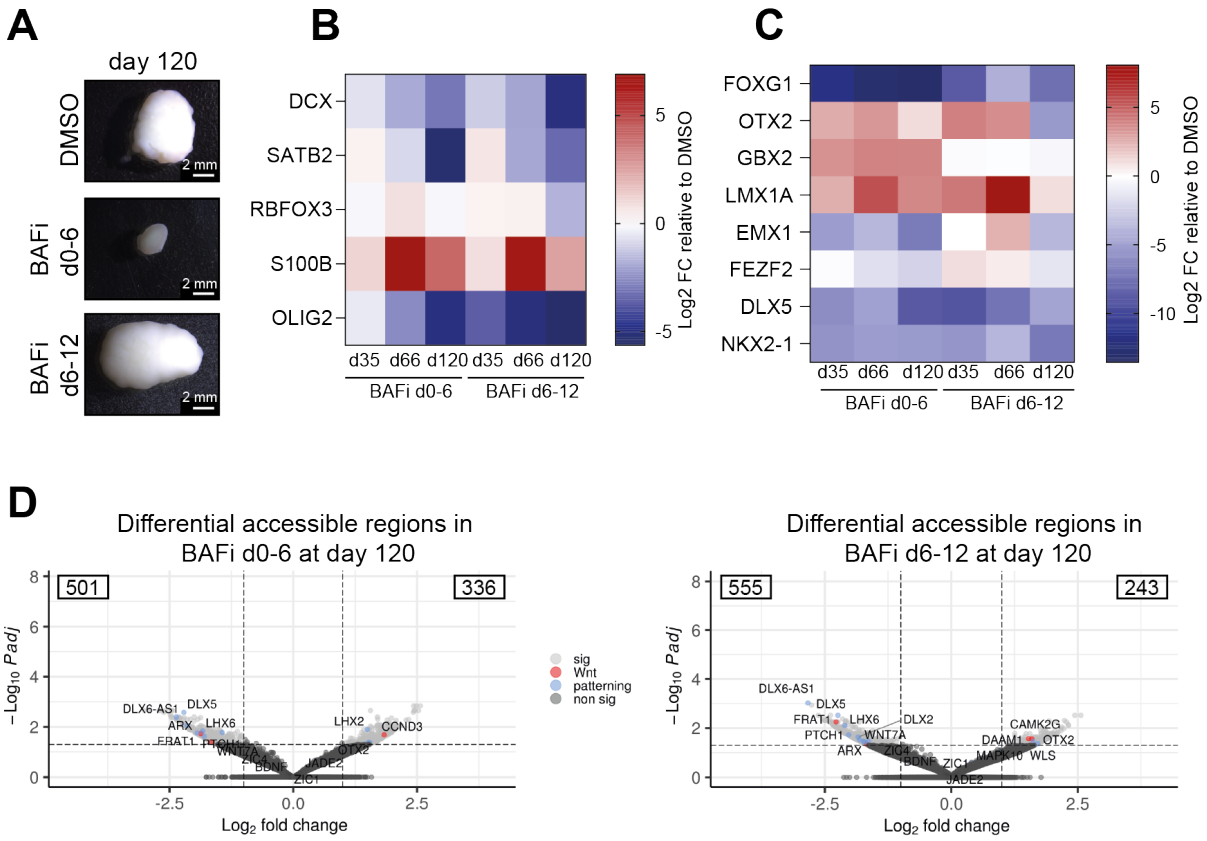

Figure 5.6-1: Gene programs and their associated chromatin landscape in BAFi organoids cannot be rescued over time. *A) Representative images of day 120 old DMSO, BAFi d0-6 and BAFi d6-12 organoids. Images were captured using the stereo microscope M205FA from Leica. B, C) Heatmap showing RT-qPCR-derived log2 fold change (FC) of neural genes (B) and patterning genes (C) in BAFi d0-6 and BAFi d-12 relative to DMSO on days 35, 66, and 120 (n=2). The values were normalized to the housekeeping gene ATP5F1B. d = day. D) Volcano plots showing the differential accessible regions in BAFi d0-6 and BAFid6-12 organoids at day 120 (FDR < 0.01, bulk ATAC-seq, n = 3). The x-axis represents log2 fold change, and the y-axis shows statistical significance (–log10 adjusted p-value). Regions associated with patterning-related genes are highlighted in blue, and those linked to WNT signalling are marked in red. Significantly altered regions are shown in light grey, while non-significant regions are marked in dark grey. Genes associated to selected regions are labelled. The numbers in the upper corners of the volcano plots indicate the count of regions with decreased accessibility (left) and increased accessibility (right).*

On the other hand, some gene expression changes were not rescued over time. Notably, the (pre-) astrocytic marker gene *S100B* was strongly upregulated in both BAF inhibitor-treated groups, particularly at day 66 and still at day 120. In contrast, *OLIG2*, which serves as both an oligodendrocyte marker and a regulator of ventral cell fates, was downregulated, aligning with the dorsalised cell fates observed in BAF inhibitor-treated samples (**Figure 5.6-1 B**).

Persistent patterning differences were also observed, especially along the rostral-caudal axis. Forebrain marker *FOXG1* was downregulated, while caudal markers *OTX2*[353], *LMX1B*[43], and *GBX2*[31] were upregulated. Regarding the dorsal-ventral axis, ventral markers such as *DLX5* and *NKX2-1*[125] remained persistently downregulated. Interestingly, dorsal marker genes were less affected. In BAFi d6-12 samples, a slight increase in dorsal markers was observed at days 35 and 66, but by day 120, these markers showed a decrease in expression. This suggests

that DMSO-treated samples continued generating dorsal cells at later stages (**Figure 7.2-3**), while BAFi d6-12 samples could not compensate for ventral cell fate at these stages (**Figure 5.6-1 C**).

Chromatin accessibility analysis at day 120 revealed few significant differences compared to earlier timepoints, suggesting that BAF complexes resumed their physiological function after inhibitor withdrawal. The observed chromatin changes likely stem from the altered gene programs set in early neurodevelopmental stages, which persisted over time. Specifically, dysregulation of patterning genes was reflected in the chromatin landscape, with minimal changes in WNT signalling-associated regions. In BAFi d0-6 samples at day 120, regions associated with ventral forebrain markers (e.g., *DLX5*[354], *ARX*[314], *LHX6*[355] and the antisense RNA *DLX6-AS1*) were less accessible, while the dorsal determinant *LHX2* and the patterning gene *OTX2* — initially involved in fore- and midbrain specification but later contributing to mid- to hindbrain development[27,321,356,357] — showed increased accessibility, indicating a persistent caudalised and dorsalised phenotype (**Figure 5.6-1 D**).

In BAFi d6-12 samples, similar regions (*DLX5*, *DLX6-AS1*, *ARX*, and *LHX6*) were less accessible, but additionally, the ventral marker *DLX2* showed decreased accessibility. Among the upregulated genes, more caudal markers such as *OTX2* and *WLS* were more accessible, though this slightly contradicts the gene expression results for *OTX2* at day 120 (**Figure 5.6-1 D**). These findings suggest that the patterning gene programs established during early neurodevelopment are difficult to rescue over time, potentially due to the lasting effects of early transcriptional regulation and the gene programs set during these stages.

Taken together, these results showed that early BAF inhibition caused persistent disruptions in brain organoid development. BAFi d0-6 organoids were smaller, while BAFi d6-12 organoids were larger than controls. While progenitor and neuronal marker expression was only mildly affected, patterning defects were persistent. These included reduced rostral and ventral marker expression (e.g., *FOXG1*, *DLX5*) and increased caudal and dorsal markers (e.g., *OTX2*, *LHX2*). Chromatin accessibility changes at day 120 were minimal but reflected lasting alterations in early gene programs, particularly at loci of ventral forebrain marker genes. These findings highlight the critical role of BAF complexes in establishing neurodevelopmental gene programs that are difficult to rescue even after short-term disruption.

5.6.2 ARID1B KO distinctively impacts neurodevelopmental processes

To investigate the effects of ARID1B mutations on long-term brain organoid development, heterozygous ARID1B mutant hiPSCs (HMGU1) were generated using CRISPR/Cas9 technology. Since patients with neurodevelopmental disorders typically exhibit heterozygous loss-of-function mutations, the clones were validated by amplicon sequencing to confirm their

zygosity and identify the exact mutations introduced. One heterozygous clone was further validated at the protein level, showing a significant reduction in ARID1B expression to approximately 38% of the isogenic wild-type (WT) control (**Figure 5.6-2 A**, **B**).

Morphologically, no major differences were observed between the ARID1B mutant and WT brain organoids, except for a more disorganized assembly of neural rosettes at day 17 in the mutant condition (**Figure 5.6-2 C**). This indicates that subtle structural changes may occur during initial stages of neurodevelopment.

At day 120, chromatin accessibility analysis revealed limited differences between ARID1B mutant and WT organoids. However, specific loci associated with genes found to be mutated in neurodevelopmental disorders, such as *LARGE1*[358], *GABRB3*[359,360], and *PACSIN1*[361], exhibited reduced accessibility in ARID1B mutants (**Figure 5.6-2 D**). These genes are linked to conditions including autism, intellectual disability, and schizophrenia, suggesting a potential link between ARID1B dysfunction and these disorders.

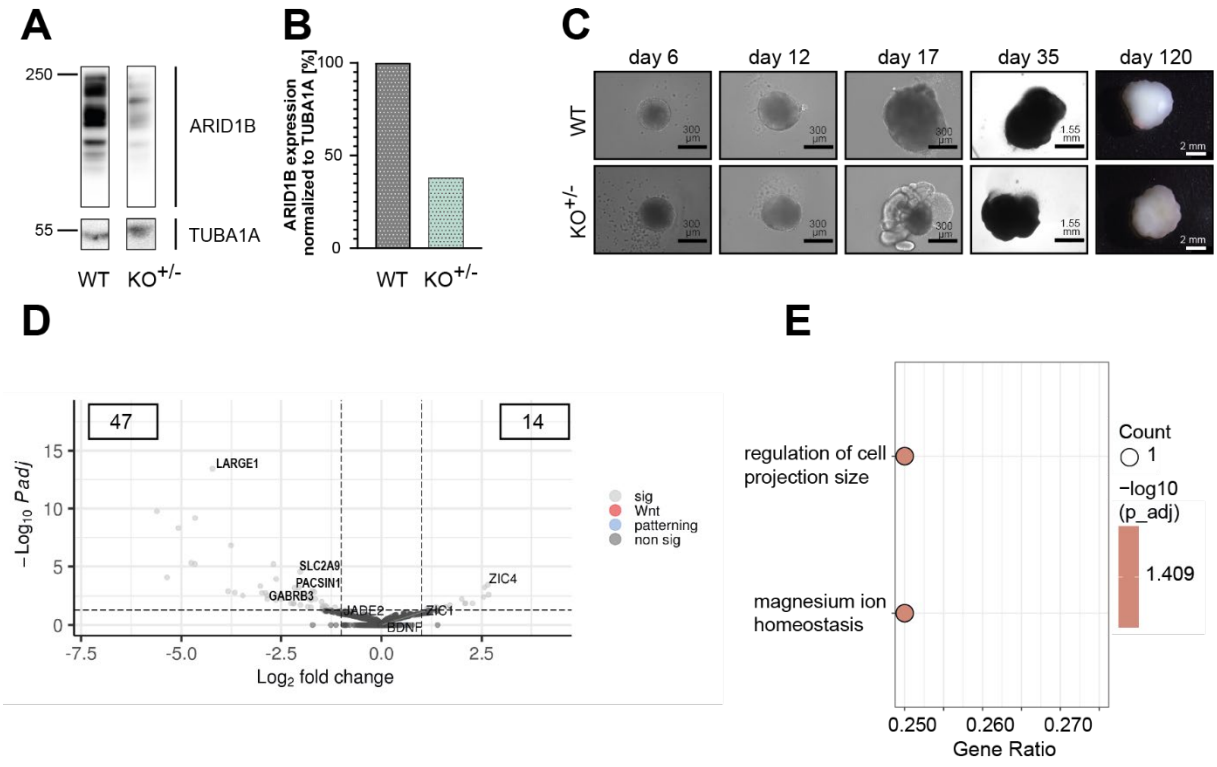

Figure 5.6-2: Heterozygous knock-out of ARID1B leads to subtle changes in morphology and chromatin accessibility. *A) Western blot analysis showing ARID1B expression in heterozygous ARID1B knockout (KO+/–) and isogenic wild-type (WT) hiPSCs. B) Quantification of ARID1B expression from the Western blot, presented as protein levels normalized to TUBA1A. C) Representative images of WT and KO+/– organoids at days 6, 12, 17, 35, and 120, captured using a Leica M205FA stereo microscope. D) Volcano plot of differential accessible regions in KO+/– organoids relative to WT at day 120 (bulk ATAC-seq, n = 3). The x-axis represents log2 fold change, and the y-axis indicates statistical significance (–log10 adjusted p-value). Regions associated with patterning-related genes are highlighted in blue, and those linked to WNT signalling in red. Significantly altered regions are shown in light grey, and non-significant regions are marked in dark grey. Genes associated to selected regions are labelled. The numbers in the upper corners of the volcano plots indicate the count of regions with decreased accessibility (left) and increased accessibility (right). E) GO term analysis [288] of regions gaining accessibility in KO+/– organoids (FDR < 0.01, bulk ATAC-seq, n = 3). d = day, –log10 padj = logarithmically transformed adjusted p-value, sig = significant, non sig = non-significant.*

Increased chromatin accessibility was observed at the *ZIC1* and *ZIC4* loci, consistent with findings from BAFi d0-6 and BAFi d6-12 samples, which also showed heightened accessibility at these sites during early developmental stages (e.g., days 6 and 12). This parallel suggests that gain in accessibility at *ZIC1* and *ZIC4* loci are probably conserved responses to dysfunctional BAF complexes, both under ATPase inhibition and in the presence of heterozygous *ARID1B* mutation (**Figure 5.5-1 B**, **C**, **Figure 5.5-3 B**, **Figure 5.6-2 D**).

As relatively few genomic loci were affected by the ARID1B mutation at day 120, the GO analysis of differentially accessible loci provided limited insights. However, one notable finding was the enrichment of the term “regulation of cell projection size”, suggesting that ARID1B mutation may influence aspects of cellular morphology (**Figure 5.6-2 E**).

These results indicate that the ARID1B mutation exerts minimal influence on brain organoid morphology and chromatin accessibility at later developmental stages. However, the genomic loci affected are directly associated with neurodevelopmental diseases, underscoring the role of BAF complex dysfunction in disrupting key neurodevelopmental gene networks. The consistent increase in accessibility at *ZIC1* and *ZIC4* loci across experimental conditions underscores their significance as important downstream effects of various BAF complex perturbations.

Future studies should focus on earlier neurodevelopmental stages, such as neurulation, to better capture the initial effects of ARID1B mutations on chromatin accessibility and gene regulation. Additionally, comprehensive gene expression analyses at both early and late developmental stages could provide deeper insights into the downstream effects of ARID1B dysfunction on cell type specification and brain patterning. These findings would contribute to a broader understanding of the clinical relevance of BAF complex mutations, their disrupted pathways, and the resulting phenotypic outcomes. Comparative studies of mutations in other ARID subunits — each associated with distinct neurodevelopmental disorders — may further elucidate the diverse roles of BAF complexes in brain development, a topic that warrants investigation in the near future.

6 Discussion

The chromatin remodelling activity of BAF complexes is essential for various cellular processes, as homozygous loss of specific subunits (e.g., ARID1A, SMARCA4)[152,362] is embryonic lethal. Furthermore, mutations in BAF complex subunits are frequently linked to neurodevelopmental disorders, including ASD, schizophrenia, CSS, NCBRS, and ID[172–175,363], emphasizing their crucial role in neurodevelopment.

This study aimed to identify the neurodevelopmental stages involving BAF complexes, uncover the molecular mechanisms by which they regulate early human brain development in a stage-dependent manner, and evaluate the clinical implications of BAF complex perturbation. The following discussion will first address morphological changes resulting from inhibition of the activity of BAF complexes by BRM014 (BAFi), followed by an in-depth focus on the molecular mechanisms underlying the observed phenotypes in samples treated during neurulation and the onset of neurogenesis (BAFi d0-6, BAFi d6-12). Finally, the clinical relevance of the findings will be explored, with a particular emphasis on differences between organoids derived from heterozygous ARID1B mutations and those treated with BRM014.

6.1 Perturbation of BAF complexes during brain organoid development affects morphology

Although brain organoids do not fully replicate brain structure, perturbations in BAF complexes can still reveal molecular and cellular alterations in the developing nervous system, often recapitulating phenotypes such as microcephaly[212]. To explore this, BAF-perturbed organoids were investigated over time.

Microscopy-based monitoring of brain organoid development under BAF complex inhibition revealed neurodevelopmental stage-dependent morphological changes. Early treatment from days 0 to 6 (BAFi d0–6) caused a marked reduction or complete loss of neural rosettes, accompanied by the emergence of highly divergent outgrowths. Organoids treated during this period remained smaller at later stages (day 120). In contrast, treatment from days 6 to 12 (BAFi d6–12) resulted in enlarged neural rosettes and pronounced overgrowth by day 120. Treatments at later stages, such as days 12 to 17 (BAFi d12–17) or 17 to 35 (BAFi d17–35), disrupted neural rosette structures, often leading to small rosettes with reduced lumens by day 35. Notably, organoids derived from hiPSC treatment (BAFi d-1-0) and heterozygous *ARID1B* knockout cells maintained overall sizes similar to DMSO controls. However, when analysing these morphological changes, several important factors must be considered. For instance, cell loss due to increased cell death or changes in size driven by an expanded progenitor pool can influence organoid morphology. Organoids at later stages may have enlarged rosettes with larger lumens, which differ structurally from organoids of the same size with denser cells and

smaller rosettes. Additionally, shifts in cell type commitment can generate distinct cell types with varying morphologies, further influencing the overall structure of the organoid. These factors, which are not all directly visible in microscopy-based monitoring, will be considered when evaluating the bulk and single-cell transcriptomic data, offering a more comprehensive understanding of the morphological alterations.

The observed morphological phenotypes in BAF-perturbed organoids, as revealed by microscopy monitoring, partially align with brain malformations linked to BAF complex subunit mutations in patients, including CSS, NCBRS, ASD and schizophrenia. Conditions like CSS and NCBRS frequently involve microcephaly, corpus callosum agenesis, and cerebellar abnormalities[182,185,364,365], though CSS can occasionally be associated with macrocephaly[349]. ASD can arise from mutations in a wide array of risk genes, and this genetic diversity is reflected in the complexity and variability of associated brain malformations. Notably, while brain size at birth is typically normal in ASD patients, later stages often show regional overgrowth, cortical thinning, and enlarged ganglionic eminences, particularly in individuals with *ARID1B* mutations[177,366]. Schizophrenia, in contrast, is characterized by progressive ventricular enlargement, a dynamic phenotype rather than a fixed developmental feature[367].

Insights from mouse models further elucidate the impact of BAF complex subunit loss on neurodevelopment. For instance, homozygous conditional knockout of *SMARCA4* in the developing murine cerebral cortex results in cortical dysplasia, cobblestone lissencephaly, and periventricular heterotopia[368], while a homozygous double conditional knockout of *SMARCC1* and *SMARCC2* in the ventricular zone similarly disrupts cortical development by impairing radial neuron migration and truncating leading processes, ultimately resulting in defective cortical lamination[369]. Correspondingly, heterozygous *ARID1B* knockout mice show underdeveloped corpus callosum, reduced cortical thickness, and a smaller dentate gyrus[370].

When contextualizing these findings with the organoid phenotypes, both similarities and discrepancies emerge in comparison to mouse models and patient data. For example, the smaller organoid size observed in BRM014-treated samples during the early developmental window (d0–6) reflects microcephaly phenotypes reported in CSS and NCBRS patients, as well as cortical thinning in mouse models with homozygous *SMARCA4* or heterozygous *ARID1B* knockout. The loss of neural rosettes and emergence of divergent outgrowths may indicate a shift towards the formation of neural crest cells, supported by increased neural crest marker expression, morphological similarities to neural crest cells, and the presence of a small mesenchymal population in the Multiome data set. This aligns with reports that neural crest cells form prior and at the expense of neural rosettes[371,372]. Conversely, treatments at later stages (d12–17 and d17–35) likely disrupted established neural rosettes and progenitor commitment, resulting in smaller, disorganized structures. These phenotypes, in turn,

resemble organoid models derived from schizophrenia patients, which also exhibit smaller neural rosettes with reduced lumens[373]. Enlarged neural rosettes in BAFi d6–12-treated organoids suggest precocious maturation, possibly from rosette fusion during development[315]. This differs from schizophrenia-related ventricular enlargement, which progressively emerges postnatally instead of during the early developmental phases[367]. The overgrowth observed at day 120 in these samples only partially reflects the brain regional overgrowth seen in ASD, which typically manifests 2–4 years postnatally[366]. Intriguingly, a study of ASD patient-derived brain organoids found a correlation between organoid size and the severity of social symptoms[374], further underscoring the complexity of interpreting organoid phenotypes.

The timing and genetic context of BAF complex perturbation are critical to understanding these morphological changes. Morphological disruptions in BRM014-treated organoids highlight the stage-specific roles of BAF complexes in regulating neural rosette formation, growth, and structural organization. Moreover, the severity and nature of these phenotypes are influenced by both the genetic background and the specific perturbations of BAF-coding genes. While complete loss of BAF complexes is embryonically lethal, heterozygous mutations in specific subunits, such as *ARID1B*, produce distinct outcomes. The differences between BRM014-treated organoids and those derived from heterozygous *ARID1B* knockout cells emphasize the unique effects of subunit-specific disruptions. The comparatively milder phenotypes seen in heterozygous *ARID1B* knockout organoids may contribute to the ability of affected individuals to develop into functional organisms.

Although brain organoids provide a powerful tool for modelling early brain development in a human genetic context, addressing gaps left by mouse models, their limitations must also be acknowledged, particularly in terms of morphology. In fact, brain organoids cannot replicate the full complexity of *in vivo* brain morphology or the postnatal developmental changes observed in patients. For example, while CSS malformations are evident both postnatally[364] and in fetal studies[375], conditions like ASD and schizophrenia primarily manifest after birth[366,367]. Discrepancies between patient data and brain organoid models, such as the ventricular enlargement seen in schizophrenia patients versus the smaller ventricles in organoids[373], may reflect postnatal onset or a lack of embryonic developmental data. Nevertheless, brain organoids excel at elucidating molecular changes in early development, which may influence cell type specification and contribute to postnatal phenotypes.

In conclusion, these findings highlight the critical role of BAF complexes in early brain development, revealing stage-specific and perturbation-specific disruptions that influence organoid morphology. While brain organoids offer valuable insights into early neurodevelopment, challenges remain in translating findings into human brain malformations or overall brain morphology. Nonetheless, this model system remains a powerful tool for

unravelling the molecular basis of neurodevelopmental disorders. The observed morphological alterations in this study likely arise from underlying changes in molecular mechanisms, such as cell type specification and brain patterning processes, which will be further explored in the following section.

6.2 BAF complexes regulate stage-specific neurodevelopmental gene programs

To elucidate the molecular mechanisms underlying the observed morphological changes, a variety of omics approaches was employed. As an initial step, bulk RNA-seq was performed on organoids treated with BRM014 at distinct developmental timeframes.

The RNA-seq data revealed the critical role of BAF complexes in neurodevelopment, particularly during the early stages of differentiation and neural specification. PCA highlighted a progressive gene expression trajectory under DMSO treatment, indicative of normal differentiation. This trend was largely mirrored in BRM014-treated samples, although early-stage inhibition of BAF complexes (BAFi d0-6) disrupted this trajectory by inducing precocious expression patterns. By day 35, gene expression in these samples converged with DMSO controls, suggesting potential compensatory mechanisms that mitigate the overall effects of early disruption. This convergence observed in bulk RNA-seq analysis may reflect the averaging of cellular responses, whereas Multiome data, which preserves individual cellular heterogeneity, revealed distinct phenotypic patterns at day 35 in BAFi-treated samples that are not fully captured by bulk analysis. However, the heightened sensitivity of early neurodevelopmental stages to BAF complex inhibition was evident, as BAFi d0-6 and d6-12 samples exhibited the highest DEG counts and phenotypic alterations.

The premature transition of these two early-stage inhibitions (BAFi d0-6 and BAFi d6-12) is underscored by the observed expression of premature differentiation markers, such as NPC markers (e.g., *PAX6, DCX*), immature neuron markers (e.g., *NEUROD1, MAP2*), and mature neuron and glial markers (e.g., *SLC17A6, S100B*). This highlights the essential role of BAF complexes in coordinating the timing of differentiation and maintaining proper developmental progression. The role of BAF complexes in regulating pluripotency and the switch to differentiation states provides a plausible explanation for these findings. For instance, the BAF complex subunits ARID1A and ARID1B have been implicated in this regulation[376–378], as has SMARCB1, which specifically governs the transition of neuroepithelial cells to neural stem cells and subsequent differentiation[379]. In contrast, later-stage inhibition (BAFi d12-17, BAFi d17-35) exhibited a more limited impact, characterized by fewer DEGs and a more rapid recovery, suggesting greater resilience at advanced stages of neurogenesis. This difference may be

attributed to the establishment of a robust progenitor pool by later stages, coupled with the transient nature of BAF complex inhibition, allowing recovery and continuation of differentiation processes.

While most studies investigating the role of BAF complexes in neurodevelopment rely on either mouse or patient-/mutant-derived hiPSCs models, these approaches have limitations in capturing stage-specific dynamics. Mouse models, where individual BAF complex subunits are deleted in neural progenitors or defined cell types[147,158,164,167,380], primarily reflect early-stage or cell type-specific disruptions. In contrast, differentiation of patient- or mutant-derived hiPSCs capture the effects of constant, clinically relevant BAF complex perturbation but lack temporal resolution[176–178,378,381]. Consequently, the stage-specific roles of BAF complexes in neurodevelopment remain understudied. The resilience observed during later-stage inhibition might highlight differences between transient disruptions and continuous loss of BAF complex function, emphasizing the importance of timing in understanding their role in neurodevelopmental processes.

Interestingly, shared DEGs across samples and time points revealed the presence of BAF complex-dependent targets independent of developmental stage. Many of these genes are involved in key neurodevelopmental pathways, particularly WNT and NOTCH signalling. For example, WNT-related genes such as *SFRP1* (downregulated) and *LEF1* (upregulated) suggest altered WNT pathway activity, which may impact cell fate decision and brain patterning processes given the critical role of WNT signalling in these processes[30,76,77,329,382,383]. Similarly, NOTCH-related genes, including the downregulation of *NOTCH1*, emphasize the potential disruption of progenitor maintenance and differentiation timing[103,326,384,385]. GO term enrichment analyses further reinforced the central role of these pathways in processes like cell fate determination, brain regionalization, and axonal development.

The comparison between BAFi d0-6 and BAFi d6-12 revealed both overlapping and distinct effects. Early-stage inhibition (d0-6) resulted in pronounced gene expression alterations, with precocious developmental programs evident in PCA analyses and GO terms highlighting the dysregulation of WNT signalling alongside forebrain development and patterning processes directly after the treatment (day 6). In contrast, BAFi d6-12 samples, while still affected, displayed a more attenuated response by day 12. Notably, the upregulation of genes related to neuronal differentiation (e.g., *VCAN*, *ONECUT3*) and GO terms associated with axon development and guidance suggests a premature progression toward differentiation, potentially linked to the observed dysregulation of chromatin accessibility-related processes. These findings underscore that both BAFi d0-6 and BAFi d6-12 are significantly affected in

their neurodevelopmental processes, albeit in distinct ways, with each exhibiting unique disruptions in gene expression and developmental pathways.

BAF complex inhibition at different developmental stages revealed both shared and distinct effects on gene expression. Some genes, including those involved in NOTCH and WNT signalling, were consistently altered, suggesting they may be BAF-specific targets independent of the treatment timeframe. Notably, BAF complexes have been shown to interact with components of these pathways. For instance, SMARCA2 interacts with factors in the NOTCH pathway to prevent the dedifferentiation of intermediate progenitors into neuroblasts in *Drosophila*[386], while SMARCD1 reduces the expression of *NOTCH1* and its targets *HES1* and *HEY1* in mammals[387]. Additionally, ARID1B has been shown to repress WNT/β-catenin signalling[388]. Despite these shared gene and pathway alterations, the outcomes differed between samples. This can be attributed to the dynamic nature of neurodevelopment, where gene programs, signalling pathways, and the chromatin landscape change over time. Consequently, BAF inhibition affecting the same targets results in varying outcomes depending on the developmental stage. This holds true for NOTCH signalling, which is crucial for neural progenitor maintenance early in development but shifts its role later on to promote glial cell fate[103,104]. Similarly, WNT signalling, which is involved in both rostrocaudal and dorsoventral patterning, exhibits a bimodal role as development progresses[13,30,76,82]. Additionally, as gene programs change during differentiation, BAF complexes are directed to distinct genomic regions, increasing the complexity of their function and contributing to the distinct outcomes observed at different developmental stages. Another consideration is that BAF complex targets may differ between distinct neural cell types, as shown in several mouse model studies. While bulk RNA-seq provides insights into overall gene expression changes, it does not offer information on cell-type distribution and how these are affected by BAF complex inhibition.

In conclusion, these findings highlight the essential role of BAF complexes at distinct neurodevelopmental stages, where they dynamically regulate the activation of specific gene programs. Although several affected genes and signalling pathways were shared across samples, the outcomes differed, with the highest sensitivity to BAF complex disruption observed at earlier neurodevelopmental stages. In contrast, brain organoids exposed to the inhibitor at later stages of neurodevelopment (BAFi d12-17, BAFi d17-35) demonstrated a less pronounced response, suggesting decreased susceptibility to BAF complex perturbation during these periods. While these findings provide valuable insights into the affected processes, they do not fully address the role of BAF complexes in cell type distribution and specification. This aspect will be further explored in the following section.

6.3 BAF complexes ensure cell type specification and brain patterning processes

To investigate how BAF complex inhibition at early neurodevelopmental stages influences cellular distribution and cell type specification, single-nuclei RNA-seq coupled with ATAC-seq was performed, enabling the correlation of gene expression with chromatin accessibility at the single-cell level in DMSO, BAFi d0-6, and BAFi d6-12 samples at day 35. Additionally, bulk ATAC-seq and CUT&Tag-seq were employed at days 6 and 12, immediately following BAF inhibitor treatment, to examine how chromatin landscape changes affect neurodevelopmental processes, ultimately leading to the phenotypes observed at day 35.

The observed differences in cell type composition between DMSO-treated and BAFi-treated organoids underscore the critical role of BAF complexes in orchestrating cell fate commitment. While the comparable distributions of radial glia and neurons in DMSO control and BAFi d0-6 samples suggest that the overall balance of progenitors and neurons remains largely unaffected by BAF complex inhibition from days 0 to 6, subtle variations in less prevalent cell subtypes point to lineage specification disruptions. For example, the increased presence of OPCs and pre-astrocytic markers in BAFi d0-6 samples indicates a potential alteration in glial lineage trajectories. Notably, as these changes in glial marker expression were subtle and did not localize to a specific cluster in the UMAP, the cells expressing these genes likely represent intermediate states rather than committed lineages. Additionally, BAFi d6–12 samples exhibited an increased population of NPCs and a reduced proportion of neuronal cell types compared to both DMSO controls and BAFi d0–6 samples. This imbalance may account for the overall larger size of BAFi d6–12 samples, as NPCs possess a higher proliferative capacity. Moreover, altered cell type distribution was particularly evident in the ratio shift of excitatory to inhibitory neurons, with both BAFi-treated organoids showing a higher proportion of excitatory neurons and a notable depletion of inhibitory neurons compared to the DMSO control. The higher proportion of non-telencephalic excitatory neurons in BAFi d0-6 samples compared to both BAFi d6-12 and DMSO control further indicates that late-stage inhibition primarily affects differentiation and fate specification, while early inhibition disrupts foundational patterning processes.

These findings align with observations from other studies. For instance, heterozygous *ARID1B* knockout hiPSC-derived brain organoids exhibited early OPC marker expression, driven by an increased proportion of ventral radial glia with higher transition probabilities to OPCs over inhibitory neurons[177]. While these results share similarities with BAFi-treated samples, particularly in the reduction of inhibitory neuron populations, the underlying causes in BAFi-treated conditions are likely distinct. This divergence stems from evidence showing that lineage

specification is differentially affected by distinct forms of BAF complex perturbation. For instance, BAFi-treated samples exhibited a pronounced reduction in ventral-specific marker genes, suggesting that an increased ventral radial glia population is unlikely in this context. Moreover, SMARCA4-containing BAF complexes are known to be recruited by OLIG2, a transcription factor critical for oligodendrocyte lineage specification, to activate oligodendrocyte-specific enhancers and facilitate lineage commitment[164]. In turn, neural progenitors lacking SMARCA4 fail to differentiate into OPCs[158]. Similarly double knockout of *SMARCC1* and *SMARCC2* in telencephalic progenitor cells resulted in perturbed oligodendrogenesis[389]. Given that BRM014 inhibits the ATPase activity of SMARCA2 and SMARCA4, it is plausible that recruitment of OLIG2 to enhancer regions remains intact, but the inability of BAF complexes to perform chromatin remodelling impairs proper OPC differentiation. In contrast, specific subunit knockouts, such as *BCL7A* and *BCL7B*, produced distinct outcomes: *BCL7A* knockout led to an increase in astrocytic populations, while *BCL7B* knockout resulted in elevated oligodendrocyte numbers[390]. Collectively, these findings illustrate that gliogenesis depends on BAF complexes, with individual subunits playing distinct roles. For example, *ARID1B* or *BCL7A*/*B* knockouts increased glial populations, while SMARCA4 loss or the loss of the whole BAF complexes by *SMARCC1* and *SMARCC2* knockout, diminished OPC numbers, indicating SMARCA4's essential role in glial commitment. These samples also showed significant caudalisation. Interestingly, analysis of first-trimester human embryonic brains revealed that pre-astrocytes and pre-oligodendrocytes emerge earlier in caudal brain regions, by pcw 8 in the hindbrain and pcw 9 in the midbrain, while the forebrain generates these cell types later, around pcw 11[42]. The increased expression of glial-specific marker genes in BAFi d0-6 samples may therefore reflect the higher proportion of caudal progenitor cells, linking these changes to altered brain patterning upon BAF complex inhibition.

6.3.1 Early BAF complex inhibition drives caudalisation and alters cell fate commitment

Further supporting this hypothesis, cell type annotations incorporating brain region identity markers revealed a pronounced caudalisation of cell fate in BAFi d0-6 samples. The increased representation of mesencephalic and rhombencephalic NPCs, coupled with a reduced proportion of telencephalic NPCs, underscores the disruption of forebrain-specific developmental programs.

The molecular changes underlying shifts in cell fate and regional identity in BAFi d0-6 samples can be attributed to dysregulation of key transcription factors and signalling pathways. Notably, *FOXG1*, a critical forebrain marker, exhibited significant downregulation by day 35, coinciding with chromatin inaccessibility at its locus. While *FOXG1* was initially slightly upregulated post-

treatment, pronounced downregulation occurred from day 12 onwards. This temporal pattern suggests that BAF complex inhibition primarily disrupts upstream regulators of early patterning, such as WNT and YAP signalling pathways, which may drive the strong downregulation of forebrain identity genes like *FOXG1*, rather than directly targeting these genes. Supporting this, increased expression and chromatin accessibility of WNT-related genes, including *WLS*, *TCF7L2*, and *PAX3*, were observed, identifying these factors as central regulators in the gene regulatory network (GRN) of BAFi d0-6 samples by day 35.

The observed caudalisation phenotype aligns with the established role of WNT signalling in promoting caudal neural identities during early development[30–32]. Elevated expression of caudal markers such as *UNC5C* and *GBX2*, along with decreased expression of forebrain markers, underscores a disrupted balance in regional identity. Furthermore, the enrichment of axon guidance genes, including *SLIT2* and *ROBO1*, within the GRN at day 35 indicates that, in addition to altered patterning, neural circuit formation may also be impaired.

To dissect the mechanisms driving these changes, a detailed epigenetic landscape of BAFi-treated cells was analysed by using ATAC-seq and CUT&Tag-seq and compared to the gene expression alterations. By day 6, gene expression data indicated a shift towards caudal and dorsal identities, evidenced by upregulation of markers such as *WLS* and *IRX3* and downregulation of forebrain markers, including *SIX3*, *FOXH1*, and *SFRP1*. For instance, *FOXH1*, one of the earliest forebrain markers, was downregulated by day 6, correlating with decreased H3K27ac (an active mark) and increased H3K27me3 (a silencing mark) at its locus. Interestingly, no SMARCA4 binding to *FOXH1* was detected in the DMSO controls, nor was it identified among the differentially bound sites for SMARCA4 in BAFi-treated samples. This observation suggests that the downregulation of *FOXH1* may result from indirect consequences of BAF complex inhibition rather than through direct chromatin remodelling at its locus.

Chromatin accessibility changes did not always correspond directly to gene expression patterns, highlighting the complexity of epigenetic regulation and potentially reflecting the prolonged inhibitor treatment over several days. For example, increased *WLS* expression at day 6 coincided with reduced chromatin accessibility at a distal enhancer but increased accessibility at intronic regions, suggesting the involvement of compensatory mechanisms or indicating that the intronic regions might exhibit stronger regulatory influence. By day 12, chromatin regions associated with *WLS* became more accessible, aligning with its elevated expression and underscoring the dynamic role of chromatin remodelling in gene regulation over time.

Further analysis of WNT pathway-related loci, including the WNT inhibitor *NKD1* and *SENP2*, revealed reduced chromatin accessibility in BAFi d0-6 samples, indicating a role for BAF complexes in regulating WNT signalling. Dysregulation of YAP signalling was also evident, with increased chromatin accessibility at *TEAD1* and elevated H3K27ac at *YAP1*. Notably, chromatin at dorsal and caudal brain region associated genes, such as *ZIC1* and *ZIC4*, exhibited consistently increased accessibility and expression. These loci showed decreased H3K27me3 and increased H3K27ac. This suggests that BAF complex inhibition promotes a dorsalised and caudalised fate by reshaping chromatin accessibility at key patterning loci, thereby altering the chromatin landscape and the expression of associated genes.

Despite the inhibition of ATPase activity by BRM014, SMARCA4 binding persisted at several loci, including *WLS* and *ZIC* genes. This suggests that BAF complexes may still be recruited but are unable to execute chromatin remodelling, prompting inquiries into SMARCA4's role in marking regions for transcriptional activation or repression in the absence of remodelling.Taking the ZIC loci as an example, one possibility is that other chromatin remodellers or transcription factors maintain or enhance chromatin openness in the absence of BAF activity as a compensatory mechanism. Alternatively, SMARCA4 may persist at these loci as part of a stalled complex or perform non-canonical roles, such as recruiting histone-modifying enzymes or facilitating transcription factor binding. These potential mechanisms could explain the observed alterations in histone modifications, such as the reduction in H3K27me3 and the increase in H3K27ac, potentially driving the upregulation of *ZIC1* and *ZIC4*.

By day 120, profound morphological and molecular alterations were observable. The reduction in organoid size reflects impaired neurodevelopment during a critical phase of progenitor expansion and patterning. Gene expression analysis revealed consistent downregulation of the progenitor marker *DCX* and the neuronal marker *SATB2*, suggesting broad impairment of neurogenesis and maturation. Although some modest recovery in *SATB2* and *RBFOX3* expression was observed at later timepoints, the persistence of differences compared to controls indicates that these early disruptions were only partially reversible.

The upregulation of the astrocytic marker *S100B* and downregulation of the ventral marker *OLIG2* further highlight the dysregulated lineage specification. This is consistent with the dorsalised and caudalised phenotypes, as *OLIG2* plays dual roles in promoting ventral and oligodendrocytic fates. The observed downregulation of forebrain markers such as *FOXG1* and upregulation of caudal markers, including *OTX2* and *GBX2*, strongly support a shift toward caudalised cell fates that were maintained over time.

Chromatin accessibility data at day 120 reinforce the persistence of these early gene program disruptions. Reduced accessibility at ventral marker loci, such as *DLX5*, *ARX*, *LHX6*, and

DLX6-AS1, underscores the enduring repression of ventral forebrain programs, while increased accessibility at *LHX2* and *OTX2* reflects a shift toward dorsal and caudal fates. Importantly, these chromatin changes likely reflect the early gene regulatory alterations established during BAFi d0-6 treatment, which were maintained over time until day 120, as overall changes in chromatin accessibility were minimal at later stages. This suggests that the transcriptional disruptions set during the initial stages of neurodevelopment were sufficient to drive the long-term phenotypes observed in these organoids.

A recent study reported a similar caudalisation phenotype associated with SMARCA4 degradation throughout the differentiation process of human embryonic stem cells (hESCs) into NPCs[179]. Their findings showed an increased proportion of NPCs with caudal signatures attributed to mid- and hindbrain regions, as well as more dorsal telencephalic populations. Additionally, key genes dysregulated in SMARCA4-degraded NPCs, such as *PAX3* or *ZIC1*, and a higher abundance of neural crest cells were noted[179]. These observations align with the phenotype of BAFi d0-6 samples, which exhibited a higher proportion of caudal NPCs by day 35 and increased expression of genes involved in neural crest development. While BAFi d0-6 samples showed upregulation of neural crest-associated genes, such as *ETS1*, *TWIST1*, and *TWIST2*, no distinct neural crest cell cluster marked by *SOX10* expression was identified by day 35. Interestingly, the expression of these neural crest-related genes delineated a cluster in the UMAP that partially overlapped with the mesenchymal cell population. This suggests that neural crest-like cells might have contributed to mesenchymal subpopulations within the organoids rather than forming a distinct neural crest cluster. The absence of *SOX10*-positive cells might be due to several factors. In mouse models, SMARCA4 is known to regulate *SOX10* expression during early oligodendrocyte precursor cell (OPC) differentiation, while its role diminishes at later stages[164,391]. Similarly, in the context of neural crest cells, *SOX10* expression could depend on SMARCA4 activity during initial formation but may be lost under the conditions used in this study. Moreover, technical limitations, such as Matrigel degradation over time and physical forces from orbital shaking, could have further reduced the presence of migratory neural crest cells. Additionally, *SOX10* is not exclusive to neural crest cells and plays a key role in oligodendrocyte maturation via OLIG2 activity[392]. Another notable discrepancy lies in the dorsalised phenotype reported in differentiated SMARCA4-degraded hESCs, which slightly differs from the findings observed in BAFi d0-6 samples. This phenotype was instead more pronounced in BAFi d6-12 samples, highlighting potential differences in the timing and context of BAF complex disruption. These findings suggest distinct roles for BAF complexes at different stages of neurodevelopment, a topic further explored in the following section.

In contrast to the 2D culture system used in the SMARCA4 study, which investigated a single developmental timeframe in NPCs, this study utilized brain organoids and examined multiple

developmental stages. The organoid model provides additional spatiotemporal resolution, enabling insights into how BAF complex perturbations affect neurodevelopmental processes over time and within a three-dimensional tissue context. These results suggest that while SMARCA4 plays a conserved role in regulating caudalisation and neural crest gene programs, the distinct culture systems and developmental timing have to be considered, as they influence the observed phenotypes.

In summary, BAF complexes are indispensable for neurodevelopment, orchestrating cell fate commitment, regional patterning, and lineage specification. Early inhibition (BAFi d0-6) disrupted foundational processes, resulting in caudalised progenitor identities and alterations in neural crest-associated programs, likely through modifications to the chromatin landscape of patterning-related signalling pathways and marker genes. These findings build upon prior research on SMARCA4's involvement in neural and glial lineage commitment, offering new perspectives on the spatiotemporal roles of BAF complexes within a three-dimensional context. The distinct consequences of later inhibition (BAFi d6-12) will be addressed in the following section.

6.3.2 Post-neurulation BAF complex inhibition disrupts dorsoventral patterning and cell fate specification

BAF complex inhibition during late neurulation and the onset of neurogenesis (d6-12) profoundly disrupts dorsoventral patterning, driving a dorsalised phenotype in brain organoids. Temporal analysis revealed a progressive increase in dorsal telencephalic markers, such as *GLI3* and *NFIA*, while ventral markers, including *DLX1*, *DLX2*, and *DLX5*, declined over time. Interestingly, this dorsal specification only emerged post-treatment, becoming prominent from day 17 onward. In contrast, ventral markers were transiently upregulated immediately after treatment, suggesting that BAF complexes regulate upstream gene programs rather than directly controlling dorsoventral marker expression.

This temporal switch may involve compensatory activation of dorsalising and caudalising pathways to counterbalance the initial upregulation of ventral markers. Dysregulated WNT signalling, a pathway modulated by BAF complexes, likely plays a central role in this process. Specifically, BAF inhibition might dysregulate WNT signalling, progressively overriding ventralising cues and triggering dorsalising and caudalising pathways. This aligns with the role of BAF complexes as modulators that fine-tune WNT activity to maintain dorsoventral balance[369,388,393,394]. Although rostral-caudal and dorsal-ventral patterning processes overlap temporally, rostrocaudal patterning begins slightly earlier in neurodevelopment[4,11–13,395,396]. This may account for the stronger dorsalisation seen in BAFi d6-12 samples, while BAFi d0-6 samples exhibit more pronounced caudalisation.

The chromatin accessibility changes observed at day 12 provide a deeper understanding of the transcriptional dysregulation caused by BAF complex inhibition during days 6 to 12. Reduced accessibility at regions associated with WNT signalling inhibitors, such as *NKD1*, *SFRP1*, and *SFRP4*, suggests elevated WNT signalling activity following BAF inhibition. This is consistent with the hypothesis that increased WNT activity drives early dorsalisation, as these inhibitors play critical roles in modulating WNT signalling. However, the reduced accessibility at *LHX2*, a key determinant of dorsal telencephalic identity, highlights an incomplete dorsal fate commitment at this stage. This aligns with the simultaneous expression of ventral markers, indicating that dorsalisation occurs as a gradual process rather than an immediate outcome, becoming more apparent by later stages, such as day 35.

Interestingly, the reduced chromatin accessibility at loci associated with non-telencephalic genes, such as *WLS*, *YAP1*, and *UNC5C*, appears inconsistent with the partially caudalised phenotype observed in BAFi d6-12 samples. This could represent an intermediate stage of patterning, where chromatin changes have not yet fully aligned with the developmental progression. Specifically, the gene regulatory network driving caudalisation has been initiated but remains in the process of establishment, with the chromatin landscape reflecting this transitional phase. Furthermore, rostrocaudal patterning is likely partially established at the time of inhibition in BAFi d6-12 samples, which may account for the less pronounced caudalisation in these samples, compared to BAFi d0-6. However, similarly to the findings in BAFi d0-6 samples, the increased accessibility at *ZIC* loci, particularly *ZIC4*, underscores the conserved role of these regions as targets of BAF complexes. While *ZIC* genes are not primary determinants of caudal fates during early neurodevelopment, their later association with caudal cell types supports their involvement in establishing the caudalised phenotype observed at day 35.

Beyond WNT signalling, the impact of BAF complex inhibition extended to other neurodevelopmental pathways, including BMP and NOTCH signalling. Increased expression of the NOTCH effector *HEY1* and the BMP signalling gene *BMP7* indicates a broader disruption of signalling networks, further complicating the patterning and fate decisions of progenitor cells. These signalling disruptions likely converge with alterations in chromatin at key developmental genes to produce the observed phenotypes. GO term enrichment analysis revealed that regions with reduced accessibility were enriched for processes such as “forebrain development,” “axonogenesis,” and “axon guidance,” emphasizing the widespread impact on neurodevelopmental processes. Notably, the predominance of regions with reduced chromatin accessibility in GO analysis underscores the global repressive effects on chromatin remodelling upon BAF complex inhibition.

By day 35, the dorsal identity of BAFi d6-12 organoids was evident at the protein level, with markers like EMX1 uniquely expressed in treated samples, while ventral markers such as DLX1 were restricted to controls. Chromatin accessibility analysis further supported these findings, showing enrichment of open chromatin regions associated with dorsal markers (EMX2) in treated samples and ventral markers (NKX2.1) in controls.

GRN analysis identified *NFIA* and *DACH1* as key regulators mediating dorsalisation in BAFi d6-12 samples, while ventral programs in controls were associated with factors like *FOXG1* and the antisense RNA *DLX6-AS1*. Dysregulated pathways linked to WNT, axon guidance (e.g., *SLIT2*, *ROBO1*), and YAP signalling mirrored observations in BAFi d0-6 samples. Genes such as *SLIT2* and *TTR*, associated with dorsal forebrain structures like the choroid plexus, were upregulated in treated samples, further confirming a dorsalised phenotype. This dorsal identity persisted, with markers like *EMX1* and *FEZF2* remaining elevated alongside caudal markers such as *OTX2*, *GBX2*, and *LMX1A* through day 66. However, by day 120, expression of these markers slightly declined, indicating a partial adjustment. Ventral markers (*FOXG1*, *NKX2.1*) remained consistently downregulated, highlighting a sustained impairment in ventral telencephalic development.

In contrast to BAFi d0-6 samples, BAFi d6-12 organoids exhibited an increase in size, suggesting distinct effects of BAF complex inhibition during this later window. Elevated *SOX2* expression, a marker of active neural stem cells[397], was observed in BAFi d6-12 samples at days 12 and 17, exceeding levels in both BAFi d0-6 samples and DMSO controls. This likely promoted increased proliferation, contributing to the increased organoid size. Accordingly, NPC populations were more abundant in BAFi d6-12 samples at day 35 compared to both controls and BAFi d0-6 samples. Similar to BAFi d0-6, progenitor and neuronal markers such as *DCX* and *SATB2* were downregulated, with partial recovery of *SATB2* and *RBFOX3* at later stages. The persistent upregulation of *S100B* and downregulation of *OLIG2* mirrored the findings in BAFi d0-6, reinforcing the notion of disrupted lineage specification and dorsalised fates.

However, dorsal-ventral and rostral-caudal patterning defects exhibited notable differences compared to BAFi d0-6 samples. While ventral markers, including *DLX5*, *NKX2-1*, and *DLX2*, remained persistently downregulated, dorsal markers showed a transient increase at days 35 and 66, followed by a decrease by day 120. This suggests that in DMSO-treated samples, dorsal fate commitment is progressively established at later stages, whereas in BAFi d6-12 samples, early patterning disruptions impair the establishment of ventral cell types, leading to lasting developmental imbalances.

Chromatin accessibility data at day 120 showed patterns similar to those in BAFi d0-6 samples, with reduced accessibility at key ventral loci such as *DLX5*, *ARX*, *DLX6-AS1*, and *LHX6*. Interestingly, additional decreases in accessibility at *DLX2* were observed, reflecting a more profound disruption of ventral patterning compared to BAFi d0-6 samples. The increased accessibility at caudal markers such as *OTX2* and *WLS*, though subtle, points to a persistent bias toward caudalisation. However, the gene expression of *OTX2* at day 120 suggests that the relationship between chromatin accessibility and transcriptional output is not always straightforward, likely due to compensatory mechanisms or temporal shifts in gene regulation.

These findings align with studies on AUTS2- and DISC1-deficient cerebral organoids, where similar dysregulated genes (e.g., *TTR*, *FOXG1*, *HES1,* GSX2, *SIX3*, *IRX3*) were observed[398,399]. Both studies attributed these effects to WNT hyperactivation, reinforcing the hypothesis that WNT signalling dysregulation is a major driver of the dorsalised and caudalised phenotypes in BAFi d6-12 samples. Conversely, *ARID1B* heterozygous knock-out brain organoids show an opposing phenotype, with increased populations of ventral radial glia, consistent with findings in ASD patients harbouring heterozygous *ARID1B* mutations and presenting with enlarged ganglionic eminences[177]. This contrast underscores subunit-specific effects within the BAF complexes. While ARID1B loss alters ventral telencephalic populations, the global disruption caused by BAF inhibition triggers dorsalisation and caudalisation. These distinctions suggest that ARID1B-specific roles and compensatory mechanisms within the BAF complexes modulate neurodevelopment differently from complete perturbation. Notably, a recent study demonstrated that YAP signalling promotes caudalisation in brain organoids by *YAP1* directly binding to the promoter region of *WLS*[315]. Moreover, *YAP1* activation was associated with the upregulation of genes such as *MSX2*, *TFAP2A*, and *WLS*, all of which are similarly upregulated in both BAFi d0-6 and BAFi d6-12 samples. Consistent with the observation that BAF complexes modulate both WNT and YAP signalling under physiological conditions[400], their inhibition was likely associated with the upregulation of target genes from both pathways, such as *PAX3* (WNT target) and *WLS* (YAP target). Given the known caudalising effects of these pathways during neurodevelopment, their dysregulation in BAFi-treated samples is highly likely to contribute to the observed phenotypes.

In summary, BAF complex perturbation during specific developmental windows disrupts neurodevelopmental trajectories, emphasizing its critical role in establishing and maintaining regional identity. Dysregulated pathways like WNT, YAP, and axon guidance appear central to these effects, driving the dorsalised and caudalised phenotypes observed in treated organoids. While partial recovery of dorsal markers is evident over time, the inability to restore ventral telencephalic populations highlights the lasting impact of transient BAF complex inhibition. These findings provide valuable insights into the gene regulatory mechanisms

governed by chromatin remodelling and underscore the temporal sensitivity of neurodevelopment to BAF complex activity. Further research disentangling subunit-specific contributions and their influence on signalling pathways will be crucial to understanding these divergent outcomes.

6.4 Heterozygous ARID1B knockout results in minimal chromatin changes in long-term organoids

In order to gain clinical relevant insights into how BAF complexes perturbed function is driving neurodevelopmental disorders, hiPSCs heterozygously mutated for ARID1B were differentiated into brain organoids, monitored over time by microscopy and analysed for chromatin accessibility changes at day 120 and compared to BAF inhibitor treated organoids that were kept in culture for the same time. Findings from the BAF inhibitor treated organoids at day 120 revealed that early BAF inhibition resulted in persistent morphological and molecular disruptions in brain organoids, with size alterations and regional patterning defects. Specifically, BAFi d0-6 and BAFi d6-12 samples displayed caudalised and dorsalised phenotypes, including diminished expression of rostral and ventral markers such as *FOXG1* and *DLX5*, alongside increased caudal and dorsal markers like *OTX2*, *WLS* and *LHX2*. These findings are consistent with changes in chromatin accessibility at loci associated with ventral forebrain specification, emphasizing the essential role of BAF complexes in establishing early neurodevelopmental gene programs. By day 120, chromatin accessibility in BAF-inhibited organoids was largely stabilized, yet early disruptions in gene regulation remained evident, underscoring the long-lasting consequences of transient early-stage perturbations.

In comparison, ARID1B mutant organoids displayed subtler phenotypic changes. Morphological analysis revealed only mild disorganization of neural rosettes at early stages (e.g., day 17), suggesting that ARID1B haploinsufficiency may cause less pronounced structural disruptions than pharmacological BAF inhibition. This difference likely reflects the partial functionality of ARID1B-containing BAF complexes in the heterozygous state in comparison to inhibition of all BAF complexes. Chromatin accessibility analysis of ARID1B mutant organoids at day 120 showed limited alterations overall, but specific loci associated with neurodevelopmental disorders, such as *LARGE1*, *GABRB3*, and *PACSIN1*, exhibited reduced accessibility. These genes are implicated in conditions like autism, intellectual disability, and schizophrenia[358–361], suggesting that ARID1B mutations selectively affect neurodevelopmental gene networks relevant to these disorders.

GABRB3, a gene crucial for integrating pyramidal neurons into the somatosensory cortex, encodes one of 19 $GABA_A$ receptor subunits and exhibits the highest prevalence of pathogenic

variants among them[401]. Mutations in *GABRB3* are associated with reduced GABAergic activity[402], leading to epilepsy in patients with these variants[403]. *PACSIN1* plays a significant role in neuromorphogenesis, particularly in the maturation of cortical pyramidal neurons[404,405]. Studies in mice have shown that *PACSIN1* deficiency leads to shorter dendritic trees, reduced arborization, and fewer terminal points, emphasizing its essential role in neuronal development[404]. Furthermore, *PACSIN1* knock-out mice exhibit impaired AMPA-type glutamate receptor (AMPA-R)-mediated excitatory post-synaptic currents in pyramidal neurons, suggesting perturbed receptor trafficking as a consequence of *PACSIN1* loss[406]. Similarly, *LARGE1* contributes to excitatory synaptic transmission by forming a protein complex with AMPA-Rs, facilitating their trafficking to the cell surface[407]. In mouse models, *LARGE1* downregulation disrupts this process, impairing neural circuitry and altering the balance between excitatory and inhibitory neuronal activity[358]. However, the underlying mechanisms differ from those observed with *GABRB3*, which primarily affects inhibitory signalling. The role of ARID1B in neurodevelopment further underscores its critical function in maintaining neuronal balance and connectivity. ARID1B is known to regulate dendritic arborization and spine morphology in pyramidal neurons, with its knockdown resulting in significantly reduced dendritic complexity in both cortical and hippocampal regions[408]. Beyond its effects on excitatory neurons, ARID1B haploinsufficiency has been linked to decreased proliferation of interneuron progenitors in the ganglionic eminence, resulting in an imbalance between excitatory and inhibitory neuronal populations in the cerebral cortex[409]. Notably, treatment with a positive allosteric modulator of $GABA_A$ receptors has been shown to rescue cognitive and social deficits in ARID1B-deficient mouse models, providing compelling evidence of the therapeutic potential of restoring GABAergic activity[409]. In the ARID1B haploinsufficient brain organoids analysed here, reduced chromatin accessibility at the *GABRB3*, *PACSIN1*, and *LARGE1* loci suggests a disruption in the genomic regulation required for the differentiation and functionality of interneurons and pyramidal neurons. These findings imply that ARID1B mutations may compromise the balance between excitatory and inhibitory neuronal activity by targeting genes critical for both GABAergic signalling and excitatory glutamatergic transmission. Moreover, the observed alterations in chromatin accessibility align with ARID1B's established roles in dendritic development and interneuron progenitor proliferation, potentially linking these molecular disruptions to the neurodevelopmental phenotypes characteristic of ARID1B-associated disorders. The evidence presented highlights the intricate interplay between ARID1B and key regulatory genes in neural circuit formation and function. It also emphasizes the importance of balanced excitatory and inhibitory signalling for normal brain development and the potential of targeted interventions to mitigate the effects of ARID1B dysfunction. These findings open avenues for further investigation into the

molecular mechanisms underlying ARID1B-mediated chromatin regulation and its broader impact on neuronal differentiation and integration.

Interestingly, both BAF-inhibited and ARID1B-mutant organoids exhibited increased chromatin accessibility at the *ZIC1* and *ZIC4* loci. This observation suggests that ZIC genes are consistent targets of BAF complexes, emphasizing their critical importance in neurodevelopment. The heightened accessibility of these loci in both conditions could reflect compensatory regulatory mechanisms or altered chromatin states resulting from BAF dysfunction. While the precise roles of *ZIC1* and *ZIC4* in these contexts remain to be fully elucidated, their consistent targeting following BAF complex perturbation highlights their significance as potential key sites of BAF-mediated regulation. Supporting this, *ZIC1* has been identified as an ASD risk gene, influencing neuronal development and cerebellar function in patients[410]. Similarly, *ZIC4* hypomethylation, leading to increased expression, has been linked to neural tube defects[411]. These findings further strengthen the hypothesis that perturbation of BAF complexes impacts key neurodevelopmental risk genes, contributing to overlapping phenotypes observed in neurodevelopmental disorders. Moreover, *ZIC1* and *ZIC4* are integral to caudal and dorsal brain region development, such as the cerebellum and the dorsal midline of the forebrain[338]. Dysregulation of these genes upon BAF complex malfunction could disrupt regional brain identity, leading to altered neuronal subtype differentiation and imbalances between distinct neural populations. This underscores their pivotal role in maintaining proper brain region specification and neuronal subtype equilibrium.

Although ARID1B mutations show a limited impact on global chromatin accessibility at later neurodevelopmental stages in the studied model system, the enrichment of the GO term “regulation of cell projection size” among differentially accessible loci suggests that ARID1B dysfunction influences cellular morphology and connectivity. This finding is consistent with the observed differential accessibility of genes involved in pyramidal projection neuron differentiation, such as *PACSIN1*. Investigating earlier stages of neurodevelopment could provide deeper insights into how ARID1B haploinsufficiency disrupts chromatin dynamics and transcriptional regulation during key developmental periods. Furthermore, integrating (single-cell) transcriptomic analyses from both early and late stages would help elucidate the downstream effects of ARID1B dysfunction on brain patterning and cell fate specification.

The observed differences between pharmacological BAF inhibition and ARID1B mutation likely reflect the distinct mechanisms of perturbation. While BAF inhibition broadly disrupts the activity of all BAF complexes, ARID1B mutations specifically affect the assembly and function of certain BAF subtypes. These nuances underscore the importance of distinguishing between genetic mutations and pharmacological interventions when studying BAF complex roles in

neurodevelopment. Comparative studies involving other ARID subunits or SMARCA4 mutations could further delineate the contributions of specific BAF components to neurodevelopmental disorders, offering valuable insights into the diverse functions of these complexes in brain development.

Taken together, differentiation of hiPSCs heterozygously mutated for ARID1B into brain organoids revealed that ARID1B haploinsufficiency causes subtle structural disruptions and selective chromatin accessibility changes at later stages, particularly at loci associated with neurodevelopmental disorders such as *GABRB3*, *PACSIN1*, and *LARGE1*. By contrast, early pharmacological BAF inhibition resulted in persistent morphological and regional patterning defects, including caudalised and dorsalised phenotypes. Both conditions exhibited increased chromatin accessibility at *ZIC1* and *ZIC4* following BAF complex perturbation, identifying these genes as conserved targets or downstream effectors essential for caudal and dorsal brain region development. These findings underscore the distinct impacts of genetic and pharmacological perturbations on chromatin regulation and neuronal differentiation.

This study highlights the pivotal role of BAF complexes in orchestrating robust neurodevelopmental programs and demonstrates the enduring effects of their disruption. Exploring the interplay between genetic mutations and pharmacological inhibition across developmental stages will be essential for understanding their contributions to neurodevelopmental disorders and for advancing targeted therapeutic strategies.

6.5 Conclusion

The chromatin remodelling activity of BAF complexes is indispensable for orchestrating early brain development. This study demonstrates their stage- and subunit-specific roles in regulating neural rosette formation, progenitor commitment, and regional patterning. Early inhibition of BAF complexes, particularly during d0-6 and d6-12, profoundly disrupts gene expression trajectories, leading to precocious differentiation, caudalisation, and a shift towards dorsal and caudal progenitor identities at the expense of telencephalic and ventral forebrain lineages. These effects observed in BAFi d0-6 and BAFi d6-12 samples result from impaired chromatin accessibility at key loci, with lasting impacts on regional and cell fate specification. In contrast, inhibition at later stages showed greater resilience, emphasizing the critical role of BAF complexes during early development.

While only transient BAF inhibition was performed, the short-term perturbations resulted in long-lasting effects. Specifically, the shift towards more caudal and dorsal brain identity was maintained even at day 120, despite partial recovery of dorsal markers. However, ventral telencephalic populations remained impaired, underscoring the enduring effects of early

patterning defects. Chromatin accessibility and transcriptomic analyses further revealed dysregulated pathways, including WNT, BMP, YAP and NOTCH signalling, which likely contributed to the observed changes in brain patterning and neural subtype specification processes, reflecting the central role of BAF complexes in coordinating neurodevelopmental programs.

The distinct outcomes of pharmacological BAF inhibition and ARID1B haploinsufficiency underscore the non-redundant roles of BAF complex subunits in neurodevelopment. While pharmacological inhibition caused widespread caudalisation and dorsalisation, ARID1B-specific perturbations produced subtler effects, including selective chromatin accessibility changes at loci linked to neurodevelopmental processes. Notably, both conditions showed increased chromatin accessibility at *ZIC1* and *ZIC4* loci, underscoring their conserved role in dorsal and caudal regional development among other functions. These observations highlight the nuanced contributions of individual BAF components to chromatin remodelling and their critical role in early neurodevelopment.

Future studies integrating transcriptomic and chromatin accessibility analyses across developmental stages and subunit-specific mutations will further refine our understanding of BAF complex function and its broader implications for neurodevelopmental disorders. Such research paves the way for targeted therapeutic strategies to address the consequences of BAF complex dysfunction.

6.6 Limitations

The analysis of gene expression, chromatin landscape changes, as well as morphological and protein expression alterations across neurodevelopmental stages provided valuable insights into the role of BAF complexes in regulating critical processes and associated signalling pathways. This study revealed how these complexes influence gene programs essential for neurodevelopment, offering a broad perspective on their function. However, several limitations must be considered.

While the brain organoid model system effectively mimics aspects of early brain development, it does not fully capture the complexity of *in vivo* brain morphology and cell types. As a result, this study cannot address all aspects of human brain development and how early molecular changes induced by BAF complex inhibition affect the adult brain. Moreover, the prolonged application of the allosteric inhibitor BRM014 raises the possibility of indirect effects caused by compensatory mechanisms. To isolate the direct consequences of BAF complex disruption and increase temporal resolution, shorter treatment durations with sampling at earlier time points, such as one hour or one day after treatment, would be necessary.

Transcriptomic and chromatin landscape analyses in this study revealed dysregulation of key signalling pathways, including WNT, YAP, BMP, and NOTCH, following BAF complex inhibition. These pathways are critical for neurodevelopment, particularly in patterning and cell subtype specification, and their disruption likely contributes to the distinct phenotypes observed. To validate these findings, signalling activity assays such as ELISA or Western blot using markers like dephosphorylated β-catenin for canonical WNT activation are essential. Additionally, assessing pathway activation at earlier time points post-treatment could clarify whether these effects are direct consequences of BAF complex inhibition or compensatory downstream responses, helping to unravel the precise regulatory interplay between BAF complexes and these pathways.

Although ATAC-seq and CUT&Tag-seq were performed, a downstream motif analysis of the sites affected by the BAF inhibition could deepen our understanding of transcriptional regulation by identifying enriched DNA motifs and the TFs driving distinct gene programs. Comparing motif enrichments across experimental conditions could clarify how TF activity changes with BAF perturbation, while temporal analyses would capture the dynamics of TF regulation during development. Together, these insights could shed light on the regulatory mechanisms disrupted by BAF complex inhibition.

While this study primarily focused on brain patterning phenotypes and differences in cell type specification, the dysregulation of axon guidance pathways also emerged as a notable finding that warrants further exploration. Investigating axon guidance differences could involve spatial transcriptomics, live imaging of axon growth in organoid systems, and analysing the expression and localization of axon guidance molecules to uncover how BAF complex perturbation affects neuronal connectivity. Lastly, synaptic function assays, such as electrophysiological recordings or calcium imaging, would provide valuable insights into how dysregulated axon guidance upon BAF complex inhibition impacts synaptic functionality.Further complicating the interpretation of results, neurodevelopmental disorders such as ASD, schizophrenia, ID, CSS, and NCBRS manifest with behavioural symptoms that cannot be replicated in brain organoids. These outcomes require validation through patient-derived samples or animal models to connect molecular changes in brain organoids with behavioural phenotypes observed in patients. For instance, imbalances in excitatory and inhibitory neuronal subtypes, frequently implicated in ASD and schizophrenia and associated with increased risk for epilepsy, may stem from disruptions in brain regional identity and cell type generation. However, testing this hypothesis lies beyond the scope of organoid models and necessitates complementary approaches.

To address clinical relevance, this study investigated heterozygous ARID1B mutations by differentiating ARID1B-mutated hiPSCs into brain organoids. Although the findings shed light

on morphological and chromatin alterations at later neurodevelopmental stages, the early molecular changes, likely crucial for understanding ARID1B's role, were not examined in detail. Compounding this limitation, the analysis relied on a single clone with a specific mutation, leaving potential clonal variability unexplored. Moreover, ARID1B mutations occur throughout the gene and different mutations may lead to diverse outcomes, even though most result in loss of function. Additionally, the genetic background may influence the observed effects.

BAF complexes consist of various subunits, and mutations in these subunits are associated with distinct neurodevelopmental disorders. While this study focused on ARID1B as well as the complete loss of BAF complexes, it did not investigate other subunits or their disorder-specific contributions. Since different subunits may influence neurodevelopmental processes in unique ways, understanding their specific roles and the molecular changes they drive requires further study. The absence of subunit- and class-specific resolution limits the scope of conclusions regarding the precise mechanisms of BAF complexes in neurodevelopment.

In summary, while this study offers important insights into the molecular mechanisms regulated by BAF complexes during early neurodevelopment, it also highlights critical areas for further investigation. Complementary models and approaches are necessary to overcome the limitations and deepen the understanding of the roles these complexes play in health and disease.

6.7 Outlook

To deepen the mechanistic understanding of BAF complex disruption in neurodevelopment, future studies should investigate how these complexes regulate key signalling pathways, including WNT, NOTCH, BMP and YAP, during neurodevelopmental processes. Specifically, it is crucial to explore how disruptions at distinct developmental time points contribute to the observed phenotypes and whether pathway regulation is timepoint-specific. This investigation should also encompass the physiological roles of BAF complexes in modulating these pathways under normal conditions, using approaches such as introducing specific mutations and/or employing targeted inhibitors or activators during brain organoid development.

Future research should aim to elucidate the binding affinities of BAF complexes to target sites associated with neurodevelopmental pathways, cell type-specific genes, axon guidance, or patterning-related loci with both temporal and single-cell resolution. This approach will provide deeper insights into the mechanisms and GRNs underlying affected developmental trajectories influenced by BAF complex inhibition at the level of individual cell types. Techniques such as optimized single-cell CUT&Tag[278,279,412] or CUT&RUN[413,414], the latter being particularly suitable for analysing transcription factor binding on chromatin, could provide deeper insights into the chromatin-binding dynamics of BAF complex subunits. Additionally, direct interactions

between BAF complex subunits and candidate signalling factors should be examined. These protein-protein interactions, critical for pathway regulation, could be explored using advanced methodologies like TurboID[415] or similar proximity-labelling assays to map interaction networks comprehensively.

While this study primarily focused on the general role of BAF complexes in neurodevelopment, future research should expand its scope to address clinically relevant molecular changes. Understanding how mutations in specific BAF complex subunits, such as ARID1A, ARID1B, or ARID2, affect chromatin binding and protein-protein interactions may elucidate the mechanisms underlying distinct phenotypic outcomes. Investigating the effects of these mutations across various neurodevelopmental time points would offer insights into stage-specific impacts of subunit properties. The dTAG system[416], which facilitates targeted degradation of specific subunits at defined developmental stages, could be employed to dissect temporal roles of BAF complex components in neurodevelopment.

Patient-derived hiPSCs offer another promising avenue for future studies. Differentiating these cells into brain organoids enables direct linkage of molecular changes to behavioural symptoms and morphological brain differences observed in patients. This approach could also identify whether distinct mutations share common dysregulated pathways or exhibit unique molecular signatures. Such insights would not only enhance our understanding of neurodevelopmental disorders but also provide a foundation for developing targeted therapeutic interventions.

In summary, the integration of advanced molecular techniques, patient-derived models, and time-resolved approaches will promote a comprehensive understanding of the functions of the BAF complexes during brain development. These efforts could reveal how their disruption contributes to neurodevelopmental disorders and support the development of precision therapies tailored to individual genetic and molecular profiles.

7 Supplement

7.1 Supplementary tables

Table 7.1-1: DEGs shared between BAFi-treated samples following treatment. *BAFi samples following treatment = BAFi d0-6 at day 6, BAFi d6-12 at day 12, BAFi d12-17 at day 17, BAFi d17-35 at day 35.*

Shared between	Down-/Upregulated	Gene
BAFi samples following treatment	Downregulated	MXRA8, IFITM3 ID3, FLNA ATCAY, CAPN6 KIF26A, EPHB2 SPINK5, ATP1A2 TUBA1C, NDRG4 CELF2, RIMS4 RNF157, HMGA1 TTYH1, NNAT LASP1, BTBD17 NKAIN4, MEST SNHG29, DPYSL2 VASH2, HOMER3 RPS3, RPLP1 UCP2, TOX2 SHMT2, JPH4 GNAI2, RPL28 TIMP1, LGALS3BP RPLP0, ARAP3 TSPOAP1, BCOR PLP1, STMN4 FXYD6, NOTCH1 PEBP1, PCBP4 ELN, IFI6 SELENBP1, CDC25B FADS1, ADGRG1 PCSK9, TMEM35A H3-3B, ARHGEF2 LFNG, EFNB1 RPS6KA2, TMEM97
	Upregulated	TFPI, CD82 ARL4C, BOC CDK6, ROBO3 BMP7, ID2 SIX5, PHACTR2 ANGPT2, LEF1 ID1, ARHGAP28 ANKRD34B, LAMC1 PCDH7, LAMA1 IQCE, ARL4A EFCC1, TMEM47 ATG10, FGF9 EDNRB, CRNDE ERBB4, ID2-AS1

Table 7.1-2: Marker gene list used for UMAP visualization of neural cell types (Figure 5.3-1 B). *Neural marker genes were selected from the literature[42,216,417–419].*

Cell Type	Marker Gene
Radial Glia	GLI3, FABP7, FGF2, HES5, NOTCH1, PAX6, PDGFD, SOX2, SLC1A3, VIM
Neuron	CALB1, DCX, ENO2, MAP2, RBFOX3, NEUROD1, NEFH, NEFL, NEFM, DLG2, DLG4, TUBB3, UCHL1
Oligodendrocyte Precursor Cell (OPC)	OLIG2, PDGFRA, MBP, SOX10, RIT2, OLIG1
(Pre-)Astrocyte	S100B, CD44, ALDOC, GJA1, NDRG2, BIRC5, SLC1A2

Table 7.1-3: Marker gene list used for the annotation of the Multiome data set. *Marker genes are derived from reference[42,271]. PNS = Peripheral nervous system.*

Cell Type (Level 1)	Subtype (Level 2)	Subtype (Level 3)	Marker Genes
Neuroprogenitor Cell (NPC)			SOX2, VIM, NES
Neuroprogenitor Cell (NPC)	Glioblast		HOPX, BCAN, TNC
Telencephalic NPC			FOXG1, EMX1, GABRA2, GABRB1, DLX2
Diencephalic NPC			TCF7L2, SIX3
Mesencephalic NPC			OTX2, PAX7
Retinal NPC			VSX2
Rhombencephalic NPC			CYP26A1, HOXA2, HOXB2, HOXD3, UNC5C, BCAN, GPC6,
Neuron	Excitatory Neuron		STMN2, DCX, SLC17A7, SLC17A6
Neuron	Excitatory Neuron	Telencephalic Excitatory Neuron	FOXG1, EMX1, SLC17A7, BCL11B, SATB2, GABRA2, GABRB1
Neuron	Excitatory Neuron	Non-telencephalic Excitatory Neuron	SLC17A6, TCF7L2, PITX2, BARHL2, TFAP2D, UNCX, INSM1, UNC5C, TFAP2A, HOXA2, HOXB2, HOXD3, HOXA3, ROBO1, NEGR1
Neuron	Inhibitory Neuron		GAD1, GAD2, SLC32A1
Neuron	Inhibitory Neuron	Telencephalic Inhibitory Neuron	FOXG1
Neuron	Inhibitory Neuron	Telencephalic Inhibitory Neuron	DLX2, DLX5, NKX2-1, ISL1, NR2F1
Neuron	Inhibitory Neuron	Non-telecephalic Inhibitory Neuron	LHX5, LHX1
Neuron	Inhibitory Neuron	Non-telecephalic Inhibitory Neuron	TCF7L2, ISL1
Neuron	Inhibitory Neuron	Non-telecephalic Inhibitory Neuron	DLX1, DLX5, OTX2, SKOR2, HOXA2, HOXB2, HOXD3, CA8, LAMP5, TFAP2A, UNC5C, ROBO1, NEGR1
Choroid Plexus Epithelium			TTR
Astrocyte			GFAP, AQP4
Oligodendrocyte			OLIG1, MBP
Microglia			AIF1
Vascular Endothelial Cell			CLDN5
Mesenchymal Cell			DCN
Neural Crest			SOX10
PNS Neurons			PRPH

7.2 Figures

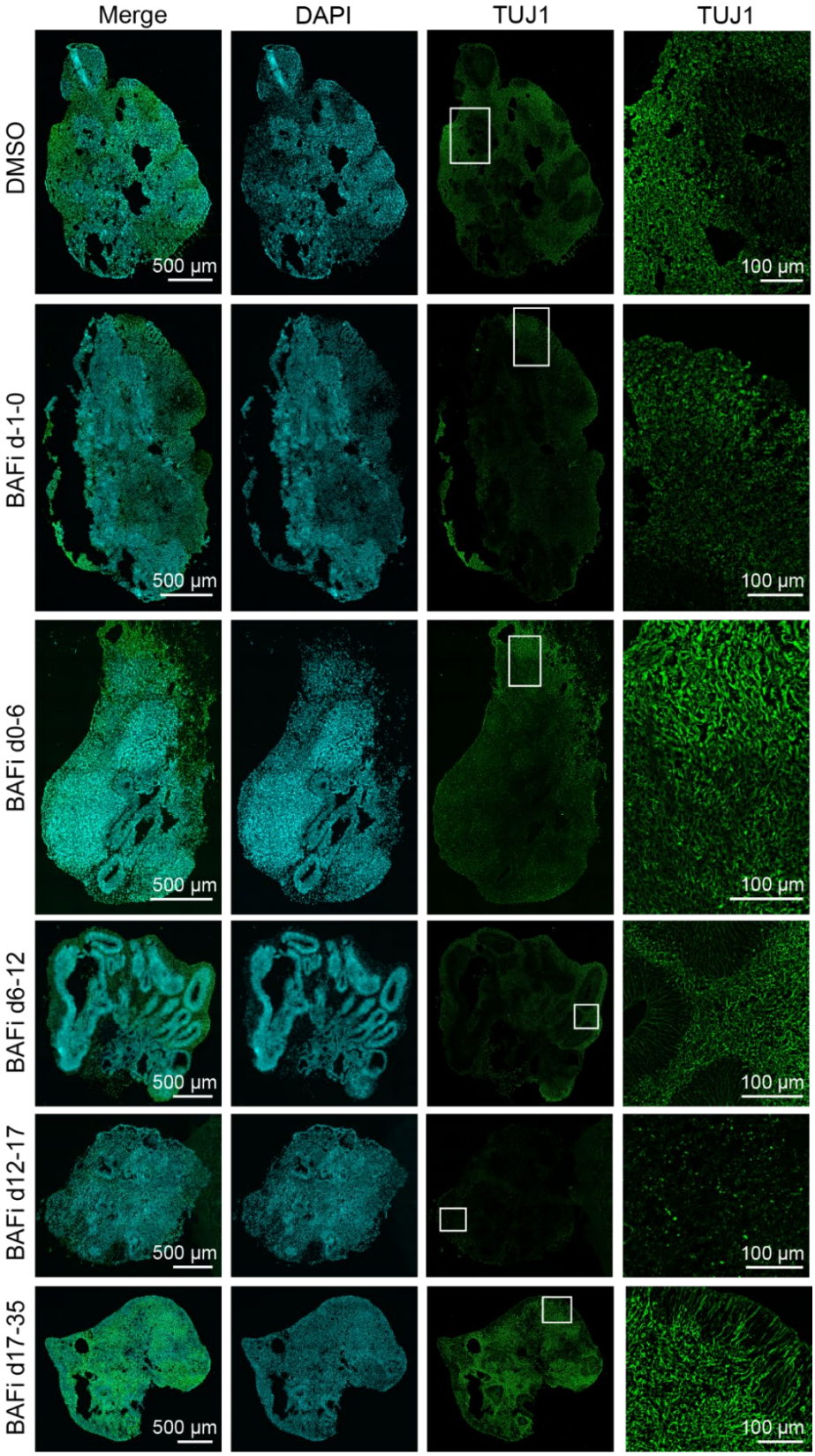

Figure 7.2-1: Immunofluorescence staining for TUJ1. *Representative immunofluorescence images show 35-day-old organoids stained for the NPC marker TUJ1 (green), with nuclei counterstained using DAPI (cyan). White rectangles in the left TUJ1 image mark the region of interest, shown on the right at higher magnification. Images are from 12 µm sections, acquired with a 40x objective on a Leica Thunder microscope.*

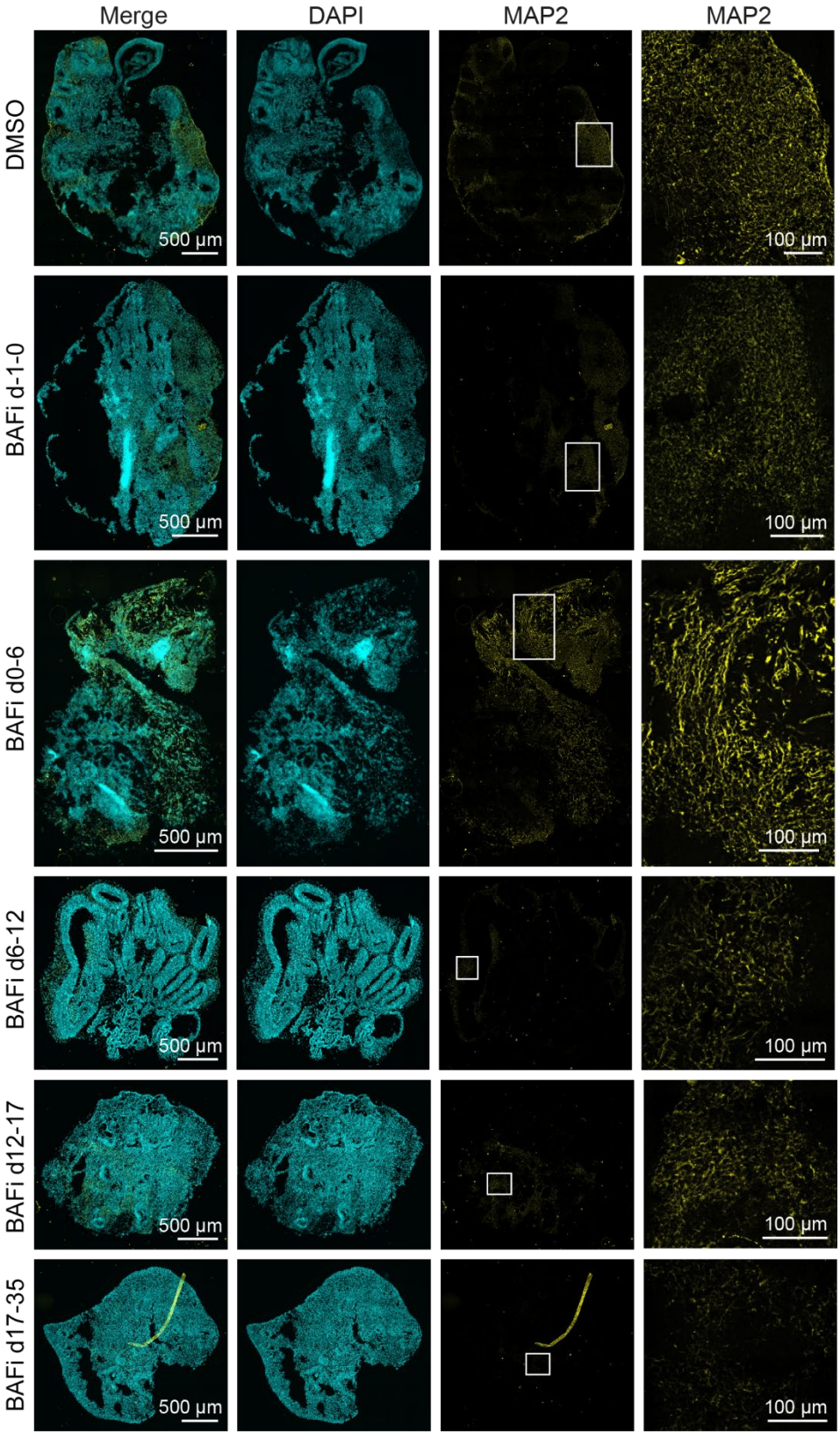

Figure 7.2-2: Immunofluorescence staining for MAP2. *Representative immunofluorescence images show 35-day-old organoids stained for the mature neuronal marker MAP2 (yellow), with nuclei counterstained using DAPI (cyan). White rectangles in the left MAP2 image mark the region of interest, shown on the right at higher magnification. Images are from 12 µm sections, acquired with a 40x objective on a Leica Thunder microscope.*

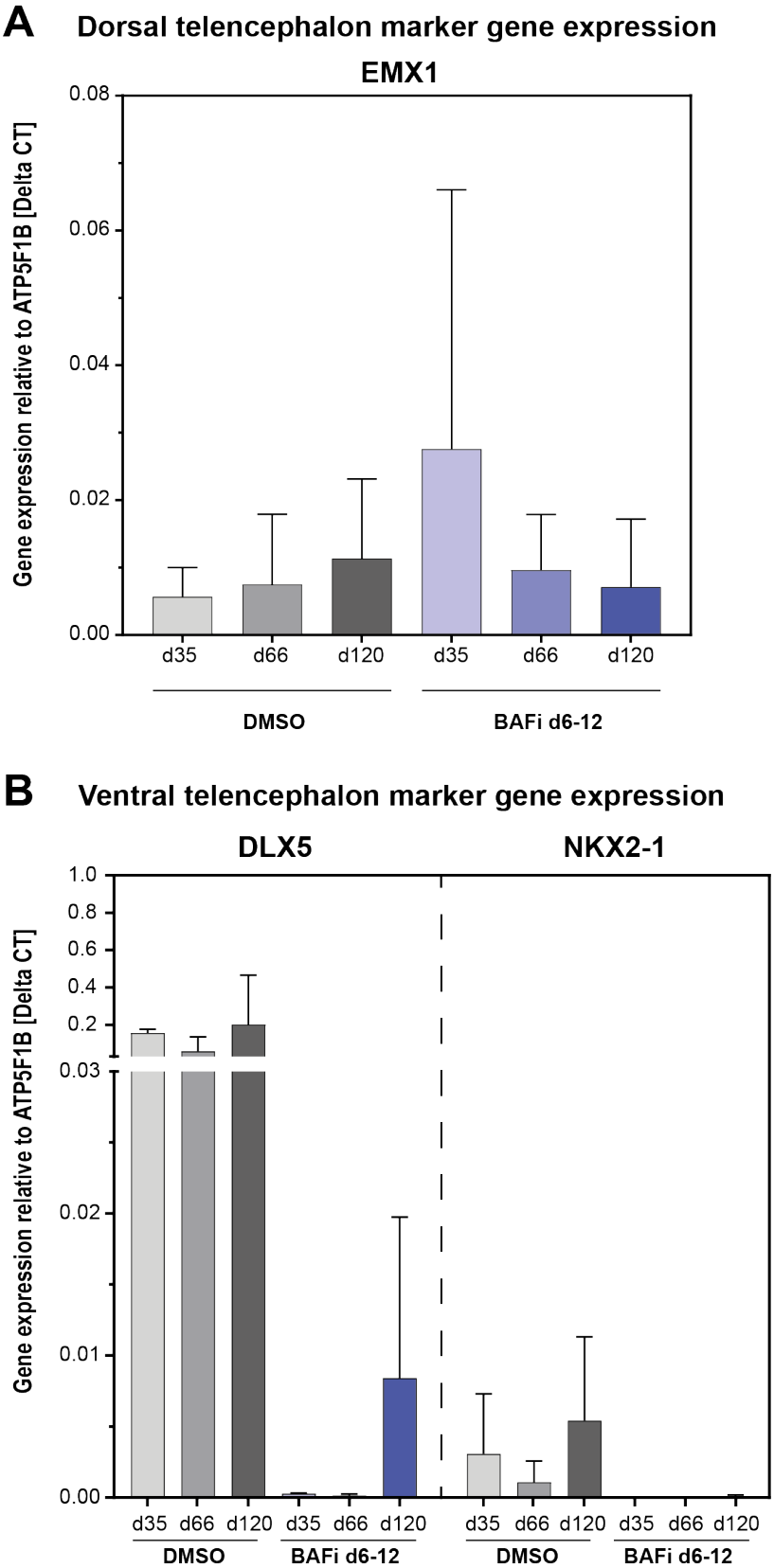

Figure 7.2-3: Gene expression of dorsal and ventral telencephalic marker genes in long-term organoid cultures. *Bar graph with whiskers showing RT-qPCR-derived delta cycle threshold (Delta CT) values of dorsal and ventral telencephalon marker genes in DMSO and BAFi d6-12 at days 35, 66, and 120 (n = 2). Values were normalized to the housekeeping gene ATP5F1B. Bars represent the mean, and whiskers indicate the standard deviation. d = day.*

8 References

1. Stiles, J. *The Fundamentals of Brain Development* (Harvard University Press, 2008).
2. Herculano-Houzel, S. The human brain in numbers: a linearly scaled-up primate brain. *Front. Hum. Neurosci.* **3**; 10.3389/neuro.09.031.2009 (2009).
3. Azevedo, F. A. *et al.* Equal numbers of neuronal and nonneuronal cells make the human brain an isometrically scaled-up primate brain. *J of Comparative Neurology* **513,** 532–541; 10.1002/cne.21974 (2009).
4. Stiles, J. & Jernigan, T. L. The Basics of Brain Development. *Neuropsychology Review* **20,** 327–348; 10.1007/s11065-010-9148-4 (2010).
5. Marín, O. Developmental timing and critical windows for the treatment of psychiatric disorders. *Nature medicine* **22,** 1229–1238; 10.1038/nm.4225 (2016).
6. Silbereis, J. C., Pochareddy, S., Zhu, Y., Li, M. & Sestan, N. The Cellular and Molecular Landscapes of the Developing Human Central Nervous System. *Neuron* **89,** 248–268; 10.1016/j.neuron.2015.12.008 (2016).
7. Zhou, Y., Song, H. & Ming, G.-L. Genetics of human brain development. *Nature reviews. Genetics* **25,** 26–45; 10.1038/s41576-023-00626-5 (2024).
8. Ozair, M. Z., Kintner, C. & Brivanlou, A. H. Neural induction and early patterning in vertebrates. *Wiley interdisciplinary reviews. Developmental biology* **2,** 479–498; 10.1002/wdev.90 (2013).
9. Campbell, N. A. *et al. Campbell Biologie.* 10th ed. (Pearson Deutschland, Hallbergmoss, 2016).
10. Bear, M. F., Connors, B. W. & Paradiso, M. A. (eds.). *Neurowissenschaften. Ein grundlegendes Lehrbuch für Biologie, Medizin und Psychologie.* 3rd ed. (Spektrum Akad. Verl., Heidelberg, 2008).
11. Gasser, R. F. *Atlas of human embryos* (Harper & Row, Hagerstown, Md., 1975).
12. Nieuwkoop, P. D. The neural induction process; its morphogenetic aspects. *The International journal of developmental biology* **43,** 615–623 (1999).
13. Kiecker, C. & Niehrs, C. A morphogen gradient of Wnt/β-catenin signalling regulates anteroposterior neural patterning in Xenopus. *Development* **128,** 4189–4201; 10.1242/dev.128.21.4189 (2001).
14. Maden, M., Gale, E., Kostetskii, I. & Zile, M. Vitamin A-deficient quail embryos have half a hindbrain and other neural defects. *Current biology : CB* **6,** 417–426; 10.1016/S0960-9822(02)00509-2 (1996).
15. Blumberg, B. *et al.* An essential role for retinoid signaling in anteroposterior neural patterning. *Development* **124,** 373–379; 10.1242/dev.124.2.373 (1997).
16. Cox, W. G. & Hemmati-Brivanlou, A. Caudalization of neural fate by tissue recombination and bFGF. *Development* **121,** 4349–4358; 10.1242/dev.121.12.4349 (1995).
17. Doniach, T. Basic FGF as an inducer of anteroposterior neural pattern. *Cell* **83,** 1067–1070; 10.1016/0092-8674(95)90133-7 (1995).
18. Kudoh, T., Wilson, S. W. & Dawid, I. B. Distinct roles for Fgf, Wnt and retinoic acid in posteriorizing the neural ectoderm. *Development* **129,** 4335–4346; 10.1242/dev.129.18.4335 (2002).

19. Bel-Vialar, S., Itasaki, N. & Krumlauf, R. Initiating Hox gene expression: in the early chick neural tube differential sensitivity to FGF and RA signaling subdivides the HoxB genes in two distinct groups. *Development* **129,** 5103–5115; 10.1242/dev.129.22.5103 (2002).

20. Shiotsugu, J. *et al.* Multiple points of interaction between retinoic acid and FGF signaling during embryonic axis formation. *Development* **131,** 2653–2667; 10.1242/dev.01129 (2004).

21. Crossley, P. H. & Martin, G. R. The mouse Fgf8 gene encodes a family of polypeptides and is expressed in regions that direct outgrowth and patterning in the developing embryo. *Development* **121,** 439–451; 10.1242/dev.121.2.439 (1995).

22. Ohuchi, H. *et al.* Involvement of Androgen-Induced Growth Factor (FGF-8) Gene in Mouse Embryogenesis and Morphogenesis. *Biochemical and Biophysical Research Communications* **204,** 882–888; 10.1006/bbrc.1994.2542 (1994).

23. Isaacs, H. V., Tannahill, D. & Slack, J. M. W. Expression of a novel FGF in the Xenopus embryo. A new candidate inducing factor for mesoderm formation and anteroposterior specification. *Development* **114,** 711–720; 10.1242/dev.114.3.711 (1992).

24. Martinez, S., Crossley, P. H., Cobos, I., Rubenstein, J. L. & Martin, G. R. FGF8 induces formation of an ectopic isthmic organizer and isthmocerebellar development via a repressive effect on Otx2 expression. *Development* **126,** 1189–1200; 10.1242/dev.126.6.1189 (1999).

25. Offen, N., Filatova, A. & Nuber, U. A. Enrichment of FGF8-expressing cells from neurally induced human pluripotent stem cell cultures. *Stem cell reports* **18,** 2240–2253; 10.1016/j.stemcr.2023.10.007 (2023).

26. Reifers, F. *et al.* Fgf8 is mutated in zebrafish acerebellar (ace) mutants and is required for maintenance of midbrain-hindbrain boundary development and somitogenesis. *Development* **125,** 2381–2395; 10.1242/dev.125.13.2381 (1998).

27. Crossley, P. H., Martinez, S., Ohkubo, Y. & Rubenstein, J. L. Coordinate expression of Fgf8, Otx2, Bmp4, and Shh in the rostral prosencephalon during development of the telencephalic and optic vesicles. *Neuroscience* **108,** 183–206; 10.1016/S0306-4522(01)00411-0 (2001).

28. Del Diez Corral, R. & Storey, K. G. Opposing FGF and retinoid pathways: a signalling switch that controls differentiation and patterning onset in the extending vertebrate body axis. *BioEssays : news and reviews in molecular, cellular and developmental biology* **26,** 857–869; 10.1002/bies.20080 (2004).

29. Ribes, V., Le Roux, I., Rhinn, M., Schuhbaur, B. & Dollé, P. Early mouse caudal development relies on crosstalk between retinoic acid,Shh and Fgf signalling pathways. *Development* **136,** 665–676; 10.1242/dev.016204 (2009).

30. Green, D. G. *et al.* Wnt signaling regulates neural plate patterning in distinct temporal phases with dynamic transcriptional outputs. *Developmental biology* **462,** 152–164; 10.1016/j.ydbio.2020.03.016 (2020).

31. Li, B., Kuriyama, S., Moreno, M. & Mayor, R. The posteriorizing gene Gbx2 is a direct target of Wnt signalling and the earliest factor in neural crest induction. *Development* **136,** 3267–3278; 10.1242/dev.036954 (2009).

32. Braun, M. M., Etheridge, A., Bernard, A., Robertson, C. P. & Roelink, H. Wnt signaling is required at distinct stages of development for the induction of the posterior forebrain. *Development* **130,** 5579–5587; 10.1242/dev.00685 (2003).

33. Kobayashi, D. *et al.* Early subdivisions in the neural plate define distinct competence for inductive signals. *Development* **129,** 83–93; 10.1242/dev.129.1.83 (2002).

34. Lagutin, O. V. *et al.* Six3 repression of Wnt signaling in the anterior neuroectoderm is essential for vertebrate forebrain development. *Genes & development* **17,** 368–379; 10.1101/gad.1059403 (2003).

35. Esteve, P., Morcillo, J. & Bovolenta, P. Early and dynamic expression of cSfrp1 during chick embryo development. *Mechanisms of development* **97,** 217–221; 10.1016/S0925-4773(00)00421-4 (2000).

36. Houart, C. *et al.* Establishment of the telencephalon during gastrulation by local antagonism of Wnt signaling. *Neuron* **35,** 255–265; 10.1016/s0896-6273(02)00751-1 (2002).

37. Baker, J. C., Beddington, R. S. & Harland, R. M. Wnt signaling in Xenopus embryos inhibits bmp4 expression and activates neural development. *Genes & development* **13,** 3149–3159; 10.1101/gad.13.23.3149 (1999).

38. Roelink, H. & Nusse, R. Expression of two members of the Wnt family during mouse development--restricted temporal and spatial patterns in the developing neural tube. *Genes & development* **5,** 381–388; 10.1101/gad.5.3.381 (1991).

39. Hollyday, M., McMahon, J. A. & McMahon, A. P. Wnt expression patterns in chick embryo nervous system. *Mechanisms of development* **52,** 9–25; 10.1016/0925-4773(95)00385-e (1995).

40. Riley, B. B. *et al.* Rhombomere boundaries are Wnt signaling centers that regulate metameric patterning in the zebrafish hindbrain. *Developmental dynamics : an official publication of the American Association of Anatomists* **231,** 278–291; 10.1002/dvdy.20133 (2004).

41. Parr, B. A., Shea, M. J., Vassileva, G. & McMahon, A. P. Mouse Wnt genes exhibit discrete domains of expression in the early embryonic CNS and limb buds. *Development* **119,** 247–261; 10.1242/dev.119.1.247 (1993).

42. Braun, E. *et al.* Comprehensive cell atlas of the first-trimester developing human brain. *Science (New York, N.Y.)* **382,** eadf1226; 10.1126/science.adf1226 (2023).

43. Matsunaga, E., Katahira, T. & Nakamura, H. Role of Lmx1b and Wnt1 in mesencephalon and metencephalon development. *Development* **129,** 5269–5277; 10.1242/dev.129.22.5269 (2002).

44. Rash, B. G. & Grove, E. A. Patterning the dorsal telencephalon: a role for sonic hedgehog? *The Journal of neuroscience : the official journal of the Society for Neuroscience* **27,** 11595–11603; 10.1523/JNEUROSCI.3204-07.2007 (2007).

45. Aoto, K., Nishimura, T., Eto, K. & Motoyama, J. Mouse GLI3 regulates Fgf8 expression and apoptosis in the developing neural tube, face, and limb bud. *Developmental biology* **251,** 320–332; 10.1006/dbio.2002.0811 (2002).

46. Theil, T., Alvarez-Bolado, G., Walter, A. & Rüther, U. Gli3 is required for Emx gene expression during dorsal telencephalon development. *Development* **126,** 3561–3571; 10.1242/dev.126.16.3561 (1999).

47. Tole, S., Ragsdale, C. W. & Grove, E. A. Dorsoventral patterning of the telencephalon is disrupted in the mouse mutant extra-toes(J). *Developmental biology* **217,** 254–265; 10.1006/dbio.1999.9509 (2000).

48. Shimamura, K., Hartigan, D. J., Martinez, S., Puelles, L. & Rubenstein, J. L. Longitudinal organization of the anterior neural plate and neural tube. *Development* **121,** 3923–3933; 10.1242/dev.121.12.3923 (1995).

49. Hatini, V., Tao, W. & Lai, E. Expression of winged helix genes, BF-1 and BF-2, define adjacent domains within the developing forebrain and retina. *Journal of neurobiology* **25,** 1293–1309; 10.1002/neu.480251010 (1994).

50. Tao, W. & Lai, E. Telencephalon-restricted expression of BF-1, a new member of the HNF-3/fork head gene family, in the developing rat brain. *Neuron* **8,** 957–966; 10.1016/0896-6273(92)90210-5 (1992).

51. Inoue, T., Nakamura, S. & Osumi, N. Fate mapping of the mouse prosencephalic neural plate. *Developmental biology* **219,** 373–383; 10.1006/dbio.2000.9616 (2000).

52. Corbin, J. G., Rutlin, M., Gaiano, N. & Fishell, G. Combinatorial function of the homeodomain proteins Nkx2.1 and Gsh2 in ventral telencephalic patterning. *Development* **130,** 4895–4906; 10.1242/dev.00717 (2003).

53. Ericson, J. *et al.* Sonic hedgehog induces the differentiation of ventral forebrain neurons: a common signal for ventral patterning within the neural tube. *Cell* **81,** 747–756; 10.1016/0092-8674(95)90536-7 (1995).

54. Echelard, Y. *et al.* Sonic hedgehog, a member of a family of putative signaling molecules, is implicated in the regulation of CNS polarity. *Cell* **75,** 1417–1430; 10.1016/0092-8674(93)90627-3 (1993).

55. Ruiz i Altaba, A. Gli proteins encode context-dependent positive and negative functions: implications for development and disease. *Development* **126,** 3205–3216; 10.1242/dev.126.14.3205 (1999).

56. Hui, C. C., Slusarski, D., Platt, K. A., Holmgren, R. & Joyner, A. L. Expression of three mouse homologs of the Drosophila segment polarity gene cubitus interruptus, Gli, Gli-2, and Gli-3, in ectoderm- and mesoderm-derived tissues suggests multiple roles during postimplantation development. *Developmental biology* **162,** 402–413; 10.1006/dbio.1994.1097 (1994).

57. Lee, J., Platt, K. A., Censullo, P. & Ruiz i Altaba, A. Gli1 is a target of Sonic hedgehog that induces ventral neural tube development. *Development* **124,** 2537–2552; 10.1242/dev.124.13.2537 (1997).

58. Ruiz i Altaba, A. Combinatorial Gli gene function in floor plate and neuronal inductions by Sonic hedgehog. *Development* **125,** 2203–2212; 10.1242/dev.125.12.2203 (1998).

59. Hettige, N. C. & Ernst, C. FOXG1 Dose in Brain Development. *Frontiers in pediatrics* **7,** 482; 10.3389/fped.2019.00482 (2019).

60. Danesin, C. *et al.* Integration of telencephalic Wnt and hedgehog signaling center activities by Foxg1. *Developmental cell* **16,** 576–587; 10.1016/j.devcel.2009.03.007 (2009).

61. Martynoga, B., Morrison, H., Price, D. J. & Mason, J. O. Foxg1 is required for specification of ventral telencephalon and region-specific regulation of dorsal telencephalic precursor proliferation and apoptosis. *Developmental biology* **283,** 113–127; 10.1016/j.ydbio.2005.04.005 (2005).

62. Martinez-Ferre, A. *et al.* Fgf15 regulates thalamic development by controlling the expression of proneural genes. *Brain structure & function* **221,** 3095–3109; 10.1007/s00429-015-1089-5 (2016).

63. Xu, J., Lawshe, A., MacArthur, C. A. & Ornitz, D. M. Genomic structure, mapping, activity and expression of fibroblast growth factor 17. *Mechanisms of development* **83,** 165–178; 10.1016/S0925-4773(99)00034-9 (1999).

64. Theil, T., Dominguez-Frutos, E. & Schimmang, T. Differential requirements for Fgf3 and Fgf8 during mouse forebrain development. *Developmental dynamics : an official publication of the American Association of Anatomists* **237,** 3417–3423; 10.1002/dvdy.21765 (2008).

65. Walshe, J. & Mason, I. Unique and combinatorial functions of Fgf3 and Fgf8 during zebrafish forebrain development. *Development* **130,** 4337–4349; 10.1242/dev.00660 (2003).

66. Hébert, J. M., Lin, M., Partanen, J., Rossant, J. & McConnell, S. K. FGF signaling through FGFR1 is required for olfactory bulb morphogenesis. *Development* **130,** 1101–1111; 10.1242/dev.00334 (2003).

67. Gutin, G. *et al.* FGF signalling generates ventral telencephalic cells independently of SHH. *Development* **133,** 2937–2946; 10.1242/dev.02465 (2006).

68. Shimamura, K. & Rubenstein, J. L. Inductive interactions direct early regionalization of the mouse forebrain. *Development* **124,** 2709–2718; 10.1242/dev.124.14.2709 (1997).

69. Storm, E. E. *et al.* Dose-dependent functions of Fgf8 in regulating telencephalic patterning centers. *Development* **133,** 1831–1844; 10.1242/dev.02324 (2006).

70. Anderson, R. M., Lawrence, A. R., Stottmann, R. W., Bachiller, D. & Klingensmith, J. Chordin and noggin promote organizing centers of forebrain development in the mouse. *Development* **129,** 4975–4987; 10.1242/dev.129.21.4975 (2002).

71. Bachiller, D. *et al.* The organizer factors Chordin and Noggin are required for mouse forebrain development. *Nature* **403,** 658–661; 10.1038/35001072 (2000).

72. Chizhikov, V. V. & Millen, K. J. Roof plate-dependent patterning of the vertebrate dorsal central nervous system. *Developmental biology* **277,** 287–295; 10.1016/j.ydbio.2004.10.011 (2005).

73. Hébert, J. M., Mishina, Y. & McConnell, S. K. BMP signaling is required locally to pattern the dorsal telencephalic midline. *Neuron* **35,** 1029–1041; 10.1016/s0896-6273(02)00900-5 (2002).

74. Timmer, J. R., Wang, C. & Niswander, L. BMP signaling patterns the dorsal and intermediate neural tube via regulation of homeobox and helix-loop-helix transcription factors. *Development* **129,** 2459–2472; 10.1242/dev.129.10.2459 (2002).

75. Theil, T., Aydin, S., Koch, S., Grotewold, L. & Rüther, U. Wnt and Bmp signalling cooperatively regulate graded Emx2 expression in the dorsal telencephalon. *Development* **129,** 3045–3054; 10.1242/dev.129.13.3045 (2002).

76. Backman, M. *et al.* Effects of canonical Wnt signaling on dorso-ventral specification of the mouse telencephalon. *Developmental biology* **279,** 155–168; 10.1016/j.ydbio.2004.12.010 (2005).

77. Alvarez-Medina, R., Cayuso, J., Okubo, T., Takada, S. & Martí, E. Wnt canonical pathway restricts graded Shh/Gli patterning activity through the regulation of Gli3 expression. *Development* **135,** 237–247; 10.1242/dev.012054 (2008).

78. Furuta, Y., Piston, D. W. & Hogan, B. L. Bone morphogenetic proteins (BMPs) as regulators of dorsal forebrain development. *Development* **124,** 2203–2212; 10.1242/dev.124.11.2203 (1997).

79. Caronia-Brown, G., Yoshida, M., Gulden, F., Assimacopoulos, S. & Grove, E. A. The cortical hem regulates the size and patterning of neocortex. *Development* **141,** 2855–2865; 10.1242/dev.106914 (2014).

80. Ikeya, M., Lee, S. M., Johnson, J. E., McMahon, A. P. & Takada, S. Wnt signalling required for expansion of neural crest and CNS progenitors. *Nature* **389,** 966–970; 10.1038/40146 (1997).

81. Zhou, C.-J., Borello, U., Rubenstein, J. L. R. & Pleasure, S. J. Neuronal production and precursor proliferation defects in the neocortex of mice with loss of function in the canonical Wnt signaling pathway. *Neuroscience* **142,** 1119–1131; 10.1016/j.neuroscience.2006.07.007 (2006).

82. Lee, S. M., Tole, S., Grove, E. & McMahon, A. P. A local Wnt-3a signal is required for development of the mammalian hippocampus. *Development* **127,** 457–467; 10.1242/dev.127.3.457 (2000).

83. Galceran, J., Miyashita-Lin, E. M., Devaney, E., Rubenstein, J. L. & Grosschedl, R. Hippocampus development and generation of dentate gyrus granule cells is regulated by LEF1. *Development* **127,** 469–482; 10.1242/dev.127.3.469 (2000).

84. Panchision, D. M. *et al.* Sequential actions of BMP receptors control neural precursor cell production and fate. *Genes & development* **15,** 2094–2110; 10.1101/gad.894701 (2001).

85. Monuki, E. S., Porter, F. D. & Walsh, C. A. Patterning of the dorsal telencephalon and cerebral cortex by a roof plate-Lhx2 pathway. *Neuron* **32,** 591–604; 10.1016/s0896-6273(01)00504-9 (2001).

86. Mangale, V. S. *et al.* Lhx2 selector activity specifies cortical identity and suppresses hippocampal organizer fate. *Science (New York, N.Y.)* **319,** 304–309; 10.1126/science.1151695 (2008).

87. Fode, C. *et al.* A role for neural determination genes in specifying the dorsoventral identity of telencephalic neurons. *Genes & development* **14,** 67–80 (2000).

88. Nery, S., Fishell, G. & Corbin, J. G. The caudal ganglionic eminence is a source of distinct cortical and subcortical cell populations. *Nature neuroscience* **5,** 1279–1287; 10.1038/nn971 (2002).

89. Simões-Costa, M. & Bronner, M. E. Establishing neural crest identity: a gene regulatory recipe. *Development* **142,** 242–257; 10.1242/dev.105445 (2015).

90. Southard-Smith, E. M., Kos, L. & Pavan, W. J. Sox10 mutation disrupts neural crest development in Dom Hirschsprung mouse model. *Nature genetics* **18,** 60–64; 10.1038/ng0198-60 (1998).

91. Labosky, P. A. & Kaestner, K. H. The winged helix transcription factor Hfh2 is expressed in neural crest and spinal cord during mouse development. *Mechanisms of development* **76,** 185–190; 10.1016/s0925-4773(98)00105-1 (1998).

92. Bronner, M. E. & LeDouarin, N. M. Evolution and Development of the Neural Crest: An Overview. *Developmental biology* **366,** 2–9; 10.1016/j.ydbio.2011.12.042 (2012).

93. Siismets, E. M. & Hatch, N. E. Cranial Neural Crest Cells and Their Role in the Pathogenesis of Craniofacial Anomalies and Coronal Craniosynostosis. *Journal of developmental biology* **8**; 10.3390/jdb8030018 (2020).

94. Hartsock, A. & Nelson, W. J. Adherens and tight junctions: structure, function and connections to the actin cytoskeleton. *Biochimica et biophysica acta* **1778,** 660–669; 10.1016/j.bbamem.2007.07.012 (2008).

95. Penisson, M., Ladewig, J., Belvindrah, R. & Francis, F. Genes and Mechanisms Involved in the Generation and Amplification of Basal Radial Glial Cells. *Frontiers in cellular neuroscience* **13,** 381; 10.3389/fncel.2019.00381 (2019).

96. Nowakowski, T. J., Pollen, A. A., Sandoval-Espinosa, C. & Kriegstein, A. R. Transformation of the Radial Glia Scaffold Demarcates Two Stages of Human Cerebral Cortex Development. *Neuron* **91,** 1219–1227; 10.1016/j.neuron.2016.09.005 (2016).

97. Cadwell, C. R., Bhaduri, A., Mostajo-Radji, M. A., Keefe, M. G. & Nowakowski, T. J. Development and Arealization of the Cerebral Cortex. *Neuron* **103,** 980–1004; 10.1016/j.neuron.2019.07.009 (2019).

98. La Pompa, J. L. de *et al.* Conservation of the Notch signalling pathway in mammalian neurogenesis. *Development* **124,** 1139–1148; 10.1242/dev.124.6.1139 (1997).

99. Lardelli, M., Williams, R., Mitsiadis, T. & Lendahl, U. Expression of the Notch 3 intracellular domain in mouse central nervous system progenitor cells is lethal and leads to disturbed neural tube development. *Mechanisms of development* **59,** 177–190; 10.1016/0925-4773(96)00589-8 (1996).

100. Chitnis, A. B. The role of Notch in lateral inhibition and cell fate specification. *Molecular and cellular neurosciences* **6,** 311–321; 10.1006/mcne.1995.1024 (1995).

101. Kageyama, R. & Ohtsuka, T. The Notch-Hes pathway in mammalian neural development. *Cell research* **9,** 179–188; 10.1038/sj.cr.7290016 (1999).

102. Sato, M., Yasugi, T., Minami, Y., Miura, T. & Nagayama, M. Notch-mediated lateral inhibition regulates proneural wave propagation when combined with EGF-mediated reaction diffusion. *Proceedings of the National Academy of Sciences of the United States of America* **113,** E5153-62; 10.1073/pnas.1602739113 (2016).

103. Gaiano, N., Nye, J. S. & Fishell, G. Radial glial identity is promoted by Notch1 signaling in the murine forebrain. *Neuron* **26,** 395–404; 10.1016/s0896-6273(00)81172-1 (2000).

104. Tanigaki, K. *et al.* Notch1 and Notch3 instructively restrict bFGF-responsive multipotent neural progenitor cells to an astroglial fate. *Neuron* **29,** 45–55; 10.1016/s0896-6273(01)00179-9 (2001).

105. Dinh Duong, T. A. *et al.* FGF Signaling Directs the Cell Fate Switch from Neurons to Astrocytes in the Developing Mouse Cerebral Cortex. *The Journal of neuroscience : the official journal of the Society for Neuroscience* **39,** 6081–6094; 10.1523/JNEUROSCI.2195-18.2019 (2019).

106. Machon, O. *et al.* A dynamic gradient of Wnt signaling controls initiation of neurogenesis in the mammalian cortex and cellular specification in the hippocampus. *Developmental biology* **311,** 223–237; 10.1016/j.ydbio.2007.08.038 (2007).

107. Woodhead, G. J., Mutch, C. A., Olson, E. C. & Chenn, A. Cell-autonomous beta-catenin signaling regulates cortical precursor proliferation. *The Journal of neuroscience : the official journal of the Society for Neuroscience* **26,** 12620–12630; 10.1523/JNEUROSCI.3180-06.2006 (2006).

108. Xuan, S. *et al.* Winged helix transcription factor BF-1 is essential for the development of the cerebral hemispheres. *Neuron* **14,** 1141–1152; 10.1016/0896-6273(95)90262-7 (1995).

109. Andrews, M. G. *et al.* LIF signaling regulates outer radial glial to interneuron fate during human cortical development. *Cell stem cell* **30,** 1382-1391.e5; 10.1016/j.stem.2023.08.009 (2023).

110. Smart, I. H. M., Dehay, C., Giroud, P., Berland, M. & Kennedy, H. Unique morphological features of the proliferative zones and postmitotic compartments of the neural epithelium giving rise to striate and extrastriate cortex in the monkey. *Cerebral cortex (New York, N.Y. : 1991)* **12,** 37–53; 10.1093/cercor/12.1.37 (2002).

111. Angevine, J. B. & Sidman, R. L. Autoradiographic study of cell migration during histogenesis of cerebral cortex in the mouse. *Nature* **192,** 766–768; 10.1038/192766b0 (1961).

112. Rakic, P. Neurons in rhesus monkey visual cortex: systematic relation between time of origin and eventual disposition. *Science (New York, N.Y.)* **183,** 425–427; 10.1126/science.183.4123.425 (1974).

113. Meyer, G., Schaaps, J. P., Moreau, L. & Goffinet, A. M. Embryonic and early fetal development of the human neocortex. *The Journal of neuroscience : the official journal of the Society for Neuroscience* **20,** 1858–1868; 10.1523/JNEUROSCI.20-05-01858.2000 (2000).

114. Meyer, G. & González-Gómez, M. The Subpial Granular Layer and Transient Versus Persisting Cajal-Retzius Neurons of the Fetal Human Cortex. *Cerebral cortex (New York, N.Y. : 1991)* **28,** 2043–2058; 10.1093/cercor/bhx110 (2018).

115. Ledonne, F. *et al.* Targeted Inactivation of Bax Reveals a Subtype-Specific Mechanism of Cajal-Retzius Neuron Death in the Postnatal Cerebral Cortex. *Cell reports* **17,** 3133–3141; 10.1016/j.celrep.2016.11.074 (2016).

116. Ogawa, M. *et al.* The reeler gene-associated antigen on Cajal-Retzius neurons is a crucial molecule for laminar organization of cortical neurons. *Neuron* **14,** 899–912; 10.1016/0896-6273(95)90329-1 (1995).

117. D'Arcangelo, G. *et al.* A protein related to extracellular matrix proteins deleted in the mouse mutant reeler. *Nature* **374,** 719–723; 10.1038/374719a0 (1995).

118. Fietz, S. A. *et al.* OSVZ progenitors of human and ferret neocortex are epithelial-like and expand by integrin signaling. *Nature neuroscience* **13,** 690–699; 10.1038/nn.2553 (2010).

119. Hansen, D. V., Lui, J. H., Parker, P. R. L. & Kriegstein, A. R. Neurogenic radial glia in the outer subventricular zone of human neocortex. *Nature* **464,** 554–561; 10.1038/nature08845 (2010).

120. Ma, T. *et al.* Subcortical origins of human and monkey neocortical interneurons. *Nature neuroscience* **16,** 1588–1597; 10.1038/nn.3536 (2013).

121. Hanashima, C., Shen, L., Li, S. C. & Lai, E. Brain factor-1 controls the proliferation and differentiation of neocortical progenitor cells through independent mechanisms. *The Journal of neuroscience : the official journal of the Society for Neuroscience* **22,** 6526–6536; 10.1523/JNEUROSCI.22-15-06526.2002 (2002).

122. Hou, P.-S., Miyoshi, G. & Hanashima, C. Sensory cortex wiring requires preselection of short- and long-range projection neurons through an Egr-Foxg1-COUP-TFI network. *Nature communications* **10,** 3581; 10.1038/s41467-019-11043-w (2019).

123. Kumamoto, T. *et al.* Foxg1 coordinates the switch from nonradially to radially migrating glutamatergic subtypes in the neocortex through spatiotemporal repression. *Cell reports* **3,** 931–945; 10.1016/j.celrep.2013.02.023 (2013).

124. Srinivasan, K. *et al.* A network of genetic repression and derepression specifies projection fates in the developing neocortex. *Proceedings of the National Academy of Sciences of the United States of America* **109,** 19071–19078; 10.1073/pnas.1216793109 (2012).

125. Sandberg, M. *et al.* Transcriptional Networks Controlled by NKX2-1 in the Development of Forebrain GABAergic Neurons. *Neuron* **91,** 1260–1275; 10.1016/j.neuron.2016.08.020 (2016).

126. Howard, B. M. *et al.* Radial glia cells in the developing human brain. *The Neuroscientist : a review journal bringing neurobiology, neurology and psychiatry* **14,** 459–473; 10.1177/1073858407313512 (2008).

127. Malatesta, P. *et al.* Neuronal or glial progeny: regional differences in radial glia fate. *Neuron* **37,** 751–764; 10.1016/S0896-6273(03)00116-8 (2003).

128. Wang, M., Li, Q. & Liu, L. Factors and Methods for the Detection of Gene Expression Regulation. *Biomolecules* **13**; 10.3390/biom13020304 (2023).

129. Liaci, C. *et al.* The Emerging Roles of Long Non-Coding RNAs in Intellectual Disability and Related Neurodevelopmental Disorders. *International journal of molecular sciences* **23**; 10.3390/ijms23116118 (2022).

130. van de Vondervoort, I. I. G. M. *et al.* Long non-coding RNAs in neurodevelopmental disorders. *Frontiers in molecular neuroscience* **6,** 53; 10.3389/fnmol.2013.00053 (2013).

131. Centore, R. C., Sandoval, G. J., Soares, L. M. M., Kadoch, C. & Chan, H. M. Mammalian SWI/SNF Chromatin Remodeling Complexes: Emerging Mechanisms and Therapeutic Strategies. *Trends in genetics : TIG* **36,** 936–950; 10.1016/j.tig.2020.07.011 (2020).

132. Reyes, A. A., Marcum, R. D. & He, Y. Structure and Function of Chromatin Remodelers. *Journal of molecular biology* **433,** 166929; 10.1016/j.jmb.2021.166929 (2021).

133. Willhoft, O. & Wigley, D. B. INO80 and SWR1 complexes: the non-identical twins of chromatin remodelling. *Current opinion in structural biology* **61,** 50–58; 10.1016/j.sbi.2019.09.002 (2020).

134. Hota, S. K. *et al.* Dynamic BAF chromatin remodeling complex subunit inclusion promotes temporally distinct gene expression programs in cardiogenesis. *Development* **146**; 10.1242/dev.174086 (2019).

135. Bultman, S. J. *et al.* Maternal BRG1 regulates zygotic genome activation in the mouse. *Genes & development* **20,** 1744–1754; 10.1101/gad.1435106 (2006).

136. Forcales, S. V. *et al.* Signal-dependent incorporation of MyoD-BAF60c into Brg1-based SWI/SNF chromatin-remodelling complex. *The EMBO journal* **31,** 301–316; 10.1038/emboj.2011.391 (2012).

137. Forcales, S.-V. The BAF60c-MyoD complex poises chromatin for rapid transcription. *Bioarchitecture* **2,** 104–109; 10.4161/bioa.20970 (2012).

138. Lickert, H. *et al.* Baf60c is essential for function of BAF chromatin remodelling complexes in heart development. *Nature* **432,** 107–112; 10.1038/nature03071 (2004).

139. Sun, X. *et al.* Cardiac-enriched BAF chromatin-remodeling complex subunit Baf60c regulates gene expression programs essential for heart development and function. *Biology open* **7**; 10.1242/bio.029512 (2018).

140. Alfert, A., Moreno, N. & Kerl, K. The BAF complex in development and disease. *Epigenetics & chromatin* **12,** 19; 10.1186/s13072-019-0264-y (2019).

141. Ieda, M. *et al.* Direct reprogramming of fibroblasts into functional cardiomyocytes by defined factors. *Cell* **142,** 375–386; 10.1016/j.cell.2010.07.002 (2010).

142. Cairns, B. R. Chromatin remodeling machines: similar motors, ulterior motives. *Trends in biochemical sciences* **23,** 20–25; 10.1016/S0968-0004(97)01160-2 (1998).

143. Mashtalir, N. *et al.* A Structural Model of the Endogenous Human BAF Complex Informs Disease Mechanisms. *Cell* **183,** 802-817.e24; 10.1016/j.cell.2020.09.051 (2020).

144. He, S. *et al.* Structure of nucleosome-bound human BAF complex. *Science (New York, N.Y.)* **367,** 875–881; 10.1126/science.aaz9761 (2020).

145. Varga, J., Kube, M., Luck, K. & Schick, S. The BAF chromatin remodeling complexes: structure, function, and synthetic lethalities. *Biochemical Society transactions* **49,** 1489–1503; 10.1042/BST20190960 (2021).

146. Wang, W. *et al.* Diversity and specialization of mammalian SWI/SNF complexes. *Genes & development* **10,** 2117–2130; 10.1101/gad.10.17.2117 (1996).

147. Lessard, J. *et al.* An essential switch in subunit composition of a chromatin remodeling complex during neural development. *Neuron* **55,** 201–215; 10.1016/j.neuron.2007.06.019 (2007).

148. Son, E. Y. & Crabtree, G. R. The role of BAF (mSWI/SNF) complexes in mammalian neural development. *American journal of medical genetics. Part C, Seminars in medical genetics* **166C,** 333–349; 10.1002/ajmg.c.31416 (2014).

149. Alpsoy, A. & Dykhuizen, E. C. Glioma tumor suppressor candidate region gene 1 (GLTSCR1) and its paralog GLTSCR1-like form SWI/SNF chromatin remodeling subcomplexes. *The Journal of biological chemistry* **293,** 3892–3903; 10.1074/jbc.RA117.001065 (2018).

150. Kidder, B. L., Palmer, S. & Knott, J. G. SWI/SNF-Brg1 regulates self-renewal and occupies core pluripotency-related genes in embryonic stem cells. *Stem cells (Dayton, Ohio)* **27,** 317–328; 10.1634/stemcells.2008-0710 (2009).

151. Ho, L. *et al.* An embryonic stem cell chromatin remodeling complex, esBAF, is essential for embryonic stem cell self-renewal and pluripotency. *Proceedings of the National Academy of Sciences of the United States of America* **106,** 5181–5186; 10.1073/pnas.0812889106 (2009).

152. Bultman, S. *et al.* A Brg1 null mutation in the mouse reveals functional differences among mammalian SWI/SNF complexes. *Molecular cell* **6,** 1287–1295; 10.1016/s1097-2765(00)00127-1 (2000).

153. Han, D. *et al.* SRG3, a core component of mouse SWI/SNF complex, is essential for extra-embryonic vascular development. *Developmental biology* **315,** 136–146; 10.1016/j.ydbio.2007.12.024 (2008).

154. Roberts, C. W., Galusha, S. A., McMenamin, M. E., Fletcher, C. D. & Orkin, S. H. Haploinsufficiency of Snf5 (integrase interactor 1) predisposes to malignant rhabdoid tumors in mice. *Proceedings of the National Academy of Sciences of the United States of America* **97,** 13796–13800; 10.1073/pnas.250492697 (2000).

155. Reyes, J. C. *et al.* Altered control of cellular proliferation in the absence of mammalian brahma (SNF2alpha). *The EMBO journal* **17,** 6979–6991; 10.1093/emboj/17.23.6979 (1998).

156. Kim, J. K. *et al.* Srg3, a mouse homolog of yeast SWI3, is essential for early embryogenesis and involved in brain development. *Molecular and cellular biology* **21,** 7787–7795; 10.1128/MCB.21.22.7787-7795.2001 (2001).

157. Zhan, X., Shi, X., Zhang, Z., Chen, Y. & Wu, J. I. Dual role of Brg chromatin remodeling factor in Sonic hedgehog signaling during neural development. *Proceedings of the National Academy of Sciences of the United States of America* **108,** 12758–12763; 10.1073/pnas.1018510108 (2011).

158. Matsumoto, S. *et al.* Brg1 is required for murine neural stem cell maintenance and gliogenesis. *Developmental biology* **289,** 372–383; 10.1016/j.ydbio.2005.10.044 (2006).

159. Limpert, A. S. *et al.* NF-κB forms a complex with the chromatin remodeler BRG1 to regulate Schwann cell differentiation. *The Journal of neuroscience : the official journal of the Society for Neuroscience* **33,** 2388–2397; 10.1523/JNEUROSCI.3223-12.2013 (2013).

160. Narayanan, R. *et al.* Loss of BAF (mSWI/SNF) Complexes Causes Global Transcriptional and Chromatin State Changes in Forebrain Development. *Cell reports* **13,** 1842–1854; 10.1016/j.celrep.2015.10.046 (2015).

161. Ninkovic, J. *et al.* The BAF complex interacts with Pax6 in adult neural progenitors to establish a neurogenic cross-regulatory transcriptional network. *Cell stem cell* **13,** 403–418; 10.1016/j.stem.2013.07.002 (2013).

162. Tuoc, T. C. *et al.* Chromatin regulation by BAF170 controls cerebral cortical size and thickness. *Developmental cell* **25,** 256–269; 10.1016/j.devcel.2013.04.005 (2013).

163. Tuoc, T. C., Narayanan, R. & Stoykova, A. BAF chromatin remodeling complex: cortical size regulation and beyond. *Cell cycle (Georgetown, Tex.)* **12,** 2953–2959; 10.4161/cc.25999 (2013).

164. Yu, Y. *et al.* Olig2 targets chromatin remodelers to enhancers to initiate oligodendrocyte differentiation. *Cell* **152,** 248–261; 10.1016/j.cell.2012.12.006 (2013).

165. Weider, M. *et al.* Chromatin-remodeling factor Brg1 is required for Schwann cell differentiation and myelination. *Developmental cell* **23,** 193–201; 10.1016/j.devcel.2012.05.017 (2012).

166. Bachmann, C. *et al.* mSWI/SNF (BAF) Complexes Are Indispensable for the Neurogenesis and Development of Embryonic Olfactory Epithelium. *PLoS genetics* **12,** e1006274; 10.1371/journal.pgen.1006274 (2016).

167. Braun, S. M. G. *et al.* BAF subunit switching regulates chromatin accessibility to control cell cycle exit in the developing mammalian cortex. *Genes & development* **35,** 335–353; 10.1101/gad.342345.120 (2021).

168. Staahl, B. T. *et al.* Kinetic analysis of npBAF to nBAF switching reveals exchange of SS18 with CREST and integration with neural developmental pathways. *The Journal of neuroscience : the official journal of the Society for Neuroscience* **33,** 10348–10361; 10.1523/JNEUROSCI.1258-13.2013 (2013).

169. Aizawa, H. *et al.* Dendrite development regulated by CREST, a calcium-regulated transcriptional activator. *Science (New York, N.Y.)* **303,** 197–202; 10.1126/science.1089845 (2004).

170. Wu, J. I. *et al.* Regulation of dendritic development by neuron-specific chromatin remodeling complexes. *Neuron* **56,** 94–108; 10.1016/j.neuron.2007.08.021 (2007).

171. Yoo, A. S. *et al.* MicroRNA-mediated conversion of human fibroblasts to neurons. *Nature* **476,** 228–231; 10.1038/nature10323 (2011).

172. Bögershausen, N. & Wollnik, B. Mutational Landscapes and Phenotypic Spectrum of SWI/SNF-Related Intellectual Disability Disorders. *Frontiers in molecular neuroscience* **11,** 252; 10.3389/fnmol.2018.00252 (2018).

173. Bramswig, N. C. *et al.* Heterozygosity for ARID2 loss-of-function mutations in individuals with a Coffin-Siris syndrome-like phenotype. *Human genetics* **136,** 297–305; 10.1007/s00439-017-1757-z (2017).

174. van Paemel, R. *et al.* Confirmation of an ARID2 defect in SWI/SNF-related intellectual disability. *American journal of medical genetics. Part A* **173,** 3104–3108; 10.1002/ajmg.a.38407 (2017).

175. van Houdt, J. K. J. *et al.* Heterozygous missense mutations in SMARCA2 cause Nicolaides-Baraitser syndrome. *Nature genetics* **44,** 445-9, S1; 10.1038/ng.1105 (2012).

176. Gao, F. *et al.* Heterozygous Mutations in SMARCA2 Reprogram the Enhancer Landscape by Global Retargeting of SMARCA4. *Molecular cell* **75,** 891-904.e7; 10.1016/j.molcel.2019.06.024 (2019).

177. Li, C. *et al.* Single-cell brain organoid screening identifies developmental defects in autism. *Nature* **621,** 373–380; 10.1038/s41586-023-06473-y (2023).

178. Paulsen, B. *et al.* Autism genes converge on asynchronous development of shared neuron classes. *Nature* **602,** 268–273; 10.1038/s41586-021-04358-6 (2022).

179. Hoffman, J. A. *et al.* BRG1 establishes the neuroectodermal chromatin landscape to restrict dorsal cell fates. *Science advances* **10,** eadj5107; 10.1126/sciadv.adj5107 (2024).

180. Koga, M. *et al.* Involvement of SMARCA2/BRM in the SWI/SNF chromatin-remodeling complex in schizophrenia. *Human molecular genetics* **18,** 2483–2494; 10.1093/hmg/ddp166 (2009).

181. Tsurusaki, Y. *et al.* Mutations affecting components of the SWI/SNF complex cause Coffin-Siris syndrome. *Nature genetics* **44,** 376–378; 10.1038/ng.2219 (2012).

182. Santen, G. W. E. *et al.* Mutations in SWI/SNF chromatin remodeling complex gene ARID1B cause Coffin-Siris syndrome. *Nature genetics* **44,** 379–380; 10.1038/ng.2217 (2012).

183. Halgren, C. *et al.* Corpus callosum abnormalities, intellectual disability, speech impairment, and autism in patients with haploinsufficiency of ARID1B. *Clinical genetics* **82,** 248–255; 10.1111/j.1399-0004.2011.01755.x (2012).

184. Wolff, D. *et al.* In-Frame Deletion and Missense Mutations of the C-Terminal Helicase Domain of SMARCA2 in Three Patients with Nicolaides-Baraitser Syndrome. *Molecular Syndromology* **2,** 237–244; 10.1159/000337323 (2012).

185. Tsurusaki, Y. *et al.* Coffin-Siris syndrome is a SWI/SNF complex disorder. *Clinical genetics* **85,** 548–554; 10.1111/cge.12225 (2014).

186. Takenouchi, T. *et al.* Hirschsprung disease as a yet undescribed phenotype in a patient with ARID1B mutation. *American journal of medical genetics. Part A* **170,** 3249–3252; 10.1002/ajmg.a.37861 (2016).

187. Smith, J. A., Holden, K. R., Friez, M. J., Jones, J. R. & Lyons, M. J. A novel familial autosomal dominant mutation in ARID1B causing neurodevelopmental delays, short

stature, and dysmorphic features. *American journal of medical genetics. Part A* **170,** 3313–3318; 10.1002/ajmg.a.37945 (2016).

188. Tang, S., Hughes, E., Lascelles, K., Simpson, M. A. & Pal, D. K. New SMARCA2 mutation in a patient with Nicolaides-Baraitser syndrome and myoclonic astatic epilepsy. *American journal of medical genetics. Part A* **173,** 195–199; 10.1002/ajmg.a.37935 (2017).
189. Errichiello, E. *et al.* SMARCA4 inactivating mutations cause concomitant Coffin-Siris syndrome, microphthalmia and small-cell carcinoma of the ovary hypercalcaemic type. *The Journal of pathology* **243,** 9–15; 10.1002/path.4926 (2017).
190. Karaer, K. Two cases of Nicolaides-Baraitser syndrome, one with a novel SMARCA2 variant. *Clinical dysmorphology* **29,** 189–192; 10.1097/MCD.0000000000000336 (2020).
191. Lu, G., Peng, Q., Wu, L., Zhang, J. & Ma, L. Identification of de novo mutations for ARID1B haploinsufficiency associated with Coffin-Siris syndrome 1 in three Chinese families via array-CGH and whole exome sequencing. *BMC medical genomics* **14,** 270; 10.1186/s12920-021-01119-2 (2021).
192. Qian, Y. *et al.* Novel Variants of the SMARCA4 Gene Associated with Autistic Features Rather Than Typical Coffin-Siris Syndrome in Eight Chinese Pediatric Patients. *Journal of autism and developmental disorders* **52,** 5033–5041; 10.1007/s10803-021-05365-2 (2022).
193. Lee, C. G. & Ki, C.-S. A Novel De Novo Heterozygous ARID1A Missense Variant Cluster in cis c.5954CG;6314CT;6334CT;6843GC causes a Coffin-Siris Syndrome. *Annals of laboratory medicine* **41,** 350–353; 10.3343/alm.2021.41.3.350 (2021).
194. Global, regional, and national burden of disorders affecting the nervous system, 1990-2021: a systematic analysis for the Global Burden of Disease Study 2021. *The Lancet. Neurology* **23,** 344–381; 10.1016/S1474-4422(24)00038-3 (2024).
195. Białoń, M. & Wąsik, A. Advantages and Limitations of Animal Schizophrenia Models. *International journal of molecular sciences* **23**; 10.3390/ijms23115968 (2022).
196. Carter, R. J. *et al.* Characterization of progressive motor deficits in mice transgenic for the human Huntington's disease mutation. *The Journal of neuroscience : the official journal of the Society for Neuroscience* **19,** 3248–3257; 10.1523/JNEUROSCI.19-08-03248.1999 (1999).
197. Oakley, H. *et al.* Intraneuronal beta-amyloid aggregates, neurodegeneration, and neuron loss in transgenic mice with five familial Alzheimer's disease mutations: potential factors in amyloid plaque formation. *The Journal of neuroscience : the official journal of the Society for Neuroscience* **26,** 10129–10140; 10.1523/JNEUROSCI.1202-06.2006 (2006).
198. Silverman, J. L., Yang, M., Lord, C. & Crawley, J. N. Behavioural phenotyping assays for mouse models of autism. *Nature reviews. Neuroscience* **11,** 490–502; 10.1038/nrn2851 (2010).
199. Mansvelder, H. D., Verhoog, M. B. & Goriounova, N. A. Synaptic plasticity in human cortical circuits: cellular mechanisms of learning and memory in the human brain? *Current opinion in neurobiology* **54,** 186–193; 10.1016/j.conb.2018.06.013 (2019).
200. Semple, B. D., Blomgren, K., Gimlin, K., Ferriero, D. M. & Noble-Haeusslein, L. J. Brain development in rodents and humans: Identifying benchmarks of maturation and vulnerability to injury across species. *Progress in neurobiology* **106-107,** 1–16; 10.1016/j.pneurobio.2013.04.001 (2013).

201. Akhtar, A. The flaws and human harms of animal experimentation. *Cambridge quarterly of healthcare ethics : CQ : the international journal of healthcare ethics committees* **24,** 407–419; 10.1017/S0963180115000079 (2015).

202. Franco, R. & Cedazo-Minguez, A. Successful therapies for Alzheimer's disease: why so many in animal models and none in humans? *Frontiers in pharmacology* **5,** 146; 10.3389/fphar.2014.00146 (2014).

203. Golding, H., Khurana, S. & Zaitseva, M. What Is the Predictive Value of Animal Models for Vaccine Efficacy in Humans? The Importance of Bridging Studies and Species-Independent Correlates of Protection. *Cold Spring Harbor perspectives in biology* **10**; 10.1101/cshperspect.a028902 (2018).

204. Dolmetsch, R. & Geschwind, D. H. The human brain in a dish: the promise of iPSC-derived neurons. *Cell* **145,** 831–834; 10.1016/j.cell.2011.05.034 (2011).

205. Ge, H. *et al.* Poly-L-ornithine promotes preferred differentiation of neural stem/progenitor cells via ERK signalling pathway. *Scientific reports* **5,** 15535; 10.1038/srep15535 (2015).

206. Hazel, T. & Müller, T. Culture of neuroepithelial stem cells. *Current protocols in neuroscience* **Chapter 3,** Unit 3.1; 10.1002/0471142301.ns0301s00 (2001).

207. Juopperi, T. A. *et al.* Astrocytes generated from patient induced pluripotent stem cells recapitulate features of Huntington's disease patient cells. *Molecular brain* **5,** 17; 10.1186/1756-6606-5-17 (2012).

208. Xu, J. *et al.* Rapid differentiation of hiPSCs into functional oligodendrocytes using an OLIG2 synthetic modified messenger RNA. *Communications biology* **5,** 1095; 10.1038/s42003-022-04043-y (2022).

209. Grskovic, M., Javaherian, A., Strulovici, B. & Daley, G. Q. Induced pluripotent stem cells--opportunities for disease modelling and drug discovery. *Nature reviews. Drug discovery* **10,** 915–929; 10.1038/nrd3577 (2011).

210. Juopperi, T. A., Song, H. & Ming, G.-L. Modeling neurological diseases using patient-derived induced pluripotent stem cells. *Future neurology* **6,** 363–373; 10.2217/FNL.11.14 (2011).

211. Xu, T. *et al.* Electrophysiological characterization of embryonic hippocampal neurons cultured in a 3D collagen hydrogel. *Biomaterials* **30,** 4377–4383; 10.1016/j.biomaterials.2009.04.047 (2009).

212. Lancaster, M. A. *et al.* Cerebral organoids model human brain development and microcephaly. *Nature* **501,** 373–379; 10.1038/nature12517 (2013).

213. Qian, X. *et al.* Brain-Region-Specific Organoids Using Mini-bioreactors for Modeling ZIKV Exposure. *Cell* **165,** 1238–1254; 10.1016/j.cell.2016.04.032 (2016).

214. Sloan, S. A. *et al.* Human Astrocyte Maturation Captured in 3D Cerebral Cortical Spheroids Derived from Pluripotent Stem Cells. *Neuron* **95,** 779-790.e6; 10.1016/j.neuron.2017.07.035 (2017).

215. Velasco, S. *et al.* Individual brain organoids reproducibly form cell diversity of the human cerebral cortex. *Nature* **570,** 523–527; 10.1038/s41586-019-1289-x (2019).

216. Fleck, J. S. *et al.* Inferring and perturbing cell fate regulomes in human brain organoids. *Nature* **621,** 365–372; 10.1038/s41586-022-05279-8 (2023).

217. Gordon, A. *et al.* Long-term maturation of human cortical organoids matches key early postnatal transitions. *Nature neuroscience* **24,** 331–342; 10.1038/s41593-021-00802-y (2021).

218. Eiraku, M. *et al.* Self-organized formation of polarized cortical tissues from ESCs and its active manipulation by extrinsic signals. *Cell stem cell* **3,** 519–532; 10.1016/j.stem.2008.09.002 (2008).

219. Miura, Y. *et al.* Generation of human striatal organoids and cortico-striatal assembloids from human pluripotent stem cells. *Nature biotechnology* **38,** 1421–1430; 10.1038/s41587-020-00763-w (2020).

220. Sakaguchi, H. *et al.* Generation of functional hippocampal neurons from self-organizing human embryonic stem cell-derived dorsomedial telencephalic tissue. *Nature communications* **6,** 8896; 10.1038/ncomms9896 (2015).

221. Jo, J. *et al.* Midbrain-like Organoids from Human Pluripotent Stem Cells Contain Functional Dopaminergic and Neuromelanin-Producing Neurons. *Cell stem cell* **19,** 248–257; 10.1016/j.stem.2016.07.005 (2016).

222. Xiang, Y. *et al.* hESC-Derived Thalamic Organoids Form Reciprocal Projections When Fused with Cortical Organoids. *Cell stem cell* **24,** 487-497.e7; 10.1016/j.stem.2018.12.015 (2019).

223. Wataya, T. *et al.* Minimization of exogenous signals in ES cell culture induces rostral hypothalamic differentiation. *Proceedings of the National Academy of Sciences of the United States of America* **105,** 11796–11801; 10.1073/pnas.0803078105 (2008).

224. Pellegrini, L. *et al.* Human CNS barrier-forming organoids with cerebrospinal fluid production. *Science (New York, N.Y.)* **369**; 10.1126/science.aaz5626 (2020).

225. Muguruma, K., Nishiyama, A., Kawakami, H., Hashimoto, K. & Sasai, Y. Self-organization of polarized cerebellar tissue in 3D culture of human pluripotent stem cells. *Cell reports* **10,** 537–550; 10.1016/j.celrep.2014.12.051 (2015).

226. Reumann, D. *et al.* In vitro modeling of the human dopaminergic system using spatially arranged ventral midbrain-striatum-cortex assembloids. *Nature methods* **20,** 2034–2047; 10.1038/s41592-023-02080-x (2023).

227. Kelava, I. & Lancaster, M. A. Dishing out mini-brains: Current progress and future prospects in brain organoid research. *Developmental biology* **420,** 199–209; 10.1016/j.ydbio.2016.06.037 (2016).

228. Gabriel, E. *et al.* CPAP promotes timely cilium disassembly to maintain neural progenitor pool. *The EMBO journal* **35,** 803–819; 10.15252/embj.201593679 (2016).

229. Mariani, J. *et al.* Modeling human cortical development in vitro using induced pluripotent stem cells. *Proceedings of the National Academy of Sciences of the United States of America* **109,** 12770–12775; 10.1073/pnas.1202944109 (2012).

230. Mellios, N. *et al.* MeCP2-regulated miRNAs control early human neurogenesis through differential effects on ERK and AKT signaling. *Molecular psychiatry* **23,** 1051–1065; 10.1038/mp.2017.86 (2018).

231. Bershteyn, M. *et al.* Human iPSC-derived cerebral organoids model cellular features of lissencephaly and reveal prolonged mitosis of outer radial glia. *Cell stem cell* **20,** 435-449.e4; 10.1016/j.stem.2016.12.007 (2017).

232. Iefremova, V. *et al.* An Organoid-Based Model of Cortical Development Identifies Non-Cell-Autonomous Defects in Wnt Signaling Contributing to Miller-Dieker Syndrome. *Cell reports* **19,** 50–59; 10.1016/j.celrep.2017.03.047 (2017).

233. Kang, Y. *et al.* A human forebrain organoid model of fragile X syndrome exhibits altered neurogenesis and highlights new treatment strategies. *Nature neuroscience* **24,** 1377–1391; 10.1038/s41593-021-00913-6 (2021).

234. Jacob, F. *et al.* A Patient-Derived Glioblastoma Organoid Model and Biobank Recapitulates Inter- and Intra-tumoral Heterogeneity. *Cell* **180,** 188-204.e22; 10.1016/j.cell.2019.11.036 (2020).

235. Goranci-Buzhala, G. *et al.* Rapid and Efficient Invasion Assay of Glioblastoma in Human Brain Organoids. *Cell reports* **31,** 107738; 10.1016/j.celrep.2020.107738 (2020).

236. Cakir, B. *et al.* Expression of the transcription factor PU.1 induces the generation of microglia-like cells in human cortical organoids. *Nature communications* **13,** 430; 10.1038/s41467-022-28043-y (2022).

237. Cakir, B. *et al.* Engineering of human brain organoids with a functional vascular-like system. *Nature methods* **16,** 1169–1175; 10.1038/s41592-019-0586-5 (2019).

238. Park, J. *et al.* A 3D human triculture system modeling neurodegeneration and neuroinflammation in Alzheimer's disease. *Nature neuroscience* **21,** 941–951; 10.1038/s41593-018-0175-4 (2018).

239. Bhaduri, A. *et al.* Cell stress in cortical organoids impairs molecular subtype specification. *Nature* **578,** 142–148; 10.1038/s41586-020-1962-0 (2020).

240. Shi, Y. *et al.* Vascularized human cortical organoids (vOrganoids) model cortical development in vivo. *PLoS biology* **18,** e3000705; 10.1371/journal.pbio.3000705 (2020).

241. Wörsdörfer, P. *et al.* Generation of complex human organoid models including vascular networks by incorporation of mesodermal progenitor cells. *Scientific reports* **9,** 15663; 10.1038/s41598-019-52204-7 (2019).

242. Giandomenico, S. L., Sutcliffe, M. & Lancaster, M. A. Generation and long-term culture of advanced cerebral organoids for studying later stages of neural development. *Nature protocols* **16,** 579–602; 10.1038/s41596-020-00433-w (2021).

243. Lepiemme, F. *et al.* Oligodendrocyte precursors guide interneuron migration by unidirectional contact repulsion. *Science (New York, N.Y.)* **376,** eabn6204; 10.1126/science.abn6204 (2022).

244. Kim, H. *et al.* Pluripotent Stem Cell-Derived Cerebral Organoids Reveal Human Oligodendrogenesis with Dorsal and Ventral Origins. *Stem cell reports* **12,** 890–905; 10.1016/j.stemcr.2019.04.011 (2019).

245. Madhavan, M. *et al.* Induction of myelinating oligodendrocytes in human cortical spheroids. *Nature methods* **15,** 700–706; 10.1038/s41592-018-0081-4 (2018).

246. Marton, R. M. *et al.* Differentiation and maturation of oligodendrocytes in human three-dimensional neural cultures. *Nature neuroscience* **22,** 484–491; 10.1038/s41593-018-0316-9 (2019).

247. Qian, X. *et al.* Sliced Human Cortical Organoids for Modeling Distinct Cortical Layer Formation. *Cell stem cell* **26,** 766-781.e9; 10.1016/j.stem.2020.02.002 (2020).

248. Lancaster, M. A. & Knoblich, J. A. Generation of cerebral organoids from human pluripotent stem cells. *Nature protocols* **9,** 2329–2340; 10.1038/nprot.2014.158 (2014).

249. Doudna, J. A. & Charpentier, E. Genome editing. The new frontier of genome engineering with CRISPR-Cas9. *Science (New York, N.Y.)* **346,** 1258096; 10.1126/science.1258096 (2014).

250. Ran, F. A. *et al.* Genome engineering using the CRISPR-Cas9 system. *Nature protocols* **8,** 2281–2308; 10.1038/nprot.2013.143 (2013).

251. Li, H. & Durbin, R. Fast and accurate short read alignment with Burrows-Wheeler transform. *Bioinformatics (Oxford, England)* **25,** 1754–1760; 10.1093/bioinformatics/btp324 (2009).

252. McKenna, A. *et al.* The Genome Analysis Toolkit: a MapReduce framework for analyzing next-generation DNA sequencing data. *Genome research* **20,** 1297–1303; 10.1101/gr.107524.110 (2010).

253. Cingolani, P. *et al.* A program for annotating and predicting the effects of single nucleotide polymorphisms, SnpEff: SNPs in the genome of Drosophila melanogaster strain w1118; iso-2; iso-3. *Fly* **6,** 80–92; 10.4161/fly.19695 (2012).

254. Boeva, V. *et al.* Control-FREEC: a tool for assessing copy number and allelic content using next-generation sequencing data. *Bioinformatics (Oxford, England)* **28,** 423–425; 10.1093/bioinformatics/btr670 (2012).

255. Laemmli, U. K. Cleavage of structural proteins during the assembly of the head of bacteriophage T4. *Nature* **227,** 680–685; 10.1038/227680a0 (1970).

256. Pouchin, P. *et al.* Easing batch image processing from OMERO: a new toolbox for ImageJ. *F1000Research* **11,** 392; 10.12688/f1000research.110385.2 (2022).

257. Martin, M. Cutadapt removes adapter sequences from high-throughput sequencing reads. *EMBnet j.* **17,** 10; 10.14806/ej.17.1.200 (2011).

258. Dobin, A. *et al.* STAR: ultrafast universal RNA-seq aligner. *Bioinformatics (Oxford, England)* **29,** 15–21; 10.1093/bioinformatics/bts635 (2013).

259. Ramírez, F. *et al.* deepTools2: a next generation web server for deep-sequencing data analysis. *Nucleic acids research* **44,** W160-5; 10.1093/nar/gkw257 (2016).

260. Liao, Y., Smyth, G. K. & Shi, W. featureCounts: an efficient general purpose program for assigning sequence reads to genomic features. *Bioinformatics (Oxford, England)* **30,** 923–930; 10.1093/bioinformatics/btt656 (2014).

261. Love, M. I., Huber, W. & Anders, S. Moderated estimation of fold change and dispersion for RNA-seq data with DESeq2. *Genome biology* **15,** 550; 10.1186/s13059-014-0550-8 (2014).

262. Yu, G., Wang, L.-G., Han, Y. & He, Q.-Y. clusterProfiler: an R package for comparing biological themes among gene clusters. *Omics : a journal of integrative biology* **16,** 284–287; 10.1089/omi.2011.0118 (2012).

263. Simon Andrews. *FastQC: A Quality Control tool for High Throughput Sequence Data. Available online at http://www.bioinformatics.babraham.ac.uk/projects/fastqc Data* (2014).

264. Wingett, S. W. & Andrews, S. FastQ Screen: A tool for multi-genome mapping and quality control. *F1000Research* **7,** 1338; 10.12688/f1000research.15931.2 (2018).

265. Zheng, G. X. Y. *et al.* Massively parallel digital transcriptional profiling of single cells. *Nature communications* **8,** 14049; 10.1038/ncomms14049 (2017).

266. Heaton, H. *et al.* Souporcell: robust clustering of single-cell RNA-seq data by genotype without reference genotypes. *Nature methods* **17,** 615–620; 10.1038/s41592-020-0820-1 (2020).

267. Hao, Y. *et al.* Integrated analysis of multimodal single-cell data. *Cell* **184,** 3573-3587.e29; 10.1016/j.cell.2021.04.048 (2021).

268. Su, K., Wu, Z. & Wu, H. Simulation, power evaluation and sample size recommendation for single-cell RNA-seq. *Bioinformatics (Oxford, England)* **36,** 4860–4868; 10.1093/bioinformatics/btaa607 (2020).

269. Choudhary, S. & Satija, R. Comparison and evaluation of statistical error models for scRNA-seq. *Genome biology* **23,** 27; 10.1186/s13059-021-02584-9 (2022).

270. Stuart, T. *et al.* Comprehensive Integration of Single-Cell Data. *Cell* **177,** 1888-1902.e21; 10.1016/j.cell.2019.05.031 (2019).

271. He, Z. *et al.* An integrated transcriptomic cell atlas of human neural organoids. *Nature* **635,** 690–698; 10.1038/s41586-024-08172-8 (2024).

272. Schep, A. N., Wu, B., Buenrostro, J. D. & Greenleaf, W. J. chromVAR: inferring transcription-factor-associated accessibility from single-cell epigenomic data. *Nature methods* **14,** 975–978; 10.1038/nmeth.4401 (2017).

273. Pedersen T. L. *ggraph: An Implementation of Grammar of Graphics for Graphs and Networks. R package version 2.2.1.9000, https://github.com/thomasp85/ggraph, https://ggraph.data-imaginist.com.* (2024).

274. Langmead, B. & Salzberg, S. L. Fast gapped-read alignment with Bowtie 2. *Nature methods* **9,** 357–359; 10.1038/nmeth.1923 (2012).

275. Zhang, Y. *et al.* Model-based analysis of ChIP-Seq (MACS). *Genome biology* **9,** R137; 10.1186/gb-2008-9-9-r137 (2008).

276. Yu, G., Wang, L.-G. & He, Q.-Y. ChIPseeker: an R/Bioconductor package for ChIP peak annotation, comparison and visualization. *Bioinformatics (Oxford, England)* **31,** 2382–2383; 10.1093/bioinformatics/btv145 (2015).

277. Ross-Innes, C. S. *et al.* Differential oestrogen receptor binding is associated with clinical outcome in breast cancer. *Nature* **481,** 389–393; 10.1038/nature10730 (2012).

278. Kaya-Okur, H. S., Janssens, D. H., Henikoff, J. G., Ahmad, K. & Henikoff, S. Efficient low-cost chromatin profiling with CUT&Tag. *Nature protocols* **15,** 3264–3283; 10.1038/s41596-020-0373-x (2020).

279. Kaya-Okur, H. S. *et al.* CUT&Tag for efficient epigenomic profiling of small samples and single cells. *Nature communications* **10,** 1930; 10.1038/s41467-019-09982-5 (2019).

280. Papillon, J. P. N. *et al.* Discovery of Orally Active Inhibitors of Brahma Homolog (BRM)/SMARCA2 ATPase Activity for the Treatment of Brahma Related Gene 1 (BRG1)/SMARCA4-Mutant Cancers. *Journal of medicinal chemistry* **61,** 10155–10172; 10.1021/acs.jmedchem.8b01318 (2018).

281. Iurlaro, M. *et al.* Mammalian SWI/SNF continuously restores local accessibility to chromatin. *Nature genetics* **53,** 279–287; 10.1038/s41588-020-00768-w (2021).

282. Schick, S. *et al.* Acute BAF perturbation causes immediate changes in chromatin accessibility. *Nature genetics* **53,** 269–278; 10.1038/s41588-021-00777-3 (2021).

283. Nasrallah, F. A., Garner, B., Ball, G. E. & Rae, C. Modulation of brain metabolism by very low concentrations of the commonly used drug delivery vehicle dimethyl sulfoxide (DMSO). *Journal of neuroscience research* **86,** 208–214; 10.1002/jnr.21477 (2008).

284. O'Sullivan, A. *et al.* Dimethylsulfoxide Inhibits Oligodendrocyte Fate Choice of Adult Neural Stem and Progenitor Cells. *Frontiers in neuroscience* **13,** 1242; 10.3389/fnins.2019.01242 (2019).

285. Tunçer, S. *et al.* Low dose dimethyl sulfoxide driven gross molecular changes have the potential to interfere with various cellular processes. *Scientific reports* **8,** 14828; 10.1038/s41598-018-33234-z (2018).

286. Verheijen, M. *et al.* DMSO induces drastic changes in human cellular processes and epigenetic landscape in vitro. *Scientific reports* **9,** 4641; 10.1038/s41598-019-40660-0 (2019).

287. Zhang, C. *et al.* Effects of dimethyl sulfoxide on the morphology and viability of primary cultured neurons and astrocytes. *Brain research bulletin* **128,** 34–39; 10.1016/j.brainresbull.2016.11.004 (2017).

288. Guangchuang Yu , Li-Gen Wang , GiovanniDall'Olio. *clusterProfiler* (Bioconductor, 2017).

289. Hamada, N. *et al.* Essential role of the nuclear isoform of RBFOX1, a candidate gene for autism spectrum disorders, in the brain development. *Scientific reports* **6,** 30805; 10.1038/srep30805 (2016).

290. Lee, J.-A. *et al.* Cytoplasmic Rbfox1 Regulates the Expression of Synaptic and Autism-Related Genes. *Neuron* **89,** 113–128; 10.1016/j.neuron.2015.11.025 (2016).

291. Vuong, C. K. *et al.* Rbfox1 Regulates Synaptic Transmission through the Inhibitory Neuron-Specific vSNARE Vamp1. *Neuron* **98,** 127-141.e7; 10.1016/j.neuron.2018.03.008 (2018).

292. Bill, B. R., Lowe, J. K., Dybuncio, C. T. & Fogel, B. L. Orchestration of neurodevelopmental programs by RBFOX1: implications for autism spectrum disorder. *International review of neurobiology* **113,** 251–267; 10.1016/B978-0-12-418700-9.00008-3 (2013).

293. O'Leary, A. *et al.* Behavioural and functional evidence revealing the role of RBFOX1 variation in multiple psychiatric disorders and traits. *Molecular psychiatry* **27,** 4464–4473; 10.1038/s41380-022-01722-4 (2022).

294. Singhal, N., Esch, D., Stehling, M. & Schöler, H. R. BRG1 Is Required to Maintain Pluripotency of Murine Embryonic Stem Cells. *BioResearch open access* **3,** 1–8; 10.1089/biores.2013.0047 (2014).

295. Blackwood, C. A. Jagged1 is Essential for Radial Glial Maintenance in the Cortical Proliferative Zone. *Neuroscience* **413,** 230–238; 10.1016/j.neuroscience.2019.05.062 (2019).

296. Sakamoto, M., Hirata, H., Ohtsuka, T., Bessho, Y. & Kageyama, R. The basic helix-loop-helix genes Hesr1/Hey1 and Hesr2/Hey2 regulate maintenance of neural precursor cells in the brain. *The Journal of biological chemistry* **278,** 44808–44815; 10.1074/jbc.M300448200 (2003).

297. Lebensohn, A. M. & Rohatgi, R. R-spondins can potentiate WNT signaling without LGRs. *eLife* **7**; 10.7554/eLife.33126 (2018).

298. Park, J., Hsiung, H.-A., Khven, I., La Manno, G. & Lutolf, M. P. Self-organizing in vitro mouse neural tube organoids mimic embryonic development. *Development* **149**; 10.1242/dev.201052 (2022).

299. Davideau, J. L. *et al.* Comparative study of MSX-2, DLX-5, and DLX-7 gene expression during early human tooth development. *Pediatric research* **46,** 650–656; 10.1203/00006450-199912000-00015 (1999).

300. Khadka, D., Luo, T. & Sargent, T. D. Msx1 and Msx2 have shared essential functions in neural crest but may be dispensable in epidermis and axis formation in Xenopus. *The International journal of developmental biology* **50,** 499–502; 10.1387/ijdb.052115dk (2006).

301. Monsoro-Burq, A.-H., Wang, E. & Harland, R. Msx1 and Pax3 cooperate to mediate FGF8 and WNT signals during Xenopus neural crest induction. *Developmental cell* **8,** 167–178; 10.1016/j.devcel.2004.12.017 (2005).

302. Wu, Y. *et al.* Versican V1 isoform induces neuronal differentiation and promotes neurite outgrowth. *Molecular biology of the cell* **15,** 2093–2104; 10.1091/mbc.e03-09-0667 (2004).

303. van der Raadt, J., van Gestel, S. H. C., Nadif Kasri, N. & Albers, C. A. ONECUT transcription factors induce neuronal characteristics and remodel chromatin accessibility. *Nucleic acids research* **47,** 5587–5602; 10.1093/nar/gkz273 (2019).

304. Lendahl, U., Zimmerman, L. B. & McKay, R. D. CNS stem cells express a new class of intermediate filament protein. *Cell* **60,** 585–595; 10.1016/0092-8674(90)90662-x (1990).

305. Stuart, T., Srivastava, A., Madad, S., Lareau, C. A. & Satija, R. Single-cell chromatin state analysis with Signac. *Nature methods* **18,** 1333–1341; 10.1038/s41592-021-01282-5 (2021).

306. Anderson, S. A., Eisenstat, D. D., Shi, L. & Rubenstein, J. L. Interneuron migration from basal forebrain to neocortex: dependence on Dlx genes. *Science (New York, N.Y.)* **278,** 474–476; 10.1126/science.278.5337.474 (1997).

307. Lodato, S. & Arlotta, P. Generating neuronal diversity in the mammalian cerebral cortex. *Annual review of cell and developmental biology* **31,** 699–720; 10.1146/annurev-cellbio-100814-125353 (2015).

308. Gorski, J. A. *et al.* Cortical excitatory neurons and glia, but not GABAergic neurons, are produced in the Emx1-expressing lineage. *The Journal of neuroscience : the official journal of the Society for Neuroscience* **22,** 6309–6314; 10.1523/JNEUROSCI.22-15-06309.2002 (2002).

309. Pombero, A., Garcia-Lopez, R. & Martinez, S. Brain mesenchymal stem cells: physiology and pathological implications. *Development, growth & differentiation* **58,** 469–480; 10.1111/dgd.12296 (2016).

310. James, J. M., Gewolb, C. & Bautch, V. L. Neurovascular development uses VEGF-A signaling to regulate blood vessel ingression into the neural tube. *Development* **136,** 833–841; 10.1242/dev.028845 (2009).

311. Raab, S. *et al.* Impaired brain angiogenesis and neuronal apoptosis induced by conditional homozygous inactivation of vascular endothelial growth factor. *Thrombosis and haemostasis* **91,** 595–605; 10.1160/TH03-09-0582 (2004).

312. Ba, H. *et al.* Insights into the molecular characteristics of embryonic cranial neural crest cells and their derived mesenchymal cell pools. *Communications biology* **7,** 1347; 10.1038/s42003-024-07056-x (2024).

313. Lim, Y. *et al.* Arx Expression Suppresses Ventralization of the Developing Dorsal Forebrain. *Scientific reports* **9,** 226; 10.1038/s41598-018-36194-6 (2019).

314. Ohira, R. *et al.* Human ARX gene: genomic characterization and expression. *Molecular genetics and metabolism* **77,** 179–188; 10.1016/S1096-7192(02)00126-9 (2002).

315. Jain, A. *et al. Morphodynamics of human early brain organoid development* (2023).

316. Fenby, B. T., Fotaki, V. & Mason, J. O. Pax3 regulates Wnt1 expression via a conserved binding site in the 5' proximal promoter. *Biochimica et biophysica acta* **1779,** 115–121; 10.1016/j.bbagrm.2007.11.008 (2008).

317. Zhao, T. *et al.* β-catenin regulates Pax3 and Cdx2 for caudal neural tube closure and elongation. *Development* **141,** 148–157; 10.1242/dev.101550 (2014).

318. Pan, Z. Z. Transcriptional control of Gad2. *Transcription* **3,** 68–72; 10.4161/trns.19511 (2012).

319. Azim, E., Jabaudon, D., Fame, R. M. & Macklis, J. D. SOX6 controls dorsal progenitor identity and interneuron diversity during neocortical development. *Nature neuroscience* **12,** 1238–1247; 10.1038/nn.2387 (2009).

320. Fleck, J. S. *et al.* Resolving organoid brain region identities by mapping single-cell genomic data to reference atlases. *Cell stem cell* **28,** 1148-1159.e8; 10.1016/j.stem.2021.02.015 (2021).

321. Larsen, K. B., Lutterodt, M. C., Møllgård, K. & Møller, M. Expression of the homeobox genes OTX2 and OTX1 in the early developing human brain. *The journal of histochemistry and cytochemistry : official journal of the Histochemistry Society* **58,** 669–678; 10.1369/jhc.2010.955757 (2010).

322. Anderson, S., Mione, M., Yun, K. & Rubenstein, J. L. Differential origins of neocortical projection and local circuit neurons: role of Dlx genes in neocortical interneuronogenesis. *Cerebral cortex (New York, N.Y. : 1991)* **9,** 646–654; 10.1093/cercor/9.6.646 (1999).

323. Rubenstein, J. L., Nord, A. S. & Ekker, M. DLX genes and proteins in mammalian forebrain development. *Development* **151**; 10.1242/dev.202684 (2024).

324. Bhaduri, A. *et al.* An atlas of cortical arealization identifies dynamic molecular signatures. *Nature* **598,** 200–204; 10.1038/s41586-021-03910-8 (2021).

325. Konno, D. *et al.* Dmrt factors determine the positional information of cerebral cortical progenitors via differential suppression of homeobox genes. *Development* **146**; 10.1242/dev.174243 (2019).

326. Piper, M. *et al.* NFIA controls telencephalic progenitor cell differentiation through repression of the Notch effector Hes1. *The Journal of Neuroscience* **30,** 9127–9139; 10.1523/JNEUROSCI.6167-09.2010 (2010).

327. Hu, H. Chemorepulsion of neuronal migration by Slit2 in the developing mammalian forebrain. *Neuron* **23,** 703–711; 10.1016/s0896-6273(01)80029-5 (1999).

328. Herbert, J. *et al.* Transthyretin: a choroid plexus-specific transport protein in human brain. The 1986 S. Weir Mitchell award. *Neurology* **36,** 900–911; 10.1212/wnl.36.7.900 (1986).

329. Megason, S. G. & McMahon, A. P. A mitogen gradient of dorsal midline Wnts organizes growth in the CNS. *Development* **129,** 2087–2098; 10.1242/dev.129.9.2087 (2002).

330. Shaul, O. How introns enhance gene expression. *The international journal of biochemistry & cell biology* **91,** 145–155; 10.1016/j.biocel.2017.06.016 (2017).

331. van Raay, T. J., Coffey, R. J. & Solnica-Krezel, L. Zebrafish Naked1 and Naked2 antagonize both canonical and non-canonical Wnt signaling. *Developmental biology* **309,** 151–168; 10.1016/j.ydbio.2007.04.018 (2007).

332. van Raay, T. J. *et al.* Naked1 antagonizes Wnt signaling by preventing nuclear accumulation of β-catenin. *PloS one* **6,** e18650; 10.1371/journal.pone.0018650 (2011).

333. Dufour, D. *et al.* Loss of SUMO-specific protease 2 causes isolated glucocorticoid deficiency by blocking adrenal cortex zonal transdifferentiation in mice. *Nature communications* **13,** 7858; 10.1038/s41467-022-35526-5 (2022).

334. Jiang, Q.-F., Tian, Y.-W., Shen, Q., Xue, H.-Z. & Li, K. SENP2 regulated the stability of β-catenin through WWOX in hepatocellular carcinoma cell. *Tumour biology : the journal of the International Society for Oncodevelopmental Biology and Medicine* **35,** 9677–9682; 10.1007/s13277-014-2239-8 (2014).

335. Aruga, J. & Millen, K. J. ZIC1 Function in Normal Cerebellar Development and Human Developmental Pathology. *Advances in experimental medicine and biology* **1046,** 249–268; 10.1007/978-981-10-7311-3_13 (2018).

336. Blank, M. C. *et al.* Multiple developmental programs are altered by loss of Zic1 and Zic4 to cause Dandy-Walker malformation cerebellar pathogenesis. *Development* **138,** 1207–1216; 10.1242/dev.054114 (2011).

337. Elsen, G. E., Choi, L. Y., Millen, K. J., Grinblat, Y. & Prince, V. E. Zic1 and Zic4 regulate zebrafish roof plate specification and hindbrain ventricle morphogenesis. *Developmental biology* **314,** 376–392; 10.1016/j.ydbio.2007.12.006 (2008).

338. Gaston-Massuet, C., Henderson, D. J., Greene, N. D. E. & Copp, A. J. Zic4, a zinc-finger transcription factor, is expressed in the developing mouse nervous system. *Developmental dynamics : an official publication of the American Association of Anatomists* **233,** 1110–1115; 10.1002/dvdy.20417 (2005).

339. Liem, K. F., Tremml, G., Roelink, H. & Jessell, T. M. Dorsal differentiation of neural plate cells induced by BMP-mediated signals from epidermal ectoderm. *Cell* **82,** 969–979; 10.1016/0092-8674(95)90276-7 (1995).

340. Guglielmi, L. *et al.* Temporal control of Wnt signaling is required for habenular neuron diversity and brain asymmetry. *Development* **147**; 10.1242/dev.182865 (2020).

341. Hu, Y.-A. *et al.* Expression pattern of Wnt inhibitor factor 1(Wif1) during the development in mouse CNS. *Gene expression patterns : GEP* **8,** 515–522; 10.1016/j.gep.2008.06.001 (2008).

342. Liu, J. *et al.* Wnt/β-catenin signalling: function, biological mechanisms, and therapeutic opportunities. *Signal transduction and targeted therapy* **7,** 3; 10.1038/s41392-021-00762-6 (2022).

343. Hussein, S. M., Duff, E. K. & Sirard, C. Smad4 and beta-catenin co-activators functionally interact with lymphoid-enhancing factor to regulate graded expression of Msx2. *The Journal of biological chemistry* **278,** 48805–48814; 10.1074/jbc.M305472200 (2003).

344. Zhai, Y. *et al.* MSX2 is an oncogenic downstream target of activated WNT signaling in ovarian endometrioid adenocarcinoma. *Oncogene* **30,** 4152–4162; 10.1038/onc.2011.123 (2011).

345. Yao, Z. *et al.* A high-resolution transcriptomic and spatial atlas of cell types in the whole mouse brain. *Nature* **624,** 317–332; 10.1038/s41586-023-06812-z (2023).

346. Valvezan, A. J. & Klein, P. S. GSK-3 and Wnt Signaling in Neurogenesis and Bipolar Disorder. *Frontiers in molecular neuroscience* **5,** 1; 10.3389/fnmol.2012.00001 (2012).

347. Janssens, S., Denayer, T., Deroo, T., van Roy, F. & Vleminckx, K. Direct control of Hoxd1 and Irx3 expression by Wnt/beta-catenin signaling during anteroposterior patterning of the neural axis in Xenopus. *The International journal of developmental biology* **54,** 1435–1442; 10.1387/ijdb.092985sj (2010).

348. Kim, D. & Ackerman, S. L. The UNC5C netrin receptor regulates dorsal guidance of mouse hindbrain axons. *The Journal of Neuroscience* **31,** 2167–2179; 10.1523/JNEUROSCI.5254-10.2011 (2011).

349. Vals, M.-A. *et al.* Coffin-Siris Syndrome with obesity, macrocephaly, hepatomegaly and hyperinsulinism caused by a mutation in the ARID1B gene. *European journal of human genetics : EJHG* **22,** 1327–1329; 10.1038/ejhg.2014.25 (2014).

350. Francis, F. *et al.* Doublecortin is a developmentally regulated, microtubule-associated protein expressed in migrating and differentiating neurons. *Neuron* **23,** 247–256; 10.1016/s0896-6273(00)80777-1 (1999).

351. Britanova, O. *et al.* Satb2 is a postmitotic determinant for upper-layer neuron specification in the neocortex. *Neuron* **57,** 378–392; 10.1016/j.neuron.2007.12.028 (2008).

352. Kim, K. K., Nam, J., Mukouyama, Y. & Kawamoto, S. Rbfox3-regulated alternative splicing of Numb promotes neuronal differentiation during development. *The Journal of Cell Biology* **200,** 443–458; 10.1083/jcb.201206146 (2013).

353. Hoch, R. V., Lindtner, S., Price, J. D. & Rubenstein, J. L. R. OTX2 Transcription Factor Controls Regional Patterning within the Medial Ganglionic Eminence and Regional Identity of the Septum. *Cell reports* **12,** 482–494; 10.1016/j.celrep.2015.06.043 (2015).

354. Lombares, C. de *et al.* Dlx5 and Dlx6 expression in GABAergic neurons controls behavior, metabolism, healthy aging and lifespan. *Aging* **11,** 6638–6656; 10.18632/aging.102141 (2019).

355. Liodis, P. *et al.* Lhx6 activity is required for the normal migration and specification of cortical interneuron subtypes. *The Journal of Neuroscience* **27,** 3078–3089; 10.1523/JNEUROSCI.3055-06.2007 (2007).

356. Rhinn, M. *et al.* Sequential roles for Otx2 in visceral endoderm and neuroectoderm for forebrain and midbrain induction and specification. *Development* **125,** 845–856; 10.1242/dev.125.5.845 (1998).

357. Vernay, B. *et al.* Otx2 regulates subtype specification and neurogenesis in the midbrain. *The Journal of Neuroscience* **25,** 4856–4867; 10.1523/JNEUROSCI.5158-04.2005 (2005).

358. Seo, B. am *et al.* LARGE, an intellectual disability-associated protein, regulates AMPA-type glutamate receptor trafficking and memory. *Proceedings of the National Academy of Sciences of the United States of America* **115,** 7111–7116; 10.1073/pnas.1805060115 (2018).

359. Absalom, N. L. *et al.* Gain-of-function and loss-of-function GABRB3 variants lead to distinct clinical phenotypes in patients with developmental and epileptic encephalopathies. *Nature communications* **13,** 1822; 10.1038/s41467-022-29280-x (2022).

360. Shi, Y.-W. *et al.* Synaptic clustering differences due to different GABRB3 mutations cause variable epilepsy syndromes. *Brain : a journal of neurology* **142,** 3028–3044; 10.1093/brain/awz250 (2019).

361. Dumont, V. & Lehtonen, S. PACSIN proteins in vivo: Roles in development and physiology. *Acta physiologica (Oxford, England)* **234,** e13783; 10.1111/apha.13783 (2022).

362. Gao, X. *et al.* ES cell pluripotency and germ-layer formation require the SWI/SNF chromatin remodeling component BAF250a. *Proceedings of the National Academy of Sciences of the United States of America* **105,** 6656–6661; 10.1073/pnas.0801802105 (2008).

363. Valencia, A. M. *et al.* Landscape of mSWI/SNF chromatin remodeling complex perturbations in neurodevelopmental disorders. *Nature genetics* **55,** 1400–1412; 10.1038/s41588-023-01451-6 (2023).

364. DeBassio, W. A., Kemper, T. L. & Knoefel, J. E. Coffin-Siris syndrome. Neuropathologic findings. *Archives of neurology* **42,** 350–353; 10.1001/archneur.1985.04060040060012 (1985).

365. Wieczorek, D. *et al.* A comprehensive molecular study on Coffin-Siris and Nicolaides-Baraitser syndromes identifies a broad molecular and clinical spectrum converging on altered chromatin remodeling. *Human molecular genetics* **22,** 5121–5135; 10.1093/hmg/ddt366 (2013).

366. Nickl-Jockschat, T. *et al.* Brain structure anomalies in autism spectrum disorder--a meta-analysis of VBM studies using anatomic likelihood estimation. *Human Brain Mapping* **33,** 1470–1489; 10.1002/hbm.21299 (2012).

367. DeLisi, L. E., Szulc, K. U., Bertisch, H. C., Majcher, M. & Brown, K. Understanding structural brain changes in schizophrenia. *Dialogues in Clinical Neuroscience* **8,** 71–78; 10.31887/DCNS.2006.8.1/ldelisi (2006).

368. Jin, Y. *et al.* Loss of BAF (mSWI/SNF) chromatin-remodeling ATPase Brg1 causes multiple malformations of cortical development in mice. *Human molecular genetics* **31,** 3504–3520; 10.1093/hmg/ddac127 (2022).

369. Sokpor, G. *et al.* Loss of BAF Complex in Developing Cortex Perturbs Radial Neuronal Migration in a WNT Signaling-Dependent Manner. *Frontiers in molecular neuroscience* **14,** 687581; 10.3389/fnmol.2021.687581 (2021).

370. Celen, C. *et al.* Arid1b haploinsufficient mice reveal neuropsychiatric phenotypes and reversible causes of growth impairment. *eLife* **6**; 10.7554/eLife.25730 (2017).

371. Menendez, L., Yatskievych, T. A., Antin, P. B. & Dalton, S. Wnt signaling and a Smad pathway blockade direct the differentiation of human pluripotent stem cells to multipotent neural crest cells. *Proceedings of the National Academy of Sciences of the United States of America* **108,** 19240–19245; 10.1073/pnas.1113746108 (2011).

372. Mica, Y., Lee, G., Chambers, S. M., Tomishima, M. J. & Studer, L. Modeling neural crest induction, melanocyte specification, and disease-related pigmentation defects in hESCs and patient-specific iPSCs. *Cell reports* **3,** 1140–1152; 10.1016/j.celrep.2013.03.025 (2013).

373. Notaras, M. *et al.* Schizophrenia is defined by cell-specific neuropathology and multiple neurodevelopmental mechanisms in patient-derived cerebral organoids. *Molecular psychiatry* **27,** 1416–1434; 10.1038/s41380-021-01316-6 (2022).

374. Courchesne, E. *et al.* Embryonic origin of two ASD subtypes of social symptom severity: the larger the brain cortical organoid size, the more severe the social symptoms. *Molecular autism* **15,** 22; 10.1186/s13229-024-00602-8 (2024).

375. Keskinen, S. *et al.* Prenatal Coffin-Siris Syndrome: Expanding the Phenotypic and Genotypic Spectrum of the Disease. *Pediatric and developmental pathology : the official journal of the Society for Pediatric Pathology and the Paediatric Pathology Society* **27,** 181–186; 10.1177/10935266231210155 (2024).

376. Eroglu, E. *et al.* SWI/SNF complex prevents lineage reversion and induces temporal patterning in neural stem cells. *Cell* **156,** 1259–1273; 10.1016/j.cell.2014.01.053 (2014).

377. Liu, P.-P. *et al.* Abnormal chromatin remodeling caused by ARID1A deletion leads to malformation of the dentate gyrus. *Cell death and differentiation* **30,** 2187–2199; 10.1038/s41418-023-01199-w (2023).

378. Pagliaroli, L. *et al.* Inability to switch from ARID1A-BAF to ARID1B-BAF impairs exit from pluripotency and commitment towards neural crest formation in ARID1B-related neurodevelopmental disorders. *Nature communications* **12,** 6469; 10.1038/s41467-021-26810-x (2021).

379. Keegan, S. E., Haskins, J., Simmonds, A. J. & Hughes, S. C. A chromatin remodelling SWI/SNF subunit, Snr1, regulates neural stem cell determination and differentiation. *Development* **150**; 10.1242/dev.201484 (2023).

380. Deng, L., Li, G., Rao, B. & Li, H. Central nervous system-specific knockout of Brg1 causes growth retardation and neuronal degeneration. *Brain research* **1622,** 186–195; 10.1016/j.brainres.2015.06.027 (2015).

381. Martins-Costa, C. *et al.* ARID1B controls transcriptional programs of axon projection in an organoid model of the human corpus callosum. *Cell stem cell* **31,** 866-885.e14; 10.1016/j.stem.2024.04.014 (2024).

382. Chenn, A. & Walsh, C. A. Regulation of cerebral cortical size by control of cell cycle exit in neural precursors. *Science (New York, N.Y.)* **297,** 365–369; 10.1126/science.1074192 (2002).

383. Kalani, M. Y. S. *et al.* Wnt-mediated self-renewal of neural stem/progenitor cells. *Proceedings of the National Academy of Sciences of the United States of America* **105,** 16970–16975; 10.1073/pnas.0808616105 (2008).

384. Li, H. S. *et al.* Inactivation of Numb and Numblike in embryonic dorsal forebrain impairs neurogenesis and disrupts cortical morphogenesis. *Neuron* **40,** 1105–1118; 10.1016/s0896-6273(03)00755-4 (2003).

385. Zhong, W., Jiang, M. M., Weinmaster, G., Jan, L. Y. & Jan, Y. N. Differential expression of mammalian Numb, Numblike and Notch1 suggests distinct roles during mouse cortical neurogenesis. *Development* **124,** 1887–1897; 10.1242/dev.124.10.1887 (1997).

386. Koe, C. T. *et al.* The Brm-HDAC3-Erm repressor complex suppresses dedifferentiation in Drosophila type II neuroblast lineages. *eLife* **3,** e01906; 10.7554/eLife.01906 (2014).

387. Zhu, Y. *et al.* Smarcd1 Inhibits the Malignant Phenotypes of Human Glioblastoma Cells via Crosstalk with Notch1. *Molecular neurobiology* **58,** 1438–1452; 10.1007/s12035-020-02190-z (2021).

388. Vasileiou, G. *et al.* Chromatin-Remodeling-Factor ARID1B Represses Wnt/β-Catenin Signaling. *American journal of human genetics* **97,** 445–456; 10.1016/j.ajhg.2015.08.002 (2015).

389. Abbas, E. *et al.* Conditional Loss of BAF (mSWI/SNF) Scaffolding Subunits Affects Specification and Proliferation of Oligodendrocyte Precursors in Developing Mouse Forebrain. *Frontiers in Cell and Developmental Biology* **9,** 619538; 10.3389/fcell.2021.619538 (2021).

390. Wischhof, L. *et al.* BCL7A-containing SWI/SNF/BAF complexes modulate mitochondrial bioenergetics during neural progenitor differentiation. *The EMBO journal* **41,** e110595; 10.15252/embj.2022110595 (2022).

391. Bischof, M., Weider, M., Küspert, M., Nave, K.-A. & Wegner, M. Brg1-dependent chromatin remodelling is not essentially required during oligodendroglial differentiation. *The Journal of Neuroscience* **35,** 21–35; 10.1523/JNEUROSCI.1468-14.2015 (2015).

392. Liu, Z. *et al.* Induction of oligodendrocyte differentiation by Olig2 and Sox10: evidence for reciprocal interactions and dosage-dependent mechanisms. *Developmental biology* **302,** 683–693; 10.1016/j.ydbio.2006.10.007 (2007).

393. Lei, I., Tian, S., Chen, V., Zhao, Y. & Wang, Z. SWI/SNF Component BAF250a Coordinates OCT4 and WNT Signaling Pathway to Control Cardiac Lineage Differentiation. *Frontiers in Cell and Developmental Biology* **7,** 358; 10.3389/fcell.2019.00358 (2019).

394. Nguyen, H. *et al.* Epigenetic Regulation by BAF Complexes Limits Neural Stem Cell Proliferation by Suppressing Wnt Signaling in Late Embryonic Development. *Stem cell reports* **10,** 1734–1750; 10.1016/j.stemcr.2018.04.014 (2018).

395. Metzis, V. *et al.* Nervous System Regionalization Entails Axial Allocation before Neural Differentiation. *Cell* **175,** 1105-1118.e17; 10.1016/j.cell.2018.09.040 (2018).

396. Leibovitz, Z., Lerman-Sagie, T. & Haddad, L. Fetal Brain Development: Regulating Processes and Related Malformations. *Life (Basel, Switzerland)* **12**; 10.3390/life12060809 (2022).

397. Mercurio, S., Serra, L. & Nicolis, S. K. More than just Stem Cells: Functional Roles of the Transcription Factor Sox2 in Differentiated Glia and Neurons. *International journal of molecular sciences* **20**; 10.3390/ijms20184540 (2019).

398. Geng, Z., Tai, Y. T., Wang, Q. & Gao, Z. AUTS2 disruption causes neuronal differentiation defects in human cerebral organoids through hyperactivation of the WNT/β-catenin pathway. *Scientific reports* **14,** 19522; 10.1038/s41598-024-69912-4 (2024).

399. Srikanth, P. *et al.* Shared effects of DISC1 disruption and elevated WNT signaling in human cerebral organoids. *Translational psychiatry* **8,** 77; 10.1038/s41398-018-0122-x (2018).

400. Chang, L. *et al.* The SWI/SNF complex is a mechanoregulated inhibitor of YAP and TAZ. *Nature* **563,** 265–269; 10.1038/s41586-018-0658-1 (2018).

401. Heyne, H. O. *et al.* De novo variants in neurodevelopmental disorders with epilepsy. *Nature genetics* **50,** 1048–1053; 10.1038/s41588-018-0143-7 (2018).

402. Hernandez, C. C. & Macdonald, R. L. A structural look at GABAA receptor mutations linked to epilepsy syndromes. *Brain research* **1714,** 234–247; 10.1016/j.brainres.2019.03.004 (2019).

403. Maljevic, S. *et al.* Spectrum of GABAA receptor variants in epilepsy. *Current opinion in neurology* **32,** 183–190; 10.1097/WCO.0000000000000657 (2019).

404. Schael, S. *et al.* Casein kinase 2 phosphorylation of protein kinase C and casein kinase 2 substrate in neurons (PACSIN) 1 protein regulates neuronal spine formation. *The Journal of biological chemistry* **288,** 9303–9312; 10.1074/jbc.M113.461293 (2013).

405. Dharmalingam, E. *et al.* F-BAR proteins of the syndapin family shape the plasma membrane and are crucial for neuromorphogenesis. *The Journal of Neuroscience* **29,** 13315–13327; 10.1523/JNEUROSCI.3973-09.2009 (2009).

406. Koch, N. *et al.* Syndapin I Loss-of-Function in Mice Leads to Schizophrenia-Like Symptoms. *Cerebral cortex (New York, N.Y. : 1991)* **30,** 4306–4324; 10.1093/cercor/bhaa013 (2020).

407. Kang, M.-G. *et al.* Proteomic analysis of α-amino-3-hydroxy-5-methyl-4-isoxazole propionate receptor complexes. *The Journal of biological chemistry* **287,** 28632–28645; 10.1074/jbc.M111.336644 (2012).

408. Ka, M., Chopra, D. A., Dravid, S. M. & Kim, W.-Y. Essential Roles for ARID1B in Dendritic Arborization and Spine Morphology of Developing Pyramidal Neurons. *The Journal of Neuroscience* **36,** 2723–2742; 10.1523/JNEUROSCI.2321-15.2016 (2016).

409. Jung, E.-M. *et al.* Arid1b haploinsufficiency disrupts cortical interneuron development and mouse behavior. *Nature neuroscience* **20,** 1694–1707; 10.1038/s41593-017-0013-0 (2017).

410. Li, H. *et al.* Identification and Analysis of ZIC-Related Genes in Cerebellum of Autism Spectrum Disorders. *Neuropsychiatric disease and treatment* **20,** 325–339; 10.2147/NDT.S444138 (2024).

411. Huang, Y. *et al.* Neural Tube Defects and ZIC4 Hypomethylation in Relation to Polycyclic Aromatic Hydrocarbon Exposure. *Frontiers in Cell and Developmental Biology* **8,** 582661; 10.3389/fcell.2020.582661 (2020).

412. Bartosovic, M., Kabbe, M. & Castelo-Branco, G. Single-cell CUT&Tag profiles histone modifications and transcription factors in complex tissues. *Nature biotechnology* **39,** 825–835; 10.1038/s41587-021-00869-9 (2021).

413. Skene, P. J. & Henikoff, S. An efficient targeted nuclease strategy for high-resolution mapping of DNA binding sites. *eLife* **6**; 10.7554/eLife.21856 (2017).

414. Kong, N. R., Chai, L., Tenen, D. G. & Bassal, M. A. A modified CUT&RUN protocol and analysis pipeline to identify transcription factor binding sites in human cell lines. *STAR protocols* **2,** 100750; 10.1016/j.xpro.2021.100750 (2021).

415. Cho, K. F. *et al.* Proximity labeling in mammalian cells with TurboID and split-TurboID. *Nature protocols* **15,** 3971–3999; 10.1038/s41596-020-0399-0 (2020).

416. Nabet, B. *et al.* The dTAG system for immediate and target-specific protein degradation. *Nature chemical biology* **14,** 431–441; 10.1038/s41589-018-0021-8 (2018).

417. Pollen, A. A. *et al.* Molecular identity of human outer radial glia during cortical development. *Cell* **163,** 55–67; 10.1016/j.cell.2015.09.004 (2015).

418. Yoon, K. *et al.* Fibroblast growth factor receptor signaling promotes radial glial identity and interacts with Notch1 signaling in telencephalic progenitors. *The Journal of Neuroscience* **24,** 9497–9506; 10.1523/JNEUROSCI.0993-04.2004 (2004).

419. Zhang, J. & Jiao, J. Molecular Biomarkers for Embryonic and Adult Neural Stem Cell and Neurogenesis. *BioMed research international* **2015,** 727542; 10.1155/2015/727542 (2015).